Removal of a dumped rock cover with a low pressure jet

J.J. Schoen

Delft University of Technology

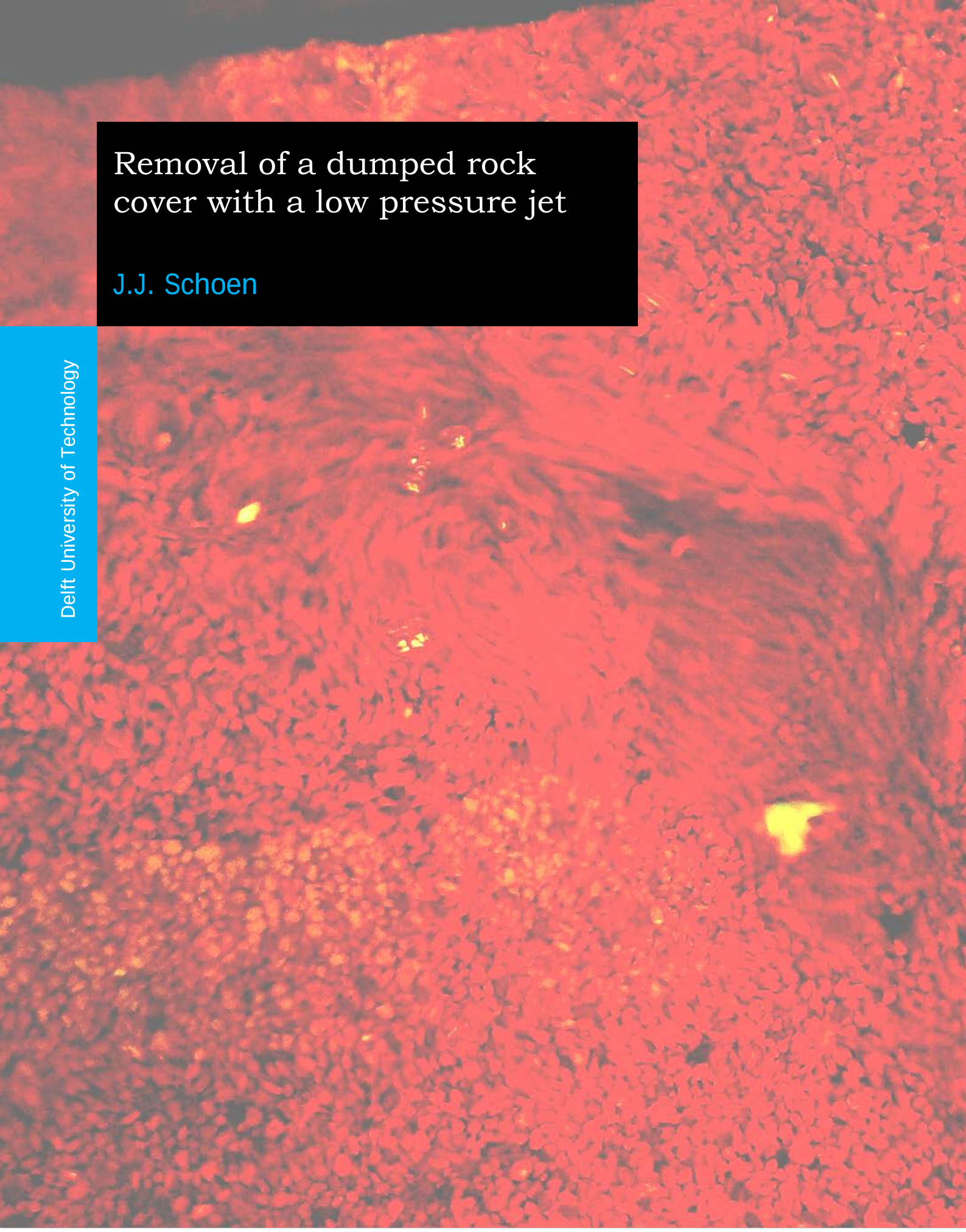

TU Delft Delft University of Technology

Challenge the future

Removal of a dumped rock cover with a low pressure jet

Master of Science Thesis
Jesper Jorrit Schoen

Delft, 2014

Graduation committee

Prof. dr. ir. C. van Rhee	Delft University of Technology
Dr. ir. A.M. Talmon	Delft University of Technology
Dr. ir. A.J. Nobel	Royal Boskalis Westminster N.V.
Ir. H.J. Verheij	Delft University of Technology

Delft University of Technology
Faculty of Civil Engineering and Geosciences
Department of Hydraulic Engineering
Delft, the Netherlands

Royal Boskalis Westminster N.V.
Dredging Development Department
Papendrecht, the Netherlands

Preface

This report forms the closure of the Master of Science program in Hydraulic Engineering at the Delft University of Technology. It is a great honour for me to have studied at the world's leading university in hydraulic engineering in arguably the best city to live in as a student.

I am grateful for the opportunities Boskalis gave me to perform my diverse graduation project at the company and I hope this report will lead to fruitful applications in the future. I would like to thank Arno for his support and academic heart, which convinced me to keep a critical eye on my results at all time. Special gratitude goes out to Pieter-Jan for enlightening our remote office location. Furthermore, I would like to thank the other members of my graduation committee for their time, knowledge and support.

Finally, I would like to thank Huize Pierre, my family and friends for helping me to forget this thesis outside office hours.

Jesper Schoen
Delft, October 2014

Abstract

Pipelines and cables on the sea bottom are usually protected by a cover of dumped rock. In case of maintenance or removal works, this cover has to be removed in order to expose the pipeline. This removal can be performed by means of a mass flow excavation process, created with a submerged jet flow. However, the exact erosion processes of a gravel bed with a low pressure water jet are not yet fully understood; as a result, the production cannot be accurately predicted.

The consisting theory about jetting in gravel is very limited. Most jet operations are performed in sand or clay, while the majority of the theory about erosion of gravel is based on relatively low energetic situations, such as rivers. Therefore, a literature study based on different aspects of hydraulic engineering is performed. The aim is to combine the theory of the various specialisations into one study, containing all relevant information.

A preliminary test series with a scale of 1:30 is performed in order to get insight in the erosion processes of a vertical jet, horizontally moving in the same direction as the pipeline. This method is commonly used with jetting operations in sand, and forms therefore a logical starting point for the experiments. However, tests shows that this working method results in a low production and seems therefore ineffective for the removal of a dumped rock cover.

Three test series focussing on alternative working methods are subsequently performed to determine the most feasible removal method. The trail direction of the nozzle, the jet angle relative to the bottom and the design of the nozzle are varied in these tests. These tests show that, depending on the flow and trail velocity, a trailing jet can behave as either a deflecting or a penetrating jet. Both jet behaviours have a different working method that is effective. The most feasible working method turns out to be a horizontal, penetrating, jet with a high hydraulic power, slowly moving along the pipeline.

An erosion model is created in order to model the penetrating behaviour of a jet. It is found that the generally used pick-up function of Van Rijn is not applicable to a situation with a jet flow eroding grains with a large diameter. The pick-up function of Fernandez Luque results in more accurate outcomes of the model, although the modelling of the settling of the stones does still not correspond with the observed processes.
A dimensionless erosion parameter E_{pen} is defined as a function of the initial flow velocity, stand-off distance, jet diameter and trail velocity. This parameter can be used to predict the penetrating behaviour of a trailing jet.

Table of contents

List of figures

List of tables

Nomenclature

Roman symbols

A	area	[m^2]
a	coefficient (with subscript)	[m/s]
b	width	[m]
	coefficient (with subscript)	[m^2/s^2]
c	concentration	[-]
C	coefficient (with subscript)	[-]
D	diameter	[m]
E	(erosion) parameter	[-]
e	fraction or percentage	[-]
	void ratio	[-]
f	function	
F	force	[N]
Fr	Froude number	[-]
g	gravitational acceleration	9.81 m/s^2
h	(water) depth	[m]
I	Momentum flux	[$kg.m/s^2$]
i	gradient	[-]
k	permeability	[m/s]
	coefficient (with subscript)	[-]
L	Length	[m]
m	coefficient	[-]
n	porosity	[-]
	scaling factor (with subscript)	[-]
p	pressure	[bar] ([Pa] or [mwc] if noted)
P	Power	[$kg.m^2/s^3$] = [W]
Pr	production rate	[m^3/s]
Q	flow rate	[m^3/s]
r	(radial) distance	[m]
	coefficient (with subscript)	[-]
R	hydraulic radius	[m]
Re	Reynolds number	[-]
s	distance	[m]
S	Sediment transport	[m^2/s]
T	Transport stage parameter	[-]
u	(flow) velocity	[m/s]

v	velocity	[m/s]
V	Volume	[m^3]
w	(settling) velocity	[m/s]
x	distance	[m]
y	depth	[m]
z	height	[m]

Greek symbols

α	angle (with subscript)	[deg]	θ	Shields parameter	[-]
	coefficient	[-]	κ	Von Kármán constant	0.41
β	angle (with subscript)	[deg]	λ	length	[m]
	coefficient	[-]	ν	kinematic viscosity	10^{-6} m^2/s
γ	angle		ρ	density	[kg/m^3]
δ	(layer) thickness	[m]	τ	shear stress	[Pa]
Δ	relative density	[-]	φ	angle (of internal friction)	[deg]
ϵ	coefficient	[-]	ψ	pick-up or settling flux	[$m^{-2}kg/s$]

Subscripts

b	bed	pw	propeller wash
c	characteristic	r	radial
ch	Chezy	rg	roughness
cr	critical	s	sediment
d	discharge	sc	scour
D	Drag	sl	slope
e	erosion	sp	sphere
j	jet	$stag$	stagnation
f	Darcy, seepage	t	turbulent
FL	Fernandez Luque	u	uniform
l	loose	vv	Van Veldhoven
m	maximum	w	water
$meas$	measured	zi	zone of impingement
n	nominal	0	initial
noz	nozzle	50	mean
p	pressure	//	parallel
pen	penetration	$\perp$	perpendicular

Abbreviations

DP	dynamic positioning
ROV	remotely operated vehicle
SOD	stand-off distance
TOP	top of pipe
TSHD	trailing suction hopper dredger

1 Introduction

Background

Due to the increasing energy demand of modern society, the extraction of oil and gas has shifted to relative remote locations, most notably offshore oil and gas fields. The offshore extraction and production facilities rely mainly on pipelines to transport the oil and gas to the shore. Furthermore, the increase of globalisation demands a connection between countries as well as continents, resulting in the offshore laying of electricity and network cables.
These developments have led to a vast network of pipelines and cables on the sea floor. Damage of this infrastructure is expensive and socially unacceptable; protection measures are therefore required. Three types of hazards can be distinguished. Waves and currents can cause movement of the pipe, but also scouring of the soil under the pipe, leading to deformation and stresses in the pipe or cable, which can result in failure. Secondly, shipping anchors or fishing trawls can damage the pipeline in case of a collision. Finally, a pipe can have the tendency to float, which has to be prevented.

A possible protection method against these hazards is to cover the cable or pipeline with rock. These rock covers are mostly constructed with a fall pipe vessel. However, this protective cover will also have the consequence that it will be more difficult to reach the pipe or cable when construction work is required. This will be the case if, despite of the protection, the pipe has been damaged and has to be repaired or even completely removed from the sea bed. It is also possible that a newly laid pipeline has to be connected to the, already covered, main transport pipeline in the network. In all these cases, the protective rock cover will have to be removed.

Water jets are commonly used by dredging companies to excavate soil. In general, two mechanisms of jetting are practiced: with high and low pressure. Jetting with relatively high pressure (>2 bar) is used to cut and loosen the soil during dredging activities. Low pressure jetting (<1 bar) is used for the so-called mass flow excavation, where soil is loosened and blown away by a single, relatively big nozzle. This last mechanism can also be used to remove the rock cover. However, experiences with, and therefore knowledge of, mass flow excavation of rocks or gravel are limited, as most excavation processes take place with sand or clay. Boskalis has the experience of removing a pipeline cover with mass flow excavation once. A nozzle was placed on the end of the ‘suction’ pipe of a TSHD for this project. Although the result was relatively convenient, accurate production rates were not acquired during the project. The production rate is defined as the removed volume of rock per unit of time and is a function of the jet flow parameters, i.e. the stand-off distance, pressure, nozzle diameter and the speed of the vessel. Moreover, Boskalis intends to use a fall-pipe ship for this kind of operations in the future. The most obvious working method with this vessel would be with a horizontally moving vertical jet, as is also common practice with similar dredging activities in sand. The combination of the uncertainties about the production rate as a function of the flow parameters and the working method has led to the necessity of this thesis.

Problem definition

The problem in this report is defined as:

A rock cover of a pipeline can be removed with the use of mass flow excavation. The exact erosion processes of a gravel bed with a low pressure water jet are however not yet fully understood; as a result, the production cannot be accurately predicted.

The main objectives of this study are defined as follows:

- To define the occurring erosion and sedimentation processes during mass flow excavation, and to determine the governing process that limits the production in the case of the removal of dumped rock
- To determine the most viable working method
- To predict the production corresponding to the most viable working method.

The study to reach this objective consists of multiple parts:

- A literature study of the existing theories of comparable processes
- A verification of the found theories with a physical scale model
- An evaluation of the possible working methods with a physical scale model
- A creation of a basic erosion, sedimentation and transport model that complies with the results of the physical model tests.

Report structure

The report consists of five parts, of which four parts correspond to the study described above. The first part treats the theory in Chapter 2, required to understand the processes occurring during the removal of dumped rock. It first discusses the characteristic soil parameters, before an extensive overview of the consisting theory about jetting, erosion, sedimentation and sediment transport is provided.
In order to make a scale model that accurately models the occurring processes, it is crucial that the scaling is performed correctly. This is discussed in Chapter 3, before a description of the experimental set-up is provided.
This experimental set-up is used for the preliminary tests, in order to get a first expression of the erosion processes and the viability of the proposed working method with horizontally moving vertical jet. The results of these tests are treated in Chapter 4.
It turns out that an analysis of the possible working methods is required in order to determine the most feasible removal method. Three test series, each focussing on a working method, are performed with the results as provided in Chapter 5. These outcomes lead to the prediction of the production of each working method in section 5.5.
Finally, an erosion model is required to predict the behaviour of the jet and the corresponding erosion processes. This model is discussed in Chapter 6, after which the conclusions and recommendations of the entire study are provided in Chapter 7.

2 Theory

2.1 Dumping of rock

A pipeline or cable can be protected against damage or floating by a rock cover. These rocks have to be accurately placed to function properly. The majority of stone dumping operations in offshore construction works are performed with a fall-pipe vessel. This vessel has the ability to accurately dump the stones by means of a fall-pipe with an inner diameter of about 0.7 m, lowered from the ship to a few meters above the sea floor. Most vessels use dynamic positioning (DP) to ensure an accurate position of the vessel. The maximum and minimum sail speed while maintaining DP and with the fall-pipe down are 0.5 m/s and 0.03 m/s respectively. To increase the accuracy of the dumping, the fall-pipe is controlled by a remotely operated vehicle (ROV) that is also capable of a visual survey of the process.

The end of the fall-pipe can be connected to a remotely operated jet system. This system contains a submerged pump and can be connected to a nozzle that concentrates the outflow of the water, effectively creating a low pressure water jet that may be able to remove the previously dumped rock cover.

2.1.1 Protective rock cover

Typical dimensions of a rock cover protecting a pipeline are provided in Figure 2.1. The width of the berm is about 1.0 - 2.0 m, with a cover height of about 1.0 m to the top of pipe (TOP). This means a total height above the sea floor of about 2.0 m. The slope of the rock cover is about 1:3, which makes the total width of the cover about 8.0 m at TOP and 14.0 m at the original sea bed level. The total width can be even larger if the pipe is placed on a rock bed as well, but this is not considered relevant for this study as only the cover height will have to be removed.

The rocks used for a pipeline cover are generally crushed rocks from a quarry near Averøy, Norway with a specific density of ρ_s = 2650 kg/m^3 and mean diameter of about D_{50} = 8.5 cm. The porosity is assumed to be between n_{max} = 0.45 and n_{min} = 0.30 for a loose and dense compaction respectively, while the permeability k of a gravel bed with the given grain diameter is about $k \approx 0.2$ m/s (Schiereck, 2004). The angle of repose φ is assumed to be $\varphi = 45°$. More information about the used rocks can be found in Appendix A.1.

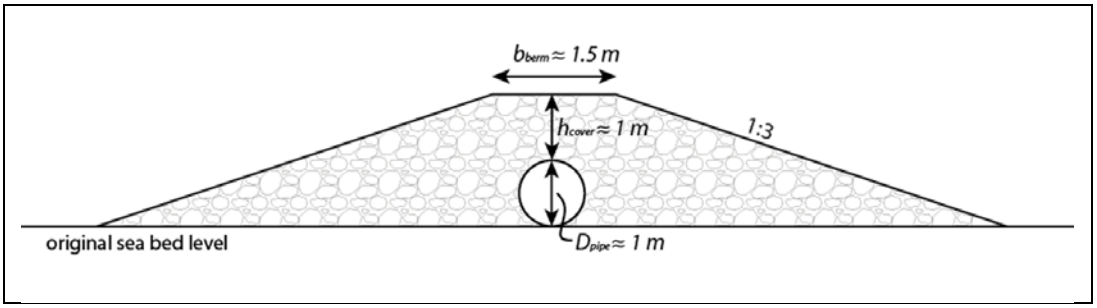

Figure 2.1 – Typical dimensions of a rock cover protecting a pipeline

2.1.2 Removal

In case of removal or maintenance works on the pipe, the protective rock cover has to be (partially) removed to clear the pipe. On at least one location the pipe may have to be cleared at all sides in order to inspect the total pipe all around. It is assumed that for the rest of the pipeline, only the cover height has to be removed to be able to take out the pipe. Also, it has to be prevented that the sand under the pipe is flushed away, creating a free span of the pipe that causes large shear forces.

A mass flow produced by a submerged jet is a common technique in dredging. This method is relatively simple and safe: the equipment is kept at a distance from the sea floor or pipe, preventing a possible collision. This technique can also be used to remove the stones, which has already been applied by Boskalis once, in Iran. During this project in Assaluyeh in 2008, a coverage of a pipeline consisting of 5'' stones was removed. The total length of the pipeline that had to be cleared was 138 m. The trailing suction hopper dredger *Seaway* was used for this job, where the dredge pump was used to deliver the required jet pressure. A nozzle was placed on the end of the suction pipe with a diameter of 0.5 m and a jet pressure that varied between 0.4 and 1.3 bar during the operation. The stand-off distance (SOD) of the jet varied between 2.5 and 3.5 m. To prevent the nozzle to collide with the bed, a minimum SOD is required that mainly depends on the wave height. It is assumed in this study that the minimum SOD should be about 3.0 m. The trail velocity of the vessel varied between 0.1 and 0.8 m/s.

2.2 Jetting

This section describes the process of jetting, including the flow development en velocity profile of the jet. A distinction has been made between a free and an impinging jet to describe the processes that will cause the erosion of the rock bed. A circular turbulent jet is generally used to create a mass flow in dredging practices; therefore, only this type of jet is assessed in this chapter.

2.2.1 Free circular turbulent jet

A typical flow profile of a jet is illustrated in Figure 2.2. Directly after the nozzle, the flow is uniform and the velocity u is equal to the maximum velocity u_m and initial velocity u_o:

$$u = u_m = u_0 \tag{2.1}$$

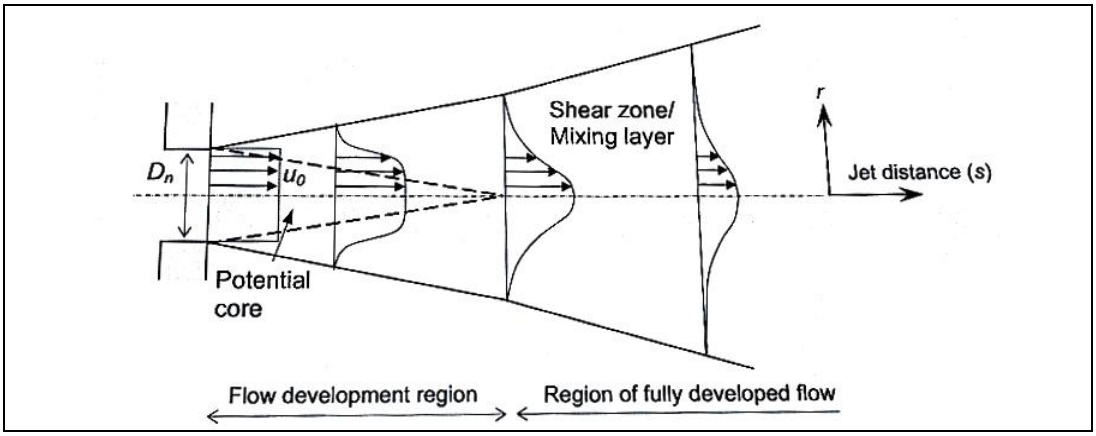

Figure 2.2 – Flow development profile of a jet (Nobel, 2013)

Since the flow velocity of the jet is higher than in the surrounding water, Reynolds shear stresses occur near the boundary of the jet flow, creating a mixing layer. This mixing layer influences the development of the flow profile. Water particles surrounding the jet flow are entrained, effectively increasing the total amount of flow and thus spreading of the jet action. However, it is stated that the momentum flux I [kg.m/s²] on any cross section of the jet flow is conserved, leading to (Rajaratnam, 1976):

$$I = \rho u Q = I_0 = \rho u_0 \cdot \left(\frac{\pi}{4} u_0 {D_0}^2\right) = \frac{\pi}{4} \rho {u_0}^2 {D_0}^2 = \text{constant} \tag{2.2}$$

With Q as the flow rate [m³/s] and D_0 the nozzle diameter [m]. This implies that the average flow velocity decreases when the flow rate increases. Entrainment has

therefore a negative relation with the flow velocity. This jet momentum also implies that a reaction force occurs in the opposite direction of the jet flow. This force causes the displacement of an insufficiently supported nozzle, and has to be taken into account when operating a jet with a relatively high hydraulic power *P* [W], expressed as:

$$P_j = Q_j \cdot p_j \tag{2.3}$$

The region where the turbulence is not yet penetrated into the flow profile has a cone-like shape and is called the potential core. In the entire potential core, the flow is uniform and Eq. (2.1) holds.

A relation between the initial velocity and the jet pressure can be found, assuming the Bernoulli principle:

$$u_0 = \sqrt{\frac{2p_j}{\rho_w}} \tag{2.4}$$

The jet flow can be divided into two regions, with the point where the mixing layer reaches the axis of the jet as boundary, which lies at about:

$$s = \sqrt{\frac{k_j}{2}} D_0 \tag{2.5}$$

With *s* the distance in axial direction [m] and k_j as an empirical constant, with an average value of 77. This means an average distance of about $6D_0$. The region before this boundary is called the flow development region, and is essentially the region where the potential core exists. The region after the end of the potential core is called the region of fully developed flow.

2.2.1.1 Flow development region

Two different flow patterns exist in the flow development region. In the potential core, the flow is uniform and equal to the initial velocity. In the mixing layer, turbulence occurs which causes the flow velocity to decrease with increasing distance from the axis. The flow velocity profile outside the potential core is assumed to be a half Gaussian distribution, which leads to the following equation to calculate the flow rate in the flow development region at a distance *s* from the nozzle (Albertson, et al., 1950):

$$Q_j = Q_0 \left[1 + 0.082\frac{s}{D_0} + 0.013\left(\frac{s}{D_0}\right)^2\right] \quad for\ s < \sqrt{\frac{k_j}{2}} D_0 \tag{2.6}$$

2.2.1.2 Region of fully developed flow

In the region of fully developed flow, the influence of the entrainment processes has penetrated to the axis of the jet flow, resulting in a decrease of the velocity in axial direction. The maximum velocity occurs in the axis and can be described as (Rajaratnam, 1976):

$$u_m = \sqrt{\frac{k_j}{2}} u_0 \frac{D_0}{s} \quad for\ s > \sqrt{\frac{k_j}{2}} D_0 \tag{2.7}$$

The velocity at each point in the jet flow can be calculated according to the equations provided in Appendix A.2. The flow rate can be found by (Albertson, et al., 1950):

$$Q_j = \sqrt{\frac{8}{k_j}} Q_0 \frac{s}{D_0} \quad for\ s > \sqrt{\frac{k_j}{2}} D_0 \tag{2.8}$$

This flow rate increases with the distance due to entrainment of the surrounding stagnant water. Differentiating Eq. (2.8) and with the use of α_{mom} as the entrainment coefficient [-] leads to:

$$\frac{dQ}{ds} = \alpha_{mom} \pi D_0 u_0 = \sqrt{\frac{1}{2k_j}} \pi D_0 u_0 \quad for\ s > \sqrt{\frac{k_j}{2}} D_0 \tag{2.9}$$

2.2.1.3 Simplification of free circular turbulent jet flow

The circular free jet has a momentum flux as described in Eq. (2.2). Together with the expressions (2.8) and (2.9), the jet can be modelled as a fictitious jet with the same momentum flux and flow rate, but with a uniform velocity. The uniform jet velocity and the fictitious jet radius can then be expressed as (Nobel, 2013):

$$u_u = u_0 \frac{D_0 \sqrt{\frac{k_j}{2}}}{s + D_0 \sqrt{\frac{k_j}{2}}} \quad for\ s < \sqrt{\frac{k_j}{2}} D_0 \tag{2.10}$$

$$r_u = \sqrt{\frac{1}{2k_j}} s + \frac{D_0}{2} \quad for\ s < \sqrt{\frac{k_j}{2}} D_0 \tag{2.11}$$

$$u_u = \frac{1}{2} \sqrt{\frac{k_j}{2}} u_0 \frac{D_0}{s} \quad for\ s > \sqrt{\frac{k_j}{2}} D_0 \tag{2.12}$$

$$r_u = \sqrt{\frac{2}{k_j}} s \quad for\ s > \sqrt{\frac{k_j}{2}} D_0 \tag{2.13}$$

With a value of k_j = 77, it can be found that at the end of the potential core, the boundary point between both flow regions, the uniform flow velocity is about 50% of the initial velocity, which is also the ratio found between the uniform and maximum velocity when comparing Eqs. (2.7) and (2.12).

2.2.2 Turbulence

The turbulence in a flow can be given as a ratio between the average fluctuation in flow velocity $\bar{u}'$ and the average flow velocity $\bar{u}$ (Schiereck, 2004):

$$r_t = \frac{\sqrt{\overline{u'}^2}}{\bar{u}} \tag{2.14}$$

The value of r_t [-] for jet flow can also be graphically derived from Figure 2.3. In these graphs, the value of r_t is related to u_m, instead of to the average flow at the location where the turbulence is determined. Note that the turbulence in the direction perpendicular to the flow is also related to u_m.

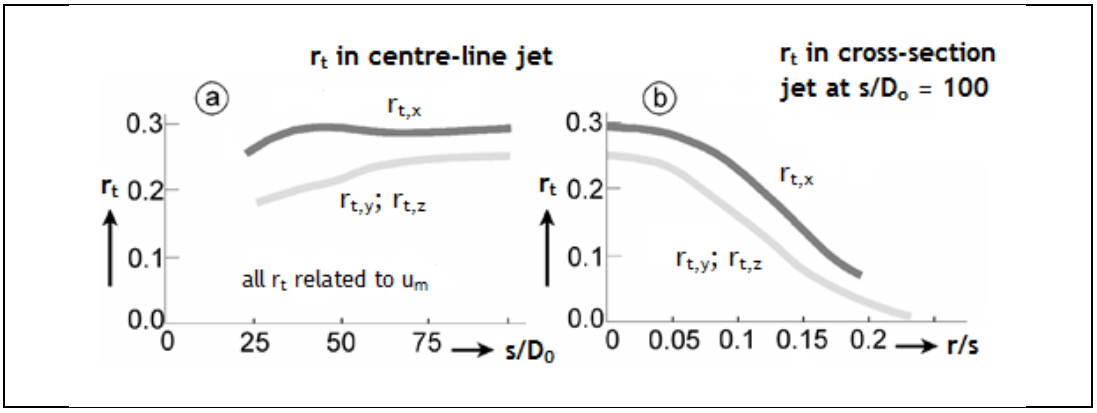

Figure 2.3 – Turbulence in a jet flow (Schiereck, 2004)

The total turbulence in all directions can be approximated by taking the average value of each direction. The total turbulent kinetic energy is therefore given by:

$$k_t = \frac{1}{2}\left(\overline{u'_x}^2 + \overline{u'_y}^2 + \overline{u'_z}^2\right) \approx \frac{3}{2}(\bar{r}_t u_m)^2 \tag{2.15}$$

For the order of magnitude of the ratio of s/D_0 corresponding to mass flow excavation, the average turbulence coefficient is about r_t = 0.1 - 0.2 in the centre line of the jet flow.

2.2.3 Stationary impinging circular turbulent jet

When the jet flow reaches the rock bed, the free circular jet will be influenced. It can either be deflected and spread radially outwards, changing into a radial wall jet, or it can penetrate the bed. The zone in which the jet hits the bed is called the zone of impingement, where a considerable amount of momentum flux is dissipated due to turbulence. The distance between the nozzle and the bed is called the stand-off distance (SOD). The behaviour of the jet in the zone of impingement depends on the flow regime. The influence of an oblique jet flow is treated in Appendix A.2.3

2.2.3.1 Flow regime

The impinging water jet can occur as two different flow regimes (Kobus, et al., 1979): a weakly and strongly deflective regime, see also Figure 2.4. The erosion parameter E_c [-] is used to describe the two regimes (Aderibigbe & Rajaratnam, 1996):

$$E_c = \frac{u_0 \cdot D_0}{s\sqrt{\Delta g D_{50}}} \tag{2.16}$$

With *s* the flow distance from the nozzle and *Δ* as the relative density [-]:

$$\Delta = \frac{\rho_s - \rho_w}{\rho_w} \tag{2.17}$$

The erosion parameter belonging to the particular flow regime is provided in Figure 2.4. The transition value between weakly and strongly deflected regime is with E_c = 0.35.

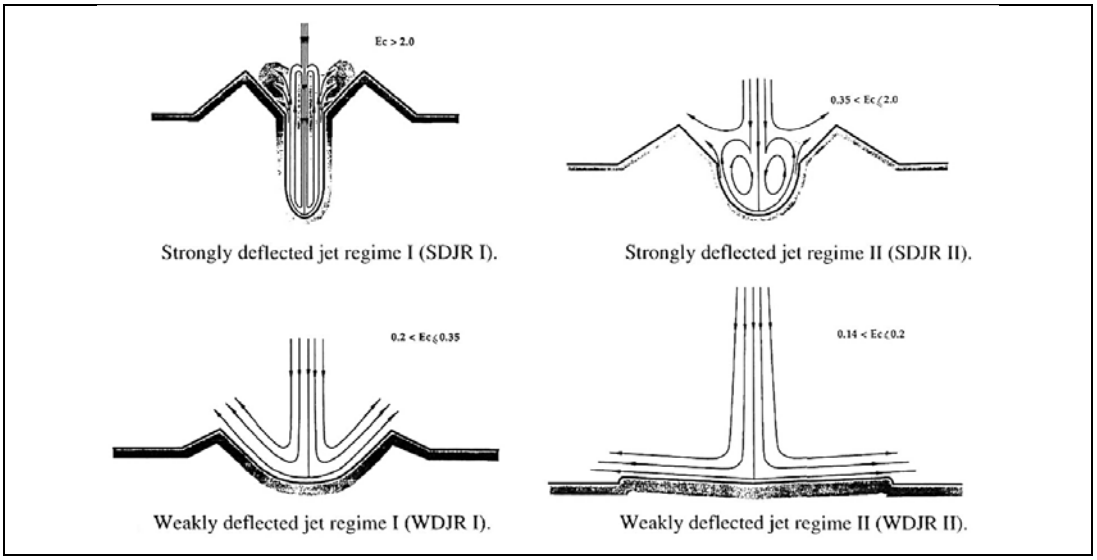

Figure 2.4 – Four possible jet flow regimes (Aderibigbe & Rajaratnam, 1996)

Kobus also found a proportional relationship for the erosion parameter:

$$E_{c,Kobus} \propto \frac{{u_b}^2}{{w_s}^2} \tag{2.18}$$

With w_s [m/s] as the fall velocity of a particle, which can be described as a function of $\sqrt{(\Delta g D_{50})}$, see also section 2.3.3. The near-bed velocity u_b can be described as proportional to the ratio of the initial jet diameter and the stand-off distance. This means that Eq. (2.16) depends on the same parameters as Eq. (2.18).

With a weakly deflective flow regime, the eroded material is transported out of the scour hole along the bed and is associated with flow velocities relatively close to the state of incipient motion. The strongly deflective flow regime shows a more concentrated scour hole with a relative high erosion velocity and relatively large

dynamic scour depth. However, the eroded sediments settle on the inner side of the scour hole. In this way, deposited material slides back towards the centre of erosion, causing renewed erosion while in fact no material is transported out of the scour hole (Aderibigbe & Rajaratnam, 1996). Also, the static scour depth, the erosion depth when the jet flow is stopped, is smaller due to the settling of suspended particles in the scour hole and the collapse of the steep slopes of the hole.

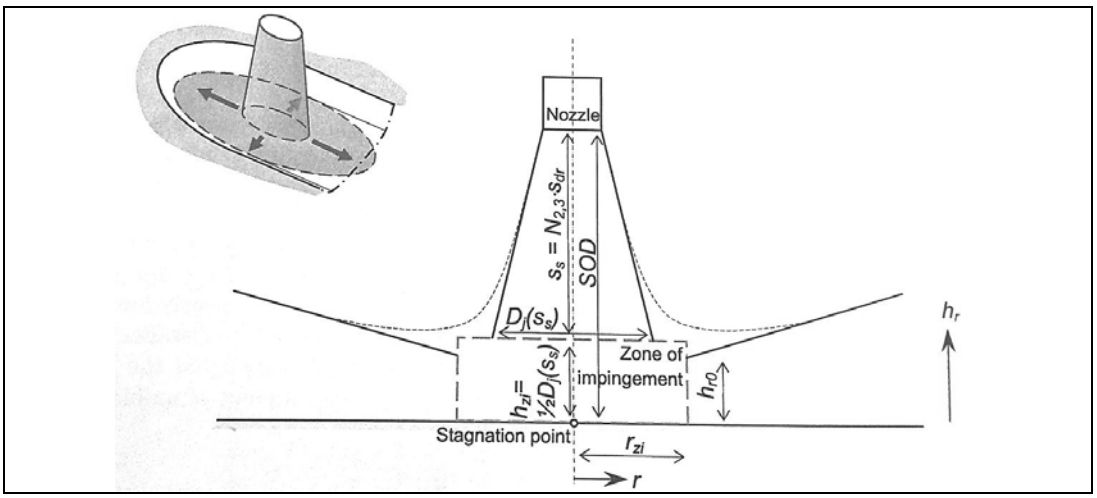

Figure 2.5 – An impinging circular jet (Nobel, 2013)

2.2.3.2 Stagnation point

The point where the axis of the jet reaches the soil is called the stagnation point, see also Figure 2.5. Because the stagnation point is the centre of the radial wall jet, the time average flow velocity in the stagnation point is $\bar{u} = 0$. If erosion depends on the shear forces acted by the flow, see also section 2.3, this would imply that no erosion occurs in this point. This is however not in correspondence with the observations in practice. This is probably caused by the relative large influence of turbulence in the stagnation point, causing fluctuating velocity components while the average velocity remains zero.

The impinging jet flow exerts a pressure on the soil in the stagnation point. A seepage flow will occur due to this pressure gradient given by:

$$Q_f = \bar{u}_f \pi {r_u}^2 \tag{2.19}$$

With $\bar{u}_f$ as the seepage velocity, that can be calculated with the Forchheimer equation (Schiereck, 2004):

$$i = \frac{dp}{dy} = -\frac{u_f}{a_f} - \frac{{u_f}^2}{b_f} \tag{2.20}$$

In which the pressure is expressed in [mwc]. The permeability of a granular filter depends on the smaller elements that can block the porous flow. Therefore, the parameters for the laminar permeability a_f [m/s] and turbulent permeability b_f [m^2/s^2] are a function of D_{15} and are respectively given by:

$$a_f = \frac{n^3}{\alpha(1-n)^2}\frac{g{D_{15}}^2}{\nu}$$
$$b_f = \frac{n^2 g D_{15}}{\beta} \quad (2.21)$$

The value of the coefficients α and β are estimated with α = 160 and β = 2.2 (Adel, 1987). The permeability k, as noted in Section 2.1.1, is a combination of the laminar and turbulent terms. For fine material, the flow through the pores is laminar and Eq. (2.20) reduces to the Darcy principle, with $k = a_f$. For more coarse material, about D_{50} > 6 cm (Schiereck, 2004), the second term on the right hand side of Eq. (2.20) is dominant. A more detailed determination of the seepage flow is provided in Appendix A.2.2.

With an increasing seepage flow rate, an increasing amount of energy is dissipated in the bed without any effect on the erosion of the bed (Kobus, et al., 1979). This seems to be logical, as the part of the jet flow that seeps into the bed cannot be converted to a radial wall jet. This process is further discussed in Section 2.2.4.

2.2.4 Radial wall jet

A deflected jet flow shows many similarities to a radial wall jet (Rajaratnam, 1976). The flow rate of this radial wall flow is given by means of a mass balance:

$$Q_r = Q_j - Q_f \quad (2.22)$$

The uniform radial jet velocity is then given by:

$$u_{u,r} = \frac{I_r}{\rho_w Q_r} = \frac{f_2 I}{\rho_w Q_r} \quad (2.23)$$

With f_2 as an empirical coefficient that describes the lost momentum flux in the zone of impingement, about f_2 = 0.7 (Nobel, 2013). The entrainment coefficient for a radial jet is given by the following expression, with the approximation of f_1 = 1.5:

$$\alpha_{mom,r} = f_1 \alpha_{mom} \quad (2.24)$$

The radial jet flow velocity and height can then be calculated with the following equations (Nobel, 2013):

$$u_{u,r} = u_0 \sqrt{\frac{f_2 {D_0}^2}{8 f_1 \alpha_{mom} r^2 + {D_0}^2 (N_2+1)^2 \left(\frac{1}{f_2} - 4 f_1 \alpha_{mom}\right)}} \quad for\ s < \sqrt{\frac{k_j}{2}} D_0 \quad (2.25)$$

$$h_r = f_1 \alpha_{mom} r + \frac{{D_0}^2 (N_2+1)^2 \left(\frac{1}{f_2} - 4 f_1 \alpha_{mom}\right)}{8r} \quad for\ s < \sqrt{\frac{k_j}{2}} D_0 \quad (2.26)$$

$$u_{u,r} = u_0 \sqrt{\frac{f_2 {D_0}^2}{8 f_1 \alpha_{mom} r^2 + 4 {D_0}^2 {N_3}^2 \left(\frac{1}{f_2} - 4 f_1 \alpha_{mom}\right)}} \quad for\ s > \sqrt{\frac{k_j}{2}} D_0 \tag{2.27}$$

$$h_r = f_1 \alpha_{mom} r + \frac{{D_0}^2 {N_3}^2 \left(\frac{1}{f_2} - 4 f_1 \alpha_{mom}\right)}{2r} \quad for\ s > \sqrt{\frac{k_j}{2}} D_0 \tag{2.28}$$

With:

$$N_2 = \frac{\frac{SOD}{D_0} - \frac{1}{2}}{\sqrt{\frac{k_j}{2}} + \frac{1}{2}} \tag{2.29}$$

$$N_3 = \frac{SOD}{D_0 \left(1 + \sqrt{\frac{k_j}{2}}\right)} \tag{2.30}$$

And valid for:

$$r > r_{zi} = \begin{cases} \frac{1}{2}\sqrt{2} D_0 (N_2 + 1) & for\ s < \sqrt{\frac{k_j}{2}} D_0 \\ \sqrt{2} D_0 N_3 & for\ s \geq \sqrt{\frac{k_j}{2}} D_0 \end{cases} \tag{2.31}$$

This schematisation of a radial wall jet assumes that the flow is deflected as if it would impinge on a sheet plate. This assumption is only true in the very first phase of erosion; subsequently, erosion will causes scouring. This has two effects for the impinging jet flow, both illustrated in Figure 2.6. First, the distance between the jet and the bed increases, as the bed level decreases. Second, the erosion results in a scour profile with an increasing bed level in radial distance. It is assumed that the flow velocity does not decrease due to the extra height difference that has to be overcome when flowing out of the scour hole. However, the radial distance increases relatively, as the length along the scour hole is longer than along the initial bed. The erosion process causes therefore only an increase of *SOD* and *r*.

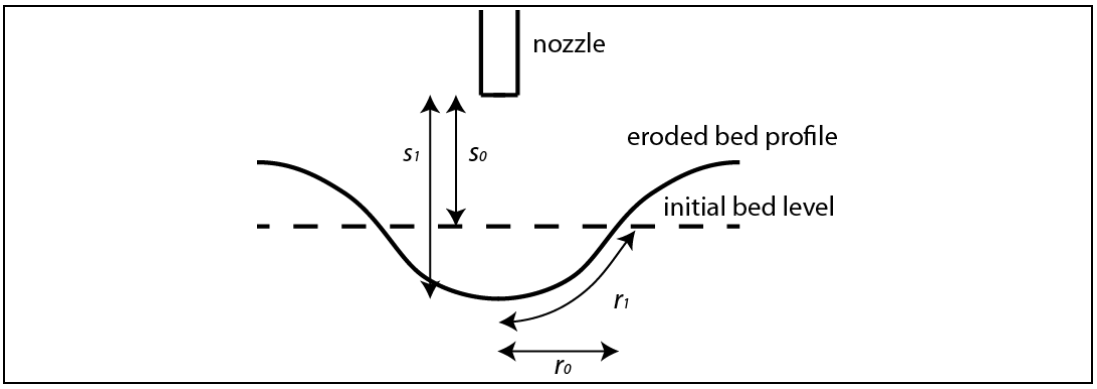

Figure 2.6 – Changes in length for the radial wall jet after erosion

2.2.5 Horizontally moving jet

The effects of a horizontally moving impinging jet are similar to the effects of a stationary jet, stopped within a short duration that depends on the transverse velocity of the moving jet. In addition to these similarities, a sediment-transporting cross-flow is created by the moving jet (Yeh, et al., 2009), which can be either in the form of the described radial wall jet or as a penetrating confined jet. In the latter case, the jet creates an asymmetrical scour hole with one side open and is sketched in Figure 2.7.

The penetration depth of a confined jet depends on the ratio between the erosion velocity, described in section 2.3.4, and the trail velocity v_{trail}. This ratio determines the bed angle α_{bed} that is created by the jet, as is illustrated in Figure 2.7. A larger v_{trail} therefore means a lower penetration. This seems logical, as one can expect that a larger speed causes that the duration of the jet impulse is shorter, meaning a lower force acting on the soil. It also causes an increase of the length of the created trench, in the opposite direction of the trailing nozzle (van de Leur, 2010).

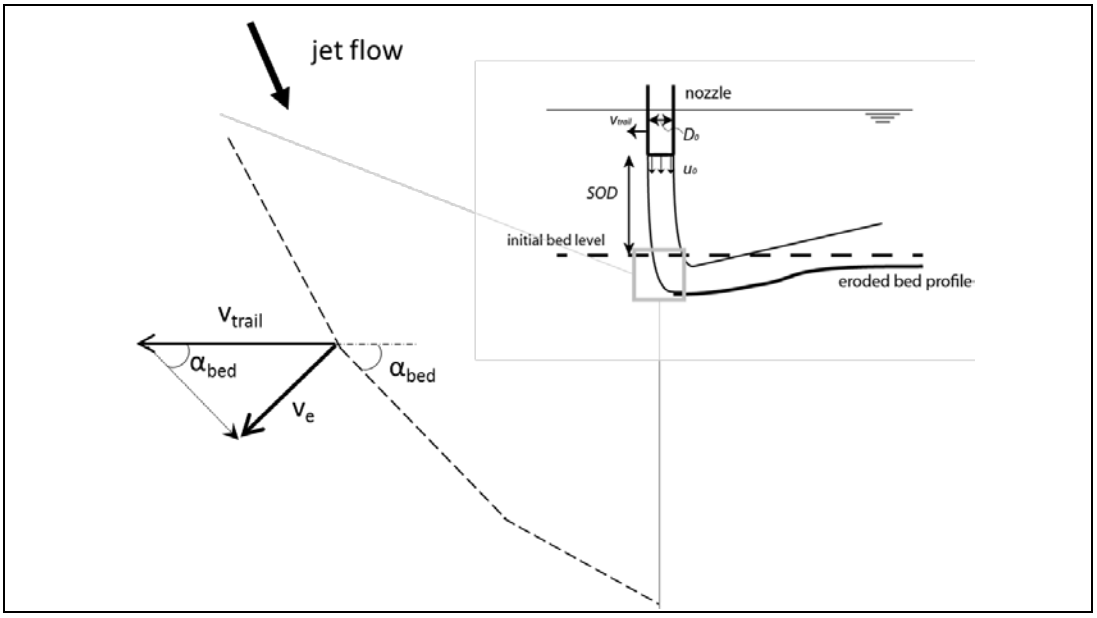

Figure 2.7 – The ratio between v_e and v_{trail} determines the bed angle α_{bed}

2.3 Erosion

The starting point for erosion are the forces on a grain. When these do not exceed the stability parameters, no erosion will take place. This chapter starts with a description of the forces acting on a single grain, after which the most important stability parameter is discussed. Next, the sedimentation processes of a single grain are explained, leading to an expression for the fall velocity. Finally, the erosion velocity is discussed.

2.3.1 Forces on a grain

The forces on a grain falling in still water are illustrated left in Figure 2.8. The grain accelerates due to the gravity force F_g, until the gravity force reaches a balance with the drag force F_D. When this balance is reached, the particle settles with a constant velocity: the fall or settling velocity w. The gravitational and drag force acting on a sphere are respectively given by Eq. (2.32) and Eq. (2.33) (Bosboom & Stive, 2012):

$$F_G = \frac{\pi}{6}(\rho_s - \rho_w) g {D_{50}}^3 \tag{2.32}$$

$$F_D = \frac{\pi}{8} C_D \rho_w w_{sp} {D_{50}}^2 \tag{2.33}$$

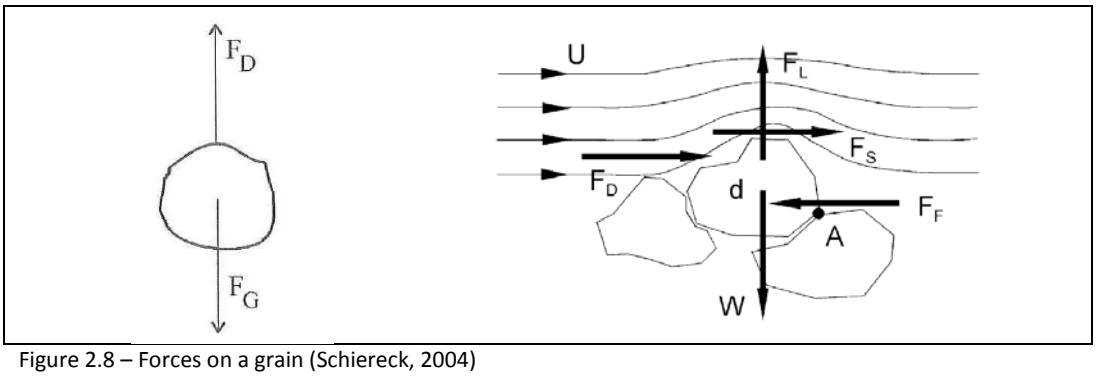

Figure 2.8 – Forces on a grain (Schiereck, 2004)

The forces acting on a grain with a flow over a horizontal bed are illustrated right in Figure 2.8. The forces caused by the flow can be expressed as (Schiereck, 2004):

$$\left.\begin{array}{ll} \text{Drag force:} & F_D = C_D \rho_w u^2 A_D \\ \text{Shear force:} & F_S = C_S \rho_w u^2 A_S \\ \text{Lift force:} & F_L = C_L \rho_w u^2 A_L \end{array}\right\} \; F_{flow} \propto \rho_w u^2 D^2 \tag{2.34}$$

When a grain is stable, the forces and the momentum around point A are in equilibrium. The lift force is balanced by the submerged weight *W* of the particle, while the drag and shear forces are balanced by the friction force F_f, which is a function of the submerged weight. This leads to the following proportional relationship:

$$\rho_w u^2 D^2 \propto (\rho_s - \rho_w) g D^3 \tag{2.35}$$

This could also be written, with the aid of a (unspecified) coefficient C_c, as follows:

$$u_{cr}{}^2 = C_c \Delta g D \tag{2.36}$$

With u_{cr} as the critical velocity at which the incipient motion of the particle takes place. All stability formulae have the same form as Eq. (2.36), the main difference is the perception of the coefficient C_c.

2.3.2 Stability

The most well-known stability parameter is the Shields parameter θ [-], giving a relation between the shear stress and the particle dimensions for uniform flow (Shields, 1936):

$$\theta = \frac{\tau}{(\rho_s - \rho_w) g D_{50}} = \frac{u_*{}^2}{\Delta g D_{50}} = \frac{u^2}{\Delta C_{ch}{}^2 D_{50}} \tag{2.37}$$

Or, as critical value, which is defined at the state of incipient motion:

$$\theta_{cr} = \frac{\tau_{cr}}{(\rho_s - \rho_w) g D_{50}} = \frac{u_{*cr}{}^2}{\Delta g D_{50}} = \frac{u_{cr}{}^2}{\Delta C_{ch}{}^2 D_{50}} \tag{2.38}$$

In which τ is defined as the shear stress [Pa] and u_* as the shear velocity [m/s]:

$$u_*{}^2 = \frac{u^2}{g C_{ch}{}^2} \tag{2.39}$$

With C_{ch} as the Chézy coefficient [√m/s], that depends on the hydraulic radius *R* [m] and grain roughness k_{rg} [m], defined as:

$$C_{ch} = 18 \log\left(12 \frac{R}{k_{rg}}\right) \tag{2.40}$$

In an open channel flow, the flow height *h* [m] is usually taken as value for *R*. In the case of a (wide) jet flow, the jet flow height can be considered as the 'water depth' *h* (Schiereck, 2004). This depth can be calculated with $2r_u$, expressed in Eqs. (2.11) and (2.13). The grain roughness k_{rg} depends on the stone diameter and shape, as well as the roughness of the entire bed. A flat rock bed shows, as to be expected, a smaller roughness than a course, irregular bed with many protruding grains. For a regular bed, the upper value of the roughness parameter can be approximated with $k_{rg} = 6D_{50}$, while

for a rough bed values of $k_{rg} = 12D_{50}$ are found (Boutovski, 1998). However, the bed roughness of an irregular bed decreases when subjected to a load caused by a flow to the roughness of a flat bed, as the (unstable) irregularities are quickly removed leading to a flat bed (Lammers, 1997). When a high θ_{cr} is chosen, the value of $k_{rg} = 5D_{50}$ can be taken. It is also found that the grading of the stones is not of influence on the roughness parameter k_{rg} (Boutovski, 1998).

It was found that the roughness increases with a higher mobility parameter, for instance in a sheet flow (Wilson, 2005), when an entire layer is eroded simultaneously. This process is discussed in more detail in Section 2.4. When the Shields parameter is greater than unity, the grain roughness can be found with:

$$k_{rg} = 5\theta D_{50} = \frac{5\tau}{(\rho_s - \rho_w)g} \quad for\ \theta \geq 1 \tag{2.41}$$

Note that in this case the roughness does not depend anymore on the grain diameter.

Van Rijn (1984) adjusted the original relation of Eq. (2.38) with the help of the dimensionless particle diameter D_*:

$$D_* = D\left(\frac{\Delta g}{\nu^2}\right)^{1/3} \tag{2.42}$$

In which ν is defined as the kinematic viscosity and has the value of 10^{-6} m^2/s. The Shields curve can now be estimated as a function of D_*:

$$\theta = 0.013{D_*}^{0.29} \quad for\ 20 < D_* < 150 \tag{2.43}$$

With $D_* > 150$, the critical Shields parameter becomes constant: $\theta_{cr} = 0.055$.
This relation is illustrated in Figure 2.10 (b), next to the graphical interpretation of the original relation, described by Eq. (2.38), in Figure 2.10 (a). It is clear from these graphs that the value of the Shields parameter is constant for a grain diameter larger than about 6 mm; which is the case for dumped rock.

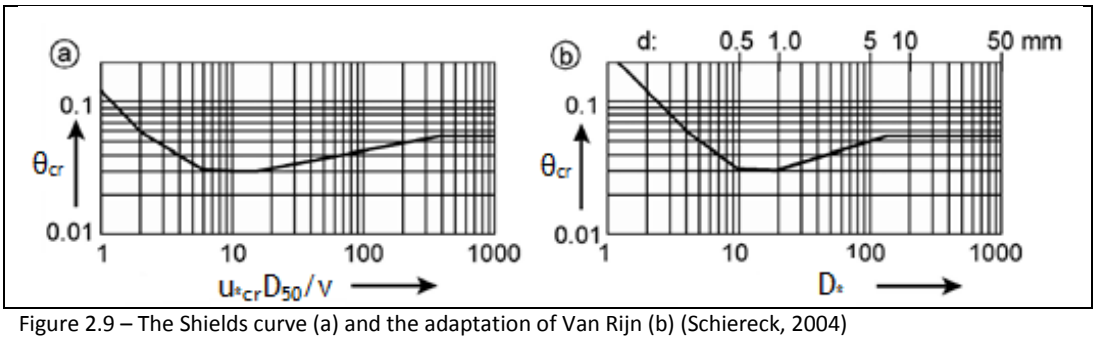

Figure 2.9 – The Shields curve (a) and the adaptation of Van Rijn (b) (Schiereck, 2004)

2.3.2.1 Adjustments of Shields

The theory of Shields has been widely used in hydraulic engineering, which led to many adaptations of the Shields parameter to compensate for different conditions.

Sloping bed

The stability of a particle decreases when it lies on a downward sloping bed, which has two main reasons. First, the gravity component has an increased influence on the stability, but the supporting strength of the bed decreases as well. The most extreme situation is a slope with an angle that equals or surpasses the angle of internal friction of the bed material. In this situation, each particle is in fact already on the threshold of motion and any load will cause movement (Schiereck, 2004).
Analogously, an upward slope has a positive effect on the stability.

The critical Shields parameter can be multiplied with a slope factor to take the effect of a bed angle α_{bed} into account. This factor is expressed as:

$$\begin{aligned} k_{slope,//} &= \frac{\sin(\varphi + \alpha_{bed})}{\sin\varphi} && for\ |\alpha_{bed}| < \varphi \\ k_{slope,//} &= 0 && for\ \alpha_{bed} \leq -\varphi \\ k_{slope,//} &= 2 && for\quad \alpha_{bed} \geq \varphi \end{aligned} \tag{2.44}$$

Permeability

The original Shields parameter was defined for flow velocities around the point of incipient motion and is based on the individual failure of grains. However, with higher flow and erosion velocities, the particles do not fail individually but erode in layers with multiple grains (van Rhee, 2010). With the shearing of layers, other factors such as dilatancy and permeability play a role as well. Conventional erosion formulae do not take these factors into account and tend to overestimate the erosion rate at high flow velocities. The effects of dilatancy and permeability can be explained by the fact that the shearing of a layer of soil causes the pore volume to increase, what is only possible if water is flowing into the bed, which leads to an inwards hydraulic gradient. The effect of this gradient is that the soil is less likely to erode due to the underpressure. The reverse is also true: if the pore volume decreases due to the shearing of soil, there will be an outwards hydraulic gradient that decreases the stability (Bisschop, et al., 2010).

This effect is accounted for in the Shields parameter with the definition of the modified critical Shields parameter θ_{cr}', given by (van Rhee, 2010):

$$\theta_{cr}{}' = \theta_{cr}\left(\frac{\sin(\varphi + \alpha_{sl})}{\sin\varphi} + \frac{v_e}{k_l}\frac{n_l - n_0}{1 - n_l}\frac{1}{\Delta(1 - n_0)}\right) \tag{2.45}$$

In which v_e = erosion velocity [m/s], which will be defined in Chapter 2.3.4, and n_l = porosity of the top layer during erosion [-]. The value of n_l can be estimated by $n_l = n_{max} - 0.01$ (Van der Schrieck, 2012). The value of k_l corresponds to the permeability of the situation with a loose state porosity n_l. The influence of a sloping surface on the stability of grains is also accounted for in Eq. (2.45).

The modified Shields parameter has the advantage that it reduces to the conventional Shields parameter for a flat bed with an initial porosity that equals the loose state porosity. The modified parameter is also still valid for a low erosion velocity. The theory of Van Rhee has been tested en found to have good agreements for particle sizes up to 600 μm. Within this range, the theory corresponds with the results found in practice that the erosion velocity increases with increasing grain diameter (van Rhee, 2010), due to the decreasing effect of permeability.

Note that the value of k_l in Eq. (2.45) is determined as the Darcy permeability for laminar flow. This is true for small particles; however, in the case of dumped rock, the grains are too large to neglect turbulent processes. Therefore, the turbulent term should also be accounted for in the determination of k_l. Moreover, Van Rhee found that the hindered erosion processes only become significant for v_e / k_l > 3. Given the relative high permeability of the rock cover, the question arises if high-velocity erosion processes becomes significant in the present study. This is discussed in section 2.3.4.

Turbulence
The average uniform velocity is used to derive the Shields parameter. However, non-uniform flow regimes with high turbulence occur often. For these situations, the conventional Shields parameter, Eq. (2.37), gives an underestimation of the actual stability parameter. The Shields parameter can be altered so turbulence is taken into account (Schiereck, 2004):

$$\theta_t = \frac{\left(\bar{u}(1 + 3r_t)\right)^2}{\Delta {C_{ch}}^2 D_{50}} \tag{2.46}$$

2.3.2.2 Other stability parameters

The theory of Shields is based on uniform flow, which is not always the occurring flow regime in practice. Multiple other stability parameters are therefore developed by various authors, all in the same form as Eq. (2.36). Important parameters are the one suggested by Izbash, Jongeling and Hofland. Although these expressions are better applicable to situation without uniform flow, many erosion functions still use the Shields parameter as base parameter. Therefore, the Shields parameter is used in this study as well. The mentioned stability parameters are explained in more detail in Appendix A.3.

2.3.3 Sedimentation

When a particle is picked up by the flow, gravity forces as described in section 2.3.1 will act on the particle, resulting in the settling of this grain.

2.3.3.1 Settling velocity of a single particle

The settling velocity occurs when a balance is reached between the gravity and drag force. A function to determine the settling velocity of a single grain is given by (Bosboom & Stive, 2012):

$$w_0 = C_s w_{sp} = C_s \sqrt{\frac{4\Delta g D_{50}}{3C_D}} \tag{2.47}$$

With C_s [-] as a shape factor to take the reduction of the settling velocity into account due to a non-spherical shape. It can be given by C_s = 0.5 – 0.7 for sand and gravel (Matousek, 2004). The drag coefficient C_D [-] depends on the particle Reynolds number, given by Eq. (2.48). The determination of C_D is described by Eq. (2.49) (van Rhee, 2002).

$$Re_p = \frac{w_0 D}{\nu} \tag{2.48}$$

$$C_D = \frac{24}{Re_p} + \frac{3}{\sqrt{Re_p}} + 0.34 \quad for\ 1 < Re_p < 2000$$
$$C_D = 0.4 \quad for\ Re_p \geq 2000 \tag{2.49}$$

The fall velocity is also included in Eq. (2.48), so a (simple) iteration is required for the determination of the particle Reynolds number, C_D and the fall velocity. However, for the turbulent case, with a high Reynolds number, the drag coefficient becomes constant. In the case of dumped rock, the particle Reynolds number is most certainly in the turbulent range. Combining Eq. (2.49) and Eq. (2.36) with C_s = 0.55, the fall velocity can be conveniently written as:

$$w_0 = \sqrt{\Delta g D_{50}} \tag{2.50}$$

For a somewhat lower particle Reynolds number, say Re_p = 500, Eq. (2.50) also holds for a shape factor C_s = 0.6. This is still in the range of C_s = 0.5 – 0.7. Equation (2.50) will therefore be taken as the fall velocity for a single grain, eliminating the required iteration to determine the drag coefficient for relatively large grains in the non-turbulent regime.

2.3.3.2 Hindered settlement

When a high concentration of sediments is entrained, the settlement of a single particle is hindered by other particles and/or the upwards flow, so the settling velocity is decreased. The hindered settling velocity is given by (Richardson & Zaki, 1954):

$$w_s = (1 - c_b)^m \cdot w_0 \tag{2.51}$$

In which m = 2.4 as empirical coefficient for Re_p > 500, and c_b is the near-bed concentration of particles in the flow. It is assumed that the concentration of particles is negligibly small with flow velocities just above critical. Individual grains are then eroded and have little interactions or collisions with other grains. However, when the flow velocity increases, and with it the Shields parameter, the number of eroded grains increase and therefore also the near-bed concentration. This is described in more detail in section 2.4. The settling flux ψ_s [m^{-2}kg/s] is defined as the settled mass per unit area and time and is given by:

$$\psi_s = \rho_s w_s c_b \tag{2.52}$$

2.3.4 Erosion velocity

When the flow velocity is larger than the critical velocity of a grain, the grain will erode. The rate of erosion can be calculated as it depends on the flow velocity, sedimentation and the stability of the sediment. The erosion velocity or erosion rate v_e [m/s] is defined as the eroded volume per unit area and is given by (van Rhee, 2010):

$$v_e = \frac{\psi_e - \psi_s}{\rho_s(1 - n_0 - c_b)} \tag{2.53}$$

With ψ_e as the pick-up flux [$m^{-2}kg/s$], basically the eroded mass per unit area and time, and ψ_s as the settling flux [$m^{-2}kg/s$], defined in Eq. (2.52). A definition of the pick-up flux is empirically found by Van Rijn (1993):

$$\psi_e = 0.00033\rho_s\sqrt{\Delta g D_{50}}{D_*}^{0.3}T^{1.5} \tag{2.54}$$

With:

$$T = \frac{\theta - \theta_{cr}}{\theta_{cr}} \tag{2.55}$$

Combining Eqs. (2.52), (2.53), (2.54) and (2.55), gives the following general expression for the erosion velocity:

$$v_e = \frac{\sqrt{\Delta g D_{50}}}{1 - n_0 - c_b}\left(0.00033{D_*}^{0.3}\left(\frac{\theta - \theta_{cr}}{\theta_{cr}}\right)^{1.5} - c_b(1 - c_b)^{2.4}\right) \tag{2.56}$$

A special case arises when the Van Rhee modified Shields parameter θ_{cr}' is substituted in Eq. (2.56) for θ_{cr}. Because the erosion velocity is also incorporated in θ_{cr}', the equation should be solved iteratively.

The comparison between the theories of Van Rijn and Van Rhee, i.e. between the use of θ_{cr} and θ_{cr}' in Eq. (2.56), is illustrated in Figure 2.11, where the erosion velocity as a function of the flow velocity is given for the situation of crushed rock with a mean diameter of D_{50} = 0.10 m and an initial porosity of n_0 = 0.35.

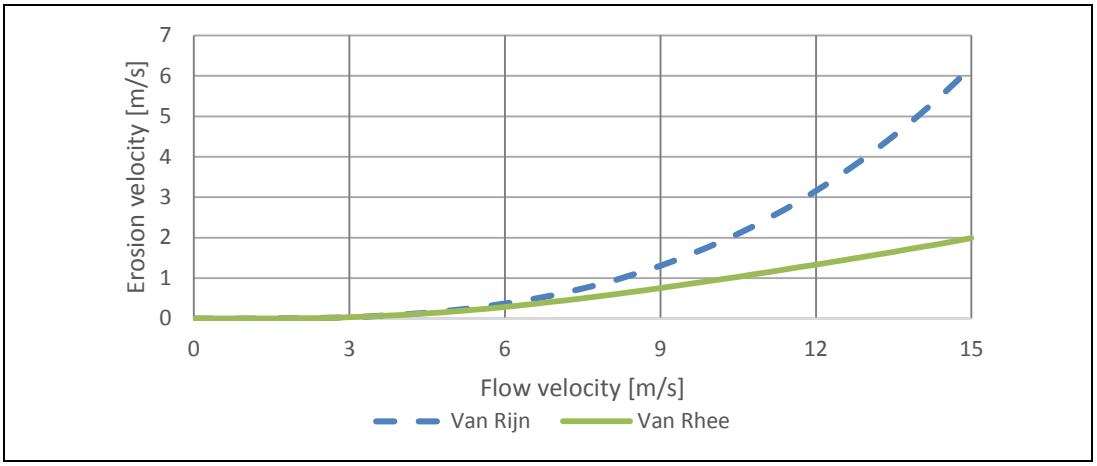

Figure 2.10 – Comparison of erosion velocity functions for D_{50} = 0.10 m

This graph shows clearly that the hindered erosion only becomes dominant for flow velocities of 9 m/s and higher. For flow velocities of 6 m/s and lower, the difference between Van Rijn and Van Rhee is negligible. It is expected that the near-bed flow velocities does not exceed this value. For example, during the removal operation in Assaluyeh, the near-bed velocities were around 5 m/s. This means that a difference between the erosion theories of Van Rijn and Van Rhee is nearly unnoticeable in the case of the removal of dumped rock.

2.3.4.1 Other pick-up functions

The pick-up function of Van Rijn, Eq. (2.54), is not the only expression for the erosion of sediments found in literature. Multiple studies were performed, almost all resulting in an empirically found relation between the pick-up rate and the Shields parameter. An example is the function of Fernandez Luque (1974), based on the erosion of bed-load sediment:

$$\psi_{e,FL} = \epsilon \rho_s \sqrt{\Delta g D_{50}} (\theta - \theta_{cr})^{1.5} \tag{2.57}$$

Fernandez Luque provided a value of ϵ = 0.04 in its study, although later Van Rijn found that ϵ = 0.02 resulted in a better agreement with its results (Van Rijn, 1993). Van Rijn also found that the value of ϵ depends on the stone diameter: the best agreement with his results with D_{50} = 1.5 mm were found with ϵ = 0.14.

2.4 Sediment transport

The transport of eroded bed material by a flow of water has been the subject of many researches in the past, all with (partly) different results. Since almost all of these studies are based on empirically found relations to determine the sediment transport rate, one should be cautious with the use of such a relation in a problem with different conditions regarding the flow velocity and grain diameter. Especially since most studies were focussed on river engineering, where usually considerably smaller flow velocities and grain diameters occur than with the removal of dumped rock with mass flow excavation. This chapter is therefore restricted to the theory that has the relative best approach to the conditions of the current problem. Also, some expressions regarding the scouring of a jet flow are discussed.

2.4.1 Forms of sediment transport

The transport of sediment can be divided in three forms: bed-load, suspended load and wash load transport. Usually, the transport of sediment with a rolling and sliding behaviour is called the bed-load, while suspended load is considered to be consisting of sediment that is supported for some time by the upwards forces of the fluid, caused by turbulent eddies. Wash load is actually a form of suspended load, consisting of sediment that was already suspended upstream and has no exchange with the bed. Wash load is therefore not considered in this study. The total sediment transport is simply the sum of all forms of transport.

Dependent on the bed material and the flow velocity, the sediment transport can either be dominated by bed-load, suspended load or in a transition zone where both forms are important. In which mode the sediment transport will be, can be estimated with the following ratio (Visser, 1995):

$$\frac{u_*}{w_s} = \frac{u\sqrt{g}}{C_{ch} w_s} \tag{2.58}$$

Generally, the bed-load transport is dominant when $u_*/w_s < 1$, while the transport is in suspended mode with $u_*/w_s > 2$. In between, the sediment transport is in a transition zone and both forms of transport are of importance. With the flow velocities associated with mass flow excavation and the fall velocity of dumped rock, it is assumed that only the bed-load transport contributes to the sediment transport, and suspended load transport has only little influence.

2.4.2 Saltating movement of particles

The typical motion of particles during bed-load movement is the saltation motion, which can be seen as a small jump, confined to a layer with a thickness of about $10D_{50}$ (Bagnold, 1954). Although a saltation can be initiated by a turbulent upwards burst of flow, or simply an upwards directed gradient, it is not expected that this upward directed force continues to act on the grain after lift-off (Bagnold, 1956). After this lift-off, the grain is accelerated by the flow in the direction of the flow. Eventually, causes the grain to settle again, see Figure 2.12. So, the particle motion with a saltation is dominated by gravitational forces, which distinguishes bed-load from suspended load. A saltation is ended when the particle strikes the bed, where it either rebounds off or impact into the surface. With an impact, most of the momentum of the particle is dissipated due to collisions with other particles. These collisions can initiate the rolling motion of multiple particles. A particle can have multiple successive saltations, interspersed with resting periods on the bed (Van Rijn, 1993).

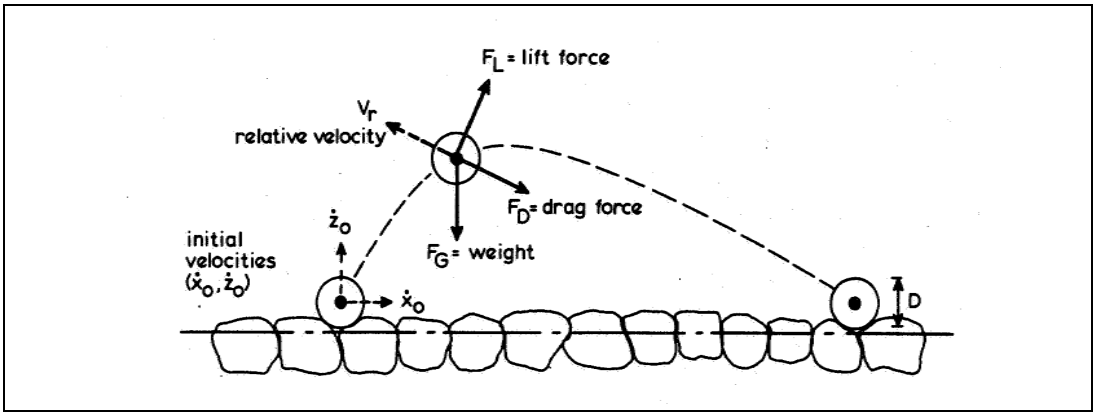

Figure 2.11 – Definition sketch of a saltation (Van Rijn, 1984)

The length and height of a saltation have been empirically found for particle diameters up to 2 mm and are given below. The input data used to derive these expressions consisted of a range for the particle diameter of 0.01 mm to 2 mm and a shear velocity of u_* = 0.04 m/s to 0.14 m/s.

The saltation height δ_s can be approximated with the following empirical expression (Van Rijn, 1984):

$$\frac{\delta_s}{D_{50}} = 0.3{D_*}^{0.7}\sqrt{T} \tag{2.59}$$

The expression for D_* is given by Eq. (2.42) and for T by Eq. (2.55). The saltation length λ_s can be approximated with (Van Rijn, 1984):

$$\frac{\lambda_s}{D_{50}} = 3{D_*}^{0.6}T^{0.9} \tag{2.60}$$

Equation (2.60) has only a limited accuracy. The experimental results, which partially led to the expression, show a saltation length in the range of $5D_{50}$ to $40D_{50}$. Note that the

values for the saltation length and height increase considerably with an increasing grain diameter. For values of D_{50} = 0.10 m and θ = 0.4, the saltation length and height become $\lambda_s \approx 150$ m and $\delta_s \approx 15$ m, which seems to be rather unreliable.

2.4.3 Bed-load movement

It can be assumed that at the threshold of motion the applied shear stress on a grain is equal to the resisting force. The resisting force can be seen as a friction force: the horizontal component of an internal friction factor. For a single grain, this relation can be expressed as:

$$\frac{\tau}{\sigma} = \tan\varphi = \frac{\tau}{(\rho_s - \rho_w)gD_{50}} \tag{2.61}$$

This is the same expression as for the Shields parameter, described by Eq. (2.37). Or, with other words, the Shields parameter is a sort of friction factor, equal to the tangent of the static friction angle. For a single grain, this value is given by the regular critical Shields parameter θ_{cr}. This corresponds with a low angle of less than 3°, probably caused by the influence of the lift force on a particle (van Rhee, 2010) that is not explicitly incorporated in the Shields equation. When the applied shear stress exceeds the resisting stress, the particle will make a saltation.

When the flow velocity increases, it can be expected that the number of saltating particles, and with it the near-bed concentration c_b, will increase as well. With an increasing number of saltating grains, the chance of collisions with other grains will also increase. At a certain moment, a free saltating movement of a grain is not possible anymore and encounters between particles are inevitable for c_b > 0.09 (Bagnold, 1956). With other words, the entire top layer of grains is sheared, instead of individual grains.

It can therefore be expected that the entire layer with a thickness δ and a volume concentration of (1-n) will erode when the applied shear stress exceeds the horizontal component of the submerged weight of this layer. At the threshold of motion, the stresses are in balance. Rewriting Eq. (2.62) with inclusion of the concentration gives:

$$\tau = (1-n)(\rho_s - \rho_w)g\delta\tan\varphi \tag{2.62}$$

The internal angle of friction was assumed to be φ = 45°. Rewriting Eq. (2.63) into the form of the Shields equations should therefore lead to a critical Shields parameter of an entire bed layer:

$$\frac{\tau}{(\rho_s - \rho_w)g\delta} = \theta_{cr,layer} = (1-n)\tan\varphi = (1-n) \tag{2.63}$$

With n = 0.4, it can therefore be expected that if the Shields mobility parameter exceeds θ = 0.6 an entire layer with a thickness δ will be sheared. If all grains in this layer would be removed as a suspension, successive topmost layers would also be sheared, resulting in a continuous erosion of the entire bed, regardless of the dimensions (Bagnold, 1956). Practical experiences show that this is not the case (Bagnold, 1954), which can be

explained by the fact that the eroded grains do not go in suspension but are rather transported as a bed-load. This bed-load introduces an additional resisting stress, which keeps the applied shear stress at the immobile bed surface below the critical value. The intergranular forces in the bed-load are the source of this resisting stress.

2.4.3.1 Sheared bed-load layer

Equation (2.64) does therefore not hold in its simple form; however, it can be rewritten to comply with the existing bed-load theory. Analogue to the steps that acquired Eq. (2.64), one can think of a situation with a sheared bed-load layer on top of an immobile bed. There is no suspended load, so the volume concentration just above the bed-load layer is zero. The concentration in the bed-load layer is expressed as c_b. The depth y_{cr} at which the immobile bed begins, i.e. where the applied shear stress is equal to the resisting stress, can be expressed as:

$$y_{cr} = \frac{\tau}{(\rho_s - \rho_w) g c_b \tan\varphi} \tag{2.64}$$

For the situation with a sheared top layer, the dynamic friction angle should be taken as value for φ. This friction angle inside the sheared top layer equals about 18°, so θ = tan 18° = 0.32 (Bagnold, 1956).

The near-bed concentration c_b is however not constant along the depth of the sheared bed-load layer. It is found that the concentration decreases linearly with the height from a value of $c_b = 1\text{-}n_l$ at $y = y_{cr}$ and $c_b = 0$ at $y = 0$. This means that the concentration at the immobile bed surface is equal to the loose-poured volumetric concentration and above the sheared layer equal to zero, as there is no suspended load (Wilson, 1984). This implies that the average value of the near-bed concentration is $c_b = 0.5(1\text{-}n_l)$ and the thickness of the bed-load layer can be found with substituting this value in Eq. (2.65):

$$\delta_b = \frac{2\tau}{(\rho_s - \rho_w) g (1 - n_l) \tan\varphi} \tag{2.65}$$

Dividing both sides with the particle diameter gives, with the aid of Eq. (2.37):

$$\frac{\delta_b}{D_{50}} = \frac{2\tau}{(\rho_s - \rho_w) g D_{50} (1 - n_l) \tan\varphi} = \frac{2\theta}{(1 - n_l) \tan\varphi} \tag{2.66}$$

With a typical value of $n_l = 0.43$ and with tan φ = 0.32, it is found that the layer thickness is about:

$$\delta_b = 11\theta D_{50} \tag{2.67}$$

2.4.4 Bed-load transport

The bed-load transport can be seen as the volume of transported sediment per unit time per unit width, and is expressed as S_b [m^2/s] (Wilson, 1987):

$$S_b = \int_0^{\delta_b} c_b u_b \, dy \tag{2.68}$$

Which can be approximated with the average value of the concentration and velocity of the sheared bed-load layer:

$$S_b = \bar{c}_b \bar{u}_b \delta_b \tag{2.69}$$

It is assumed that the sheet flow velocity equals the jet flow velocity near the bed, and that the concentration profile has the characteristics as described in section 2.4.3.1. Combining this and Eq. (2.66) with Eq. (2.70) leads to:

$$S_b = \frac{\tau \bar{u}_b}{(\rho_s - \rho_w) g \tan \varphi} = \frac{D_{50} \theta \bar{u}_b}{\tan \varphi} \tag{2.70}$$

This would be the sediment transport capacity if all particles will be moved with the flow velocity and can therefore be taken as the upper value.

Bagnold (1966) introduced the concept of stream power to the sediment transport capacity, which represents the amount of work a flow can do. This stream power delivers the work required for moving a bed-load particle. However, only a fraction *e* of the total stream power can be used for this process. Bagnold found an efficiency of *e* = 0.13 in a semi-empirical way. The sediment transport capacity is then given by:

$$S_b = \frac{e \cdot \tau \bar{u}_b}{(\rho_s - \rho_w) g \tan \varphi} = \frac{e \cdot \theta D_{50} \bar{u}_b}{\tan \varphi} \tag{2.71}$$

Equations (2.71) and (2.72) are only valid for a flat bed. In addition to a change of the stability of the grains, a slope also affects the transport of sediment (Van Rijn, 1993). The bed-load transport capacity can be multiplied with a factor k_s to correct for the influence of the bed angle α_{bed} (Bagnold, 1966):

$$k_{s,Bagnold} = \frac{\tan \varphi}{(\tan \varphi - \tan \alpha_{bed}) \cos \alpha_{bed}} \tag{2.72}$$

This however implies that the transport becomes infinitely high with a bed angle that is similar to the angle of repose of the material, which is physically not possible. Another way to include the effect of a bed slope was introduced by Koch and Flokstra (1981), leading to:

$$k_s = 1 - \varepsilon_s \tan \alpha_{bed} \tag{2.73}$$

With ε_s as a user-specified tuning parameter, used by Talmon (1992) with values for ε_s in the range of 0.15 – 0.3.

Substituting the Shields parameter of Eq. (2.37) into Eq. (2.72) gives:

$$S_b = \frac{e \cdot {u_{u,r}}^3}{\Delta {C_{ch}}^2 \tan \varphi} \tag{2.74}$$

This seems somewhat remarkable, as the grain diameter is of little importance: it is only incorporated in C_{ch} through the grain roughness, but this has a relative small influence. The sediment transport capacity depends therefore only marginally on the grain diameter. This property of the stream power theory has the advantage that it can be used for large grain diameters as well, contrary to empirical relations found for sand. This approximation is also found to have a rather good agreement with the values measured by Visser (1995) during a dike breach, and thus with relative high flow velocities.

2.4.4.1 Other sediment transport formulae

More studies are performed that subjected the sediment transport; most of them resulting in empirically based equations. Examples of these kind of formulae are the equations of Van Rijn, Paintal and Meyer-Peter-Müller. Wilson followed a more theoretical base, similar to the approach of Bagnold. All these mentioned theories are explained in more detail in Appendix A.4, only the equation of Wilson is repeated here.

Wilson (1987) followed a similar approach as Bagnold, but argued that the velocity distribution in the shear layer should be included in the determination of S_b. With relative large grains, the sheared layer thickness δ_b is much larger than the viscous sub-layers. Therefore, the fluid motion in the sheet flow is turbulent, leading eventually to:

$$S_b = 11.8\sqrt{(g\Delta {D_{50}}^3)}\theta^{1.5} \tag{2.75}$$

2.4.5 Scouring

The eventual result of the erosion and sedimentation processes is a scour hole, which is the only visible and significant part in practice. Multiple studies are therefore based on the prediction of the dimensions and development of the scour hole, resulting in expressions that are easy applicable in practice.

2.4.5.1 Theoretical approach

When the flow velocity near the bed does not exceed the critical value, no erosion will take place. It seems therefore a logical statement that erosion will go on until Eq. (2.77) holds. The locations where the near-bed flow velocity equals the critical velocity forms the scour hole.

$$u_b(s,r) = u_{cr} \tag{2.76}$$

The flow velocity of an impinging radially deflected jet can be calculated by Eq. (2.25) or Eq. (2.27). Rewriting and substituting $u_{u,r} = u_{cr}$ gives the scour depth h_{sc} as a function of

the SOD and radial distance *r*, all other parameters depend only on the jet and soil characteristics:

$$h_{sc} = D_0 \left(1 + \sqrt{\frac{k}{2}}\right) \sqrt{\frac{\frac{f_2 {D_0}^2 {u_0}^2}{{u_{cr}}^2} - 8 f_1 \alpha_{mom} r^2}{4 {D_0}^2 \left(\frac{1}{f_2} - 4 f_1 \alpha_{mom}\right)}} - SOD \tag{2.77}$$

The determination of the scour depth by Eq. (2.78) is based on the eroding capability of the flow on a single particle. Other processes, such as sedimentation and sediment transport, are not taken into account. As stated in section 2.2.3.1, the erosion with a penetrating jet is in fact the renewed erosion of a settled particle that was not transported out of the scour hole. With other words, the flow in the scour hole is not capable of transporting the sediments out of the hole, while the flow velocity is higher than the critical velocity in the centre of erosion under the jet (Aderibigbe & Rajaratnam, 1996). This means that Eq. (2.78) cannot be applied for an impinging jet.

2.4.5.2 Empirical approach

The scour profile of an impinging jet is illustrated in Figure 2.13. As described in section 2.2.3.1, there are two regimes with an impinging jet: a weakly and a strongly deflective regime. The flow regime depends on the erosion parameter E_c, given by Eq. (2.16). This erosion parameter also influences the scour profile. The scour depth can be calculated with the following empirically found relation (Aderibigbe & Rajaratnam, 1996):

$$\frac{h_{sc}}{SOD} = 1.26 {E_c}^{0.11} - 1 \tag{2.78}$$

The radius of the scour hole is found with the following empirical relations (Aderibigbe & Rajaratnam, 1996):

$$\begin{aligned} \frac{r_0}{SOD} &= 1.46 {E_c}^{0.15} - 1 \quad for\ E_c \leq 0.5 \\ \frac{r_0}{SOD} &= 0.22 + 0.2 E_c \quad for\ E_c > 0.5 \end{aligned} \tag{2.79}$$

From Eq. (2.80) it is clear that the width of the scour hole increases linearly with an increasing stand-off distance for a strongly deflective jet regime.

The height of the ridge at the outer side of the scour hole can be approximated with:

$$\frac{h_{berm} - h_{sc}}{SOD} = 0.044 E_c - 0.02 \tag{2.80}$$

The experiments carried out by Aderibigbe and Rajaratnam (1996) with u_0 varying between 2.5 and 4.5 m/s and a particle diameter D_{50} of 0.88 and 2.4 mm.

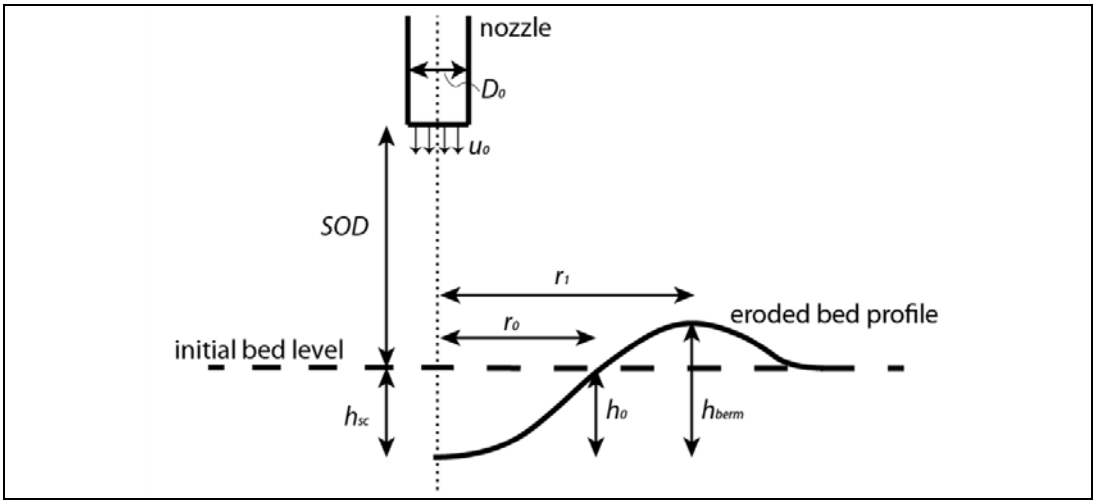

Figure 2.12 – Scour profile with characteristic lengths

Yeh, et al (2009) found that the calculated results obtained by the above given empirical relations overestimated the measured results from their experiments. Correction factors were introduced to overcome this problem, varying between 0.52 and 0.78.

The radius and depths of the scour hole as presented in this section are the values in the equilibrium situation. The time required to achieve the equilibrium situation varied between 6 and 50 hours. In the present study, the duration of the jet acting on the soil has an order of magnitude of only seconds. This shows that one should be cautious with the use of such empirical formulae in situations different than of the experiments used to obtain these relations. However, with no better alternatives present, these equations can be used as a first estimation.

3 Scaling and experimental set-up

3.1 Scaling of the processes

Tests are preferably performed in a laboratory, so that more parameters can be controlled than with an in-situ test. However, tests on actual size are often too expensive or simply too big to be performed in a laboratory. Therefore, processes are scaled. This introduces the problem of scale factors, required to make the scale model a good representation of the actual situation or prototype. When processes or dimensions are not correctly scaled, discrepancies between the scale model and the prototype will occur, called scaling effects. Scaling effects should be limited as much as possible by application of the correct scale factors. This chapter describes the scale factors and the occurring scale effects.

3.1.1 Introduction

A scale factor is determined as the ratio between the values of the prototype and the scale model:

$$n_x = \frac{x_{actual}}{x_{model}} \tag{3.1}$$

It is clear that the scale factor equals one for a constant parameter. The scale of the product of two parameters is equal to the product of the scales of the two parameters. The scale of the sum of two parameters is equal to the scale of an individual parameter. This implies that the scale of the two parameters must be equal, otherwise scaling effects will occur (Van der Schrieck, 2012)

3.1.1.1 Dimensionless indicators

Dimensionless indicators are commonly used as a tool for scaling. Since these indicators are dimensionless, it should have the same value in the prototype as in the scale model, and thus a scale factor of one.

Froude

The Froude number gives the ratio between the kinetic and potential energy:

$$Fr = \frac{u}{\sqrt{gL}} \tag{3.2}$$

With *L* as the parameter to indicate a length [m]. When a physical model is Froude-scaled, the scaling factor of the Froude number is equal to one. This implies the following for the scaling factors for velocity and length, under the assumption that the gravity is constant:

$$n_u = \sqrt{n_g \cdot n_L} = \sqrt{n_L} \tag{3.3}$$

Reynolds
The Reynolds number is an indicator for turbulence, and gives the ratio between inertial and viscous forces:

$$Re = \frac{u \cdot L}{\nu} \tag{3.4}$$

The Reynolds number is equal in the prototype and scale model if the test is Reynolds-scaled. Under the assumption that the viscosity is constant, the following relation between the scaling factors of velocity and length can be found:

$$n_u = \frac{n_\nu}{n_L} = \frac{1}{n_L} \tag{3.5}$$

3.1.2 Scale factors

The theory concerning the jetting processes is assessed in Chapter 2. The required scaling factor of each parameter is given in this section.

3.1.2.1 Soil properties

The properties of the rocks used for the coverage are provided in section 2.1. It is assumed that the porosity, density and the angle of internal friction is equal in the prototype and in the scale model (Van der Schrieck, 2012).

3.1.2.2 Ship properties

The sailing speed of the vessel, the trail velocity, has the same scale factor as the flow velocities:

$$n_{v_{trail}} = n_u \tag{3.6}$$

3.1.2.3 Jet properties

The outflow velocity of the jet has, obviously, the same scaling factor as the flow velocity:

$$n_{u_0} = n_u \tag{3.7}$$

The jet pressure is proportionally related to the density of the fluid and the flow velocity:

$$p \propto \rho {u_0}^2 \tag{3.8}$$

Which means:

$$n_p = n_\rho {n_{u_0}}^2 = {n_u}^2 \tag{3.9}$$

The diameter of the jet and the distance to the bed are both scaled according to the length scale. These parameters appear as a ratio in the expressions to determine the jet flow velocity near the bed, and therefore have no influence on the scale factor of the flow velocity. So u_m, u_u and u_b are all scaled with the flow velocity factor.

There will be a scale effect of the density, since the water used in the tests is fresh, compared to salt for the prototype situation. The influence of this density difference is assumed to be negligible, and the density of fresh water is used for calculations.

The seepage velocity is related to the permeability and the pressure gradient, see Eq. (2.20), also called the Forchheimer equation. The scale factor of the laminar and turbulent permeability are respectively given by, assuming a constant porosity, viscosity and gravity:

$$n_{a_f} = \frac{n_g {n_{D_{50}}}^2 n_n}{n_\nu} = {n_{D_{50}}}^2 \tag{3.10}$$

$$n_{b_f} = {n_n}^2 n_g n_{D_{50}} = n_{D_{50}} \tag{3.11}$$

This means the following for the scaling factor of the seepage velocity, using Eq. (3.9):

$$-\frac{n_p}{n_r} = \frac{{n_u}^2}{n_L} = \frac{n_{u_f}}{n_{a_f}} + \frac{{n_{u_f}}^2}{n_{b_f}} = \frac{n_{u_f}}{{n_{D_{50}}}^2} + \frac{{n_{u_f}}^2}{n_{D_{50}}} \tag{3.12}$$

It is obvious that both terms on the right hand side of Eq. (3.12) can never be equal in any other situation than the trivial case in which all scale factors are 1 (i.e. the prototype). Otherwise, scale factors will play a role.

The flow in the prototype can be considered as turbulent and the laminar term can therefore be neglected. If this is also assumed for the scale model, there will be no scale effects if $n_{D50} = n_L$:

$$n_{u_f} = n_u \tag{3.13}$$

However, if the flow in the scale model is in the transition regime between turbulent en laminar, the Darcy term cannot be neglected for the scale model. The seepage flow is in the transition regime for about $D_{50} < 6$ cm; this is most probably the case with a scale model. Due to the quadratic decrease of the linear permeability with decreasing grain diameter, the laminar term of the Forchheimer equation becomes relatively more pronounced in a scale model than in the prototype. This means that if the jet flow velocity is also scaled down, the seepage velocity will always be smaller in the scale model than according to the desired scale factor.

The erosion parameter E_c has the following scale factor, given a constant density and gravity acceleration:

$$n_{E_c} = \frac{n_u n_L}{n_L \sqrt{n_{D_{50}}}} = \frac{n_u}{\sqrt{n_{D_{50}}}} \tag{3.14}$$

3.1.2.4 Turbulence

The Reynolds number is an indication of the turbulence. Assuming a constant value of the fluid viscosity, the scaling factor for the Reynolds number is associated with:

$$n_{Re} = \frac{n_u n_L}{n_\nu} = n_u n_L \tag{3.15}$$

The ratio between turbulent velocity fluctuations and the average jet flow velocity r_t is assumed to be constant for all jets.

3.1.2.5 Stability parameters

Multiple expressions to determine the stability of a grain are given in section 2.3, most importantly Shields:

$$\theta \propto \frac{u^2}{\rho {C_{ch}}^2 D_{50}} \tag{3.16}$$

The Chézy coefficient has no scaling factor, and is considered to be constant, if $n_{D50} = n_L$:

$$n_{C_{ch}} = \log \frac{n_{h_r}}{n_{D_{50}}} = \log \frac{n_L}{n_{D_{50}}} = 1 \tag{3.17}$$

If the Chézy coefficient is constant, this implies the following scaling factor for the Shields parameter:

$$n_\theta = \frac{{n_u}^2}{n_{D_{50}}} \tag{3.18}$$

The critical Shields parameter is constant for values of D_{50} above 6 mm; the scale factor for θ_{cr} is one in that case. The critical velocity has the following scaling factor:

$$n_{u_{cr}} = \sqrt{n_{\theta_{cr}} n_{D_{50}}} \tag{3.19}$$

3.1.2.6 Sedimentation

The settling velocity of a particle is given by Eq. (2.51), which means the following for the scale factor:

$$n_{w_s} = \left(1 - n_{c_b}\right)^{2.4} \sqrt{n_\rho n_g n_{D_{50}}} \tag{3.20}$$

The near-bed concentration of particles c_b is assumed to be either zero or a function of the loose state porosity. This means that the scale factor of the concentration is 1, assuming the loose state porosity is constant. The scale factor of the settling velocity therefore becomes:

$$n_{w_s} = \sqrt{n_{D_{50}}} \tag{3.21}$$

3.1.2.7 Erosion

The erosion velocity as provided by Van Rijn, Eq. (2.56), has the scale factor as described in Eq. (3.22). For this expression, a similar determination of the scale effect of c_b is used as for the settling velocity. For D_{50} > 6 mm, the critical Shields parameter is constant. The porosity is also assumed to be constant.

$$n_{v_e} = \frac{\sqrt{n_{D_{50}}}}{(1-n_n)} {n_{D_{50}}}^{0.3} \left(\frac{n_\theta - n_{\theta_{cr}}}{n_{\theta_{cr}}} \right)^{1.5} = {n_{D_{50}}}^{0.8} {n_\theta}^{1.5} \tag{3.22}$$

It was shown in section 2.3.4 that the difference between de erosion velocity functions of Van Rijn and Van Rhee is small for low flow velocities. The scale factor of the Van Rhee function is difficult to determine, as the erosion velocity function has to be solved iteratively. Moreover, the erosion process is not considered to be governing, which is the sediment transport capacity, so a small overestimation of the erosion velocity is acceptable. Taken all this into account, only Eq. (3.22) will be used to determine the scale factor of the erosion velocity.

3.1.2.8 Sediment transport

The saltation height and length depend mainly on the Shields parameter and the grain diameter and the scale factors are respectively given by:

$$n_{\delta_s} = {n_{D_{50}}}^{1.7} \sqrt{\frac{n_\theta - n_{\theta_{cr}}}{n_{\theta_{cr}}}} \tag{3.23}$$

$$n_{\lambda_s} = {n_{D_{50}}}^{1.6} \left(\frac{n_\theta - n_{\theta_{cr}}}{n_{\theta_{cr}}} \right)^{0.9} \tag{3.24}$$

The scale factor for the various sediment transport formulae are:

Bagnold: $n_{S_b} = n_\theta n_{D_{50}} n_u$
Wilson: $n_{S_b} = n_\theta n_{D_{50}} n_u$
Van Rijn: $n_{S_b} = {n_{D_{50}}}^{1.2} \left(\frac{n_\theta - n_{\theta_{cr}}}{n_{\theta_{cr}}} \right)^{2.1}$ (3.25)
Paintal: $n_{S_b} = {n_{D_{50}}}^{1.5} {n_\theta}^{2.5}$
MPM: $n_{S_b} = {n_{D_{50}}}^{1.5} {n_\theta}^{1.5}$

Following the argumentation of Wilson (1987), the scale factors for Bagnold, Wilson and Meyer-Peter-Müller are in fact similar and equal to:

$$n_{S_b} = {n_u}^3 \tag{3.26}$$

The scale factors of the saltation length and height, and of the formula of Van Rijn, can potentially have a scale effect induced if the scale factor of the Shields parameter is different than the critical Shields parameter. The expression of Meyer-Peter-Muller uses a constant value of 0.047; this will lead to scale effects when the Shields value has a scale factor.

3.1.2.9 Scouring properties

The erosion depth should be equal to the other length scales. The equilibrium scour depth factor is mainly dependent on the scale factor E_c, which has a similar scale factor as the Shields parameter.

3.1.3 Scale scenario

There are three commonly used scale scenarios: Froude, Reynolds and linear scaling. The difference between these three scenarios is in fact the scaling of time. If the scale factor for the length is taken as the base scale factor, in which all other factors are expressed, the difference between the scaling scenarios is as follows:

Froude: $n_t = \sqrt{n_L}$
Reynolds: $n_t = {n_L}^2$
Linear: $n_t = 1$

This implies the following for the scale factor for velocity:

Froude: $n_u = \sqrt{n_L}$
Reynolds: $n_u = \frac{1}{n_L}$
Linear: $n_u = n_L$

The scale effects that could occur are obviously different for each scenario. Therefore, the described scale factors are applied to each scaling scenario. This complete analysis is provided in Appendix B.1, here only the results of the chosen scenario, the Froude scale scenario, is treated.
To determine the scale effect, the theoretical and desired scale factor has to be known. The theoretical scale factor is determined by the scale scenario and the dependency on the scaled dimensions (length and time), as provided in Section 3.1.2. The desired scale factor depends on the dimensions of the scaled parameter; the desired scale factor for a dimensionless parameter is therefore always one. When there is a difference between the desired and theoretical scale, scale effects will occur. A scale effect is expressed as:

$$scale\ effect = \frac{desired\ scale}{theoretical\ scale}$$

3.1.3.1 Froude scale scenario

With a Froude scaled scenario, the velocity is scaled according to $n_u = \sqrt{n_L}$. With the desired scale, the Froude number is kept constant. This implies however that the turbulence indicator, the Reynolds number, has a scale effect. Other parameters can have a scale effect as well, as can be seen in Table B.1 in Appendix B.1. Many of these scale effects are a ratio of n_{D50} and n_L. A logical first choice for the scaling of the grain diameter would therefore be $n_{D50} = n_L$. However, when the grain diameter will be scaled according to the length scale, some scale effects will still occur, see Table 3.1.

Table 3.1 – Scale effects with Froude scaling with $n_{D50} = n_L$

	Parameter	**Theoretical scaling**	**Desired scale**	**Scale effect**
Soil	Grain diameter†	n_L	n_L	1
	Lam. permeability	n_L^2	$\sqrt{n_L}$	$1/n_L^{1.5}$
	Turb. permeability	n_L	n_L	1
Ship	Trail velocity†	$\sqrt{n_L}$	$\sqrt{n_L}$	1
Jet	Pressure†	n_L	n_L	1
	Flow velocity	$\sqrt{n_L}$	$\sqrt{n_L}$	1
	Seepage velocity	n_L^m, m>0.5	$\sqrt{n_L}$	n_L^b, b<0
	Froude	1	1	1
	Reynolds	$n_L^{1.5}$	1	$1/n_L^{1.5}$
Stability	Shields	1	1	1
	Critical Shields*	1	1	1
	Critical velocity*	$\sqrt{n_L}$	$\sqrt{n_L}$	1
Sedimentation	Fall velocity	$\sqrt{n_L}$	$\sqrt{n_L}$	1
Erosion	Erosion velocity	$n_L^{0.8}$	$\sqrt{n_L}$	$1/n_L^{0.3}$
Sediment transport	Saltation height	$n_L^{1.7}$	n_L	$1/n_L^{0.7}$
	Saltation length	$n_L^{1.6}$	n_L	$1/n_L^{0.6}$
	Bagnold, Wilson	$n_L^{1.5}$	$n_L^{1.5}$	1
	Van Rijn	$n_L^{1.2}$	$n_L^{1.5}$	$n_L^{0.3}$
	Paintal	$n_L^{1.5}$	$n_L^{1.5}$	1
	Meyer-Peter-M.	$n_L^{1.5}$	$n_L^{1.5}$	1
Scouring	Erosion parameter	1	1	1
	Scour depth	n_L	n_L	1
	Scour radius	n_L	n_L	1

† parameter that can be controlled
* for D_{50} > 6 mm in the scale model

The Froude scale scenario is considered to be the best option of the three possible scale scenarios, although some scale effects will still occur. The scale effect of the Reynolds number is $1/n_L^{1.5}$, which means that the turbulence is underestimated; for example, the Reynolds number is 125 times too small with a scale factor of 1:25. However, as long as the scale model also displays a turbulent flow, the scale effects are assumed to be negligible. Turbulent flow is achieved with Re > 2000.

The scale effects for permeability and seepage velocity lead to a similar underestimation for these parameters. The permeability in the scale model is, with other words, too low. The seepage velocity is therefore also too low, although the scale effect cannot be given

in terms of a scale factor. This may affect the processes of the intrusion of the jet. Also, an underestimation of the permeability implies an overestimation of the radial flow velocity. This should be taken into account when analysing the results of the tests, but can also be anticipated for with the set-up of the test configurations. This is discussed in Chapter 3.1.4.

When the particle diameter in the scale model is smaller than 6 mm, the critical Shields value will show some scale effects. This scale effect can however not be expressed in a value of n_L due to the nature of the critical Shields value. This scale effect will also influence other parameters, such as some sediment transport formulae en the erosion velocity. The scale effects of critical velocity depends quantitatively on the applied scale value of the test, just as the seepage velocity, see Chapter 3.1.4.

The erosion velocity also shows a scale effect: it is too low in the scale model. It is assumed that the erosion velocity is not the governing process; this is considered to be sediment transport process. An underestimation of the erosion should therefore not lead to the fact that the erosion will become the governing process. As long as this is not the case, the scale effect on the erosion velocity will not be considered to be an issue, although the scale effect should be borne in mind when analysing the results. This is also discussed in section 3.1.4.

Due to the correct scaling of the Shields parameter, the sediment transport formulae are almost all correctly scaled. Only the Van Rijn formula shows a scale effect, just as the saltations. These expressions of Van Rijn are however empirical, the question therefore arises if these scale effects indeed occur or if these deviations still fall within the accuracy margin.

3.1.4 Applied scale

The chosen scale to be applied in the tests is preferably as large as possible to limit the scale effects. The limiting factor determines the upper value of the scale factor; any larger factor will introduce unwanted wall effects or is practically not possible. The width of the water tank is in this case the limiting factor. A scale factor of 1:30 is considered to be the maximum in order to be able to make a physical model of the rock cover over the entire width of the tank without introducing wall effects. This implies that the mean diameter of the grains used in the scale model should be about D_{50} = 3 mm. The Froude scale scenario is chosen, which means that the velocity will be scaled with a factor of 1:√30. This means that the values as provided in Table 3.2 can be expected in the scale model.

Table 3.2 – Scaled values of characteristic parameters independent on u_j

Parameter	Symbol		Unscaled value	Scaled value
Grain diameter	D_{50}	[mm]	90	3
Jet diameter	D_0	[mm]	500	16.7
Fall velocity	w_0	[m/s]	1.2	0.22
Critical velocity	u_{cr}	[m/s]	1.2	0.2

3.1.4.1 Scale effects

The applied Froude scale scenario has certain scale effects incorporated. How to mitigate these effects, and what will be the influence on the test results, is discussed in this section.

Seepage flow

It was stated that the permeability is lower than desired for a correct scaling of the seepage processes. Therefore, the flow available for the radial wall jet, and thus the near-bed velocity, is too high. In fact, the seepage flow does not have a big influence and is therefore relatively unimportant; but it is particularly important that the radial jet flow is correctly scaled. In order to limit the scale effects, it can be chosen to alter (one of the) other parameters that have an influence on the seepage flow. The sensitivity analysis that is performed to determine which parameter can be altered is provided in Appendix B.2. It turns out that an increase of the porosity leads to an increase of the seepage flow, resulting in a decrease of the scale effects without significant negative side effects. With this point of view, the scale model should have a higher porosity than in the prototype situation to limit the scale effects for seepage flow.

Critical Shields parameter

With D_{50} = 3 mm, the critical Shield parameter does not have a constant value anymore. Instead of θ_{cr} = 0.06, the value of about θ_{cr} = 0.045 is assumed for the grains used in the scale model, according to Eq. (2.43). The effect on the critical velocity is however relatively small; a factor √(4.5/6) = 0.87 according to Eq. (3.19). The adjustment of the critical Shields parameter also has an effect on the value of the erosion velocity and some sediment transport formulae. For the erosion velocity, this is a positive effect: a decrease of the critical Shields parameter leads to an increase of the erosion velocity. Since the erosion velocity in the scaled model is lower than desired according to the scale rules, a decrease of θ_{cr} leads to a somewhat smaller scale effect for the erosion velocity. The same holds for the increase of the porosity, applied because of the scale effects of the seepage flow. A higher porosity means that the pick-up of the sediments leads to a faster decrease of the bed level.

The scale effects for different scaling options are provided in Table 3.3 for a Shields value of θ = 1.0, which corresponds to $u_b \approx 1$ m/s and a grain diameter of D_{50} = 3 mm.

Table 3.3 – Scale effects with D_{50} = 3 mm

Parameter	**Scale effect**			
	n=0.3, θ_{cr}=0.06	n=0.4, θ_{cr}=0.06	n=0.35, θ_{cr}=0.045	n=0.4, θ_{cr}=0.045
Erosion velocity	3.0	2.4	1.7	1.5
Saltation length	7.7	7.7	5.8	5.8
Saltation height	10.8	10.8	9.3	9.3

The effect of hindered erosion is larger in the scale model than in the prototype situation. The provided scale effects of the erosion velocity in Table 3.3 are therefore calculated with the adaptation of Van Rhee, described in section 2.3.2.1. However, thanks to the decrease of the critical Shields parameter and the increase of the porosity, the scale effect can be limited to only 1.5.

The scale effect on the erosion velocity is therefore accepted, also because the erosion is not expected to be the governing process, opposed to sediment transport. As long as the erosion velocity in the model is not so low that the erosion becomes the governing process, the small scale effect on the erosion velocity is acceptable.

The scale effect for the formulae to determine the saltation length and height remains high. However, there is some uncertainty about the applicability for these empirical Van Rijn expressions outside the range used by Van Rijn. Moreover, the expressions already show a relative large inaccuracy, as was already mentioned in section 2.4.2. Finally, the expressions result in doubtful values for the prototype. The calculated saltation height and length are 14 m and 132 m respectively for a situation with $\theta = 0.4$. The expressions to determine the saltation movements are therefore considered unreliable with the conditions of a dumped rock cover.

3.2 Experimental set-up

The process of the mass flow excavation with a horizontally moving vertical jet can be modelled by a moving nozzle, submerged in a water tank, along a prepared gravel bed, see also Figure 3.1. This situation sketch forms the basis of the different test set-ups, described in this section. The moving jet can be obtained by connecting the nozzle to a movable cart, riding along the water tank.
A similar set-up is used for the preliminary tests as for the working method tests. However, there are some differences between the test series. The fundamental changes will be mentioned in this chapter, the specific differences in the chapter describing the corresponding test series.

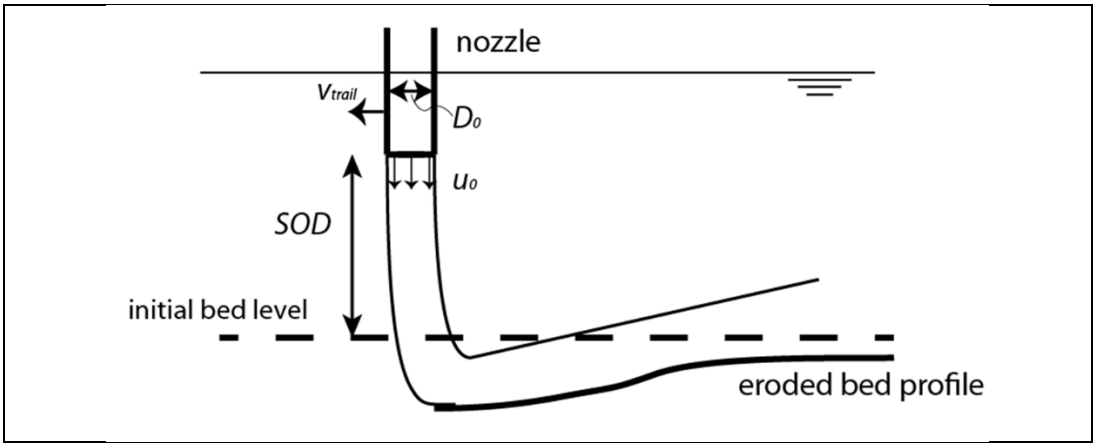

Figure 3.1 – Physical base model of the jetting operation

3.2.1 Horizontally moving vertical jet

With a horizontally moving vertical jet, the free jet flow is perpendicular to the bed while the nozzle moves in the longitudinal direction of the water tank with a constant distance relative to the tank bottom. The pipeline cover is created on top of the tank bottom with an orientation that depends on the desired moving direction of the nozzle. A logical orientation of the cover is in the same direction of the tank, so the nozzle moves over the scale model in the longitudinal direction. This test set-up is sketched in Figure 3.2.

With this set-up however, all important erosion and sedimentation processes occur in the middle of the water tank and are not clearly visible for the observer. It can therefore be chosen to apply an experimental set-up with a symmetry wall. With this method, the scaled pipeline cover and nozzle are “cut” through the middle and placed against a

transparent wall, see also Figure 3.3. The important erosion and sedimentation processes have a better visibility in this way, which can lead to a better understanding of the phenomena. However, the wall can have an influence on the processes as well, which have to be taken into account when interpreting the results of a test.

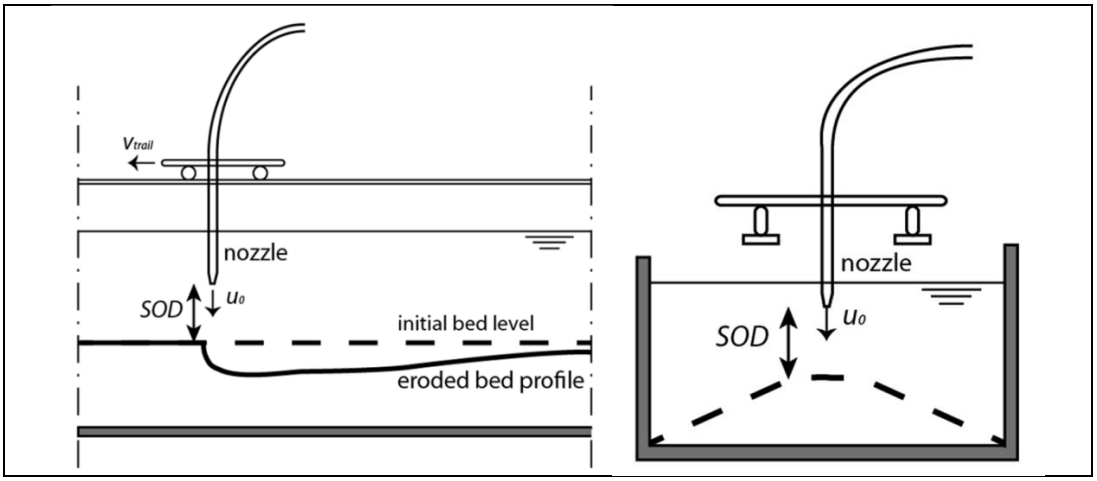

Figure 3.2 – Set-up for horizontally moving vertical jet, side view (left) and cross-section (right)

As can be seen from both set-ups, it should be possible to connect the nozzle to the cart at two locations: in the middle and at one of the sides.

With the application of the symmetry wall, the jet is cut in half as well. This should therefore be modelled with half a nozzle, pressed against the glass. This will probably lead to flow losses due to connection problems with the fully circular garden hose. It can however also be modelled as a fully circular nozzle, although the scaled nozzle diameter should be adapted according to Eq. (3.27), so that the flow velocity will still have the desired value. A detailed explanation about the set-up with a symmetry wall is provided in Appendix B.3, together with a general description about possible wall effects.

$$D_{0_{scaled}} = \sqrt{\frac{1}{2}} \frac{D_{0_{proto}}}{n_L} \tag{3.27}$$

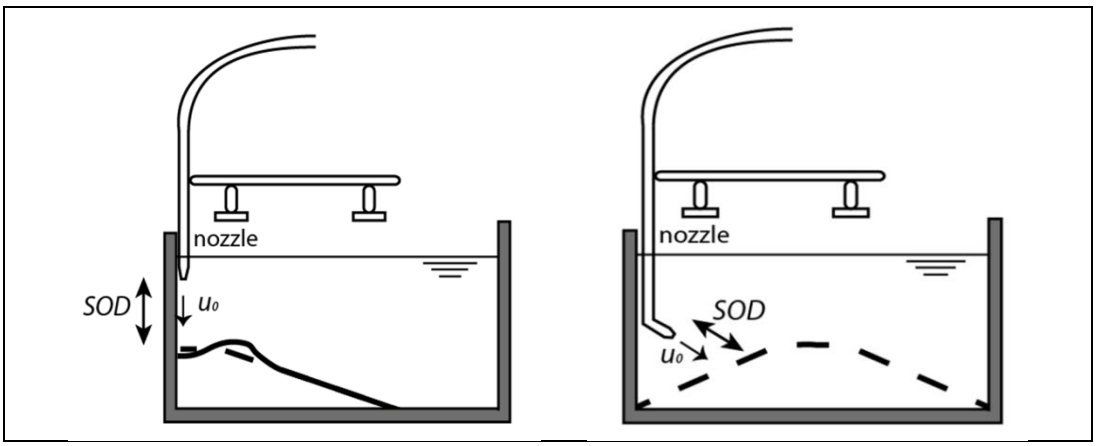

Figure 3.3 – Cross-section of set-ups with a symmetric wall (left) and oblique jet (right)

3.2.1.1 Horizontally moving oblique jet

A similar set-up can be used to model the jetting processes when the jet flow is not perpendicular to the bed, but at an angle. With this set-up, the nozzle is placed in an oblique position by inserting a bend of PVC just before the end of the nozzle. The connection with the cart is equal with the set-up with a symmetric wall, but the scaled rock cover bed is now placed in the middle of the tank, see also Figure 3.3.

3.2.2 Test equipment

A water tank with the dimension of 2.5 x 0.40 x 0.45 m^3 is used for the experiments. This water tank has transparent side walls that enable the visual observation of the entire experiment. A grid of 5x5 cm^2 is painted on the glass wall to facilitate easy visual measurements. This grid also helps by the determination of the stand-off distance. For the ease of access, the water tank is placed on a number of wooden pallets. Emptying of the tank takes place by opening the valve. Because of the higher level of the tank, the emptying process automatically takes place once the valve is opened. The water is stored in a container, located directly under the valve. The test set-up is illustrated in Figure 3.4, with the container coloured red.
The water used to fill the water tank is fresh water. In most situations, the prototype will be situated in the sea and therefore be surrounded with salt water. The difference of the density is assumed to be negligible. The diameter of the water hose is 1.68 cm. The nozzle can be modelled by either the hose or a PVC pipe, with a diameter of 1.36 cm.

Figure 3.4 – Water tank used for small scale tests

A submerged water pump is placed in this container, connected to the nozzle with a garden hose system, see also Figure 3.5. This system can be used to change the resistance that the pump has to overcome, so the flow through the nozzle can be controlled. However, this flow rate is relatively difficult to determine when in a submerged testing position. The flow is therefore calculated by measuring the time taken to fill a basket with a known volume. The initial flow velocity and jet pressure are determined for various nozzle designs that are used in the test series. The obtained values are provided in more detail in Appendix B.3; the discharge coefficient of each nozzle type is repeated in Table 3.4.

Table 3.4 – Discharge coefficient C_d for each nozzle type

Nozzle type	C_d [-]
Straight PVC pipe; D_{noz} =1.36 cm	0.95
Straight hose; D_{noz} = 1.6 cm	0.85
Inclined jet; θ_j = 0 deg; D_{noz} = 1.6 cm	0.60
Inclined jet; θ_j = 30 deg; D_{noz} = 1.6 cm	0.65
Inclined jet; θ_j = 60 deg; D_{noz} = 1.6 cm	0.70
3 nozzles; D_{noz} = 4.5 mm	0.70
7 nozzles; D_{noz} = 4.5 mm	0.65
10 nozzles; D_{noz} = 4.5 mm	0.60

A frame is placed on top of the water tank, containing a pair of rails on which the cart rides. This cart is driven by a motor, connected to the cart via a spindle, see also Figure 3.5. The power of the motor is adjustable, so the revolutions of the spindle and thus the trailing velocity of the cart are controllable. A steel frame is welded to the cart and located underneath the cart, at the inside of the water tank. The nozzle can be connected to this frame, to create a trailing jet. The nozzle can be connected either in the middle of the water tank or at the side, see also Figure 3.5. A general lay-out of the test set-up for a small scale test with a symmetrical wall is provided in Figure 3.7. Extra information about the camera and the length of the scale model is given in Appendix B.3

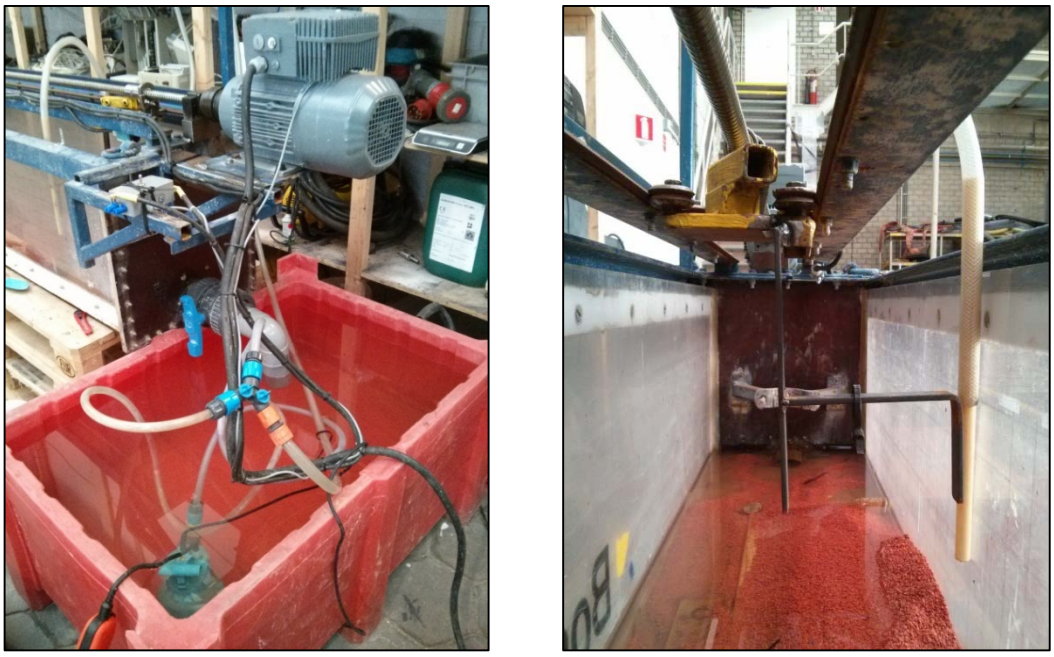

Figure 3.5 – Pumping system (left) and cart with jet nozzle (right, empty tank)

3.2.3 Soil characteristics

The stones used in the scale model have a mean grain diameter of D_{50} = 3 mm, are angular shaped and have a relative uniform grading, as can be seen in Figure 3.6. The fall velocity has been determined to be w_0 = 0.2 m/s, which is very close to the calculated value of Eq. (2.50). The grains are red coloured to enhance the visibility.

The compaction of the soil, or the value of the porosity, depends on the way the scale model has been created. This parameter is an important tool to limit scale effects, as was discussed in Section 3.1.4. These predicted effects, and whether the compaction has a considerable influence on the outcome of the tests, are the subject of a short test. The entire test report is provided in Appendix B.4, here only the conclusions are repeated.

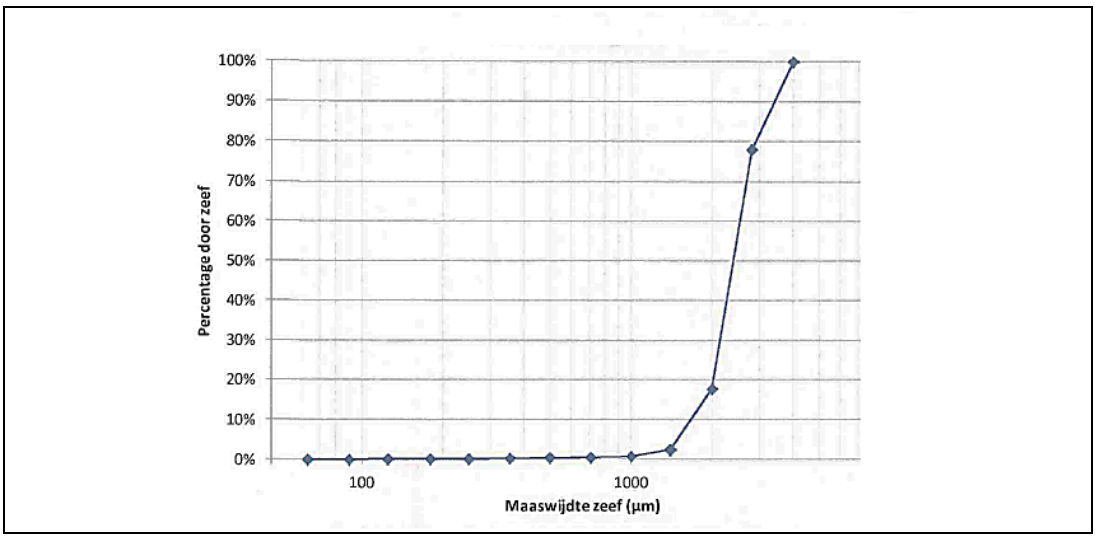

Figure 3.6 – Grading curve of the material used in the tests

The compaction has found to have little influence on the eventual eroded bed profile. The compaction does have an influence on the number of runs required to reach the equilibrium situation. It seems therefore that the porosity has an influence on the erosion velocity, but not on the scour depth. It can therefore be concluded that the influence of the compaction can be assumed to be negligible in the determination of the scour depth, although it affects the erosion velocity. The assumptions made in Chapter 3.1.4 are therefore confirmed. Analogue to these assumptions, all forthcoming tests will therefore be performed with a relative loose compaction to limit the scale effects as much as possible.
It should however be borne in mind that a dense compaction experiences a bulking effect: the porosity is increased and therefore the total volume as well. Due to this increase of volume, the apparent scour depth is lower with an initial dense compaction, although the eroded number of stones is about equal.

It was also concluded that the initial bed profile had a large influence on the scour depth, although it did not influence the eventual eroded bed profile. The initial bed level should therefore be paid attention to as it should comply to the existing profile of the protective cover in order to give a more accurate scour depth.

3.2.4 Data acquisition

The bed profile is measured before and after each run of a test, so that the changes of the bed level can be determined. This process is performed at three different points that are compared with each other to obtain the average bed level. If one point obviously differs from the other two points, it is neglected. In this way, local deformations of the bed does not influence the general outcomes of the test.

There are two processes of data acquisition; the one used for the preliminary tests is different than for the working method test. The measurement for the first two series of tests, the compaction and preliminary test, is performed by determining the distance between the bed and a constant reference level with a ruler. Due to a limited accessibility of the water tank, only the profile up to 80 mm from the wall can be measured. This process is sufficiently accurate for the purpose of the preliminary tests, but not for the working method tests. The measurements for these test are therefore performed with the use of a laser beam that can be converted into an accurate representation of the bed profile. This process is explained in more detail in Appendix B.3.

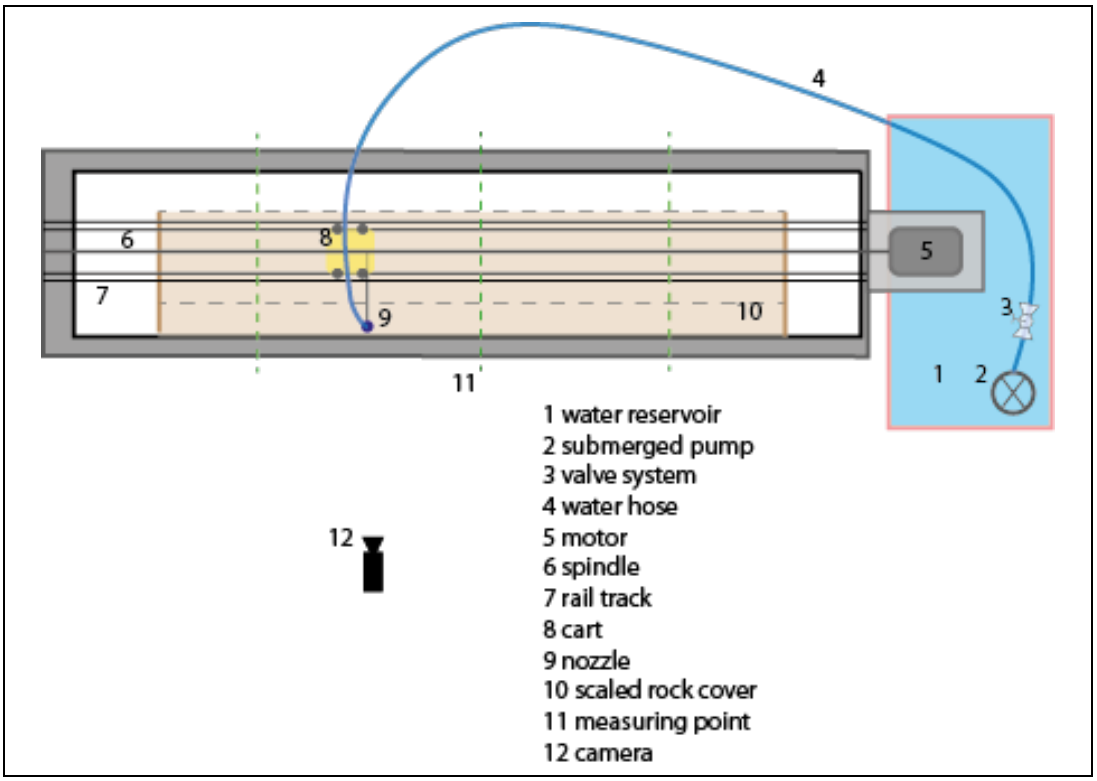

Figure 3.7 – Lay-out of a small scale test with a symmetrical wall

4 Preliminary tests

4.1 Preliminary test results

In order to get insight in the occurring processes with a horizontally moving vertical jet, a preliminary test series is performed. Five tests are executed to model the erosion processes of a horizontal moving jet in the longitudinal direction of the rock cover. The focus in these tests is more on the qualitative part, rather than the quantitative.

4.1.1 Test set-up

The set-up of these preliminary tests is with a symmetry wall, which was described in section 3.2, with a Froude scale of 1:30. The compaction and mean diameter are kept constant, just as the nozzle diameter. The test is executed with a symmetry wall, the nozzle diameter of the PVC pipe with D_{noz} = 1.36 cm has therefore an unscaled value of D_{noz} = 0.58 m according to Eq. (3.27). The other parameters are taken as a variable with the corresponding jet configurations as provided in Table 4.1 are used for these series of tests, which corresponds with the prototype values as given in Table 4.2.
These configuration are chosen in order to obtain two tests with a high flow velocity and two tests with a relative low flow velocity, both performed with a high and low trail velocity. As a sort of reference case, a configuration with a medium flow velocity is chosen; equal to the configuration used for the compaction tests of Appendix B.4.

Table 4.1 – Test configurations for preliminary tests, scaled values

Parameter	Test 2.1	Test 2.2	Test 2.3	Test 2.4	Test 2.5	
p_j	0.028	0.028	0.008	0.008	0.004	[bar]
u_0	2.4	2.4	1.2	1.2	0.9	[m/s]
SOD	0.1	0.1	0.1	0.15	0.15	[m]
u_b	1.0	1.0	0.5	0.3	0.2	[m/s]
v_{trail}	0.2	0.05	0.15	0.15	0.05	[m/s]

Table 4.2 – Test configurations preliminary tests, unscaled values

Parameter	Test 2.1	Test 2.2	Test 2.3	Test 2.4	Test 2.5	
p_j	0.83	0.83	0.22	0.22	0.11	[bar]
u_0	13	13	6.7	6.7	4.7	[m/s]
SOD	3.0	3.0	3.0	4.5	4.5	[m]
u_b	5.3	5.3	2.8	1.8	1.3	[m/s]
v_{trail}	1	0.3	0.8	0.8	0.3	[m/s]

One run corresponds with one passing of the jet. After the three runs, the profile of the bed is measured with the ruler; hereafter, the bed profile is measured after each fifth run. The total number of runs is chosen until the point that the observed erosion between two runs has become negligibly small. Erosion is considered to be grains that are transported over the berm out of the scour hole. The actual equilibrium situation will be reached after multiple runs when the absolute erosion velocity has become zero. However, a maximum average bed level change of less than a stone diameter is chosen as a practical value of the equilibrium situation during the tests.

4.1.2 Test results

The results of the tests are discussed and graphically presented in Appendix C, with graphs displaying the bed profiles with the values given in [mm]. Here, only the numerical summary is provided, together with the profiles of test 2.5 as an example. The value of z is only to give an impression of the differences: $z = 0$ is chosen so that the initial situation is around this value, but has no real meaning. In Figure 4.3, $h = 0$ corresponds with the initial bed level. All parameters are sketched in Figure 4.1.

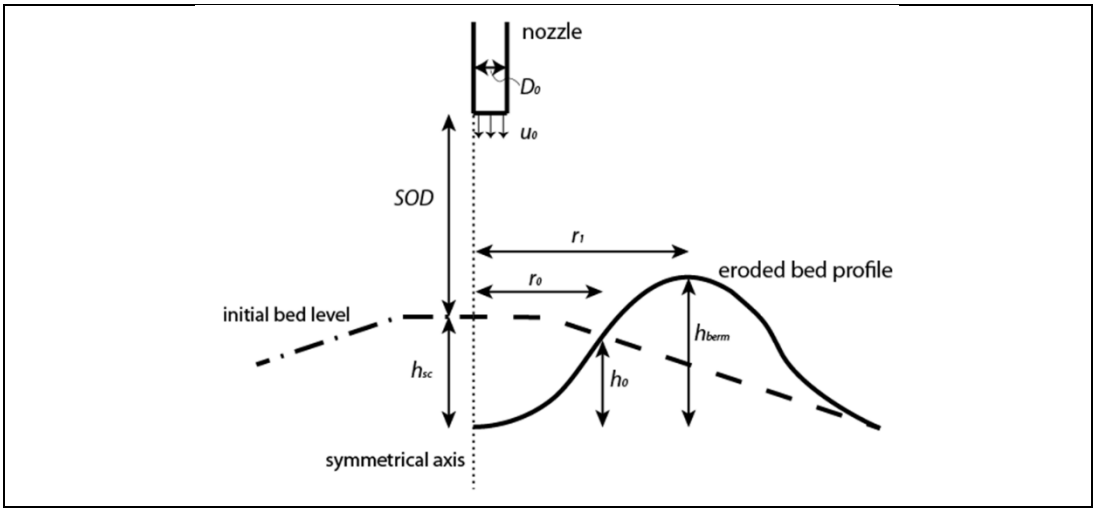

Figure 4.1 – Scour profile with characteristic parameters

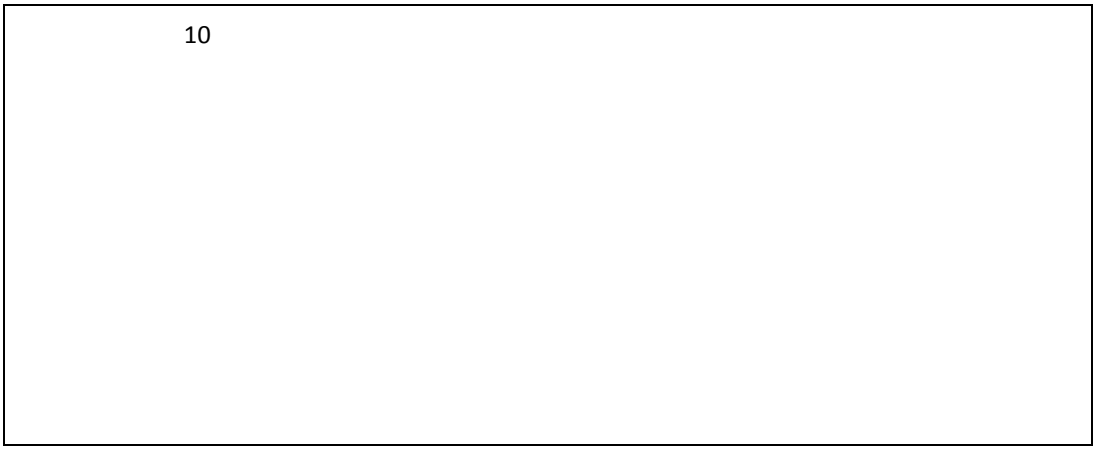

Figure 4.2 – Profile of bed level for test 2.5

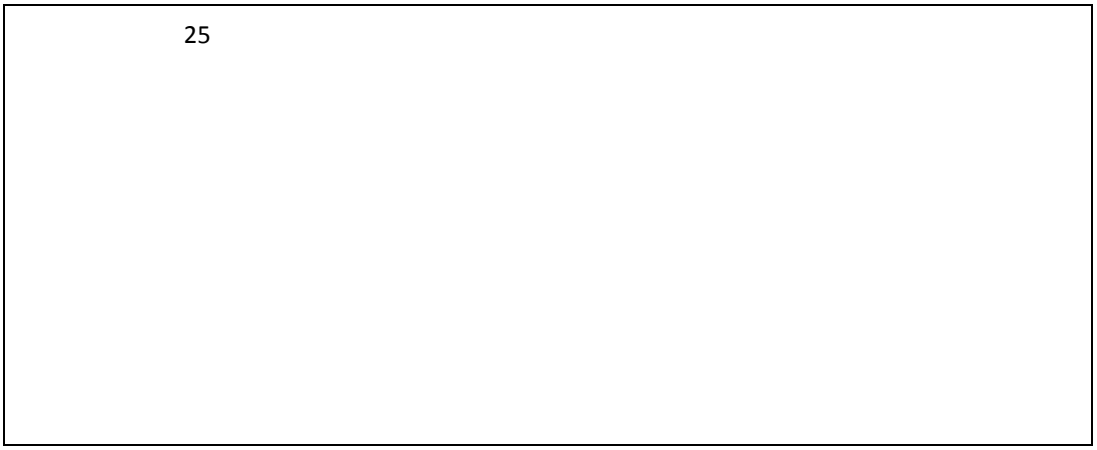

Figure 4.3 – Profile of bed level for test 2.5, relative to initial situation

4.1.2.1 Summary of results

Table 4.3 – Primary data obtained after the preliminary test series

The radially deflected jet forms a scour hole in the tests 2.1, 2.3 and 2.5. The bed level increased during test 2.2, most probably due to the stirring action of the penetrating jet that increases the porosity. The bed volume therefore increases as well. Almost no radial transport is observed in this test. The erosion during test 2.4 already stops before a scour hole with a berm is created; the jet does not penetrate the bed.

Table 4.4 – Applied data after the preliminary test series

4.1.3 Analysis of results

The following visual observations were made during the tests:

- With a high ratio between the flow and trail velocity, the jet acts as a penetrating confined jet. For a small ratio, it is a non-penetrating radial wall jet. In between, the jet penetrates in the soil, but also has radial transport in forward and sideward directions and forms a scour hole profile.

- When a scour hole profile is formed, the 'equilibrium' situation is formed when stones cannot be transported over the berm. Erosion still occurs in the scour hole in that situation. So actually, it is not the erosion that stops, which could be concluded out of the bed profiles in the graphs, but the sediment transport out of the scour hole.
- In this equilibrium situation, there is still transport in longitudinal direction, opposite to the moving direction of the nozzle. This transport does not seem to have a direct influence on the erosion. However, when the longitudinal transport is high, such as with test 2.1, the penetrating jet causes a decrease of support for the adjacent berm, which then partly collapses into the pit. This has as an effect that the scour hole is flatter and wider.
- The erosion is the highest in the first run, regardless of the configuration.
- The stirring action of the jet causes an increase of the porosity, with a higher bed level as a result. This limits the scour depth, or can even cause negative production with Test 2.2. This can however also be caused due to the extra supporting force of the glass symmetry wall, and can thus be a wall effect.
  In the tests with the high jet pressure, the entire bed is stirred as the jet penetrates to the bottom. This means the bottom of the water tank in this model, which has probably effect on the measurements, although it is expected that it does not affect the qualitative results of the test. Note that in the actual situation, this means that the jets penetrates even into the sand bed under the rock cover, with possible scouring of the subsoil as a result.

A more quantitative analysis can be derived from the numerical results.

- The scour depth seems to depend little on the flow or trail velocity, but much more on the initial bed profile. This seems logical as erosion still takes place during the equilibrium situation, but the stones cannot be transported far enough to obtain more production.
  - The average value of the scour depth is about 6-7 times D_{50}. Note that the porosity has increased under the jet, so the number of removed layers of stones is probably more than 7 stone diameters thick.
- The length of r_1, which can be seen as the width of the scour hole, seems to depend mainly on the initial bed profile rather than the jet configuration. In all tests with a scour hole, the value of r_1 is about the same.
- It cannot be concluded from the results whether the profile of the scour hole depends on the flow and trail velocities. With a smaller ratio u_b/v_t, the scour hole seems to become smaller, but the differences between the tests are too small to base conclusions on these results.
- The height of the berm is about 5 to 6 times D_{50} for each test with a scour hole.
- The erosion is the highest with the configurations with a scour profile, although an equilibrium state is reached that stops the erosion after only a few runs. This means that an increase of the jet pressure does not lead automatically to an increase of the erosion. On the contrary, an increase of p_j can even lead to negative production due to the bulking effect.
- Based on the relations found in section 2.4.5, the equilibrium scour depth can be calculated, with the results as found in Table 4.5.

Table 4.5 – Calculated results for preliminary tests

Test	E_c [-]	h_{sc} [mm]			h_{berm} [mm]	r_o [mm]
		Eq. (2.78)	Eq. (2.79)	Yeh (2009)	Eq. (2.80)	Eq. (2.80)
2.1	2.0	375	36	23	43	62
2.2	2.0	375	36	23	43	62
2.3	1.0	140	26	17	28	42
2.4	0.7	90	32	20	34	52
2.5	0.5	30	25	16	25	48

The test results show that the approximation of Eq. (2.78) gives a severe overestimation of the scour depth. The empirical relations found by Rajaratnam (1996) give a more accurate result and can therefore be used as a first approximation. However, these expressions still give an overestimation of the results found in the tests. With the correction factor of Yeh, the results are closer to the measured scour depth. The reason for the difference between the calculated and measured outcomes is probably because the equations are based on a stationary jet; the effect of the trail velocity on the erosion is not taken into account. Moreover, Rajaratnam measured the profiles corresponding to the eventual situation, which was achieved after several hours. The situation in the test model had an acting time of the jet of only seconds. Finally, the initial bed level in the tests is not flat, in contrary to the experiments that led to the empirical relations of Rajaratnam.

4.1.4 Conclusions

It is found that the ratio between the near-bed flow velocity and the trail velocity influences the erosion processes. The highest erosion was obtained with a ratio of $u_b/v_{trail} > 3$, with which a radially reflected jet was created. A lower ratio does not have enough erosion capacity to give a profitable production, while with a higher ratio a penetrating confined jet occurs with a low erosion capacity.

The depth of the scour hole, created by a radially deflected jet, was about equal for different jet configurations with an order of magnitude of 6-7 times the stone diameter. This is not sufficient to remove the cover height above the pipeline of more than 10 stone diameters. The reason for this relative small depth is the berm of the scour hole; the jet is not able to transport the grains over this berm, probably due to the relative high fall velocity of the sediments. If this berm would be removed, it is expected that the process can start over again, enabling to create a similar scour hole and thereby further reducing the bed level. However, the removal of the berm seems to be a precarious operation: when a vertical jet is used to remove the berm, many grains will indeed be transported back into the previously created scour hole. This filling process that causes a bed level increase was also observed by a ROV during the removal of the Assaluyeh pipeline crossing.

The method of a horizontally moving vertical jet in the longitudinal direction seems therefore ineffective for the removal of a dumped rock cover.

5 Working method tests

5.1 Working method test program

The results from the preliminary tests showed that the initially proposed working method of a vertical jet, horizontally moving in the same direction as the pipeline, seems to be ineffective to remove a dumped rock cover. It would therefore be reasonable to focus the next test series on different working methods that are possibly more effective for the removal. The same test set-up is used as described in section 3.2. Some adjustments are required for each individual test series, which is provided in the corresponding chapter.

Three different working method test series are performed: with the jet direction at an angle, the trail direction at an angle and with an adjusted nozzle design. These three test set-ups are sketched in Figure 5.1. During the description of these tests, multiple definitions of an angle are used. An overview of these angles is provided in Table 5.1.

Table 5.1 – Overview of used angle definitions

Angle	**Description**	**In which plane?**
α_{bed}	bed angle	x-z or y-z plane
β_j	jet angle	x-z plane
γ_{trail}	trail angle	x-y plane

5.1.1 Jet direction at an angle

The reason why a vertical jet moving along the direction of the cover does not seem to be an effective working method is mostly because the transport capacity of the radially deflected jet is not sufficient. After a certain amount of time, the incapability of the jet flow to move stones out of the scour hole forms the equilibrium condition. However, erosion still occurs inside this scour hole. The jet flow is therefore still able to erode the bed, although it is insufficient to transport the stones far enough sideways to effectively lower the bed level.

The preliminary tests were focussed on creating a radially deflected jet. With a lower trail velocity or with a higher value of the erosion parameter E_c, given by Eq. (2.16), the jet would penetrate into the bed. This process did not add to the production regarding the sideways transport of the stones. However, if the jet direction becomes inclined instead of vertical, this penetration process may be advantageous for the production.

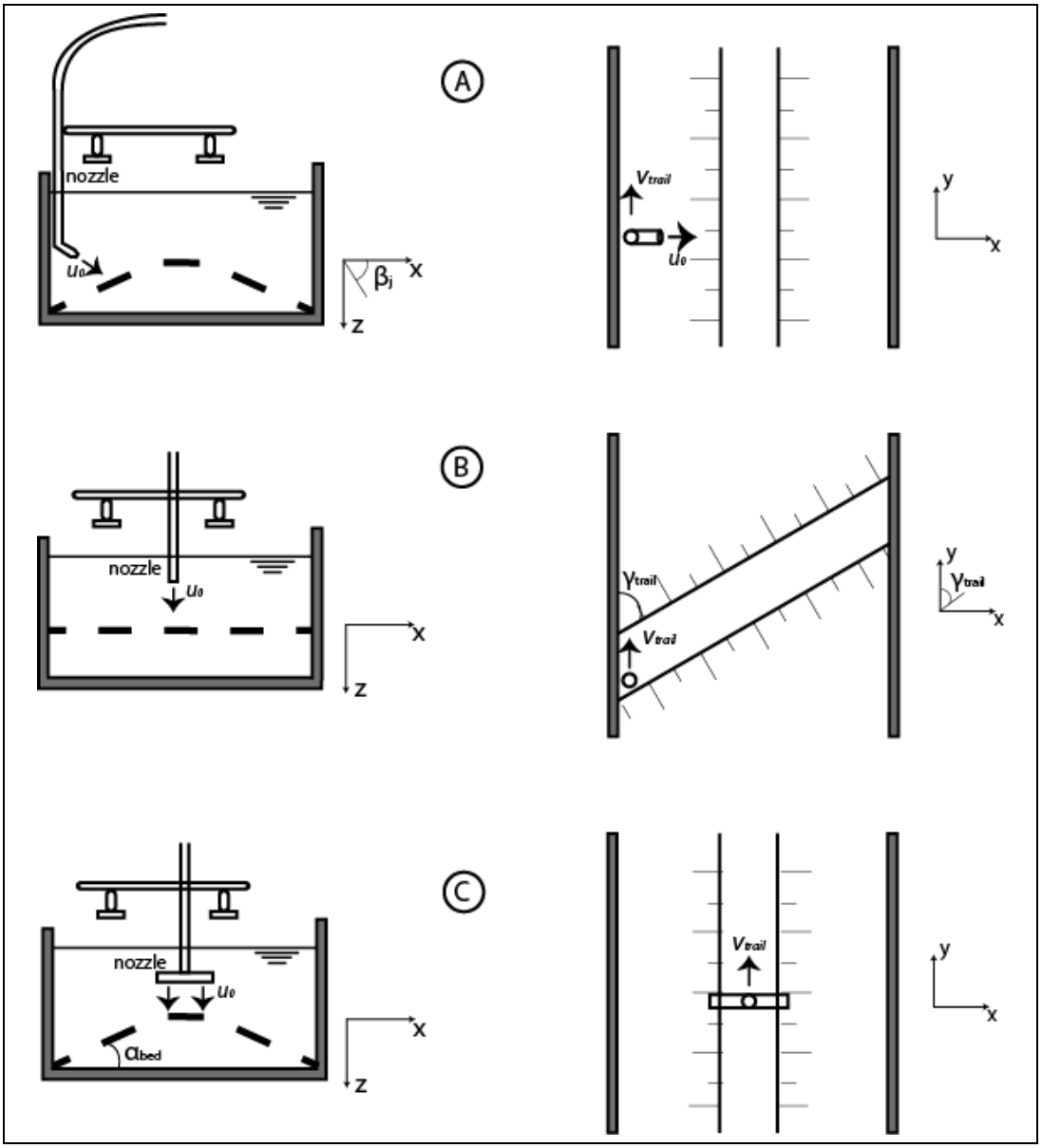

Figure 5.1 – Sketched test set-ups for jet direction at an angle (A), trail direction at an angle (B) and an adjusted nozzle design (C)

This configuration of the jet direction β_j is sketched in Figure 5.1 (A). Stones will then be 'blown away' from the part on top of the pipe to a location next to the pipe. It seems therefore logical to study the possibilities of the mass flow removal of rocks by placing the nozzle at an angle, relative to the dumped rock cover.

However, this working method has some practical disadvantages. First of all, an up- or downwards movement of the nozzle would cause an inaccurate aiming of the jet; therefore, the nozzle has to remain at the correct location throughout the operation. This means that the motions of the ship due to waves, such as rolling and heaving, has to be corrected, so that it does not affect the position of the nozzle. Moreover, due to strong currents, the heading of a vessel is not always in the direction of the forwards movement, as is illustrated in Figure 5.2. Since the direction and magnitude of the

current is different for each operation, the connection between the nozzle and the vessel should be adjustable so the nozzle can be placed in a position next to the cover as illustrated in Figure 5.1 (A). This problem does obviously not occur with a vertical nozzle, which can be correctly placed above the pipeline regardless the heading. Finally, the reaction force of the inclined jet flow causes a momentum in the disadvantageous roll direction of the ship. This force will therefore have to be compensated for to prevent a movement and thus dislocation of the nozzle.

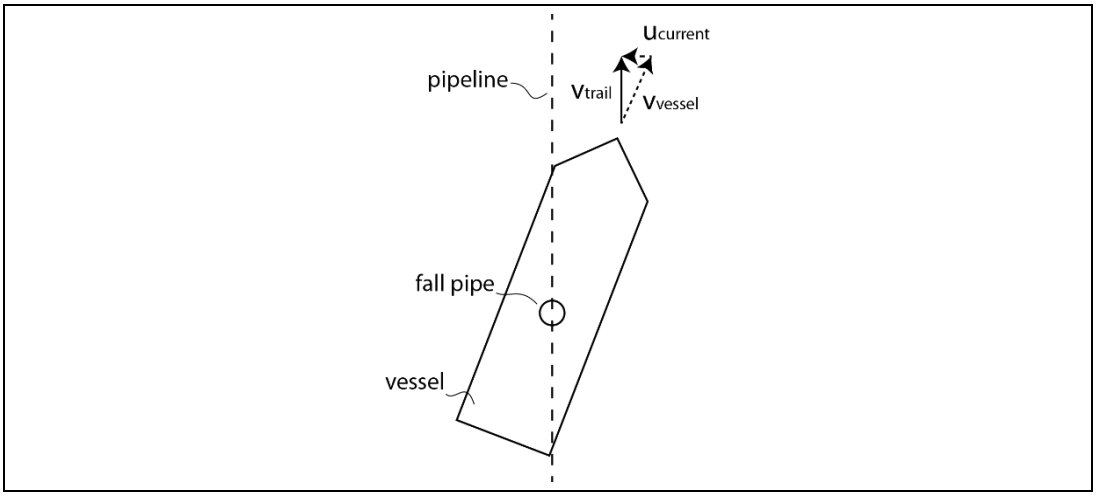

Figure 5.2 – The heading of the vessel depends on the current

Notwithstanding these disadvantages, this working method can result in a high production rate. A test series will therefore be dedicated to this working method.

5.1.2 Trail direction at an angle

Another observation from the preliminary tests was that the transport rate in the longitudinal direction, 'behind' the trailing jet, was higher than in the radial direction. Even in the equilibrium situation, when the sideways transport was negligible, transport in the backwards direction still occurred. With a trail movement in the same direction of the rock cover, the longitudinal transport is of no use. But with a trail direction perpendicular to the rock cover, this transport can be more useful, as stones on top of the pipe are then moved to a location next to the pipe. A variation of the trail direction γ_{trail} seems therefore a plausible starting point for a series of tests.

However, this method requires many, short, moves of the vessel in order to remove the entire cover. Also, the length over which the jet can act is also very small, namely only the width of the cover, so the total production volume per run is probably not maximal. The highest production lies therefore possibly somewhere in between the two extreme trail directions. On the variation of the trail direction is therefore the focus with the second series of tests. The jet direction β_j remains vertical, as this is the preferred configuration to be applied by a fall pipe ship. The set-up is sketched in Figure 5.1 (B).

5.1.3 Adjusted nozzle design

The small scale tests were performed with a single, circular jet. One can however also think of other designs for the nozzle configuration. Although the circular jet has the advantage that it is very simple and can be performed with regular equipment without a specially designed nozzle, a specially designed nozzle can be feasible if it would deliver a high production. An interesting possible design of a nozzlehead consists of multiple small nozzles creating multiple small jets, comparable to a showerhead. With this design, a higher rate of entrainment is created than with a circular jet with the same initial jet pressure and stand-off distance. Due to this entrainment, all small jets eventually form together one big jet. Moreover, special shapes can be created by placing the small jets in particular positions, such as in a circle, a row or a V-shape. Such shapes can be used to control the direction of the jet flow in order to increase the production. Multiple nozzle designs are tested in the last series. In Figure 5.1 (C), the test set-up is sketched.

5.2 Jet direction at an angle

The first test series about the possible working methods focusses on a variation of the jet angle β_j. Firstly, some minor adjustments to the regular test set-up are described, together with the test configuration. After a summary of the test results, the outcomes of the tests are analysed. This analysis eventually leads to the conclusions.

5.2.1 Test set-up

The regular set-up as described in chapter 3.2 is used to model the jetting processes, but now with an inclined nozzle. With this set-up, the outflow of the nozzle is directed on the scale model of the rock cover. The nozzle can be placed in an oblique position by inserting a bend of PVC just before the end of the nozzle. By shortening the length of the bend, which originally makes a corner of 90 degrees, the jet angle β_j can be adjusted. With no shortening of the bend, a horizontal jetting direction, β_j = 0 degrees, is achieved, see also Figure 5.3. The nozzle is positioned in such a way that the jet flow is directed on the point at halve the cover height above the pipeline, see also Figure 5.4.

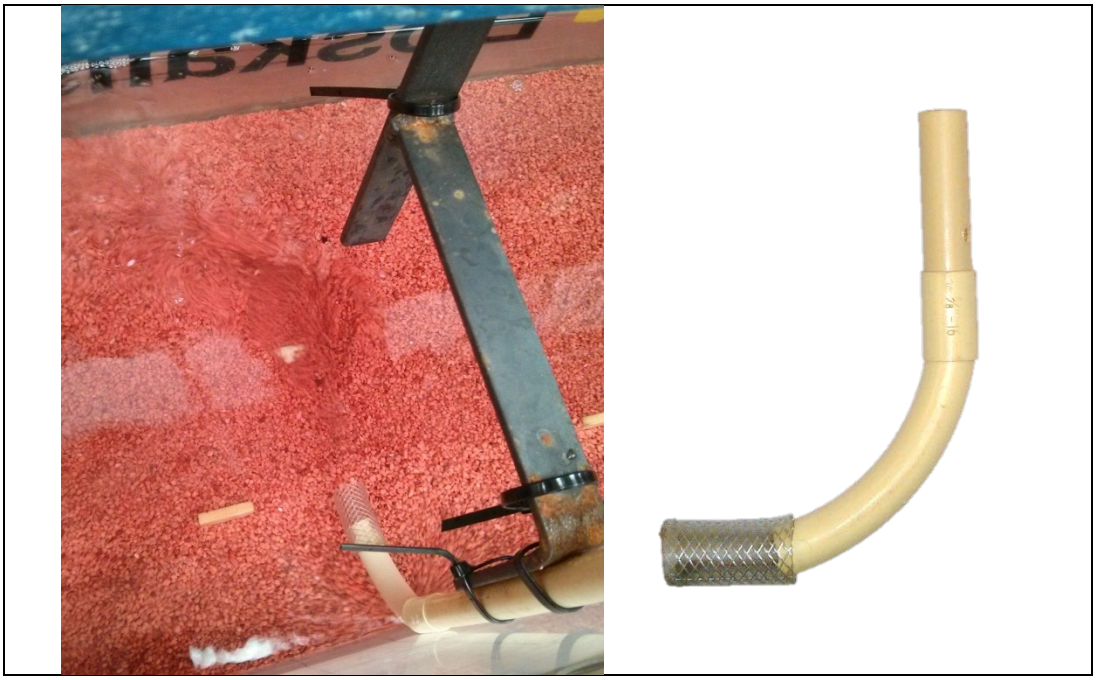

Figure 5.3 – A bend of PVC creates a nozzle directed at an angle

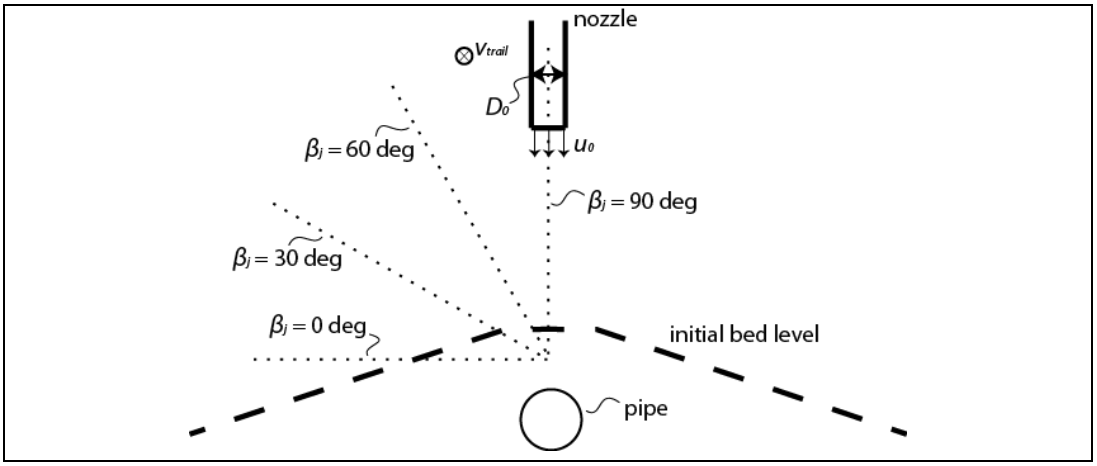

Figure 5.4 – The jet flow is directed at the same point for each angle

5.2.1.1 Test configuration

The most important variable in the tests is the jet angle β_j, which is varied to determine the influence of the impingement angle on the erosion and sediment transport processes.

The best possible outcome would be that the top layers above the pipeline are "blown away" by the jet. It is therefore expected that this process is more pronounced with a high jet penetration, which can be reached with a high jet pressure and/or a low trail velocity. With a low pressure and/or high trail velocity, the jet flow is deflected into radial directions. This will be less interesting, especially with a horizontal jet. In order to obtain a relation between the erosion and the flow velocity, the jet pressure will be varied, where the focus will be on a high jet pressure in combination with a small angle.
The trail velocity influences the penetrating behaviour as well and is therefore also varied. The trail direction is constant with γ_{trail} = 0 deg.

All other parameters are kept constant, with the diameter of the nozzle D_{noz} = 16 mm and the stand-off distance *SOD* = 0.1 m. However, the stand-off distance with the test set-ups with β_j = 30 deg and β_j = 90 deg were slightly larger with *SOD* = 0.12 m compared to *SOD* = 0.10 m for the other two test set-ups. This should be taken into account when analysing the results of the tests. The near-bed flow velocity is therefore varied by changing the jet pressure.

The jetting angle is varied between 90, 60, 30 and 0 degrees, with β_j = 0 deg corresponding to a horizontal jet. A more accurate jet pressure corresponding to each jet angle is provided in Table B.9. The trail velocity is varied between 0.1 and 0.4 m/s on prototype scale, or 0.02 and 0.07 m/s in the scale model.
This leads to the matrix as given in Table 5.2. Not every test is considered to be interesting, therefore only the marked configurations, with the corresponding test ID, are carried out. These thirteen tests are expected to be sufficient to lead to conclusions regarding the feasibility of this working method.

Table 5.2 – Test matrix for jetting at an angle test series (indicated number is test ID)

Trail velocity [m/s]	Jet pressure [bar]				Jet angle [deg]
	0.03	0.02	0.01	0.005	
0.02		3.10			90
		3.8			60
	3.3	3.6	3.13	3.14	30
	3.1	3.5	3.12		0
0.07		3.11			90
		3.9			60
	3.4	3.7			30
	3.2				0

Tests with a jet angle of β_j = 90 degrees were already performed in the preliminary tests, although with another combination of the jet pressure and trail velocity. Therefore, only test 3.10 and 3.11 will be carried out for a jet angle of β_j = 90 degrees.
For the combination with v_{trail} = 0.02 m/s and p_j = 0.02 bar, tests are performed for each jet angle in order to retrieve a relation between erosion and jet angle; with all other parameters kept constant. For β_j = 30 degrees and a trail velocity of v_{trail} = 0.07 m/s, all jet pressures are tested in order to find a relation between the flow velocity and erosion.

The initial bed level is measured before each test; this is the reference value to which the changes of bed level are compared to. The test ends when a negligible amount of extra production is observed during a run, i.e. when the equilibrium situation is reached. With these test configurations, this is typically the case after two or three runs.

5.2.2 Test results

All results of the tests are provided in Appendix D.1, only the summarised overview of these outcomes are given here. A definition sketch of all parameters is provided in Figure 5.5.

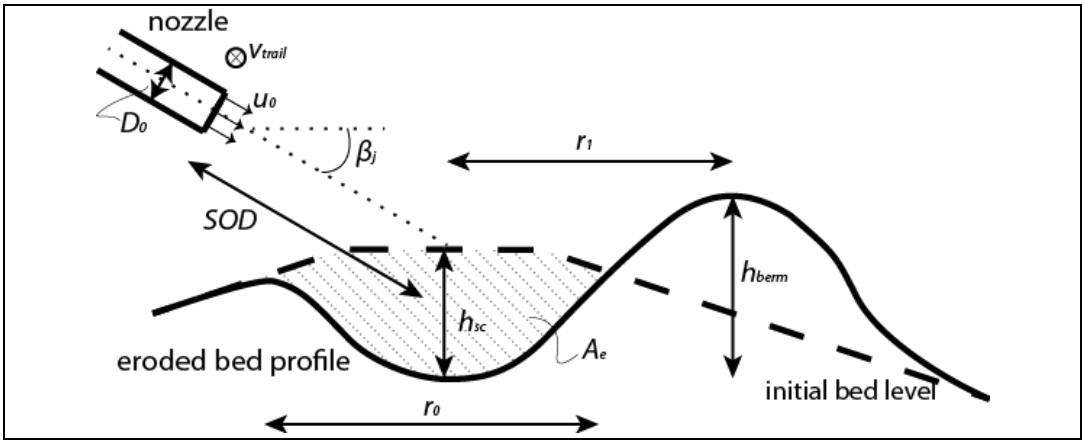

Figure 5.5 – Definition sketch for the jetting at an angle test series

By multiplying the eroded area A_e with the trail velocity v_{trail} and dividing by the number or runs, the production rate Pr [m^3/s] is obtained. The vessel has to be turned and

positioned between two subsequent runs. For a complete turnaround (a change of direction of 180 degrees) the ship simply sails ‘backwards’ with the same heading. This procedure takes in practice about two minutes. This time should be taken into account with the determination of the gross production rate with multiple runs. The net production is defined as the production rate without the reverse time. The reverse time becomes relatively less important when the clearance length of the rock cover increases.

5.2.2.1 Observations

The first four tests are focussed on a high jet pressure, resulting in a penetrating jet. If this penetration ‘depth’ of the jet is long enough, the flow ‘pushes away’ the berm, leading to relative good production rates. However, the jet flow is incapable of transporting all the stones over the berm and out of the created trench, as can also be seen in Figure 5.6. The forwards movement of the nozzle causes the jet flow to be deflected backwards, creating an eddy on top of the location of the pipe. A large part of the stones settle back in the trench; this process is also sketched in Figure 5.7. The eventual scour depth is therefore lower than the penetration depth. These observations also means that with a penetrating jet, the lack of sediment transport capacity causes the equilibrium, and not the eroding capability of the jet. Also, the created berm seemed to collapse after passage of the jet.

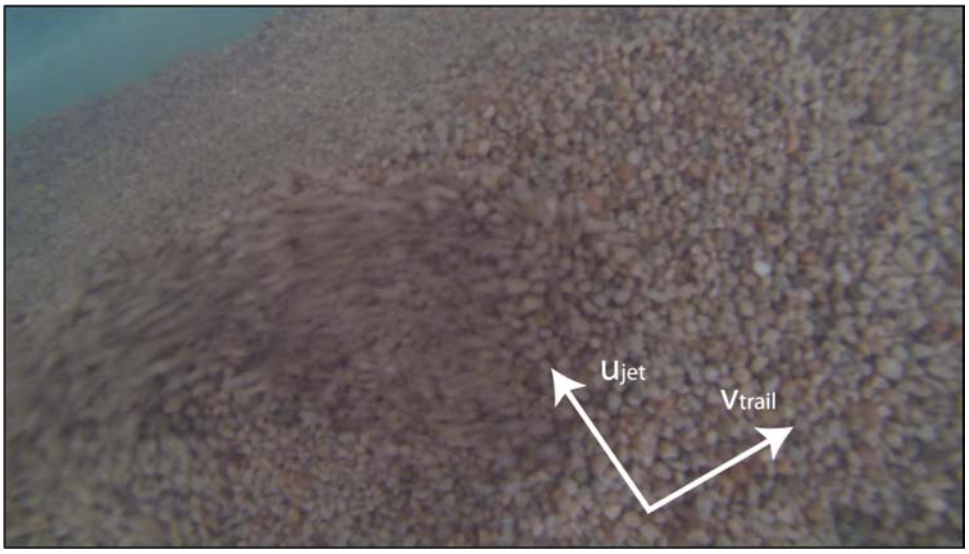

Figure 5.6 – Picture taken during test 3.3

With an increase of the trail velocity, as performed in tests 3.2 and 3.4, the jet has observably less time to develop the penetration depth. As a result, the created eddy is smaller and remains ‘inside the bed’, i.e. it does not exit the soil through the initial outer slope as is sketched in Figure 5.7. The erosion rate in these tests is therefore lower than in test 3.1 and 3.3, since the jet flow was less capable to ‘push away’ the berm.

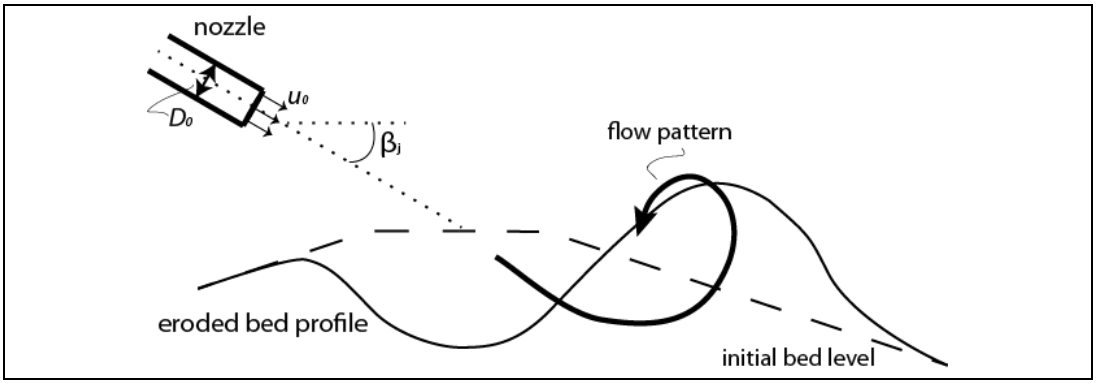

Figure 5.7 – Sketch of the flow processes with test 3.3

The penetration depth decreases considerable with a lower jet pressure, as is seen during test 3.5. The eddy was too small to 'push away' the berm, and remains at the location on top of the pipe.
During test 3.6, a similar jet pressure but now with β_j = 30 deg, it was observed that the jet was directed 'too low', i.e. at the inner slope of the rock cover. The eddy remained therefore even more inside the bed: it did not leave the bed through the outer slope. With the test with a higher trail velocity and the same jet pressure, test 3.7, the erosion caused by the radially deflected jet is more pronounced than the erosion caused by penetration.

With the tests with β_j = 60 deg, the initial bed was formed less accurately, see also Appendix D.1, leading to a sharp tip instead of a shallow berm. This tip was entirely pushed away, resulting in relative high erosion rates. This also stresses that an accurate aiming of the jet is crucial to reach a high production.
With a higher trail velocity, test 3.9, the jet acts partly as a radially deflected jet. This combination of both jet behaviours creates a relative shallow, wide trench.

Test 3.10 proved out to cause no positive effect on the bed level. All energy is just dissipated by the penetrating jet, only stirring the stones but with no effective transport. During the test with the same jet configuration but with a higher trail velocity, test 3.11, a partly deflected jet is observed, that transports the sediment radially outwards. This sideways movement of the stones creates a berm that is only after a short time already too high, preventing the sediment transport over the berm. Because the stones cannot be transported over the berm, it settles inside the scour hole. The sediment is then transported backwards by the flow, with a direction contrary to the trail direction. This flow eventually becomes an eddy, curved back from the berm towards the middle of the scour hole. Here it joins the eddy from the other side of the jet, causing the stones to settle in the middle of the created trench. This process is also sketched in Figure 5.8. This piling up of the stones in the middle of the scour hole was also observed in the preliminary test series, but was then partly attributed to a result of a wall effect.

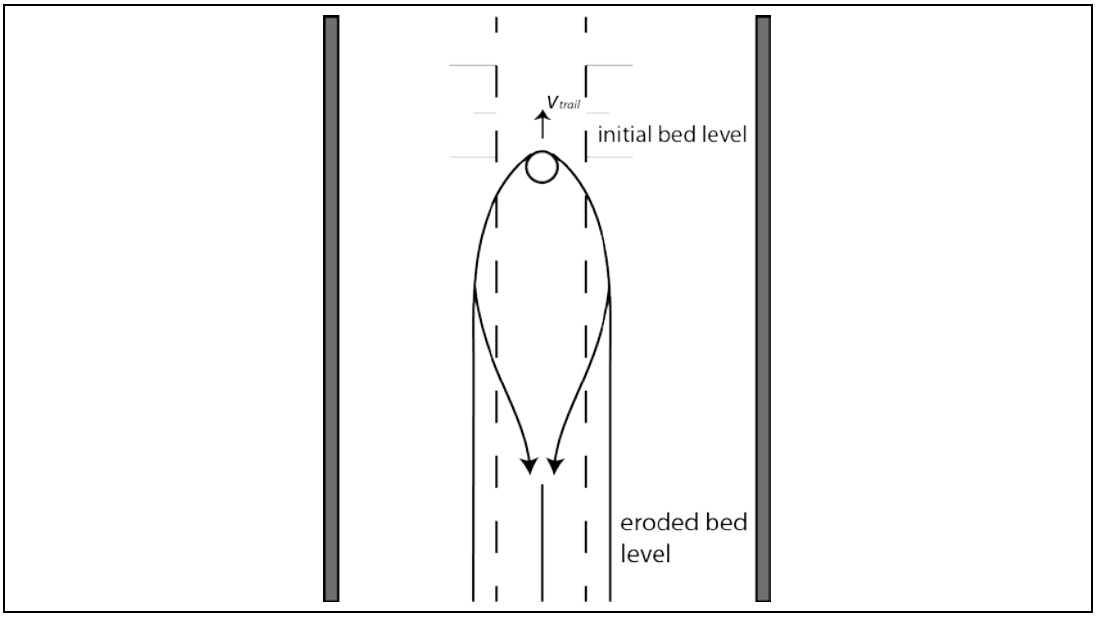

Figure 5.8 – Sketch of the flow processes of test 3.11

The piling up in the middle of the trench is obviously not beneficial for the removal of the cover, as the decrease of the bed level is limited with this little berm. It is also visible that this sedimentation process inside the trench becomes more pronounced after later runs. This can however also be attributed to the bulking effect: the increase of the porosity caused by the stirring movement of the penetrated jet.

After test 2.12 it is obvious that the jet flow with this configuration is far too small to cause any production. No transport is observed, only some stirring action by the penetrating jet.

During test 3.13, the effect of the penetration on the production is limited. However, a part of the jet flow is deflected radially outwards, which causes some production. However, this production is still limited. The difference between the first and later runs is larger than in the previous test. It is possible that this difference is caused by the fact that the main erosion process during this test is the radially deflected jet flow, which needs more time to reach its equilibrium situation as it peels off the bed layer for layer.

Observations show that the jet in test 3.14 is almost completely deflected into a radial wall jet. The production seems fairly low: the cover is eroded layer by layer. Moreover, the erosion only takes place on the slope of the cover: the jet does not penetrate into the bed.

The erosion after the first run is far higher than in later runs in all tests.

5.2.2.2 Summary of test results

All results are summarized in this section. The data of all tests are provided in individual tables to give a clear overview, enabling a quick way to compare all outcomes. Table 5.3 and Table 5.4 give the data after the first run, Table 5.5 and Table 5.6 provide the outcomes after all runs.

The near-bed velocity u_b corresponds with the theoretical uniform free jet flow velocity u_u at the location of the bed. The maximum flow velocity u_m is about twice this value, see also section 2.2.1 for more information.
Note that the values belonging to the scour parameters in the end situation are not necessarily the maximum value, which is sometimes obtained in a previous run.

Table 5.3 – Primary data obtained after first run for the test series 'jet direction at an angle'

Table 5.4 – Applied data after first run for the test series 'jet direction at an angle'

Table 5.5 – Primary data obtained after all runs for the test series ‘jet direction at an angle’

Table 5.6 – Applied data after all runs for the test series ‘jet direction at an angle’

5.2.3 Analysis

The jet angle is varied in this test series to study the effects on the erosion and sedimentation processes. To understand the influences of the flow velocity and speed of the vessel as well, the jet pressure and trail velocity were also varied. The influences of these three parameters are discussed separately before the general conclusions regarding the test series with jetting at an angle are presented. Also, the influence of multiple runs is analysed.

5.2.3.4 Influence of multiple passes

Even with a high trail velocity, the majority of the erosion occurred in the first run. Multiple passes at the same location are therefore not very useful, especially since the time required to stop and turn the vessel decreases the production rate even more.

However, the required erosion to clear the pipe was almost never reached after one run. A useful working method would be to aim the jet in the second run at the berm that was created in the first run. In this way, the berm that prevented the eroded stones from being transported out of the scour hole will be removed. A third run can then be executed with the jet directed on the other side of the scour hole, under the original jet location, to make the scour hole even wider. This makes it also simpler to direct the jet on the location above the pipe in the fourth run. In every run, a similar berm height and width is created since these parameters does not depend on the initial bed level. Such a sequence of runs is illustrated in Figure 5.17. If the obtained scour depth is not sufficient to clear the pipe, the procedure can be repeated.

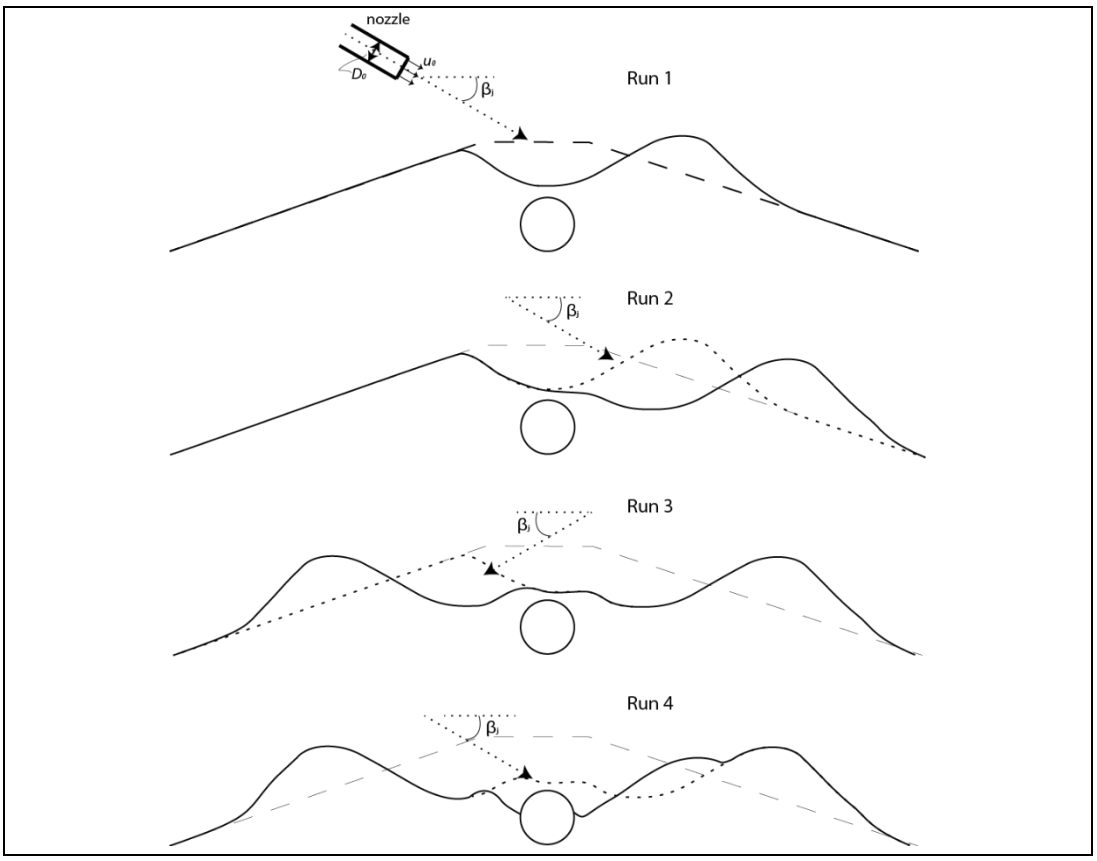

Figure 5.17 – A possible sequence of runs to clear a pipe with an inclined jet

A working method such as illustrated in Figure 5.17 is not useful for a radially deflected jet: stones would be transported back into the trench created in the run before. The application of such a sequence is also not possible for a horizontal jet, as the jet flow cannot be directed on a berm without the other berm getting in the way of the jet flow.

Note that the bed profile obtained after the third run looks similar to the profile obtained in test 3.14. If the jet direction is easily changeable, it is advantageous for the production to perform the first run with a vertical jet and switching to an inclined jet for the second run for the operation as illustrated in Figure 5.17, run 4. Another possible working sequence with a changeable jet angle could be that the first run is performed with a horizontal jet, after which the subsequent runs, if required, can be executed with a smaller jet angle.

It is possible that a vertical jet is the only viable option due to practical considerations, such as strong side currents. A working method with a longitudinal trail direction, $\gamma_{trail} = 0$ degrees, may still be sufficient to clear the pipe, although this method was rejected after the preliminary tests. It was shown in test 3.11 that a scour depth of about halve the cover height is reached after one pass of the jet. More passes with the jet at the same position leads to negative production. However, if a working sequence as illustrated in Figure 5.18 is applied, the pipe is expected to be cleared after 8 passes. If this sequences of eight passes is not sufficient to clear the pipe, five extra passes can be executed, with locations similar to the first five runs

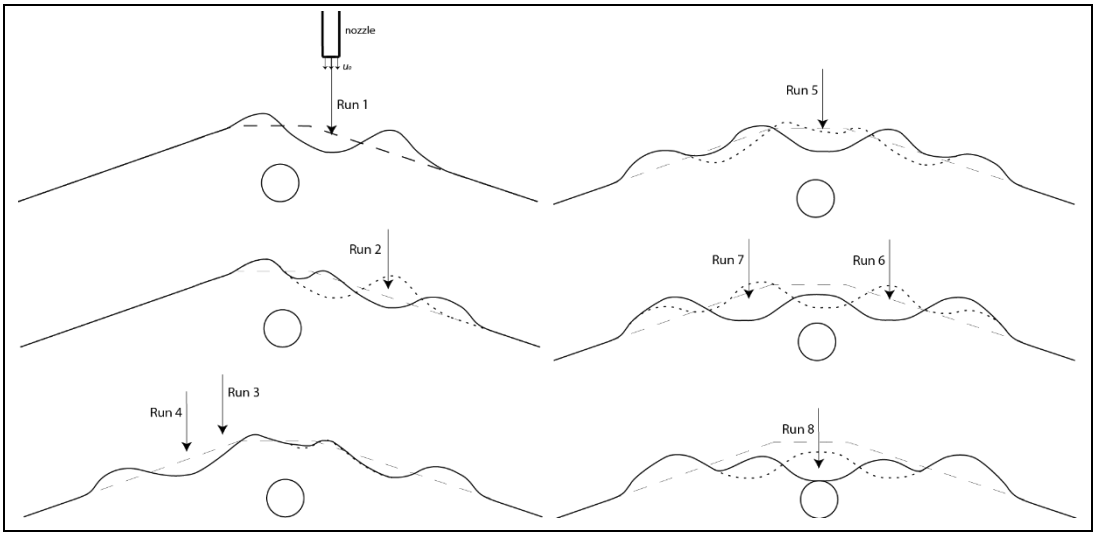

Figure 5.18 – A possible working sequence for a vertical jet

A disadvantage of this working method is that the jet should be accurately aimed at the specific locations as indicated in Figure 5.17 and Figure 5.18. Also, a ROV survey may be required to determine the exact jet location for the next run. Such an operational delay to perform a ROV survey drastically decreases the production rate.

5.2.4 Conclusions

- The jet regime can be penetrating, deflecting or a combination of them. A more penetrating regime can be created by increasing the jet pressure and/or lowering the trail velocity. For a deflective regime, this is the other way around.
- With a penetrating jet, a decrease of the jet angle and trail velocity leads to an increase of the erosion. With a trail velocity of $v_{trail} = 0.02$ m/s, the penetrating jet became effective if the hydraulic power of the jet was higher than 0.5 W, or 75 kW in the prototype situation. An increase of the power leads with small jet angles to a higher erosion.
- When the jet flow is deflected on the bed surface, a vertical jet is a more effective working method than an inclined jet. With a high jet pressure, the trail velocity can be increased to prevent the jet from penetrating into the rock bed. Moreover, the production rate is relatively high due to the large trail velocity. However, the dimensions of the scour hole do not increase considerably with an increasing jet pressure and are constant with about $h_{berm} = 2$ cm and $r_1 = 6$ cm.

- The execution of multiple runs with the same jet location is not useful as it adds only little to the erosion achieved in the first run. Unless a relative high jet pressure is used with a horizontal jet, the scour depth after a single pass was not sufficient to clear the cover height above the pipe. The execution of multiple runs with the jet at the same location does not increase the erosion much, and the scour depth h_{sc} in the equilibrium state is not sufficient to clear the pipe.
- However, when the location of the jet impingement is changed after each run, multiple passes do increase the scour depth and should be able to clear the pipe in only a few runs. This process is illustrated in Figure 5.17, but was not tested in the scale model.
- The use of an inclined jet has some practical problems. Most of all, an accurate aiming of an inclined jet flow is crucial to achieve the maximum erosion. Also, the reaction force of the jet should be compensated to prevent that a moment in the sensitive roll direction of the vessel takes place. Finally, a ROV survey is probably required when executing a multiple pass working scheme as illustrated in Figure 5.17 or Figure 5.18, reducing the production rate.
- A working method with a vertical jet and high trail velocity has a relative high production rate. However, the scour depth is not sufficient to clear the pipe, while this working method requires more runs with a multiple pass working sequence than an inclined jet.
- The working method with the highest production rate *Pr* [m^3/s] is not necessarily the working method with the largest scour depth. The eventually achieved erosion should therefore always be borne in mind when interpreting the values of the production rate.

5.3 Trail direction at an angle

The second working method test that will be the subject of a test series focusses on the trail direction of the nozzle γ_{trail}. This variable trail direction has some implications for the test set-up, which is discussed first. Afterwards, the results of the tests are provided. These outcomes are analysed, leading eventually to the conclusions.

5.3.1 Test set-up

The same equipment is used as described in section 3.2.2 for the tests. Because the direction of this track cannot be changed, the direction of the rock cover itself should be changed in order to obtain the correct trail direction. When the direction of the pipeline is along the water tank, as with the previous tests, the trail direction is defined as $\gamma_{trail} = 0$ degrees. See also Figure 5.18. The nozzle direction in all tests is $\beta_j = 90$ degrees.

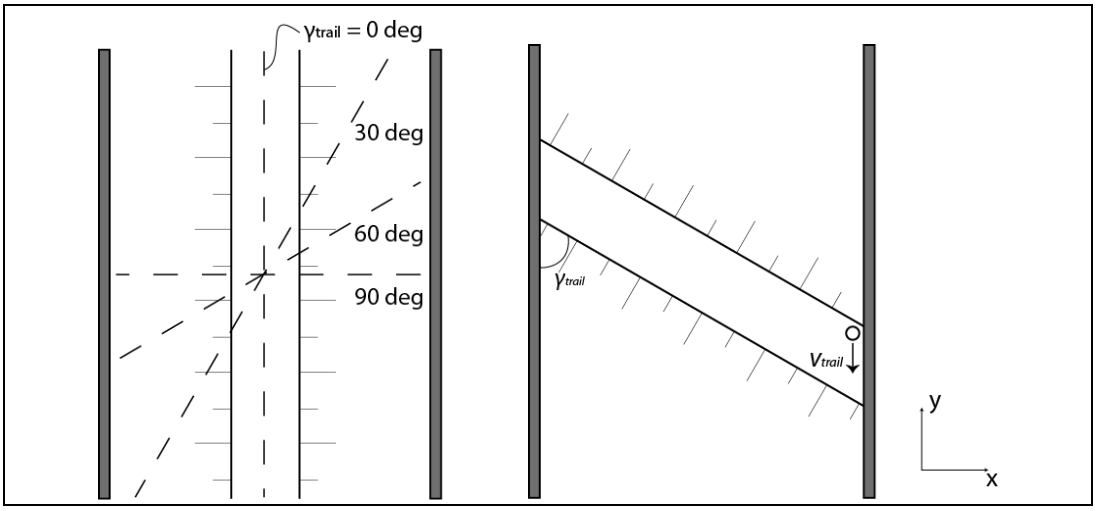

Figure 5.19 – Trail directions correspond to bed direction scale model, right $\gamma_{trail} = 60$ deg

In order to obtain a clear view on the jet behaviour, a symmetry wall set-up is used. Since the scale model is already 'cut' in all cases but $\gamma_{trail} = 0$ degrees, there is no need for any adaptations of the rock bed with a symmetry wall set-up. The cover is cut according to the lines illustrated in Figure 5.18 to create the corresponding cross sections.
The case of $\gamma_{trail} = 0$ degrees has already been studied by the preliminary tests by means of a symmetry wall set-up. It is therefore chosen to execute this test in this series without symmetry wall set-up. In this way, the results of the test can be compared with the results of the jetting at an angle tests.

5.3.1.1 Test configuration

The trail direction γ_{trail} is varied to determine the direction the ship has to sail to have the highest production. It is expected that with the trail direction perpendicular to the rock cover, γ_{trail} = 90 degrees, the impact on the bed profile is the highest. After all, with this configuration, the required sedimentation length λ_s behind the jet in order to effectively move the cover is minimal. The required sedimentation length will increase with a decreasing trail angle, since the length of the cover on which the jet acts is longer. See also Figure 5.19 for a definition sketch. The sedimentation length λ_s and penetration depth h_{pen} are determined by the combination of the flow and trail velocity u_b / v_{trail}. With a high ratio, the penetration depth is relatively high and the sedimentation length short. When the ratio decreases, the depth decreases as well while λ_s increases. However, if the penetration depth is too small, the sedimentation length decreases again. The optimal combination of λ_s and h_{pen} should give the maximum production.

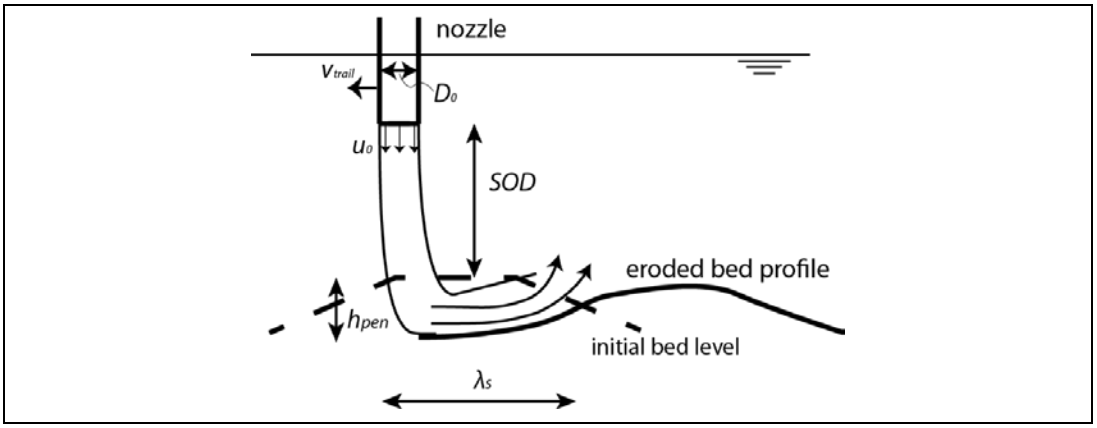

Figure 5.20 – Definition sketch of the trail direction at an angle test series

Although the impact on the bed level of one pass with the jet is the highest with γ_{trail} = 90 degrees, the vessel requires more passing movements in order to overcome the entire cover. The total effectiveness of the method can therefore be higher with a smaller trail angle, although the effectiveness of a single passing is lower. Note that a trail angle of γ_{trail} = 60 degrees causes an increase of the length over which the jet acts of 1/(sin 60), which is about 15%. Analogously, γ_{trail} = 30 degrees means an increase of 1/(sin 30), which is twice as large

For the situation with γ_{trail} = 0 degrees, the results of test 3.11 are used. For the tests with a symmetrical wall, a small PVC-pipe will be used to model the nozzle with a D_{noz} = 1.36 cm, which corresponds to a non-symmetrical diameter of D_{noz} = 1.9 cm, or D_{noz} = 0.58 m in the prototype. The stand-off distance is constant with SOD = 0.1 m.
It has been made clear that the ratio of u_b / v_{trail} is important for this working method. These parameters will therefore be varied as well, mainly by means of v_{trail}. The jet pressure p_j determines the value of u_b, since the stand-off distance is constant. See Table 5.7 for the test matrix for this series.
A jet pressure of p_j = 0.02 bar is chosen for the first six tests. The corresponding jet flow and diameter are provided in Appendix B.3. Depending on the outcomes with this jet pressure, it is determined whether to increase or decrease the flow velocity, and with which trail direction and velocity. It turned out that only the yellow marked cells were considered as interesting follow-up tests.

Table 5.7 – Test matrix for trail direction at an angle test series (indicated number is test ID)

Jet pressure [bar]	Trail velocity [m/s]				Trail angle [deg]
	0.02	0.05	0.07	0.1	
0.03					0
					30
					60
			4.7, 4.9	4.8	90
0.02			4.6		0
			4.5		30
			4.4		60
	4.1	4.2	4.3		90

For the last test, test 4.9, a removal operation is imitated at multiple locations in the scale model. In order to do so, the location of the jet is changed after each passing. The results can be used to investigate the effectiveness of this working method on the entire cover, instead of a single cross-section. The jet pressure during this test corresponds with p_j = 0.025 bar and a trail velocity of v_{trail} = 0.07 m/s. Note that this jet pressure is slightly lower than the other tests in this series, because of the larger nozzle diameter combined with a similar pump configuration. This test 4.9 is - together with the already performed test 4.6 - the only test with the data acquisition procedure with the laser beam. All other tests will be performed with a symmetrical axis; the changes of the bed profile are therefore directly visible behind the transparent wall.

5.3.2 Test results

All results of the tests are presented in Appendix D.2. Only the most important observations and the summary of the outcomes are provided here. The most important parameters are also illustrated in the definition sketch, see Figure 5.20. The definition of the collapsed area A_{breach} [mm²], the eroded volume V_e [dm³] and the production rate Pr [dm³/s] are also provided in Appendix D.2.

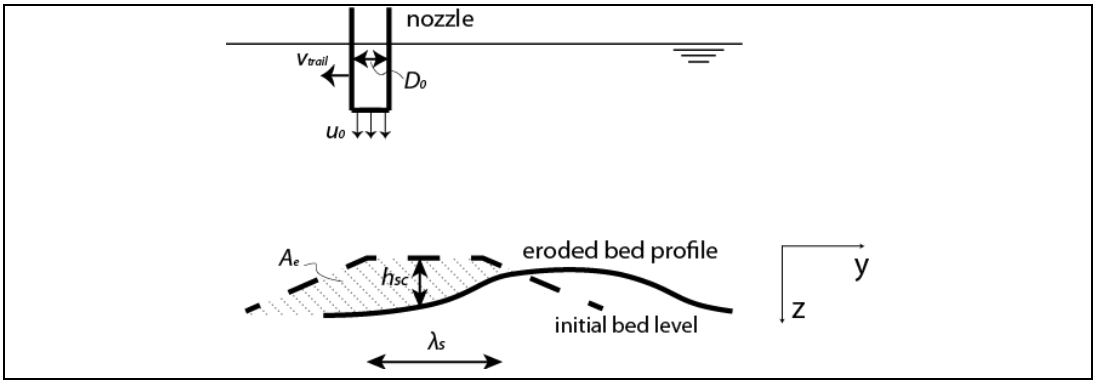

Figure 5.21 – Definition sketch of the most important output parameters of this test series

5.3.2.1 Observations

The jet shows a clear penetrating behaviour in all tests, except with test 4.6 (where a larger D_0 is used, leading to a lower jet pressure). The penetration depth is so high that the flow is deflected by the tank bottom with the lower trail velocities v_{trail} = 0.02 m/s

and v_{trail} = 0.05 m/s. With higher values of $v_{trail,}$ the penetration depth is about the same as the total height of the cover.
With the lowest trail velocity, v_{trail} = 0.02 m/s in test 4.1, the penetration causes a breaching process in front of the jet, where the soil collapses. This process is the most pronounced at the side with an upwards slope. At the downward slope of the bed profile, the trailing jet 'catches up' with the breaching slope. The sedimentation length is relatively small, see also Figure 5.21. The observed scour is also relatively low.

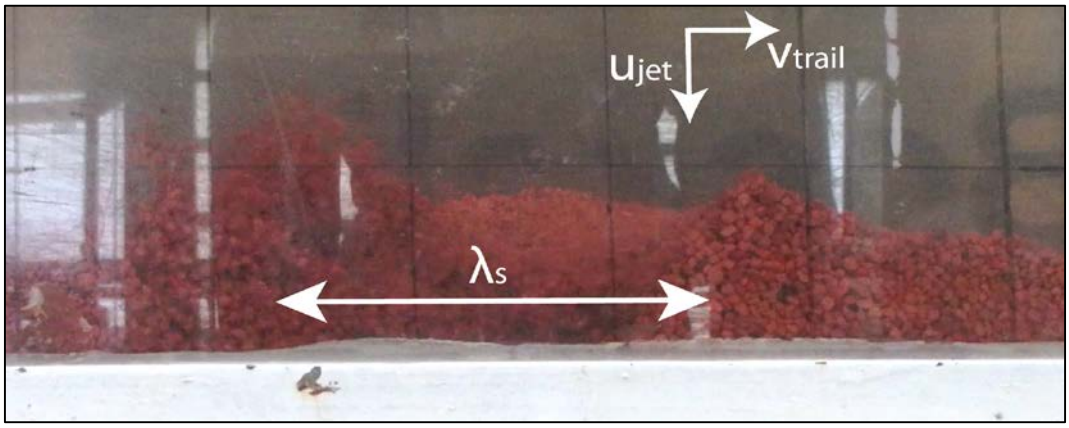

Figure 5.22 – Picture made during test 4.1, run 1

With a higher trail velocity, v_{trail} = 0.05 m/s in test 4.2, the breaching process is not observed: the jet impinges clearly on the bed without a collapse of the soil in front of the jet. The sedimentation length is also obviously larger than in test 4.1, see also Figure 5.22. With a larger speed, v_{trail} = 0.07 m/s in test 4.3, λ_s increased even more.

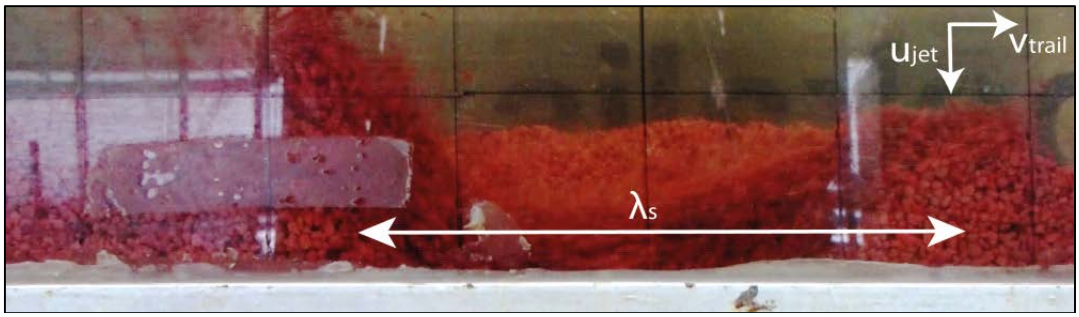

Figure 5.23 – Picture taken during test 4.2

The impact with a longer jetting length in test 4.4 and 4.5, caused by a decrease of the trail angle, is observably smaller than with γ_{trail} = 90 degrees.
The erosion in test 4.6 is, in contrary to the other tests in this series, caused by a radially deflected jet. The sedimentation length λ_s plays no role in this test. Moreover, the backwards transport of eroded stones causes the small berm in the middle of the trench, decreasing the effectiveness of the method.
For test 4.7 and test 4.8, the jet pressure is increased, leading clearly to a higher penetration depth, reaching the bottom of the tank even with v_{trail} = 0.1 m/s. The effect on the erosion during the tests is also observably higher than in the other tests.

A removal operation at multiple locations is modelled with test 4.9. It shows than an extra run adds about 80% of the erosion of the first run. The filling effect, i.e. when a

second pass causes stones to settle in a previously created trench, is limited. Using extra passes seems therefore a relative effective method to increase the total erosion. However, four runs are required to expose a pipe over a distance of about 50 mm in the scale model, which corresponds to only 1.5 m in the prototype situation. A possible extra run with a jet location at around s = 70 mm will probably expose the pipe over a distance of about 100 mm, or 3 m in the prototype. Note that a survey operation after the third pass is required in practice to determine the jet location of the next runs, decreasing the total production.

It is observed in each test that a passing of the jet moves the cover in the direction opposite of the trail direction, but it also has a flattening effect. Also, the part of the cover adjacent (in x-direction) to the penetrated section collapses because the created slope becomes too steep. This process causes an increase of the sediment transported by the flow that cannot be related to the erosion of the initial bed profile.

5.3.2.2 Summary of test results

The data of all tests are provided in individual tables to give a clear overview, enabling a quick way to compare all outcomes. Outcomes after the first run are provided in Table 5.8 and Table 5.9; Table 5.10 and Table 5.11 give the outcomes in the end situation.

Table 5.8 – Primary data obtained after the first run 'trail direction at an angle'

Table 5.9 – Applied data after the first run for the test series 'trail direction at an angle'

Table 5.10 – Primary data obtained after all runs for the test series ‘trail direction at an angle’

Table 5.11 – Applied data after all runs for the test series ‘trail direction at an angle’

Two types of production are provided in Table 5.11: the total production and the net production. The total production includes the required turning time of the vessel of two minutes between two passes. Because this turning time is much longer than the net jetting time, it has a large influence on the total production. To illustrate this effect the net production is also provided, which is defined as the eroded volume per amount of jetting time - so without the reverse time.

5.3.3 Analysis

The trail direction, trail velocity and the jet pressure were varied in this test series. The analysis to find the influence of these parameters on the erosion processes is provided in this section. The number of runs does also play a role, as will also be discussed in this section. Finally, the general conclusions regarding this working method are presented.

5.3.3.1 Influence of trail angle

The initial bed profile depends on the chosen trail direction. With a lower trail angle, the length of the initial profile is longer. This also means that the slopes of the cover are smaller, or even zero in the case of γ_{trail} = 0 deg. The displacement in the backward direction is the most useful with a short length and steep slope. After all, a displacement of the bed over the sedimentation length has a smaller influence on the bed level

The deformation of the bed profile is not simply a convection over the sedimentation length, it also shows a diffusive behaviour as the profile is 'smeared out'. The bed profile becomes therefore more flattened after each run, also attributing to the scour depth.

5.3.4 Conclusions

- The eroded area of the dumped rock cover is higher with a large trail angle, i.e. when the trail direction is about perpendicular to the pipeline. A penetrating jet is required for this method to be effective. Because of the short jet time and many necessary turns, the reverse time of a vessel becomes relatively pronounced. This results in a sharp reduction of the production with multiple runs.
- The erosion for a trail direction similar to the pipeline is considerably smaller than for larger angles and the required scour depth is not reached when the nozzle remains in the same location. However, the production with γ_{trail} = 0 deg is much higher than with larger trail angles, since only one turning movement is required.
- If the penetration depth reaches the bottom of the cover, the sedimentation length λ_s depends linearly on the trail velocity. However, it is not known whether such a large penetration depth is viable in practice. After all, the subsoil should not be eroded to prevent free span of the pipe. It is recommended to investigate the behaviour of a penetrating jet into the subsoil.
- An increase of the trail velocity, and thus sedimentation length, does not lead to a higher erosion with γ_{trail} = 90 degrees. The eroded volume remains about equal for v_{trail} > 0.05 m/s. The production increases therefore linearly with an increase of the trail velocity. The trail velocity should however not become so high that the jet behaviour becomes like a radially deflected wall jet, or that the DP capability cannot be maintained anymore.
- In a test simulating a removal operation, only 0.1 m pipe, 3 m in the prototype situation, was found to be cleared after five runs. This working method is therefore only suitable when the part of the pipeline cover that needs to be cleared is relatively short, for instance at a crossing of two pipelines. The added erosion of an extra run with this working method was about 80% of the erosion of the first run.

5.4 Adjusted nozzle design

The last working method is focussed on the erosion processes with an adjusted nozzle design. Which designs are tested is described first, after which the test configuration is provided. After a short summary of the results, these outcomes are analysed. Finally, the conclusions about the applicability of this working method is given.

5.4.1 Test set-up

All tests are performed in the regular set-up with the bed and nozzle located in the middle of the tank, executed with a trail direction of $\gamma_{trail} = 0$. Multiple nozzle designs were tested for effectiveness, such as a simple horizontal row of jets and even a regular shower head, see Figure 5.33. These two designs proved out to cause similar erosion processes as with a circular nozzle, but with a different relation between the stand-off distance and the near-bed velocity due to a different entrainment process. It is therefore chosen that these designs will not be a subject in the test series, so the focus can be laid on a design that is substantially different from a circular nozzle.

Figure 5.34 – Special nozzle designs in an unsubmerged situation

A nozzle head design that seemed to work effectively is based on the concept of a plough. The small nozzles are placed in V-shape, with the centre nozzle placed in front. With this design, all stones are theoretically pushed sideways by each jet with a sufficient trail velocity, effectively creating a wide, deep trench on top of the pipe. This sideways transport is caused by the radial deflection of the jet. This method is sketched in Figure 5.34.

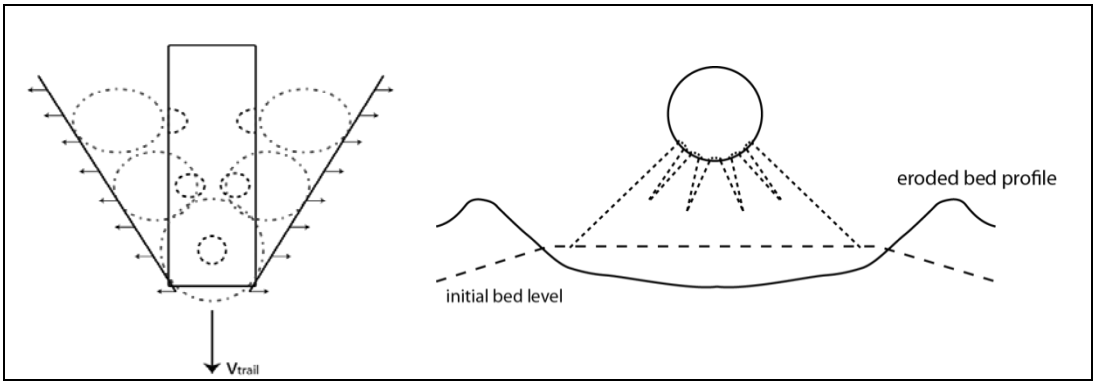

Figure 5.35 – Sketch of the operation with a jet plough, left a top view and right a front view

When such a jet plough system is created with a cylinder, other advantages are introduced as well. The outer nozzles are than able to create a jet flow at an angle. This means that such an inclined nozzle can create an influence area located further to the side than with the case of a vertical jet. Moreover, it can also use its penetrating capability to transport the stones even further away than with the case of a radially deflected vertical jet. Pictures of this nozzle head design in an unsubmerged situation are provided in Figure 5.36.

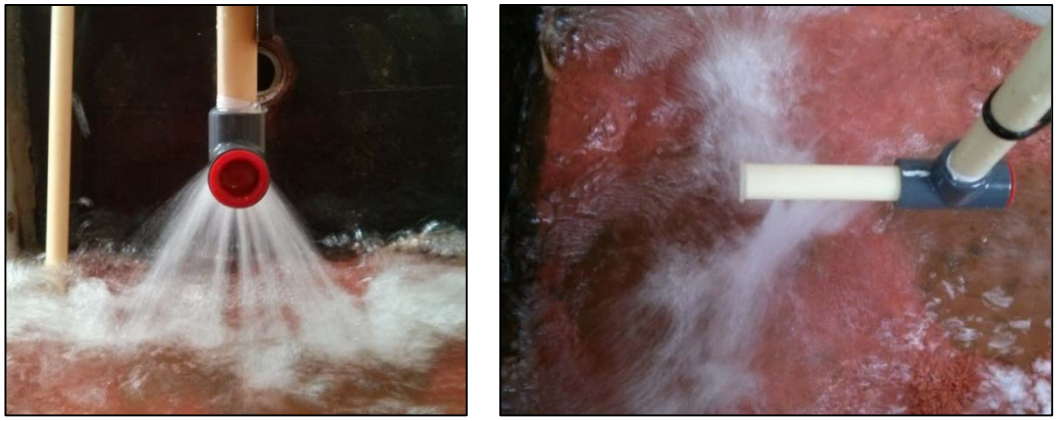

Figure 5.36 – A jet plough in an unsubmerged situation

Three variants of a jet plough design are used in the tests, see also Figure 5.36. The most important difference between each nozzle head is the total nozzle area. Each small nozzle has a diameter of 4.5 mm, so the total number of nozzles defines the total jet area. The flow velocity will therefore decrease with an increase in the number of nozzles. The jet pressure corresponding to each design is determined in Appendix B.3.

The removal can be executed with the equipment located vertically under the vessel, above the rock cover. This method has in that way the advantage compared to the working method with an inclined jet, where the created jet force creates a momentum in the disadvantageous roll direction of the ship. Also, the jet flow does not have to be aimed as precisely as with an inclined jet. Lastly, the required number of turns of the ship are less than with the trail direction at an angle. These advantages make the removal by means of an adjusted nozzle design potentially interesting.

Figure 5.37 – Three different designs of a jet plough, from left to right: 3 nozzles, 7 nozzles and 10 nozzles

5.4.1.1 Test configuration

Three different variants of the jet plough will be tested, see also Figure 5.36. The first configuration has three nozzles, resulting in a relative low flow rate but high jet pressure. It is expected that the penetration depth is larger due to this higher jet pressure. The configuration with ten nozzles has a similar nozzle area as with a single circular nozzle, although the contraction is much higher, see for more information Appendix B.3. The third design has seven nozzles.

The test matrix of this test series is provided in Table 5.12. Just as with the previous test series, different combinations of the trail and flow velocity are studied. The flow velocity can be varied by changing the jet pressure.

Table 5.12 - Test matrix for adjusted nozzle design test series (indicated number is test ID)

Trail velocity [m/s]	Number of nozzles [-]			Pump config. [-]
	3	7	10	
0.02		5.4	5.6	1 (high)
	5.1	5.3		3 (low)
0.07	5.2	5.5		1 (high)
				3 (low)

The jet pressure belonging to the combination of a nozzle and a pump configuration are determined and provided in B.3.3. The corresponding value will also be mentioned at each test in the next section. The stand-off distance is 0.1 m for each test. The nozzle diameter is also constant, only the number of nozzles are varied. The total jet area A_j is therefore also a variable parameter, depending on the type of nozzle configuration. The used data acquisition method is with the laser beam.

5.4.2 Test results

The results of each test are in full detail presented in Appendix D.3. The most important observations are discussed in this section, together with the summary of the test results. A definition sketch illustrating the most important parameters is provided in Figure 5.37.

By multiplying the eroded area with the trail velocity, the production rate Pr [m^3/s] is obtained. Again, difference is made between the gross and net production time, respectively with and without the reverse time taken into account.

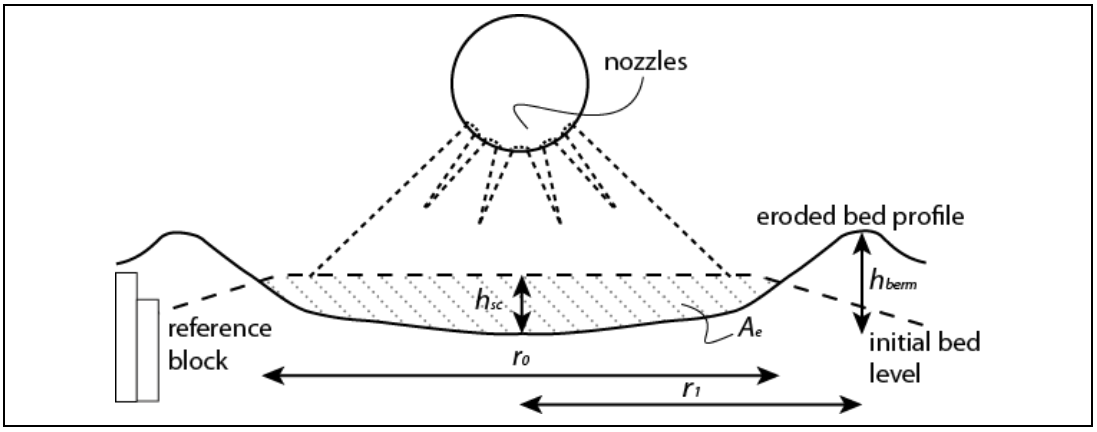

Figure 5.38 – Definition sketch of the test outcomes with a jet plough

5.4.2.1 Observations

The jets clearly penetrate the soil with test 5.1, but they seem to lack the power to 'push' the berms far away. As a result, a wide and shallow trench is created. Almost all erosion is achieved in the first run.
When the jet pressure and trail velocity is increased for test 5.2, the first run shows only a flattening effect, no actual trench is created. The second run does form this trench with a scour hole, although the total width of the trench does not seem to increase. The extra production of the second run is therefore limited.

Observations made during test 5.3, the first test with seven nozzles, show that the jets do not have sufficient power to fully penetrate into the bed. Instead, a radially deflected jet flow is clearly visible, resulting in a process in which the bed is 'scraped' layer by layer. The effect on the reduction of the bed level is limited and no considerable extra production is observed after the second run.
An increase of the jet pressure with a constant trail velocity, test 5.4, causes the jets to penetrate. A wide trench is created; almost all production is reached after one run. The trench created by the jet does not show a uniform course but forms a more stepwise profile. This probably means that the different jets does not exactly overlap each other at this point, limiting the transport capacity.
With test 5.5 the trail velocity is increased with a similar jet configuration. The jets now show both a penetrating and a deflecting behaviour, creating a wide, but relatively shallow, trench. The majority of the production is achieved during the first run, although the second run also has a considerable contribution to the scour depth.

The test with ten nozzles, test 5.6, shows similar processes as the other tests. The first run flattens the berm, but no real trench or scour hole is visible. This hole is created in the second run, although the extra production seems to be limited: the slopes of the scour hole just become steeper, no bed level change takes place outside the trench.

5.4.2.2 Summary of test results

All results of the test for this series are summarized in this section. All outcomes are given in one table to give a clear overview, enabling a quick way to compare all results. The outcomes after one run are provided in Table 5.13 and Table 5.14. Table 5.15 and Table 5.16 give the results after the last run of the test.

Table 5.13 – Primary data obtained after first run for the test series 'adjusted nozzle design'

Parameter / Test	p_j [bar]	nozzles [-]	v_{trail} [m/s]	h_{sc} [mm]	r_0 [mm]	r_1 [mm]	h_{berm} [mm]	A_e [mm^2]
5.1	0.12	3	0.02	22	130	80	20	1 800
5.2	0.24	3	0.07	33	148	-	-	2 500
5.3	0.03	7	0.02	18	120	-	-	1 200
5.4	0.09	7	0.02	29	150	-	-	3 000
5.5	0.09	7	0.07	23	140	-	-	2 000
5.6	0.06	10	0.02	20	130	-	-	1 600

Table 5.14 – Applied data after first run for the test series 'adjusted nozzle design'

Parameter / Test	P_j [W]	A_j [cm^2]	u_b [m/s]	u_b/v_{trail} [-]	Q_0 [dm^3/s]	P_j [W]	Pr [dm^3/s]	h_{sc}/D_{50} [-]
5.1	1.9	0.33	0.6	28	0.16	1.9	0.036	7.3
5.2	5.6	0.33	0.8	12	0.23	4.6	0.18	11.0
5.3	0.5	0.72	0.3	14	0.17	0.5	0.024	6.0
5.4	2.6	0.72	0.5	24	0.30	3.1	0.060	9.7
5.5	2.6	0.72	0.5	7	0.30	3.1	0.14	7.7
5.6	1.8	0.95	0.4	18	0.32	2.4	0.032	6.7

Table 5.15 – Primary data obtained after all runs for the test series 'adjusted nozzle design'

Parameter / Test	p_j [bar]	nozzles [-]	v_{trail} [m/s]	h_{sc} [mm]	r_0 [mm]	r_1 [mm]	h_{berm} [mm]	A_e [mm^2]
5.1	0.12	3	0.02	24	115	70	20	1 900
5.2	0.24	3	0.07	44	130	90	18	3 100
5.3	0.03	7	0.02	24	122	-	-	1 600
5.4	0.09	7	0.02	33	140	-	-	3 400
5.5	0.09	7	0.07	36	140	100	17	3 200
5.6	0.06	10	0.02	28	130	100	15	2 300

Table 5.16 – Applied data after all runs for the test series 'adjusted nozzle design'

Parameter / Test	A_j [cm^2]	u_b [m/s]	u_b/v_{trail} [-]	Q_0 [dm^3/s]	P_j [W]	Pr_{gross} [dm^3/s]	Pr_{net} [dm^3/s]	h_{sc}/D_{50} [-]
5.1	0.33	0.6	28	0.16	1.9	0.018	0.019	8.0
5.2	0.33	0.8	12	0.23	4.6	0.090	0.110	14.7
5.3	0.72	0.3	14	0.17	0.5	0.015	0.016	8.0
5.4	0.72	0.5	24	0.30	3.1	0.021	0.023	11.0
5.5	0.72	0.5	7	0.30	3.1	0.057	0.075	12.0
5.6	0.95	0.4	18	0.32	2.4	0.022	0.023	9.3

5.4.3 Analysis

After performing six tests with three different nozzle designs, the results are analysed to study the influence of the design, jet pressure, trail velocity and the number of runs.

5.4.3.1 Influence of the number of nozzles

A smaller number of nozzles leads to an increase of the jet pressure and thus flow velocity. Because the design is different for each variant, the jet angle of each nozzle also differs. However, the effect on the erosion is limited. As can be seen in Figure 5.38, no variant strongly deviates from the other results and the scour depth seems to depend linearly on the jet power. The value of the erosion area, Figure 5.39, for a configuration with seven nozzles are slightly higher though. This is because the configuration of seven nozzles has a higher value of r_0, i.e. the created scour hole is wider. A probable reason could be that the jet angle is more advantageous with the design with seven nozzles.

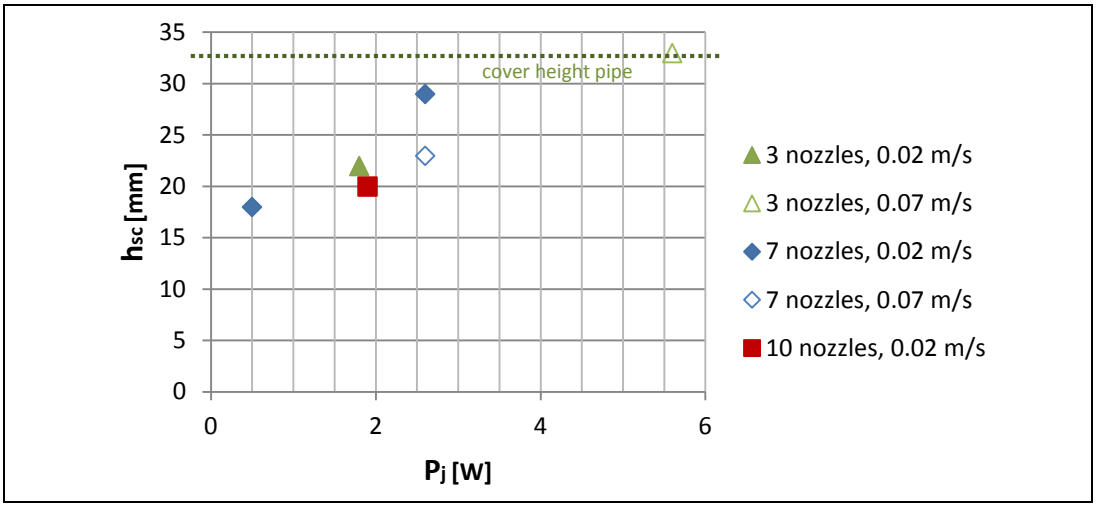

Figure 5.39 – Scour depth h_{sc} versus the hydraulic power P_j after one run

5.4.3.2 Influence of jet pressure

The design with multiple nozzles are in fact a combination of a vertical jet with various inclined jets. It was already mentioned in section 5.2.4 that an increase of the jet pressure leads to a higher erosion with an inclined jet. This is also visible in Figure 5.39.

Note that the used jet pressures in this test series are relatively high. Four tests were performed with about p_j = 3 bar in the prototype situation with even one test with approximately p_j = 6 bar. Especially this last pressure cannot be achieved in practice, but it gives a useful insight of the influence of the jet pressure. Only the test with the smallest jet pressure, p_j = 0.03 bar in the scale model situation, is comparable to the test series with jetting at an angle. It turns out that the outcomes are similar with an eroded area of about A_e = 1500 mm^2.

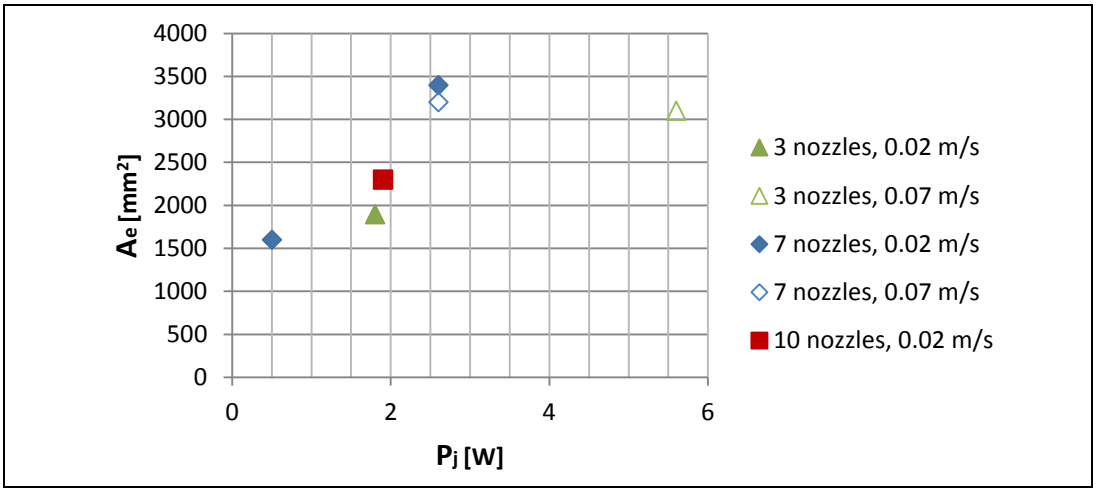

Figure 5.40 – Eroded area A_e versus the hydraulic jet power P_j after all runs

5.4.3.3 Influence of trail velocity

Only one pair of tests was performed that had the same jet configuration but varied in trail velocity: test 5.4 and test 5.5. From Figure 5.39 follows that the scour depth after the first run is higher in the case with a lower trail velocity. However, after three runs the scouring is similar. The trail velocity therefore seems to have no influence on the total eroded volume in the equilibrium situation. It does however affect the situation after a single run, because a higher trail velocity simply means that the jet has less time to act.

An increase of the trail velocity limits the penetration depth, and therefore the erosion of an inclined jet. This effect is not visible in the results for an adjusted nozzle configuration, while such a design can also be seen as a combination of inclined jets. However, the near-bed velocity u_b of a jet with a small jet diameter D_0 is relatively low due to a large entrainment rate. The jet acts therefore more as a deflecting jet, although the jet pressure is higher than in the test series focussing on an inclined jet. This also explains why the trail velocity has only a small influence on the total eroded area.
Although the scour depth is lower in the first run with a higher trail velocity, the production is also higher due to this greater speed, as is depicted in Figure 5.40.

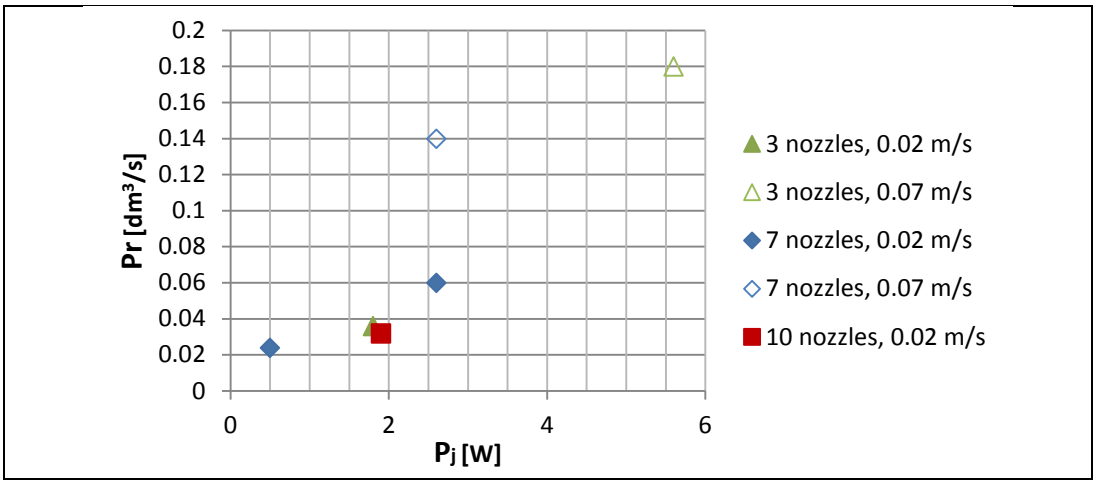

Figure 5.41 – Production Pr versus the hydraulic jet power P_j after the first run

5.4.3.4 Influence of multiple runs

The added erosion in later runs with tests with v_{trail} = 0.02 m/s is only limited, see Figure 5.41. A second run therefore only decreases the production rate. The extra production with v_{trail} = 0.07 m/s is more significant. The scour depth is about the cover height for almost all tests; with the test with P_j = 4.6 W the pipe is clearly exposed.

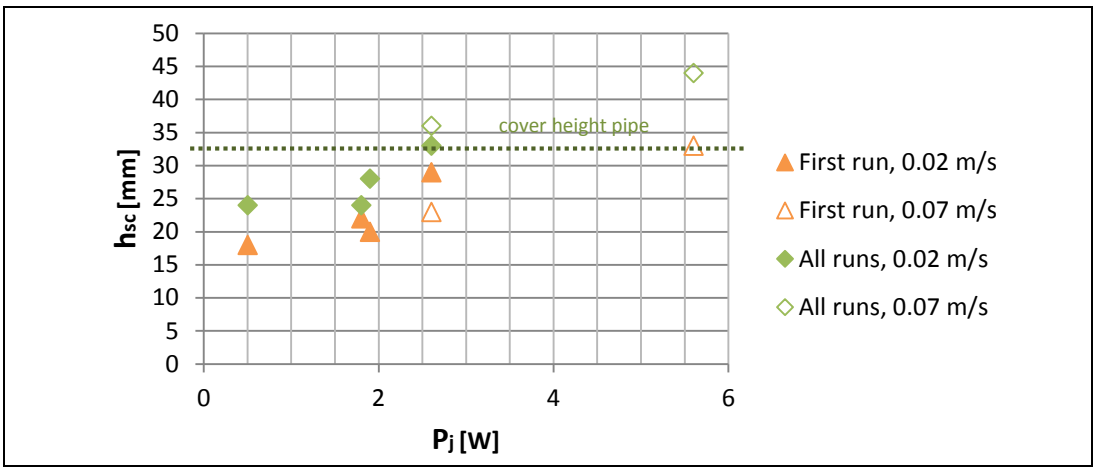

Figure 5.42 – Scour depth h_{sc} versus the hydraulic jet power P_j after all runs

5.4.4 Conclusions

- The scour depth depends mostly on the value of the jet power. With an increasing power, the scouring is higher. The effect of the design or the number of nozzles is only small.
- An adjusted nozzle design based on the V-plough can create a wide trench without the need of accurate aiming. However, the scour depth is relatively low compared to the width of the scour hole; thus creating a shallow trench.
- A higher trail velocity leads to a lower erosion in the first run, but the eventual equilibrium situation is not changed. An increase of v_{trail} does cause that more runs are required before the equilibrium situation is reached.
- The production increases with the trail velocity, since the difference in eroded area is less than the increase of the vessel's speed.
- With about P_j > 2 W, the scour depth h_{sc} is just sufficient to remove the cover height above the pipe. This required jet power is relatively high with a prototype value of about P_j = 300 kW. A powerful pump is thus required to achieve the high production rates with an adjusted nozzle. As the hydraulic power is relatively high, this design can also be considered as a combination of multiple inclined jets.

6 Erosion model

6.1 Erosion model description

It was concluded from the scale model tests that either a penetrating or a deflecting jet regime can be obtained, which has a large influence on the erosion processes and thus the viability of a working method. It is therefore important to predict the jet behaviour in order to choose a feasible working method. The results from the scale model tests give a good description of the erosion processes that occur with a jetting operation. However, a computer model would be a crucial tool to predict the penetrating behaviour in other situations than were tested. This erosion model is based on the theory as described in Chapter 2 and depicts the situation with a horizontally moving vertical jet. A definition sketch of the erosion model is illustrated in Figure 6.1.

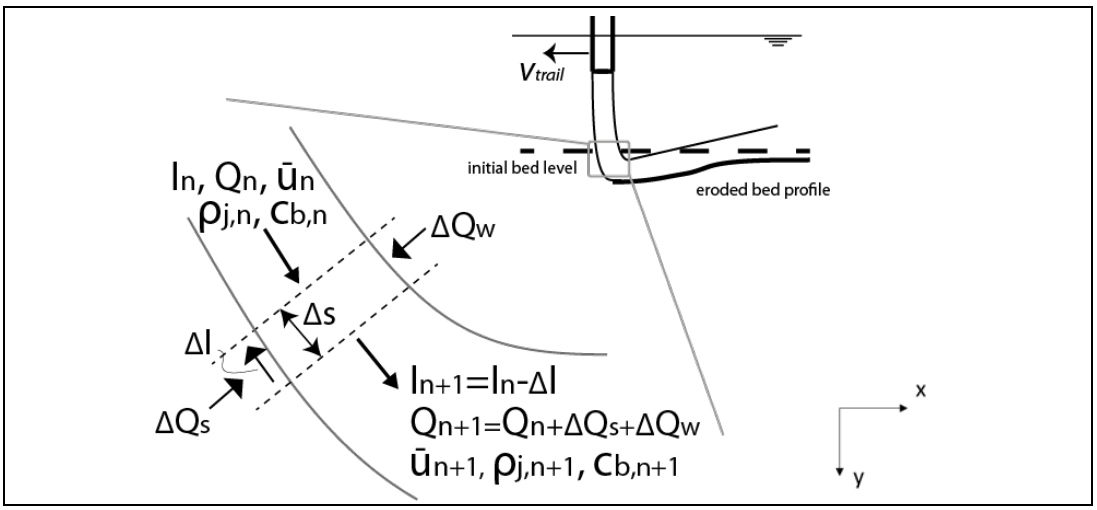

Figure 6.1 – Definition sketch of the erosion model

Firstly, a computer model is created, based on the theory of an eroding jet flow. This model is then executed and compared with the observed processes during the test. A prediction is finally made about the penetrating behaviour of the jet.

6.1.1 Model equations

A more detailed description of the processes and corresponding equations of the erosion of a granular bed by a jet flow is provided in Chapter 2. The most important principles incorporated in the erosion model are repeated here.

6.1.1.1 Flow development

The average (uniform) flow velocity at each point is determined by the momentum *I*, density *ρ* and flow rate *Q*:

$$\bar{u} = \frac{I}{\rho Q} \tag{6.1}$$

A penetrating jet flow can be modelled as a pipe flow, as illustrated as a cross-section in Figure 6.2. This "pipe" with a height h_j and width b_j is initially circular and is partly enclosed by soil and partly by water. It is assumed that the distribution between these two parts is initially equal. This means that halve of the jet flow is enclosed by soil, exercising a shear stress τ on the jet flow, reducing the jet momentum:

$$\frac{dI}{ds} = -\frac{1}{2}\pi b_j \tau \tag{6.2}$$

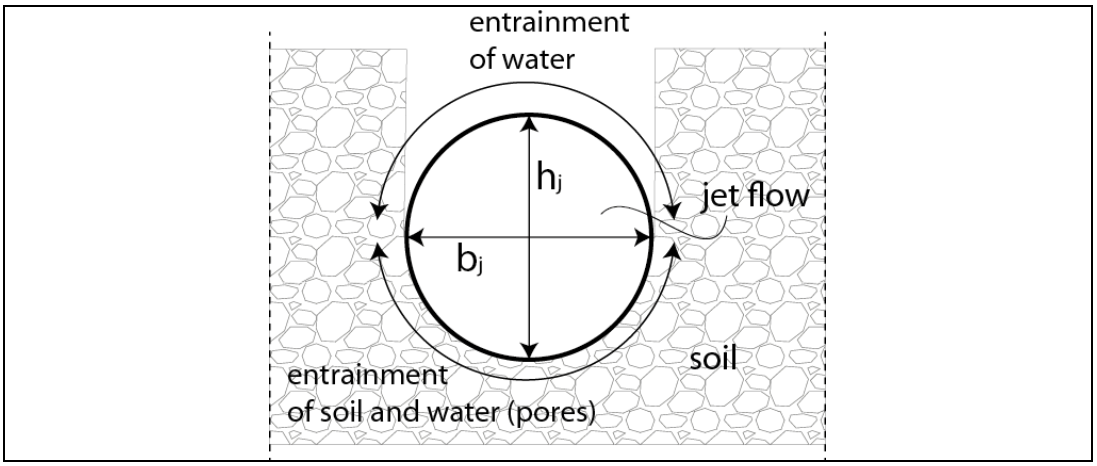

Figure 6.2 – Cross-section of the jet flow

This flow entrains both water and soil, affecting the flow rate. The entrainment of soil is determined as the eroded soil times the trail velocity. Using Eq. (2.9), this results in the total entrainment rate of:

$$\begin{aligned}\frac{dQ}{ds} = \frac{dQ_w}{ds} + \frac{dQ_s}{ds} &= \left(\frac{1}{2}\alpha_{mom}\pi b_j u + \frac{dy}{ds} b_j n_0 v_{trail}\right) + \frac{dy}{ds} b_j (1 - n_0) v_{trail} \\ &= \frac{1}{2}\alpha_{mom}\pi b_j u + b_j v_e\end{aligned} \tag{6.3}$$

Since the total entrained soil Q_s as a fraction of the total flow *Q* equals the concentration *c*, the following is also true:

$$\frac{dQ_s}{ds} = \frac{d(Qc)}{ds} = c\frac{dQ}{ds} + Q\frac{dc}{ds} = c\left(\frac{dQ_w}{ds} + \frac{dQ_s}{ds}\right) + Q\frac{dc}{ds} \tag{6.4}$$

Rewriting and substitution of Eq. (6.3) leads to:

$$\frac{dc}{ds} = \frac{1}{Q}\left(\frac{dQ_s}{ds} - c\frac{dQ}{ds}\right) = \frac{1}{Q}\left((1-c)\frac{dQ_s}{ds} - c\frac{dQ_w}{ds}\right) = \frac{b_j}{Q}\left((1-n_0-c)v_e - c\frac{1}{2}\alpha_{mom}\pi u - cn_0 v_e\right) \tag{6.5}$$

The increase of the flow rate also means an increase of the density, since the entrained soil has a different density than (entrained) water. This density of the jet flow ρ_j can be calculated using the average concentration:

$$\bar{c} = \frac{\rho_j - \rho_w}{\rho_s - \rho_w} \tag{6.6}$$

It was stated in section 2.4 that the concentration profile can be assumed to be linear, with $c = 0$ at the top of the flow and $c = c_b$ at the bottom. This means that the near-bed concentration c_b is twice the average concentration.

6.1.1.2 Erosion

When all jet flow parameters are known for a single point, the erosion can be calculated. First, the stability of the stones has to be determined by means of the Shields parameter, already described in section 2.3.2:

$$\theta = \frac{{u_*}^2}{\Delta g D_{50}} = \frac{\bar{u}^2}{\Delta {C_{ch}}^2 D_{50}} \tag{6.7}$$

The Chézy value now corresponds with the situation of a pipe flow:

$$C_{ch} = 18\log\left(12\frac{R}{k_{rg}}\right) = 18\log\left(3\frac{b_j}{k_{rg}}\right) \tag{6.8}$$

And the relative density Δ is no longer constant, but depends on the jet flow density:

$$\Delta = \frac{\rho_j - \rho_w}{\rho_w} \tag{6.9}$$

The erosion velocity is described by Eq. (2.53), repeated here:

$$v_e = \frac{\psi_e - \psi_s}{\rho_s(1-n_0-c_b)} \tag{6.10}$$

With the known expressions for the pick-up flux Ψ_e and settling flux Ψ_s, respectively:

$$\psi_e = 0.00033\rho_s\sqrt{\Delta g D_{50}}{D_*}^{0.3}\left(\frac{\theta - \theta_{cr}{}'}{\theta_{cr}{}'}\right)^{1.5} \tag{6.11}$$

$$\psi_s = \rho_s c_b (1-c_b)^{2.4}\sqrt{\Delta g D_{50}}\cos\alpha_{bed} \tag{6.12}$$

It was stated in section 2.3.4 that the difference between θ_{cr} and θ_{cr}' was negligible. However, this was the case for the soil characteristics in the prototype situation. The permeability in the scale model is lower, leading to a, now significant, increase of θ_{cr}'. The expression for θ_{cr}' was already described by Eq. (2.45), here repeated:

$$\theta_{cr}{}' = \theta_{cr}\left(\frac{\sin\varphi - \sin\alpha_{bed}}{\sin\varphi} + \frac{v_e}{k}\frac{n_l - n_0}{1 - n_l}\frac{1}{\Delta(1-n_0)}\right) \tag{6.13}$$

The bed angle α_{bed} depends on the ratio between the erosion and trail velocity. Due to the trail velocity, the flow tends to be deflected backwards, in the opposite direction of the movement of the nozzle. However, when the jet has an eroding capability, the jet will penetrate into the soil, affecting the direction of the jet flow. This flow direction also determines the bed angle α_{bed}:

$$\alpha_{bed} = \begin{cases} \arcsin\dfrac{v_e}{v_{trail}} & for\ v_e \le v_{trail} \\ 90\ \text{deg} & for\ v_e > v_{trail} \end{cases} \tag{6.14}$$

6.1.2 Model set-up

The erosion model computes the jet flow development so that the flow velocity at the bed level, where erosion occurs, can be calculated. The area of interest has been two-dimensionally discretized in space, in x- and y-direction. The trail direction corresponds with the negative direction of *x*, the initial (vertical) flow direction corresponds with *y*. Note that these axes are different then used during the scale tests. At each grid point *x,y* the flow velocity is used as input to calculate the erosion velocity, which determines the bed deformation. The flowchart describing the model is provided in Figure 6.4. The model is performed for each grid point *n*, with a step size of the grid of *Δs*. A definition sketch is provided in Figure 6.1 for the flow and in Figure 6.3 for the bed deformation.

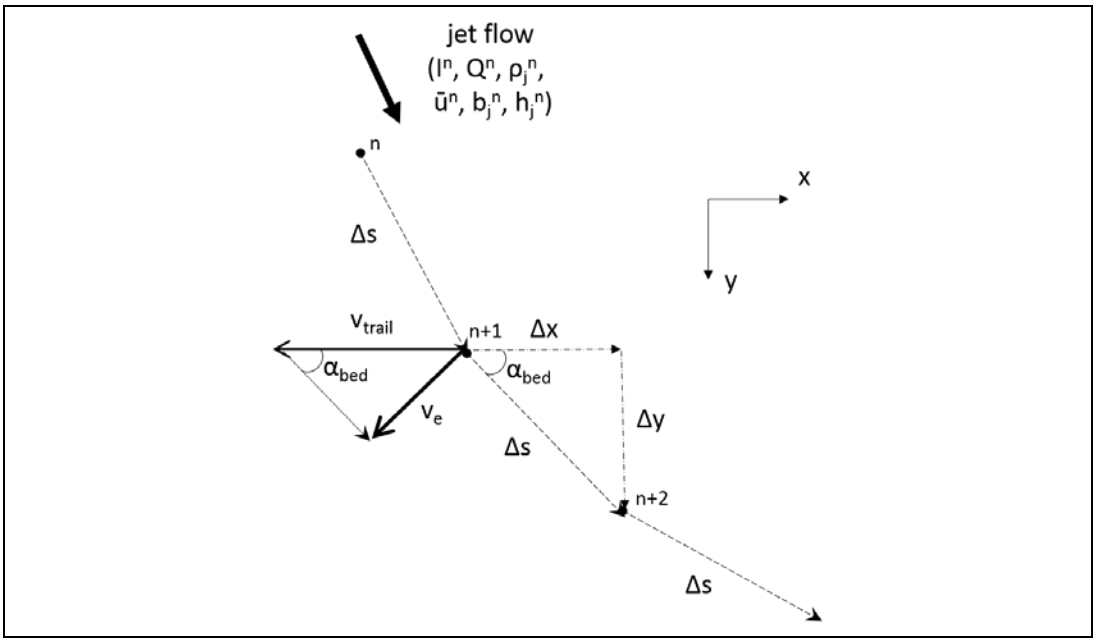

Figure 6.3 – Definition sketch of bed deformation

The calculation is performed by approaching Eqs. (6.2) and (6.3) for each grid point *n* by means of discretizing these differential equations:

$$\frac{I^n - I^{n-1}}{\Delta s} = -\frac{1}{2}\pi {b_j}^n \tau^{n-1} \tag{6.15}$$

$$\frac{Q^n - Q^{n-1}}{\Delta s} = \frac{\Delta {Q_w}^n}{\Delta s} + \frac{\Delta {Q_s}^n}{\Delta s} \tag{6.16}$$

An expression for the dimension of the jet at each point is required to calculate the entrainment rates. The entrainment on its turn causes an increase of the dimensions of the jet. The increase of b_j depends on the trail and erosion velocity at each point, which is in fact the sum of the increase of the width in horizontal and vertical direction:

$$\Delta {b_j}^n = {v_e}^{n-1}\left(\frac{\Delta x^{n-1}}{v_{trail}} + \frac{\Delta y^{n-1}}{\Delta s}\frac{\Delta {b_j}^{n-1}}{v_{trail}}\right) \tag{6.17}$$

However, when the eroding capability of the flow is less than the sedimentation, the width b_j does not increase anymore. This means that the flow width is constant in the settling phase. Moreover, the maximum possible entrainment angle of a jet is α_{mom}. This means that the width of the jet flow can be calculated with:

$$\begin{gathered} {b_j}^n = {b_j}^{n-1} + 2\min\begin{cases}\Delta {b_j}^n \\ \alpha_{mom}\end{cases} \quad for\ v_e > 0 \\ {b_j}^n = {b_j}^{n-1} \quad for\ v_e \le 0 \end{gathered} \tag{6.18}$$

The increase of the jet flow height h_j is different than the width since the entrainment of water is different than the entrainment of soil. This means that the pipe gradually loses its circular shape; instead it is assumed to have an oval shape:

$$\frac{Q^n}{\bar{u}^n} = \frac{1}{4}\pi {b_j}^n {h_j}^n \tag{6.19}$$

This leads to the expressions of the entrainment rates for water and soil, described as ΔQ_w and ΔQ_s respectively in Eq. (6.16):

$$\frac{\Delta {Q_w}^n}{\Delta s} = \left(\frac{1}{2}\alpha_{mom}\pi {b_j}^n u^{n-1} + \frac{y^n - y^{n-1}}{\Delta s}{b_j}^n n_0 v_{trail}\right) \tag{6.20}$$

$$\frac{\Delta {Q_s}^n}{\Delta s} = (1 - n_0)v_{trail}\left(\frac{y^n - y^{n-1}}{\Delta s}{b_j}^n + \frac{{b_j}^{n-1} - {b_j}^{n-2}}{\Delta s}y^{n-1}\right) \tag{6.21}$$

The entrainment of water consists of two terms. The first is the actual entrainment of the surrounding water at the upper side of the flow, see Figure 6.2. The second term consists of the water in the pores of the entrained soil. The entrainment of soil also has two terms, with the first term again the actual entrainment due to the erosion of the

soil. The second term is caused by the increase of b_j, leading to an increase of the entrained sediments in the flow.

The differential equation of the concentration was rather complex. Instead, a mass-balance is used to calculate the jet flow density at each grid point:

$$\rho_j{}^n = \frac{Q^{n-1}\rho_j{}^{n-1} + \Delta Q_w{}^n \rho_w + \Delta Q_s{}^n \rho_s}{Q^n} \tag{6.22}$$

The concentration can now be calculated using Eq. (6.6).

With the value of the jet momentum flux, flow rate and density known, the flow velocity at each point can be calculated according to Eq. (6.1). Subsequently, the erosion velocity and resulting bed angle for each grid point can be calculated, resulting in the bed deformation. This deformation is used to define the next grid point at which the flow velocity will be calculated:

$$\begin{aligned} s^{n+1} &= s^n + \Delta s \\ x^{n+1} &= x^n + dx^n = x^n + \Delta s \cos(\alpha_{bed}{}^n) \\ y^{n+1} &= y^n + dy^n = y^n + \Delta s \sin(\alpha_{bed}{}^n) \end{aligned} \tag{6.23}$$

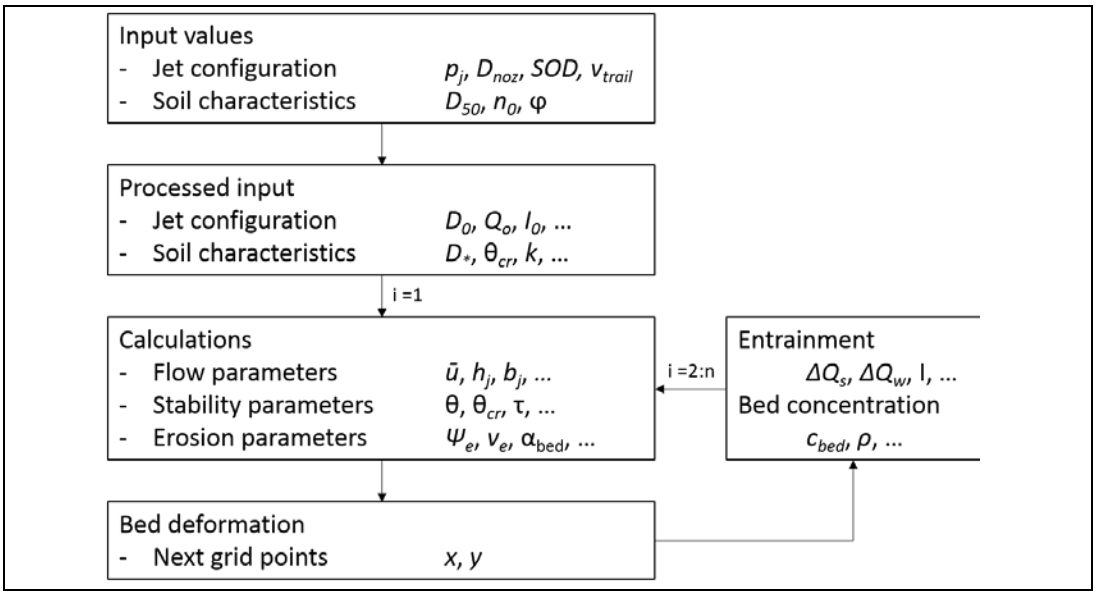

Figure 6.4 – Erosion model flowchart

6.1.2.1 Initial conditions

The flow characteristics *I, Q,* b_j and h_j at the first grid point are calculated according to the theory of a free jet, described in section 2.2.1. Since no soil has yet entrained at the first grid point, the density of the flow equals the density of water. Given these values, the flow velocity and the corresponding erosion velocity can be calculated for the first point. Since the value for *Q* for *n* = 1 is imposed, the values of ΔQ_w and ΔQ_s are set to zero for this step. It is further assumed that $b_j^0 = b_j^1$; implying that the influence of the increase of the flow width on the entrainment of soil is neglected for the first two steps.

6.2 Erosion model results

The model as described in section 6.1 is now executed and compared with the scale test results. To validate the erosion model, the modelled results are compared with the observed penetration profiles of three different tests, with the jet configurations as provided in Table 6.1. These tests were executed with a symmetrical axis set-up, while the model displays a situation with a 'regular set-up', without symmetry wall. Therefore, the flow rates in the erosion model are doubled so that erosion processes corresponds to the scale model situation. This also leads to an increase of the initial jet diameter of all tests to D_0 = 0.019 m, with all other parameters constant.

Table 6.1 – Jet configurations for the test comparisons, symmetry wall set-up

Parameter	p_j [bar]	D_0 [m]	Q_0 [dm³/s]	SOD [m]	v_{trail} [m/s]	n_0 [-]
Test 1	0.023	0.013	0.30	0.1	0.07	0.35
Test 2	0.008	0.013	0.17	0.1	0.05	0.30
Test 3	0.028	0.013	0.33	0.1	0.2	0.35

6.2.1 Results with pick-up function of Van Rijn

When the model is executed for the three test configurations, the results are as illustrated in Figure 6.5, Figure 6.6 and Figure 6.7. The calculated profiles show two distinctive behaviours that are not visible in the observed profile: a vertical penetration and a sudden transition from the erosion-dominated to the settling-dominated part.

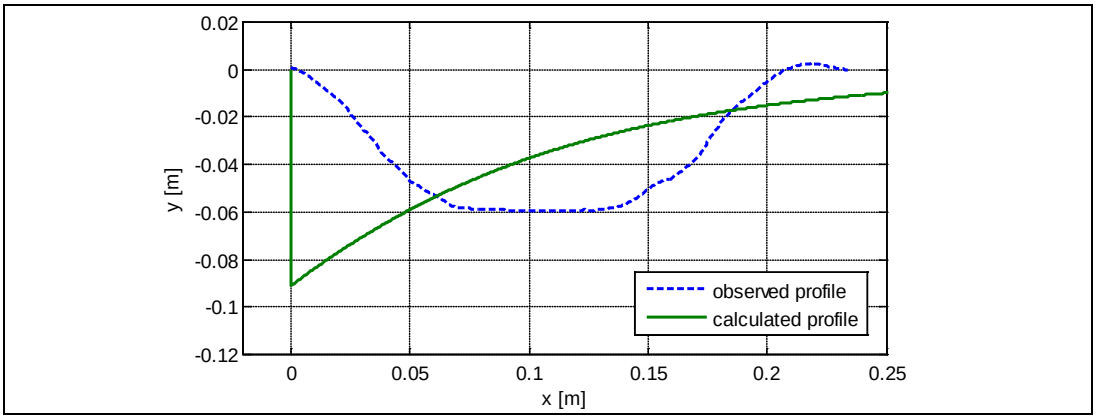

Figure 6.5 – Calculated and observed profile for p_j = 0.023 bar and v_{trail} = 0.07 m/s

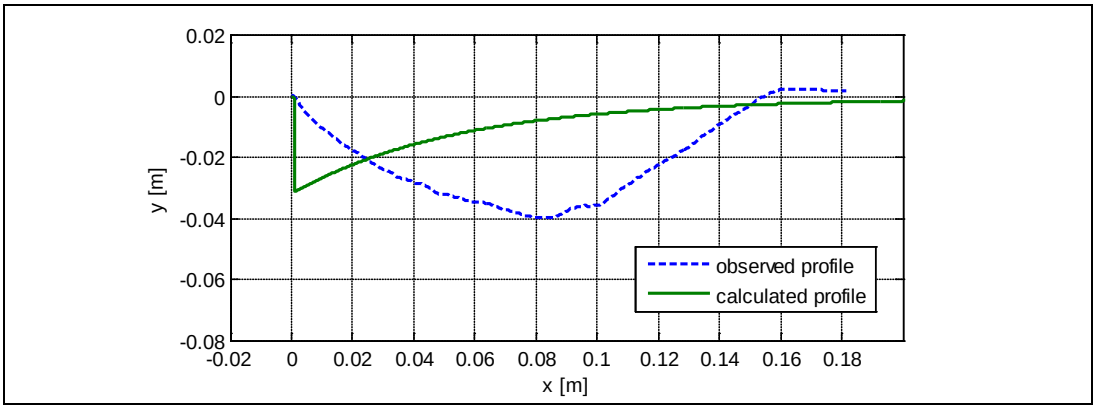

Figure 6.6 – Calculated and observed profile for p_j = 0.008 bar and v_{trail} = 0.05 m/s

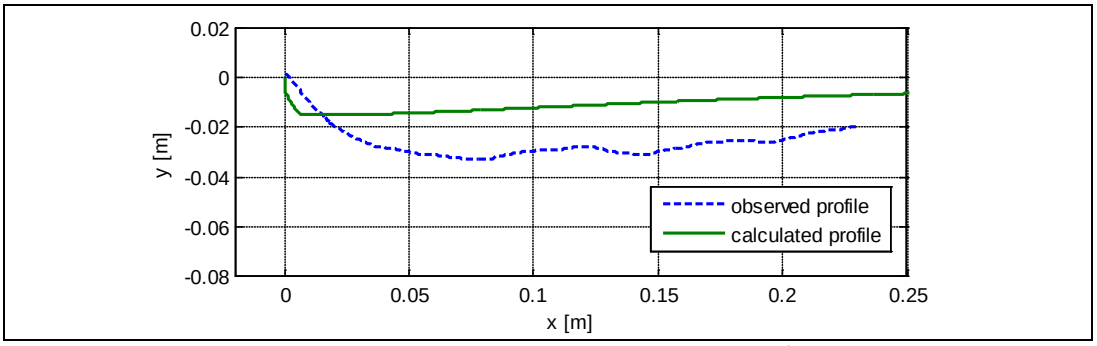

Figure 6.7 – Calculated and observed profile for p_j = 0.028 bar and v_{trail} = 0.2 m/s

It appeared in the scale model tests that the bed angle at the zone of impingement was about α_{bed} = 45 degrees with two significant different near-bed flow velocities, see Figure 6.8 and Figure 6.9. Since the flow velocity and therefore the erosion velocity is significantly higher in the first test while the trail velocity is only slightly higher, the bed angle should be steeper in Test 1 than in the second test. However, the observed value of the bed angle for both tests is α_{bed} = 45 degrees. Apparently, the soil is not able to have a bed angle larger than this 45 degrees. This phenomenon of a maximum bed angle is analysed in more detail in Appendix E.1.1.

Figure 6.8 – Observed penetration profile for p_j = 0.023 bar and v_{trail} = 0.07 m/s (Test 1)

Figure 6.9 – Observed penetration profile for p_j = 0.008 bar and v_{trail} = 0.05 m/s (Test 2)

In order to correctly model the erosion according to the observed behaviour, a maximum bed angle is introduced. This is in fact a limitation of the erosion velocity, proportional to the trail velocity. The most logical value for this maximum bed angle would be the observed $\alpha_{bed,max} = \varphi = 45$ degrees.
The jet now impinges on a slope, which causes that a part of the jet flow is deflected forwards as well. As a result, stones are also eroded and transported in the same direction as the nozzle's movement, creating a small berm in front of the jet. This local increase of the bed level is also clearly visible in Figure 6.8 and Figure 6.9. The magnitude of this increase can be easily calculated by the distribution of an impinging flow (Battjes, 2002):

$$Q_{1,2} = \frac{1}{2} Q_0 (1 \pm \sin \alpha_{bed}) \tag{6.24}$$

With α_{bed} = 45 degrees, this distribution is about 0.15/0.85. It is therefore assumed that the height of the berm in front of the jet, the so-called erosion front, is about 15% of the total penetration depth. This effect should be added to the eventual results of the model. The application of Eq. (6.24) does however also mean that the amount of flow and momentum available for the erosion decreases.

Applying the assumptions described above gives the results as illustrated in Figure 6.10, Figure 6.11 and Figure 6.12.

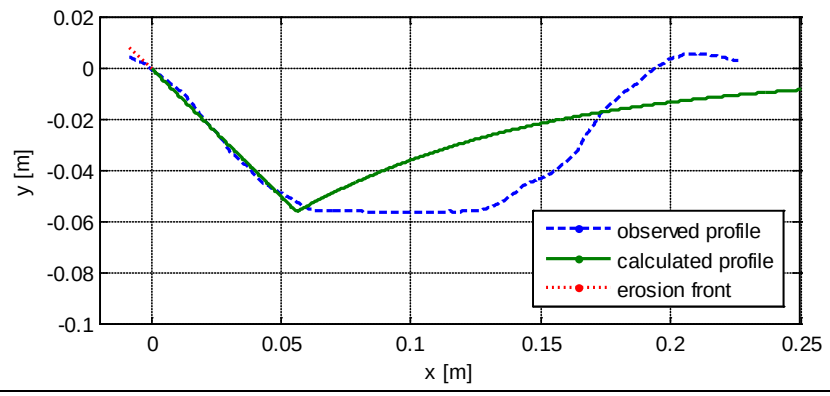

Figure 6.10 – Profiles for p_j = 0.023 bar and v_{trail} = 0.07 m/s with $\alpha_{bed,max}$ = 45 deg

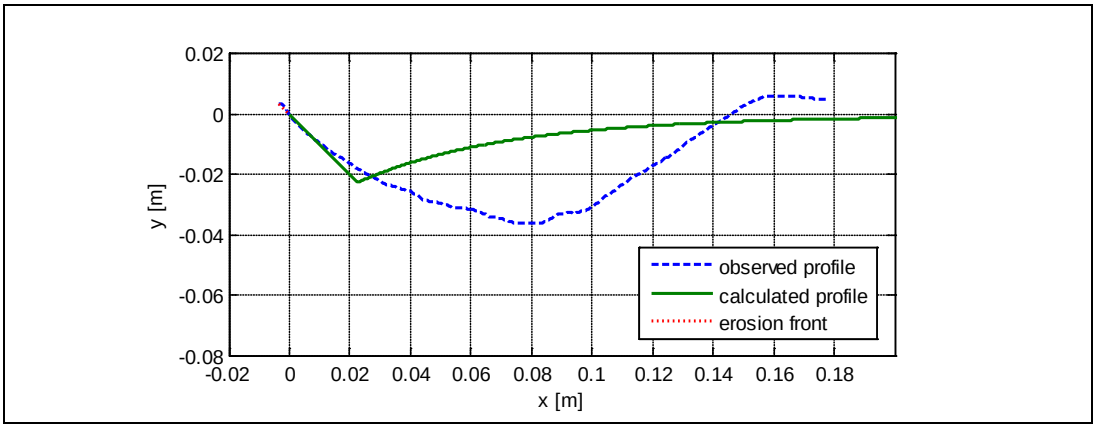

Figure 6.11 – Profiles for p_j = 0.008 bar and v_{trail} = 0.05 m/s with $\alpha_{bed,max}$ = 45 deg

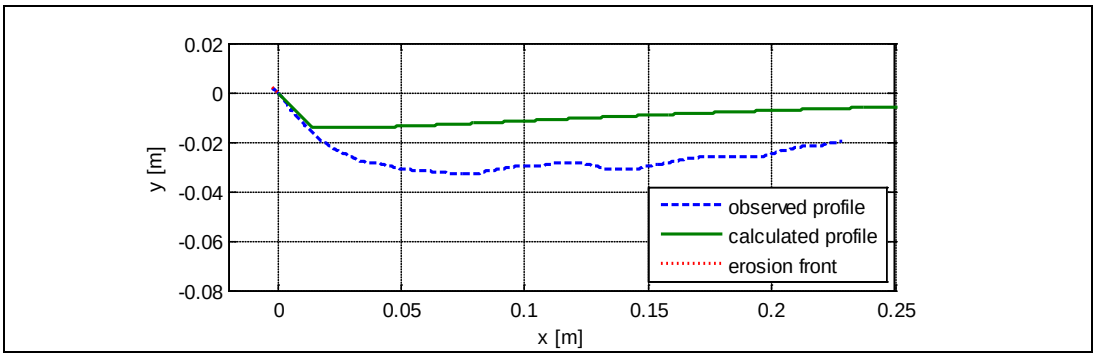

Figure 6.12 – Profiles for p_j = 0.028 bar and v_{trail} = 0.2 m/s with $\alpha_{bed,max}$ = 45 deg

The results are still not satisfactory. The penetration profile is now formed with a slope angle of α_{bed} = 45 degrees over almost the entire part where erosion is dominant. The transition into the sedimentation-dominated part is only a few gird points long, resulting in a very sharp edge in the calculated profile. This change is far more gradual in the observed profile. This sudden transition is caused by the decrease of θ_{cr}' due to the slope correction factor $k_{slope,//}$. With a slope of $\alpha_{bed} \approx \varphi$, the value of θ_{cr}' in Eq. (6.13) approaches zero, because the dilatancy term is small due to the relative large permeability. As a result, the pick-up of sediments becomes high due to the division by θ_{cr}' in Eq. (6.11). However, $k_{slope,//}$ is no longer zero when the bed angle decreases. The slope correction factor then becomes very quickly dominant in Eq. (6.13), due to the low value of the dilatancy term. The increase of θ_{cr}' sharply decreases the pick-up rate, which on its turn causes a further decrease of the bed angle. This snowball effect creates the sharp angle in the profile and is explained in more detail in Appendix E.1.2.

The slope correction factor thus causes a modelled behaviour that is physically not possible. It can therefore be argued that the pick-up function of Van Rijn, even with the modification of Van Rhee, is not applicable to the situation with these flow velocities and stone diameter. Van Rijn validated its pick-up functions with tests with flow and soil characteristics of up to:

$$D_*^{0.3}\left(\frac{\theta-\theta_{cr}}{\theta_{cr}}\right)^{1.5} \leq 60$$

Values of 600 and higher can be found in the present study. Van Rhee validated its modified equation for situation with high flow velocities, but also with a relatively small grain diameter. The dilatancy factor was therefore dominant, so the influence of the slope correction factor was relatively low. This is not the case with dumped rock. The circumstances of the removal of rock is therefore outside the validated domain of the pick-up function of Van Rijn and Van Rhee.

Since the division by θ_{cr}' has a large effect on the modelled pick-up rate, another pick-up function without this division should be used in the model.

6.2.2 Results with pick-up function of Fernandez Luque

The pick-up function of Fernandez Luque is now applied to the model. The function is expressed in Eq. (2.57), repeated here:

$$\psi_{e,FL} = \epsilon \rho_s \sqrt{\Delta g D_{50}} (\theta - \theta_{cr}')^{1.5} \tag{6.25}$$

A value of ϵ = 0.6 is found to give the best results of the calculated profile, which is discussed in Appendix E.1.3. The results are illustrated in Figure 6.13, Figure 6.14 and Figure 6.15 for the three tests with the configurations as given in Table 6.1.

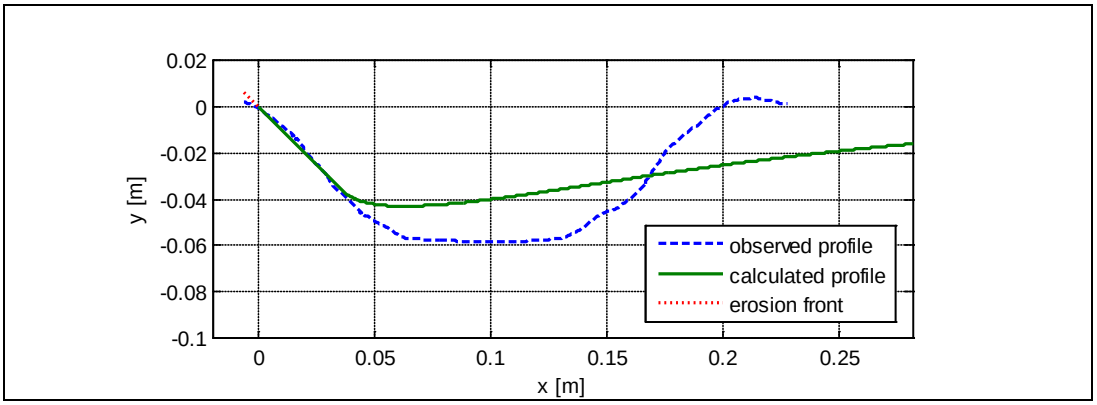

Figure 6.13 – Calculated and observed profile for p_j = 0.023 bar and v_{trail} = 0.07 m/s with ϵ = 0.6

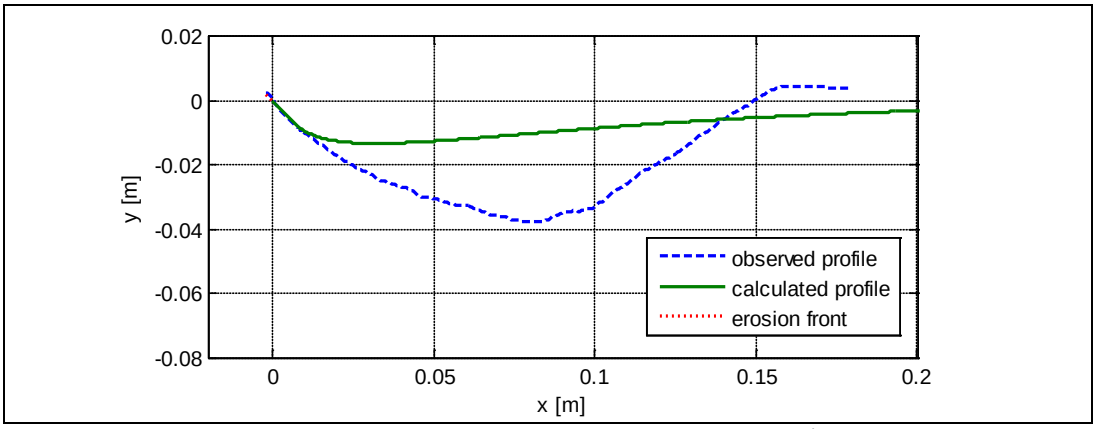

Figure 6.14 – Calculated and observed profile for p_j = 0.008 bar and v_{trail} = 0.05 m/s with ϵ = 0.6

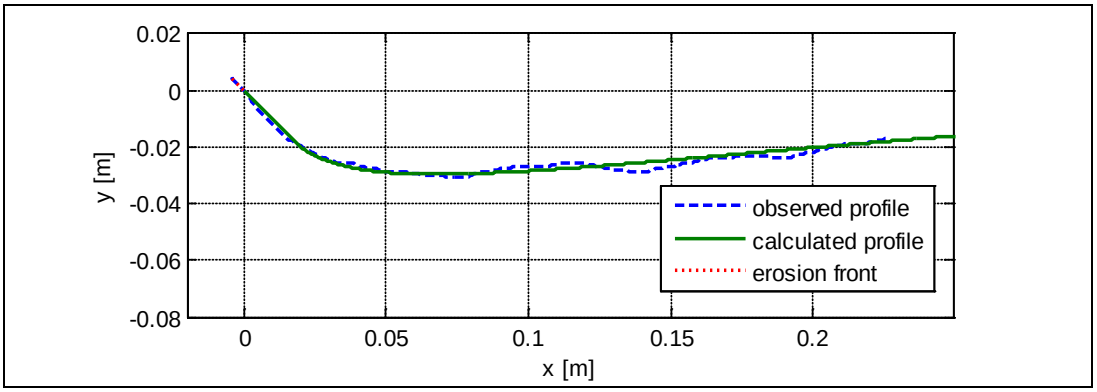

Figure 6.15 – Calculated and observed profile for p_j = 0.028 bar and v_{trail} = 0.2 m/s with ϵ = 0.6

The model results show a very good agreement with p_j = 0.028 bar, although the calculated penetration depth in the first two tests is obviously too low. Moreover, the sedimentation is also too low, resulting in a long and shallow settling-dominated part of the profile. Therefore, the reason for this incorrectly calculated behaviour is probably not due to a wrongly modelled pick-up. Instead, the settling flux seems to be the cause for the discrepancies between the calculated and observed profile. This is confirmed by the analysis performed in Appendix E.1.4. It shows that when the penetration profile is calculated without settling, the erosion-dominated part of the profile has a relative accurate agreement with the observed results. This confirms that the settling is not correctly incorporated in the erosion model, although apparently the combination of pick-up and settling is modelled correctly for p_j = 0.028 bar. A discussion about the possible reasons for the differences is also provided in Appendix E.1.4, but did not result in an applicable solution. Further research is thus required to get more insight in the pick-up and settling processes in order to model the behaviour correctly.

It is possible that the occurring erosion processes does not only depend on the pick-up and settling of individual sediment. A different approach to calculate the erosion of a granular bed is by means of the sediment transport capacity. The processes of sediment transport and the methods to calculate the capacity are described in section 2.4. The application of the theory to the erosion model is performed in Appendix E.1.5, but did not render better results than with the method of Van Rijn.
Other physical processes can affect the erosion as well. For instance, centrifugal forces due to the curved penetration profile are not taken into account. These forces possibly cause an increase of the stability of the soil and therefore an increase of the critical Shields parameter. Finally, it is assumed in this report that the stones are picked-up by the (water) flow. It is possible that the collisional effects of the grains becomes more important than the shear stress created by the flow. As a result, the flow can be seen as a Bagnold's fluid, or a granular flow, where the grain collision processes are more important than the viscous fluid stresses. The flow is then in a so-called grain-inertia regime. These effects are not taken into account in this study.

6.3 Prediction of penetration

The results of the erosion model did not always show a good agreement with the observed results of three different tests. However, it was shown that the pick-up using the function of Fernandez Luque showed reasonably good results as long as the settling flux did not have a large influence on the total erosion. This means that although the modelling of the entire penetration profile is not accurate, the erosion model can still be used to predict whether the jet will penetrate or deflect, which is determined at the start of the penetration profile where the settling flux is still very low. This prediction would be very useful, since the penetrating behaviour of the jet determines which working method is the most effective.

6.3.1 Penetration of a jet

The impingement zone of a deflecting jet was introduced in section 2.2.3 and was described to have a width of $2r_{zi}$ and a height of h_{zi}. The definition sketch is repeated in Figure 6.16, with the expression for r_{zi} provided by Eq. (2.31).

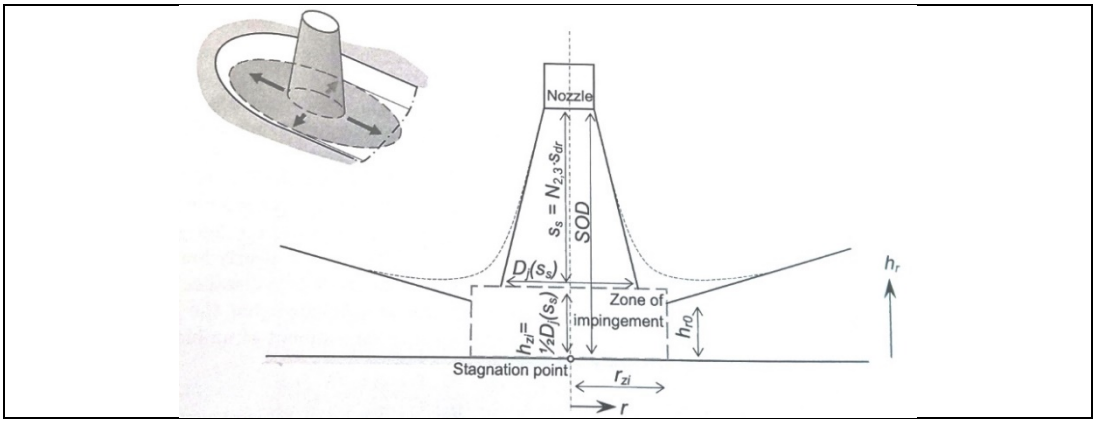

Figure 6.16 – An impinging circular jet, Figure 2.5 (Nobel, 2013)

One can expect that if the penetration depth in the centre of the impingement zone, i.e. x = r_{zi}, is higher than the zone height h_{zi}, the jet will penetrate fully. After all, the height of the radially deflected jet is insufficient to get out of the created trench. The entire jet flow therefore remains inside the trench, effectively causing a penetrating jet. On the other hand, if the penetration depth at x = $2r_{zi}$ is less than the zone height h_{zi}, the radially deflected jet is able to leave the trench, creating a deflecting jet. In between, the jet behaviour has characteristics of both regimes, similar to the processes observed during test 3.11 and described by Figure 5.8, and is therefore in a transitional state. A definition sketch containing all three jet regimes is provided in Figure 6.17.

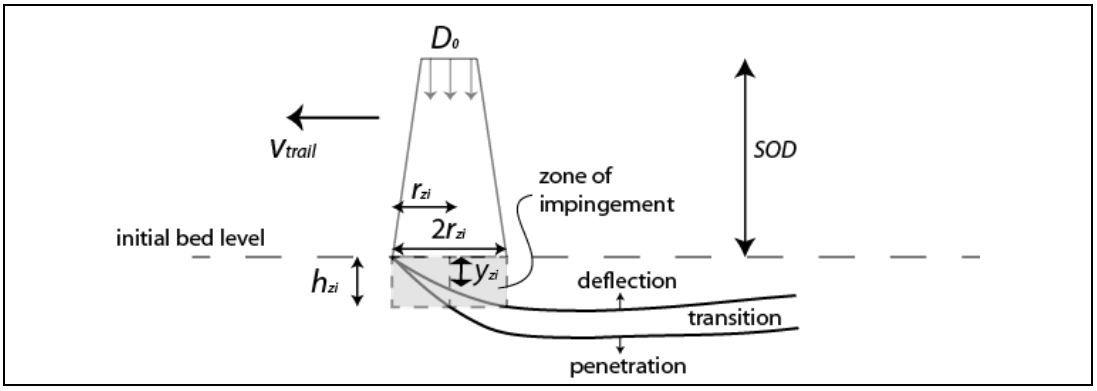

Figure 6.17 – Definition sketch of a penetrating, deflecting or transitional jet regime

The acting regime can therefore be described as follows, in which y^{rzi} and y^{2rzi} are the penetration depth at location $x = rzi$ and $x = 2rzi$ respectively:

$$\begin{aligned} penetrating\ if\ \frac{y^{rzi}}{h_{zi}} > 1 \\ deflecting\ if\ \frac{y^{2rzi}}{h_{zi}} < 1 \end{aligned} \tag{6.26}$$

A simple way to calculate the penetration depth at these two locations is desired in order to predict whether a jet will deflect or penetrate. The penetrating behaviour of a stationary jet can be described by the erosion parameter E_c, given by Eq. (2.16), here repeated with s = SOD:

$$E_c = \frac{u_0 \cdot D_0}{SOD\sqrt{\Delta g D_{50}}} \tag{6.27}$$

This expression is however not useful in the case of a translating jet, and has to be adjusted for the effect of v_{trail}.

The penetration of a jet can be expressed as a function of the bed angle α_{bed}, and is therefore also related to the ratio v_e/v_{trail}:

$$\text{jet penetration} = f(\alpha_{bed}) = f\left(\frac{v_e}{v_{trail}}\right) \tag{6.28}$$

The early stage of erosion determines whether the jet will penetrate or not. The settling is not yet of much influence during this stage and can therefore be neglected; meaning that the erosion velocity only depends on the pick-up rate $\psi_{e,FL}$. Assuming a constant value for g, n_0, c_b, ϵ and θ_{cr}', this means the following relationship:

$$v_e \propto \sqrt{D_{50}\Delta} \cdot \theta^{1.5} \tag{6.29}$$

Rewriting the Shields parameter results in:

$$v_e \propto \frac{{u_b}^3}{D_{50}\Delta} \tag{6.30}$$

The near-bed velocity is related to:

$$u_b \propto \frac{u_0 D_0}{s} \tag{6.31}$$

For a developed jet, the height of the impingement zone h_{zi} can be expressed as halve the fictitious free jet diameter, see also Figure 6.16. Using Eq. (2.13) and assuming that s = SOD, leads to:

$$h_{zi} \propto SOD \tag{6.32}$$

The relationship for an undeveloped jet can unfortunately not be expressed as conveniently as Eq. (6.32).

Combining all expressed relations, the following relationship can be expressed for a developed jet:

$$\frac{y^{rzi}}{h_{zi}} = f\left(\frac{E_{pen}}{SOD}\right) \tag{6.33}$$

With E_{pen} [-] as a newly defined erosion parameter that is made dimensionless with the inclusion of g. E_{pen} can also be seen as the proportional relation described in Eq. (2.18), times a velocity ratio to compensate for the trail velocity:

$$E_{pen} = \frac{{u_0}^3 \cdot {D_0}^3}{v_{trail} \Delta g D_{50} SOD^3} \propto \frac{{u_b}^2}{{w_s}^2} \frac{u_b}{v_{trail}} \tag{6.34}$$

A sensitivity analysis is performed in Appendix E.2.1, showing that the penetration parameter E_{pen} can be a suitable way to describe the penetration of a jet.

6.3.2 Penetration or deflection

The values for y/h_{zi} are calculated for a varying p_j, v_{trail}, SOD and D_0 (see also Appendix E.2.1) and are plotted against E_{pen}/SOD in Figure 6.18. With the results from this figure, it is possible to express the conditions of Eq. (6.25) as a function of E_{pen} and SOD:

$$\begin{array}{rl} E_{pen} > 50 \cdot SOD & penetration \\ 30 \cdot SOD \leq E_{pen} \leq 50 \cdot SOD & transition \\ E_{pen} < 30 \cdot SOD & deflection \end{array} \tag{6.35}$$

It is visible that the transition regime is valid for only a small range. The horizontal line for higher values of E_{pen}/SOD is caused by the limited maximum bed angle that prevents a steep penetration profile. However, the assumption of $\alpha_{bed,max}$ = 45 degrees has no effect on the conditions as expressed in (6.35), since these values are also larger than one with no maximum bed angle.

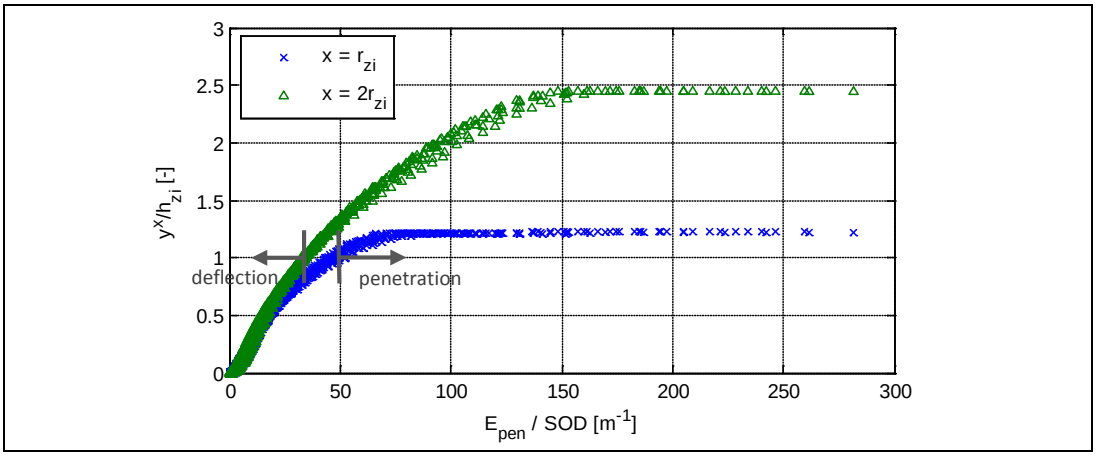

Figure 6.18 – Penetration depth h_{pen} plotted against E_{pen}/SOD

In order to validate the expressions in Eq. (6.35), the erosion parameter E_{pen} is calculated for each performed test and checked whether the predicted behaviour corresponds with the observed behaviour. The results are provided in Table 6.2.

Table 6.2 – Validation of jet behaviour prediction

Test	u_0 [m/s]	v_{trail} [m/s]	E_{pen} [-]	SOD [m]	Prediction	Observation
1.1	1.3	0.15	2.0	0.10	Deflection	Deflection
2.1	2.4	0.2	10	0.10	Penetration	Penetration
2.2	2.4	0.05	39	0.10	Penetration	Penetration
2.3	1.3	0.15	2.0	0.10	Deflection	Deflection
2.4	1.3	0.15	0.8	0.10	Deflection	Deflection
2.5	0.9	0.05	1.2	0.10	Deflection	Deflection
3.1	2.8	0.02	37	0.10	Penetration	Penetration
3.2	2.8	0.07	11	0.10	Penetration	Penetration
3.3	2.6	0.02	23	0.12	Penetration	Penetration
3.4	2.6	0.07	6.6	0.12	Penetration	Penetration
3.5	2.4	0.02	25	0.10	Penetration	Penetration
3.6	2.2	0.02	15	0.12	Penetration	Penetration
3.7	2.2	0.07	4.2	0.12	Transition	Transition
3.8	2.0	0.02	18	0.10	Penetration	Penetration
3.9	2.0	0.07	5.2	0.10	Penetration	Transition
3.10	1.9	0.02	15	0.12	Penetration	Penetration
3.11	1.9	0.07	4.4	0.12	Transition	Transition
3.12	1.4	0.02	5.0	0.10	Penetration	Penetration
3.13	1.3	0.02	3.2	0.12	Deflection	Transition
3.14	0.9	0.02	1.6	0.12	Deflection	Deflection
4.1	2.1	0.02	72	0.10	Penetration	Penetration
4.2	2.1	0.05	29	0.10	Penetration	Penetration
4.3	2.1	0.07	21	0.10	Penetration	Penetration
4.4	2.1	0.07	21	0.10	Penetration	Penetration
4.5	2.1	0.07	21	0.10	Penetration	Penetration
4.7	2.4	0.07	27	0.10	Penetration	Penetration
4.8	2.4	0.1	19	0.10	Penetration	Penetration
4.9	2.1	0.07	13	0.10	Penetration	Penetration

It shows that the jet behaviour in almost all tests was correctly predicted; only tests 3.9 and 3.13 have a difference between the observation and the prediction. However, these values of E_{pen} = 5.2 and E_{pen} = 3.2 are very close to the boundary values as provided in Eq. (6.33). Already a small difference between the measured and modelled jet configurations can result in this deviation. Moreover, the change between both jet regimes is very gradual; the label given to the observed regime close to the transitional stage is therefore a very subjective perception.
Note that for some tests the actual stand-off distance of *SOD* = 0.12 m is used; all other tests have a value of *SOD* = 0.10 m. This difference was neglected in the tests where all stand-off distances were given as *SOD* = 0.1 m.

The following issues are still a point of discussion for the implementation of Eq. (6.33) to other situations than in the used scale model:

- The parameters u_0, D_0 and *SOD* are all incorporated into E_{pen} to the third power. This means that small deviations, or an inaccurate measurement, already leads to a relative large change of the penetration parameter.
- The calculations are based on an erosion model that has not yet been satisfactory validated for multiple configurations. Moreover, the use of E_{pen} is based on the assumption that the erosion velocity only depends on the pick-up. Finally, the entrainment of a jet is not taken into account: the penetration is based on the flow velocity at the point of impingement. For instance, a situation with a high pressure jet with a small D_0 and stand-off distance leads to high values of E_{pen}, while it is not expected that the penetration will be as high as a situation with a jet configuration similar to the set-up in the used scale model, although the latter case would have a lower value of E_{pen} due to a lower initial flow velocity.
- The expressed relation for E_{pen}/SOD is only valid for a developed jet and cannot be used for low ratios of SOD / D_0.
- The influence of β_j, i.e. the influence of the initial bed slope at the point of impingement as illustrated in Figure 5.4, is not taken into account. However, this has seemingly little influence, since the predictions of the penetrating behaviour in the scale tests were almost entirely correct.
- The influence of the grain diameter on E_{pen} is complex, see also Appendix E.2.1. Especially the relation with θ_{cr}' cannot be conveniently described in E_{pen} without making the simple parameter more complicated. However, the erosion parameter E_c also assumes a simple relation with D_{50}. Moreover, there are only a few different stone classes used in practice; the variance in grain diameter is therefore limited for dumped rock. Finally, the critical Shields parameter for these stone classes are all equal since D_{50} > 6 mm.
- The threshold values in Eq. (6.33) which indicate whether a jet will penetrate or deflect depend on the stand-off distance. Unfortunately, this means that the threshold values of 50 and 30 have a dimension of [m^{-1}] and are therefore expected to have a scale factor. This means that the expected threshold values in the prototype situation are 1.7 and 1.0 respectively. Moreover, the erosion velocity was found to have a scale effect in the tests. Together with the influence of the grain diameter, it is therefore recommended to validate Eq. (6.33) for the prototype situation. The found threshold values can be used to predict the jet behaviour in practice.

- The effect of hindered erosion on E_{pen} is not taken into account, since the effect with grain diameters as found with dumped rock is very small. This however means that E_{pen} cannot be applied to a situation with small grains without adjustments.

7 Conclusions and recommendations

The results of the three main objectives and the answer to the problem definition as described in the introduction are provided in the conclusions. Furthermore, recommendations to improve the results of the study are given.

Conclusions

Scale model tests with a scale of 1:30 show that a trailing jet, impinging on a rock soil, can behave in two different ways: deflecting or penetrating. Each behaviour has its own erosion processes, depending on the combination of flow and trail velocity. With a deflecting jet, the flow is deflected radially outwards, eroding the top layers of the soil. This leads to a symmetric scour profile of which the berms are eventually too high to transport the stones out of the trench. In this equilibrium situation, the stones inside the trench are still eroded, but since there is no transport, the effective production is zero.
A penetrating jet enters the soil as a confined jet, eroding the soil along its trajectory. The forward movement of the nozzle causes the confined jet flow to be deflected backwards, resulting in a backwards transport of the eroded stones. The combination of the flow and trail velocity determines the 'magnitude' of this penetration; i.e. the penetration depth and the sedimentation length.

These two behaviours can be linked to a working method to remove a dumped rock cover. With a deflecting jet behaviour, the most effective method is a vertical jet, horizontally moving in the same direction as the cover. The radial transport of the eroded stones decreases the bed level on top of the pipe. However, the equilibrium situation sets in before the cover height is removed. Subsequent relocations of the nozzle can lead to a sequence of multiple passes, which should be able to eventually clear the pipe with a moderate production rate. Such a sequence was however not tested during the scale model tests.
A vertical, penetrating jet can be used when the trail direction becomes perpendicular to the direction of the rock cover. In this way, the backwardly transported stones are moved to a location next to the cover, away from its place above the pipeline. This working method requires multiple, short movements in order to clear the entire length of rock cover, resulting in a low production rate.
The most feasible working method is with an inclined jet, combined with a penetrating behaviour. The jet flow is directed at an angle on the rock cover, with the nozzle moving in the same direction as the pipeline cover. The penetrating jet 'pushes away' the stones on top of the pipe, decreasing the bed level above the pipeline. The scale model tests shows that a horizontal jet is the most effective jet angle. With a high hydraulic power and a low trail velocity, the jet is able to remove the cover height after a single pass.

An erosion model is created in order to model the penetrating behaviour of a jet. The model shows that the pick-up function of Van Rijn is not applicable to a situation with erosion of soil with a large diameter by means of a jet flow. The modification of Van Rhee has only a limited influence due to the relatively high permeability. The pick-up function of Fernandez Luque with the modified critical Shields parameter results in a

more accurate outcome of the model. The modelling of the settling of the stones is still not according to the observed processes.

A dimensionless erosion parameter E_{pen} is defined as a function of the initial flow velocity, stand-off distance, jet diameter and trail velocity:

$$E_{pen} = \frac{{u_0}^3 \cdot {D_0}^3}{v_{trail} \Delta g D_{50} SOD^3}$$

When this parameter has a value higher than 50 times the stand-off distance, the jet shows a penetrating behaviour in the scale model. In order to obtain the highest erosion with an inclined jet, this penetration should be as high as possible. The applicability of E_{pen} outside the scale model situation should be studied before implementation, though.

Recommendations

New scale model tests should be performed to increase the accuracy of the results. For instance, the pressure of the (submerged) jet should be measured during the test. Also, the accuracy of the determination of the SOD, the nozzle diameter with a symmetry wall set-up and the pump configuration should be improved so different tests can be better compared with each other. It is recommended to increase the scale of the tests to limit the scale effects of the erosion velocity and penetration depth; preferably so that the mean diameter is in the constant domain of the critical Shields parameter (D_{50} > 6 mm).

It should also be studied if the recommended working method is achievable in practice. The influence of the jet flow on the erosion of the subsoil, and the possible free span as result, should be a subject in this study. Another focus should be on the practical application of an inclined jet: is it possible to accurately aim an oblique jet on the cover, and is the reaction force of the jet a risk for the stability? Furthermore, the submerged pump at the end of the fall pipe has only a limited power. It should be ensured that this power is large enough to create a penetrating jet.

The pick-up and settling processes should be studied in more detail in order to explain the discrepancies between the modelled and observed profile. This study should be focussed on the observed maximum bed angle of 45 degrees, on the pick-up rate of large sediments (on a steep slope) and on the settling processes of gravel. The possible occurrence of a granular flow and its corresponding grain-inertia effects should also be studied. The outcomes of this study should be used to improve the erosion model.

The defined erosion parameter can predict the jet behaviour in the used scale model situation. New scale model tests with a different grain and nozzle diameters should be performed in order to validate the use of this parameter for other situations as well. Moreover, the effect of hindered erosion is not incorporated in this erosion parameter.
Also, the erosion model cannot predict the production for a given jet configuration. It is recommended to further develop an erosion model that can quantitatively model the production of a removal operation.

Finally, one can also think of other purposes of an impinging jet on a gravel bed. A horizontal moving vertical jet, for instance, may be promising for flattening purposes.

Bibliography

Adel, H. d., 1987. *Heranalyse doorlatendheidsmetingen door middel van de forchheimer relatie,* Delft: Deltares.

Aderibigbe, O. O. & Rajaratnam, N., 1996. Erosion of loose beds by submerged circular impinging vertical turbulent jets. *Journal of Hydraulic Research,* 34(1), pp. 19-33.

Albertson, M. L., Dai, Y. B., Jenson, A. & Rouse, H., 1950. Diffusion of submerged jets. *Trans. Am. Soc. Civil Engineering,* Issue 115, pp. 639-664.

Bagnold, R., 1954. Experiments on a gravity-free dispersion of large solid spheres in a Newtonian fluid under shear. *Proceedings of the Royal Society,* Volume 225A.

Bagnold, R., 1956. On the flow of cohesionless grains in fluids. *Philosophical Transactions of the Royal Society of London,* 249A(964), pp. 235-297.

Bagnold, R., 1966. An approach to the sediment transport problem from general physics. *Geological Survey Professional Paper,* I(422).

Battjes, J., 2002. *Dictaat Vloeistofmechanica.* Delft: TU Delft.

Beltaos, S., 1976. Oblique impingement of circular turbulent jets. *Journal of Hydraulic Research,* 14(1), pp. 17-36.

Bisschop, F., Visser, P., van Rhee, C. & Verhagen, H., 2010. *Erosion due to high flow velocities: a description of relevant processes.* Shanghai, ICCE.

Blokland, T., 1997. *Bodembescherming belast door schroefstralen,* Rotterdam: Gemeentelijk Havenbedrijf Rotterdam.

Bosboom, J. & Stive, M., 2012. *Coastal Dynamics I, lecture notes CIE4305.* 0.3 red. Delft: VSSD.

Boutovski, A., 1998. *Stabiliteit van gestorte steen,* Delft: Technische Universiteit Delft.

De Boer, G., 1998. *Transport van stenen van een granulaire bodemverdediging,* Delft: Technische Universiteit Delft.

Fernandez Luque, R., 1974. *Erosion and transport of bed-load sediment,* Meppel: Krips Repro B.V..

Hoan, N. et al., 2007. *Stone stability under non-uniform flow,* Delft: Technische Universiteit Delft.

Hoffmans, G. & Verheij, H., 1997. *Scour manual.* Rotterdam: A. A. Balkema.

Hofland, B., 2005. *Rock & Roll, Turbulence induced damage to granular bed protections,* Delft: Technische Universiteit Delft.

Izbash, S. V., 1935. *Construction of dams by dumping of stone in running water.* Moscow: sn

Jongeling, T. et al., 2003. *Design method granular protections,* sl: Delft Hydraulics.

Kobus, H., Leister, P. & Westrich, B., 1979. Flow field and scouring effects of steady and pulsating jet impinging on a movable bed. *Journal of Hydraulic Research,* 17(3), pp. 175-192.

Koch, F. & Flokstra, C., 1981. *Bed level computations for curved alluvial channels.* New Delhi, sn

Lammers, J., 1997. *Shields in de praktijk,* Delft: Technische Universiteit Delft.

Matousek, V., 2004. *Dredge pumps and slurry transport, OE4625.* Delft: Technische Universiteit Delft.

Meyer-Peter, E. & Müller, R., 1948. *Formulas for bed-load transport.* Stockholm, sn

Nobel, A., 2013. *On the excavation process of a moving vertical jet in cohesive soil,* Delft: Technische Universiteit Delft.

Paintal, A., 1971. Concept of critical shear stress in loose boundary open channels. *Journal of Hydraulic Research,* 9(1).

Rajaratnam, N., 1976. *Turbulent Jets.* Amsterdam: Elsevier.

Regout, W. D., 1996. *Flowdredging - Het spuiten van sleuven in zand,* Delft: Technische Universiteit Delft.

Richardson, J. & Zaki, W., 1954. Sedimentation and fluidisation. *Transactions of the Institution of Chemical Engineers,* Volume 32, pp. 35-53.

Schiereck, G. J., 2004. *Introduction to bed, bank and shore protection.* Delft: Delft University Press.

Shields, A., 1936. *Anwendung der Ahnlichkeitsmechanik und der Turbulenzforschung auf die Geschiebebewegung,* Berlin: Mitteilungen Preussischen Versuchsanstalt fur Wasserbau und Shiffbau.

Talmon, A., 1992. *Bed topography of river bends with suspended sediment transport,* Delft: sn

van de Leur, K., 2010. *Post-trenching with a trailing suction hopper dredger,* Delft: Technische Universiteit Delft.

Van der Schrieck, G., 2012. *Dredging Technology, guest lecture notes CIE5300.* Delft: GLM van der Schrieck BV.

van Rhee, C., 2002. *On the sedimentation process in a trailing suction hopper dredger,* Delft: Technische Universiteit Delft.

van Rhee, C., 2010. Sediment entrainment at high flow velocity. *Journal of Hydraulic Engineering,* 136(9), pp. 572-582.

Van Rijn, L., 1981. *Computation of bed-load concentration and bed-load transport,* Delft: Delft Hydraulics Laboratory.

Van Rijn, L., 1984. Sediment Transport. *Journal of Hydraulic Engineering,* 110(10), pp. 1431-1456.

Van Rijn, L., 1993. *Principles of sediment transport in rivers, estuaries and coastal seas.* Amsterdam: Aqua Publications.

Van Veldhoven, V., 2002. *Vooronderzoek schroefstraal op een talud met breuksteen,* Delft: Technische Universiteit Delft.

Verhagen, H., 2012. *Ships: Loads, stability and erosion.* Delft: Technische Universiteit Delft.

Verheij, H. J., 1988. *Aantasting van dwarsprofielen in vaarwegen,* Delft: RWS/DHL.

Verruijt, A., 2010. *Grondmechanica.* Delft: Technische Universiteit Delft.

Visser, P., 1988. *A model for breach growth in a dike-burst.* Malaga, Spain, sn

Visser, P., 1995. *Application of sediment transport formulae to sand-dike breach erosion,* sl: Technische Universiteit Delft.

Wilson, K., 1984. Analysis of contact-load distribution and application to deposition limit in horizontal pipelines. *Journal of Pipelines,* Volume 4, pp. 171-176.

Wilson, K., 1987. Analyis of bed-load motion at high shear stresses. *Journal of Hydraulic Engineering,* Volume 113, pp. 97-103.

Wilson, K., 2005. Rapid increase in suspended load at high bead shear. *Journal of Hydraulic Engineering,* 131(1), pp. 46-51.

Yeh, P. et al., 2009. Large-scale laboraty experiment on erosion of sand beds by moving circular vertical jets. *Ocean Engineering,* Volume 36, pp. 248-255.

Youd, T., 1973. Factors controlling maximum and minimum densities of sands. *ASTM STP,* Volume 523, pp. 98-112.

Appendix A Theory

A.1 Dumping of rock

This chapter of the appendix provides extra information to section 2.1.

The rocks used by Boskalis for a pipeline cover are generally crushed rocks from a quarry near Averøy, Norway with diameter of 1"-5" (2.5 – 12.5 cm). The conservative upper limit of the mean diameter D_{50} can be taken from the grading curve of the quarry, see Figure A.1, and is slightly larger than 10 cm. The mean diameter D_{50} means a 50% sieve pass through from Figure A.1. Analogously, D_{15} is the diameter with only a 15% sieve pass.

For relatively large particles, such as the dumped small rocks used for the cover, the mean nominal grain diameter D_{n50} is used. This is essentially the side of a cube with the same volume as the considered stone (Schiereck, 2004), and can be expressed by:

$$D_{n50} = 0.84 \cdot D_{50} \tag{A.1}$$

This nominal diameter should be used as value for D_{50} in equations when regarding larger stones; which is also done in this report, but is not specifically mentioned each time. Given Eq. (A.1) and the provided mean grain diameter of the used rocks, this leads to D_{n50} = 8.5 cm.

The porosity of a bed of small rock can be estimated with Figure A.2. This diagram shows the relation between the maximum and minimum void ratio and the so-called coefficient of uniformity, defined as D_{60}/D_{10}. This ratio can be derived from Figure A.1 and is about D_{60}/D_{10} = 3. From Figure A.2 and assuming a subangular shape factor, the void ratio is found to be between e = 0.4 and e = 0.8.

Instead of the void ratio, the porosity n is often taken as a description of the relative volume of the pores. The relation between the porosity and the void ratio is given by:

$$e = \frac{n}{1-n} \tag{A.2}$$

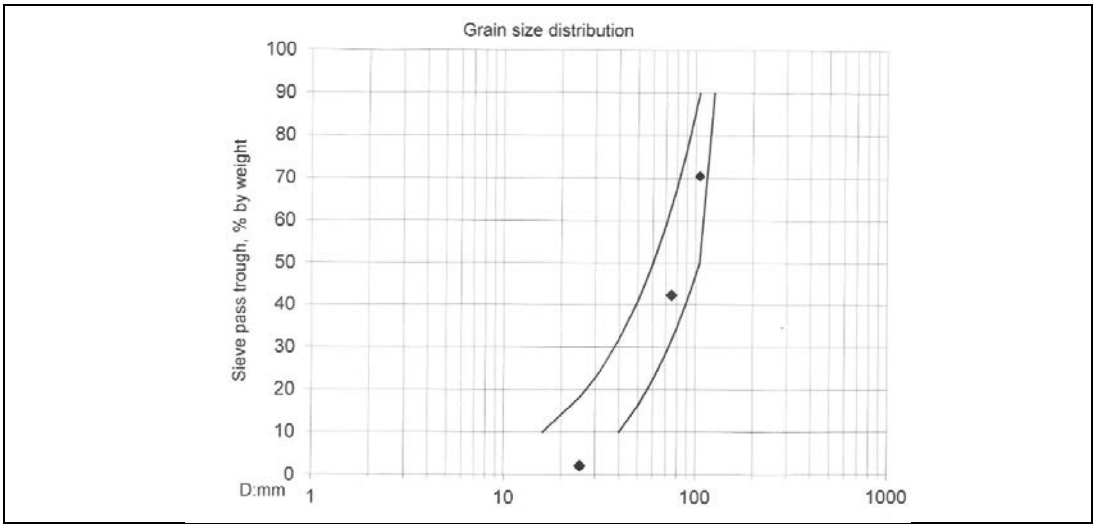

Figure A.1 – Grading curve of the Averøy quarry

This means that the porosity is assumed to be between n_{max} = 0.45 and n_{min} = 0.30 for a loose and dense compaction respectively.

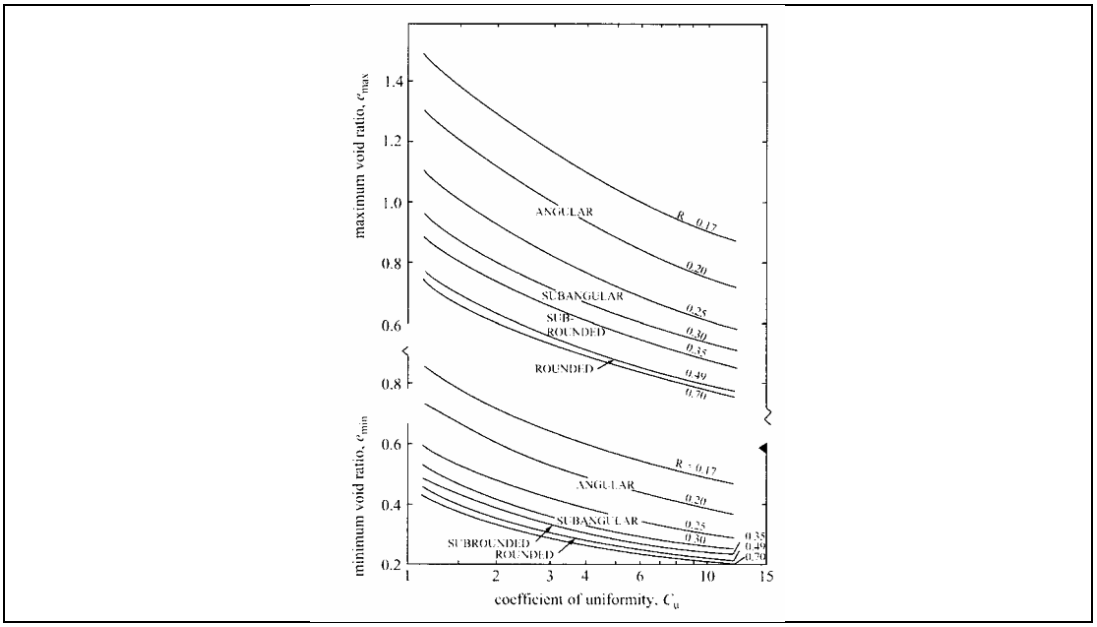

Figure A.2 – Minimum and maximum void ratio for granular sediments (Youd, 1973)

The permeability k of a gravel bed with the given grain diameter is about $k \approx 0.2$ m/s (Schiereck, 2004). The angle of repose φ is assumed to be $\varphi = 45°$ and the density $\rho = 2650$ kg/m^3.

The characteristics and dimensions of the rock cover will change over time after construction. One can think of marine growth on and between the rocks or the inclusion of sand in the pores. These changes will affect the characteristics of the rock bed, most notably the permeability. However, it is assumed that the small particles that have settled in the pores will be instantly flushed away and will have no influence on the actual permeability of the rock cover once under influence of a jet flow.

A.2 Jetting

More information about specific parts of the theory about jetting is provided in this chapter of the appendix. Firstly, the derivation of the expression to calculate the flow velocity at each point in the jet flow is given. Afterwards, more information is provided about the stagnation point of an impinging jet and the corresponding pressure.

A.2.1 Region of fully developed flow

In the region of fully developed flow, the influence of the entrainment processes has penetrated to the axis of the jet flow, resulting in a decrease of the velocity in axial direction. The maximum velocity occurs on the axis and can be described as (Rajaratnam, 1976):

$$u_m = \sqrt{\frac{k_j}{2}} u_0 \frac{D_0}{s} \quad for\ s > \sqrt{\frac{k_j}{2}} D_0 \tag{A.3}$$

The velocity profile of the jet flow in the region of fully developed flow is assumed to be Gaussian distributed. The boundary of the jet flow is therefore difficult to determine, due to the asymptotical nature of this Gaussian velocity distribution. Often, a typical width of the jet b is defined where $u = 0.5u_m$. The typical diameter of the jet is therefore $2b$. The relation between this typical width and the axial distance to the nozzle is defined as (Rajaratnam, 1976):

$$b = 0.10s \tag{A.4}$$

Given the Gaussian velocity distribution in radial direction and the decreasing maximum velocity in axial direction, the velocity at each point in the jet flow can be calculated using (Schiereck, 2004):

$$u = u_m e^{-\frac{k_j}{s^2/b^2}\left(\frac{r}{b}\right)^2} \quad for\ s > \sqrt{\frac{k_j}{2}} D_0 \tag{A.5}$$

Combining equations (A.3), (A.4) and (A.5) gives:

$$u = \sqrt{\frac{k_j}{2}} u_0 \frac{D_0}{s} e^{-k_j\left(\frac{r}{s}\right)^2} \quad for\ s > \sqrt{\frac{k_j}{2}} D_0 \tag{A.6}$$

A.2.2 Impinging circular turbulent jet

The pressure *p* [Pa] exerted by the jet on the soil is related to the (free) jet velocity through the principle of Bernoulli:

$$p = \frac{1}{2}\rho u^2 \tag{A.7}$$

In the stagnation point, *r* = 0 m and *s* = SOD, the pressure exerted by the jet is maximum and can be calculated by using the maximum velocity found in Eq. (A.3) in Eq. (A.7), resulting in:

$$p_m = \frac{1}{2}\rho {u_m}^2 \tag{A.8}$$

Combining equations (A.4), (A.5) and (A.8) gives:

$$\frac{p}{p_m} = \frac{u^2}{{u_m}^2} = e^{-2k_j\left(\frac{r}{s}\right)^2} \tag{A.9}$$

Note that the use of the approximation of the free jet with uniform flow to calculate the pressure distribution will result in a rectangular pressure distribution.

The flow through a permeable layer can be described with the Forchheimer equation (Schiereck, 2004):

$$i = \frac{dp_{mwc}}{dy} = \frac{u_f}{a_f} + \frac{{u_f}^2}{b_f} \tag{A.10}$$

In which the seepage velocity in the bed is indicated with u_f [m/s], *dy* the length over which the pressure gradient is determined and the pressure expressed in [mwc], using:

$$p_{mwc} = \frac{p}{\rho g} = \frac{1}{2g}u^2 \tag{A.11}$$

The permeability of a granular filter depends on the smaller elements that can block the porous flow. Therefore, the parameters for the laminar permeability a_f [m/s] and turbulent permeability b_f [m^2/s^2] are a function of D_{15} and are respectively given by:

$$a_f = \frac{n^3}{\alpha(1-n)^2}\frac{g{D_{15}}^2}{\nu}$$
$$b_f = \frac{n^2 g D_{15}}{\beta} \tag{A.12}$$

The value of the coefficients α and β can be estimated with α = 160 and β = 2.2 (Adel, 1987). The permeability *k*, as noted in Section 2.1.1, is a combination of the laminar and

turbulent terms. For fine material, the flow through the pores is laminar and Eq. (A.10) reduces to the Darcy principle, with $k = a_f$. For more coarse material, about D_{50} > 6 cm (Schiereck, 2004), the second term on the right hand side of Eq. (A.10) is dominant.

In order to determine the seepage velocity, the pressure gradient should be known at each point where the jet flow impinges the bed. This leads to an elaborate integral that has to be solved. For a first approximation, the uniform jet flow velocity can be used. Although this approach leads to a rectangular pressure distribution, it suffices for a first approximation to determine the average pressure gradient over the entire stagnation point. The following average pressure gradient is assumed:

$$\overline{\frac{dp}{dy}} = \frac{{u_u}^2}{2gD_0} = \frac{\bar{u}_f}{a_f} + \frac{{\bar{u}_f}^2}{b_f} \tag{A.13}$$

The length over which the jet pressure drops to zero is assumed to have the order of magnitude of the nozzle diameter

Integration of u_f over the area of the impingement zone gives the seepage flow rate. For the approximation, this area is determined by the diameter of the fictitious uniform jet, leading to:

$$Q_f = \bar{u}_f \pi {r_u}^2 \tag{A.14}$$

The pressure gradient in the bed can also cause fluidisation of the bed when the increasing water pressure causes the effective soil stress to become zero. It is assumed that the critical gradient is not reached with low pressure jets as used in mass flow dredging, and fluidisation processes therefore have no influence (Regout, 1996).

A.2.3 Influence of obliqueness

The influence of an angle of impingement on the velocity distribution of a radial wall jet has been studied by Beltaos (1976). He found the following expression for the near-bed velocity:

$$u_{b,r} = u_0 \frac{f(\alpha_j, \varphi_j) D_0}{r} \tag{A.15}$$

With:

$$f(\beta_j, \varphi_j) = \frac{1.1}{\sin \beta_j} \cdot \frac{1 + \cos \beta_j \cdot \cos \varphi_j}{\cos^2 \varphi_j + (\frac{\sin \varphi_j}{\sin \beta_j})^2} \tag{A.16}$$

With β_j the angle of the jet in the x,z plane and φ_j the angle in x,y plane, see also Figure A.3. With φ_j = 0 deg, Eq. (A.16) decreases to:

$$f(\beta_j) = \frac{1.1(1+\cos\beta_j)}{\sin\beta_j} \qquad \text{(A.17)}$$

Note that the distance between the bed and the nozzle is not included in Eq. (A.15). This leads inevitably to discrepancies, as the SOD has a clear influence on the near-bed velocity. Furthermore, the influence of the jet angle on the scour depth is negligible for values of β_j between 60 deg and 90 deg (Hoffmans & Verheij, 1997).

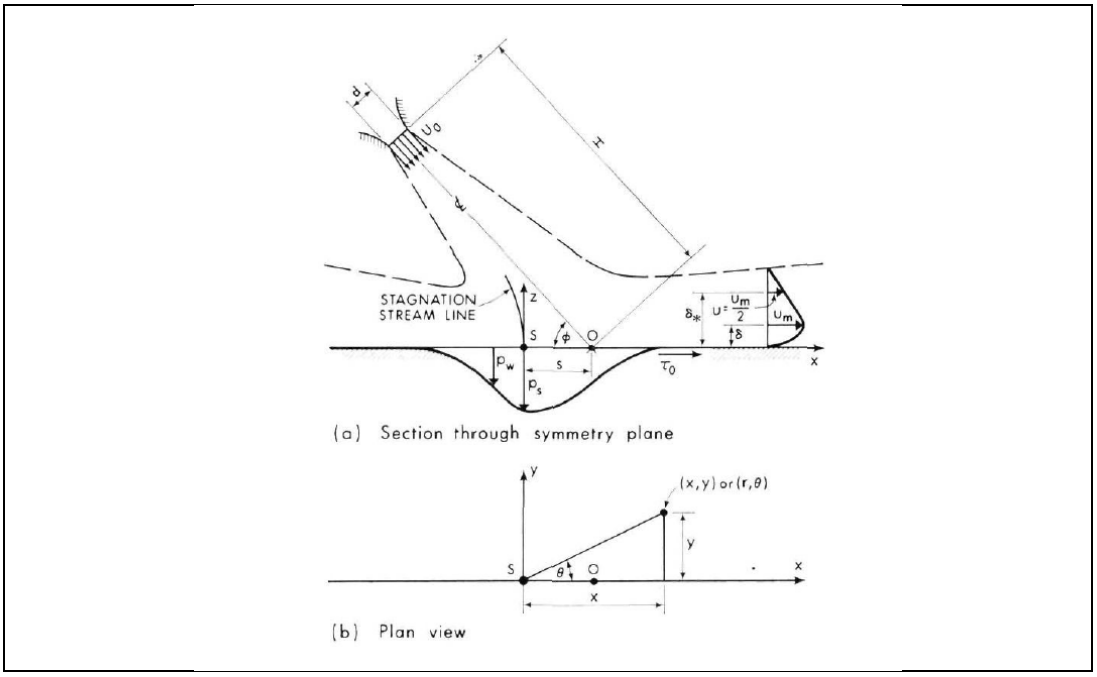

Figure A.3 – Definition sketch of an oblique impinging jet (Beltaos, 1976)

A.3 Erosion

A.3.1 Izbash

Izbash (1935) found the following relation between the velocity and the diameter of a particle with the use of the dimensionless coefficient β_{Iz}:

$$\frac{2\Delta g D_{50}}{{u_{cr}}^2} = \beta_{Iz} \tag{A.18}$$

Or:

$$u_{cr} = \sqrt{\frac{2\Delta g D_{50}}{\beta_{Iz}}} \tag{A.19}$$

The location of the velocity is however not defined, neither is there any influence of the water depth. This makes the Izbash formula useful as a first approximation in cases where the velocity is known and the relation with the water depth is not relevant (Schiereck, 2004), as is the case for a jet flow. A disadvantage for this method is that the coefficient β_{Iz} is not qualitatively defined; it is a so-called 'dustbin coefficient' in which all (un)known mechanisms, influences and parameters are included. It therefore has to be empirically defined for each situation separately.

The relationship found by Izbash has been used in various literature to describe the stability of a bed protection under the effects of the propeller wash of a ship. It is interesting to evaluate the found values of the Izbash coefficient since propeller wash behaves similarly as a circular jet. Moreover, the flow velocities and stone diameters are of the same order of magnitude as with the mass flow excavation of a dumped rock cover.

Verheij (1988) found a critical value of β_{Iz} = 3.0 at which some transport of the stones in a bed protection is acceptable. Schiereck (2004) gives a bit lower value of β_{Iz} = 2.5, which was found by Blokland (1997) as well. The term 'critical value' is however a bit arbitrary, as it is impossible to find a value of the flow velocity at which 'the' motion of all particles takes place: some grains move at a lower critical velocity than other grains. When no transport is accepted, the values of β_{Iz} are about two times higher (Schiereck, 2004). Contrary to many hydraulic engineering problems, the aim of mass flow excavation is erosion, instead of maintaining the stability of the stones. Some transport of the stones is therefore not only acceptable; it is required. Based on the mentioned literature, the

critical value of β_{lz} = 2.5 should therefore be taken as an upper value to determine the critical velocity.

Van Veldhoven (2002) investigated the similarities between propeller wash and a free jet and also analysed the found values for β_{lz}. His main conclusion was that although there are similarities, jets cannot be used to calculate the stability of a propeller wash and vice versa. Stones moved at a significant higher value of the critical flow velocity with a jet than with propeller wash, most probably because of the higher turbulence caused by thrusters compared to a jet. He also found much higher values for β_{lz} in his experiments: β_{lz} = 6.8 for flow produced by bow thrusters and β_{lz} = 1.3 for jets.

The influence of turbulence is implicitly incorporated in this value of the Izbash coefficient. It is however also possible to explicitly mention the turbulence influence in an Izbash-like function, generally used to calculate the strength of a bed under attack of propeller wash (Verhagen, 2012):

$$u_{cr} = \sqrt{\frac{2k_{slope} \cdot g\Delta D_{50}}{0.47(1+3r_t)^2}} \tag{A.20}$$

The turbulence in a free jet flow can be derived from Figure 2..

The influence of a bed slope is also included in Eq. (A.20) with the slope correction factor k_{slope}, which becomes 1 for a flat bed (Schiereck, 2004). A distinction is made between the flow parallel to the slope (so 'downhill') and perpendicular to the sloping surface.

$$k_{slope,//} = \frac{\sin(\varphi - \alpha_{sl})}{\sin\varphi} \tag{A.21}$$

$$k_{slope,\perp} = \sqrt{1 - \frac{\sin^2\alpha_{sl}}{\sin^2\varphi}} \tag{A.22}$$

With φ = angle of internal friction [deg] and α_{sl} = slope angle [deg]. When the flow is reverse ('uphill'), the bed becomes more stable and the inverse value of k_{slope} should be used.

With k_{slope} = 1 and r_t = 0.2, Eq. (A.20) equals Eq. (A.19) for a value of the Izbash coefficient of β_{lz} = 1.2. This is close to the value Van Veldhoven found.

A.3.2 Jongeling and Hofland

Because the Shields parameter is based on uniform flow, Jongeling, et al (2003) introduced a different mobility parameter. Although with the same concept, it is now mainly based on the turbulent kinetic energy:

$$\theta_{WL} = \frac{\left(\bar{u} + \alpha\sqrt{k_t}\right)^2}{\Delta g D_{50}} \tag{A.23}$$

With α as an empirical turbulence factor, with an originally proposed value of α = 6, but later studies proposed a value of about α = 3.5 (Hoan, et al., 2007) (van de Leur, 2010). Note that this parameter cannot be directly compared to the Shields parameter; in fact, the stability parameter θ_{WL} is determined with an Izbash-type of equation. An approximation of the critical value of $\theta_{WL,cr}$ = 4.4 (Hoan, et al., 2007), which corresponds remarkably well with the found values for the general Izbash coefficient.

Hofland (2005) argued that a characteristic length scale L_m should be incorporated in Eq. (A.23), leading to:

$$\theta_H = \frac{\max\left(\langle \bar{u} + \alpha\sqrt{k_t}\rangle_{L_m} \frac{L_m}{y}\right)^2}{\Delta g D_{50}} \tag{A.24}$$

With L_m the Bakhmetev mixing length, to be determined with:

$$\frac{L_m}{y} = \kappa\sqrt{1 - \frac{y}{h}} \tag{A.25}$$

And with y the vertical distance of the turbulence to the bed [m] and κ = 0.41 as the Von Karman constant. Not that the Hofland mobility parameter is again not to be directly substituted for the other mobility parameters. The critical value is found to be about θ_H = 0.5 (Hoan, et al., 2007).

The use of θ_{WL} or θ_H has the advantage that these parameters are still valid in the stagnation point of an impinging jet, where the average velocity is zero, in contrast to the original Shields of Izbash parameter.

A.4 Sediment transport

This chapter provides extra information to section 2.4 Sediment transport.

A.4.1 Sediment transport formulae

Wilson (1987) followed a similar approach as Bagnold, but argued that the velocity distribution in the shear layer should be included in the determination of S_b. With relative large grains, the sheared layer thickness δ_b is much larger than the viscous sub-layers. Therefore, the fluid motion in the sheet flow is turbulent. Assuming a velocity profile according to:

$$u = \frac{2u_*}{\kappa}\sqrt{\frac{y}{2\delta_b}} \tag{A.26}$$

Substituting this expression in Eq. (2.69) and solving the integral gives:

$$S_b = \frac{1.5{u_*}^3}{\kappa g \Delta \tan\varphi} \tag{A.27}$$

Using the known values of κ = 0.41 and tan φ = 0.32, Eq. (A.27) can be rewritten as (Visser, 1995):

$$S_b = \frac{11.8{u_*}^3}{g\Delta} = 11.8\sqrt{(g\Delta {D_{50}}^3)}\theta^{1.5} \tag{A.28}$$

This shows a remarkable agreement with the data used by Meyer-Peter and Müller (1948) to find their expression, which will be discussed later.

Van Rijn (1984) used the characteristic saltation movements to determine his expression for the bed-load transport, which he tested for numerous experimental data:

$$S_b = 0.053\sqrt{(g\Delta {D_{50}}^3)}\frac{T^{2.1}}{{D_*}^{0.3}} \tag{A.29}$$

This approximation is also found to a have relative good agreement with the measured values during a dike breach by Visser (1995), although the agreement was less good than with using Eq. (2.73).

Paintal (1971) performed test similar to Shields, but now with the focus on sediment transport instead the threshold of motion. For values of the Shields parameter larger than the critical value, he found the following relation for the total sediment transport:

$$S = 13\sqrt{(g\Delta {D_{50}}^3)}\theta^{2.5} \tag{A.30}$$

Meyer-Peter and Müller (1948) found a relation, purely based on experimental results, for only the bed-load transport:

$$S_b = 8\sqrt{(g\Delta {D_{50}}^3)}(k_{MPM}\theta - 0.047)^{1.5} \tag{A.31}$$

With as a coefficient the ratio between the overall roughness and grain roughness determined by the D_{90}, expressed by:

$$k_{MPM} = \frac{C_{ch}}{C_{ch,s,D90}} \tag{A.32}$$

The value of 0.047 in Eq. (A.31) should not be seen as a substitute of θ_{cr}, as Eq. (A.31) is not valid for values of θ close to incipient motion. With such small values, the main transport mechanism is the saltation of grains, and not a sheet flow to which the formula applies. The value of 0.047 is simply an extrapolation of the found data.

Wilson (1987) argued that the value of k_{MPM} is close to one and the value of 0.047 can be neglected with high values of θ. With these assumptions, Eq. (A.31) receives the same form as Eq. (A.28), only with a different multiplication factor. However, he found that using a factor of the theoretically based 11.8 still gives good results with the found experimental data. He preferred to apply the theoretically based formula instead of the empirical found expression.

Appendix B Scaling and experimental set-up

B.1 Scale scenario analysis

There are three commonly used scale scenarios: Froude, Reynolds and linear scaling. The difference between these three scenarios is in fact the scaling of time. If the scale factor for the length is taken as the base scale factor, in which all other factors are expressed, the difference between the scaling scenarios is as follows:

Froude: $n_t = \sqrt{n_L}$
Reynolds: $n_t = {n_L}^2$
Linear: $n_t = 1$

This implies the following for the scale factor for velocity:

Froude: $n_u = \sqrt{n_L}$
Reynolds: $n_u = \frac{1}{n_L}$
Linear: $n_u = n_L$

Whether the scale scenario leads to scaling effects is discussed for each scenario separately. To determine the scale effect, the theoretical and desired scale factor has to be known. The theoretical scale factor is determined by the scale scenario and the dependency on the scaled dimensions (length and time), as provided in Section 3.1.2. The desired scale factor depends on the dimensions of the parameter – the desired scale factor for a dimensionless parameter is therefore always one. When there is a difference between the desired and theoretical scale, scale effects will occur. A scale effect is expressed as:

$$scale\ effect = \frac{desired\ scale}{theoretical\ scale}$$

B.1.1 Froude scaling

With a Froude scaled scenario, the velocity is scaled according to $n_u = \sqrt{n_L}$. With the desired scale, the Froude number is kept constant. This implies however that the turbulence indicator, the Reynolds number, has a scale effect. Other parameters can have a scale effect as well, as can be seen in Table B.1.

Many scale effects in Table B.1 are a ratio of n_{D50} and n_L. A logical first choice for the scaling of the grain diameter would therefore be $n_{D50} = n_L$. However, when the grain diameter will be scaled according to the length scale, some scale effects will still occur, as can be seen in Table B.2

Table B.1 – Scale effects with Froude scaling

	Parameter	Theoretical scaling	Desired scale	Scale effect
Soil	Grain diameter†	n_{D50}	n_L	n_L / n_{D50}
	Lam. permeability	n_{D50}^2	$\sqrt{n_L}$	$\sqrt{n_L} / n_{D50}^2$
	Turb. permeability	n_{D50}	n_L	n_L / n_{D50}
Ship	Trail velocity†	$\sqrt{n_L}$	$\sqrt{n_L}$	1
Jet	Pressure†	n_L	n_L	1
	Flow velocity	$\sqrt{n_L}$	$\sqrt{n_L}$	1
	Seepage velocity	n_L^m, m>0.5	$\sqrt{n_L}$	n_L^b, b<0
	Froude	n_L / n_{D50}	1	n_L / n_{D50}
	Reynolds	$n_{D50}\sqrt{n_L}$	1	$1/(n_{D50}\sqrt{n_L})$
Stability	Shields	n_L / n_{D50}	1	n_L / n_{D50}
	Critical Shields*	1	1	1
	Critical velocity*	$\sqrt{n_{D50}}$	$\sqrt{n_L}$	$\sqrt{n_L} / \sqrt{n_{D50}}$
Sedimentation	Fall velocity	$\sqrt{n_{D50}}$	$\sqrt{n_L}$	$\sqrt{n_L} / \sqrt{n_{D50}}$
Erosion	Erosion velocity	$n_{D50}^{0.8}$	$\sqrt{n_L}$	$\sqrt{n_L} / n_{D50}^{0.8}$
Sediment transport	Saltation height	$n_{D50}^{1.7}$	n_L	$n_L / n_{D50}^{1.7}$
	Saltation length	$n_{D50}^{1.6}$	n_L	$n_L / n_{D50}^{1.6}$
	Bagnold	$n_L^{1.5}$	$n_L^{1.5}$	1
	Wilson	$n_L^{1.5}$	$n_L^{1.5}$	1
	Van Rijn	$n_{D50}^{1.2}$	$n_L^{1.5}$	$n_L^{1.5} / n_{D50}^{1.2}$
	Paintal	$n_L^{2.5} / n_{D50}$	$n_L^{1.5}$	n_{D50} / n_L
	Meyer-Peter-M.	$n_L^{1.5}$	$n_L^{1.5}$	1
Scouring	Erosion parameter	n_L / n_{D50}	1	n_{D50} / n_L
	Scour depth	n_L^2 / n_{D50}	n_L	n_{D50} / n_L
	Scour radius	n_L^2 / n_{D50}	n_L	n_{D50} / n_L

† parameter that can be controlled
* for D_{50} > 6 mm in the scale model

Considering the results provided in Table B.2, some scale effects can be expected. For instance the scale effect of the Reynolds number is $1/n_L^{1.5}$, which means that the turbulence is underestimated; for example, the Reynolds number is 125 times too small with a scale factor of 1:25. However, as long as the scale model also displays a turbulent flow, the scale effects are assumed to be negligible. Turbulent flow is achieved with Re > 2000.

The scale effects for permeability and seepage velocity lead to a similar underestimation for these parameters. The permeability in the scale model is, with other words, too low. The seepage velocity is therefore also too low, although the scale effect cannot be given in terms of a scale factor. The erosion is also underestimated in the scale model.
Thanks to the correct scaling of the Shields parameter, the sediment transport formulae are almost all correctly scaled. This could also have been expected if the relation with the velocity to the third power, Eq. (3.26), is considered. Only the Van Rijn formula shows a scale effect, just as the saltations. These expressions of Van Rijn are however empirical, the question therefore arises if these scale effects indeed occur or if these deviations still fall within the accuracy margin.

Table B.2 – Scale effects with Froude scaling with $n_{D50} = n_L$

	Parameter	Theoretical scaling	Desired scale	Scale effect
Soil	Grain diameter†	n_L	n_L	1
	Lam. permeability	n_L^2	$\sqrt{n_L}$	$1/n_L^{1.5}$
	Turb. permeability	n_L	n_L	1
Ship	Trail velocity†	$\sqrt{n_L}$	$\sqrt{n_L}$	1
Jet	Pressure†	n_L	n_L	1
	Flow velocity	$\sqrt{n_L}$	$\sqrt{n_L}$	1
	Seepage velocity	n_L^m, m>0.5	$\sqrt{n_L}$	n_L^b, b<0
	Froude	1	1	1
	Reynolds	$n_L^{1.5}$	1	$1/n_L^{1.5}$
Stability	Shields	1	1	1
	Critical Shields*	1	1	1
	Critical velocity*	$\sqrt{n_L}$	$\sqrt{n_L}$	1
Sedimentation	Fall velocity	$\sqrt{n_L}$	$\sqrt{n_L}$	1
Erosion	Erosion velocity	$n_L^{0.8}$	$\sqrt{n_L}$	$1/n_L^{0.3}$
Sediment transport	Saltation height	$n_L^{1.7}$	n_L	$1/n_L^{0.7}$
	Saltation length	$n_L^{1.6}$	n_L	$1/n_L^{0.6}$
	Bagnold	$n_L^{1.5}$	$n_L^{1.5}$	1
	Wilson	$n_L^{1.5}$	$n_L^{1.5}$	1
	Van Rijn	$n_L^{1.2}$	$n_L^{1.5}$	$n_L^{0.3}$
	Paintal	$n_L^{1.5}$	$n_L^{1.5}$	1
	Meyer-Peter-M.	$n_L^{1.5}$	$n_L^{1.5}$	1
Scouring	Erosion parameter	1	1	1
	Scour depth	n_L	n_L	1
	Scour radius	n_L	n_L	1

† parameter that can be controlled
* for D_{50} > 6 mm in the scale model

B.1.2 Reynolds scaling

With the Reynolds scaling scenario, the aim is that the parameters of the scale model are chosen in such a way that the Reynolds number remains constant. This implies that the flow velocity increases with the scale factor, while the length decreases with the scale factor. All scale factors and effects are provided in Table B.3.

The scale effect for many parameters is a product of the length scale and the grain diameter scale factor. This means that the effect can only be made undone if the grain diameter is scaled up and the length is scaled down, or otherwise. A grain or nozzle diameter with prototype dimensions is not feasible in a lab.
It is therefore chosen to choose a scaling of the grain diameter of $n_{D50} = n_L$, in order to have no scale effects with the seepage velocity; although many scale effects will still occur, see Table B.4.

Table B.3 – Scale effects with Reynolds scaling

	Parameter	Theoretical scaling	Desired scale	Scale effect
Soil	Grain diameter†	n_{D50}	n_L	n_L/n_{D50}
	Lam. Permeability	n_{D50}^2	$1/n_L$	$n_L n_{D50}^{-2}$
	Turb. Permeability	n_{D50}	$1/n_L^2$	$n_L^{-2} n_{D50}$
Ship	Trail velocity†	$1/n_L$	$1/n_L$	1
Jet	Pressure†	$1/n_L^2$	$1/n_L^2$	1
	Flow velocity	$1/n_L$	$1/n_L$	1
	Seepage velocity	$1/n_{D50}$	$1/n_L$	n_{D50}/n_L
	Froude	$1/(n_L^2 n_{D50})$	1	$n_L^2 n_{D50}$
	Reynolds	1	1	1
Stability	Shields	$1/(n_L^2 n_{D50})$	1	$n_L^2 n_{D50}$
	Critical Shields*	1	1	1
	Critical velocity*	$\sqrt{n_{D50}}$	$1/n_L$	$n_L^{-1} n_{D50}^{-0.5}$
Erosion	Erosion velocity	$n_L^{-3} n_{D50}^{-0.7}$	$1/n_L$	$n_L^2 n_{D50}^{0.7}$
Sedimentation	Fall velocity	$\sqrt{n_{D50}}$	$1/n_L$	$n_L^{-1} n_{D50}^{-0.5}$
Sediment transport	Saltation height	$n_{D50}^{1.2}/n_L$	n_L	$n_L^2/n_{D50}^{0.8}$
	Saltation length	$n_{D50}^{0.7}/n_L^{1.8}$	n_L	$n_L^{2.8}/n_{D50}^{0.7}$
	Bagnold	$1/n_L^3$	1	n_L^3
	Wilson	$1/n_L^3$	1	n_L^3
	Van Rijn	$n_{D50}^{-0.9} n_L^{-4.2}$	1	$n_L^{4.2} n_{D50}^{0.9}$
	Paintal	$n_L^{-5} n_{D50}^{-1}$	1	$n_L^5 n_{D50}$
	Meyer-Peter-M.	$1/n_L^3$	1	n_L^3
Scouring	Erosions param.	$n_L^{-1} n_{D50}^{-0.5}$	1	$n_L \sqrt{n_{D50}}$
	Scour depth	$n_{D50}^{-0.5}$	n_L	$n_L \sqrt{n_{D50}}$
	Scour radius	$n_{D50}^{-0.5}$	n_L	$n_L \sqrt{n_{D50}}$

† parameter that can be controlled
* for D_{50} > 6 mm in the scale model

The Reynolds scale scenario has the advantage, next to the equal Reynolds number, that the seepage velocity does not show scale effects, as was showed in Table B.4. On the other hand, the scale effects for the Shields mobility parameter shows a high overestimation, with as a result high scale effects for the sediment transport parameters. The scale effects of the saltations and Van Rijn can be controlled if the critical Shields value is adapted to the scale effects of the Shields number, but large scale effects still occur with the other formulae.
Besides these unwanted scale effects, the Reynolds scale scenario is practically almost impossible. Since the length parameters are scaled down, so the process can be modelled in a laboratory, the velocity should be scaled up with the same scale factor. This means for instance that the modelled trail velocity of 0.5 m/s of the prototype increases to 12.5 m/s with a scale factor of 25. It is quite impossible to move a cart with velocities of this order of magnitude. Moreover, jet velocities will increase to a value where undesired effects, such as cavitation, will probably occur. The Reynolds scale scenario is therefore not considered as a viable option.

Table B.4 – Scale effects with Reynolds scaling with $n_{D50} = n_L$

	Parameter	Theoretical scaling	Desired scale	Scale effect
Soil	Grain diameter†	n_L	n_L	1
	Lam. Permeability	n_L^2	$1/n_L$	$1/n_L^3$
	Turb. Permeability	n_L	$1/n_L^2$	$1/n_L^3$
Ship	Trail velocity†	$1/n_L$	$1/n_L$	1
Jet	Pressure†	$1/n_L^2$	$1/n_L^2$	1
	Flow velocity	$1/n_L$	$1/n_L$	1
	Seepage velocity	$1/n_L$	$1/n_L$	1
	Froude	$1/n_L^3$	1	n_L^3
	Reynolds	1	1	1
Stability	Shields	$1/n_L^3$	1	n_L^3
	Critical Shields*	1	1	1
	Critical velocity*	$\sqrt{n_L}$	$1/n_L$	$1/n_L^{1.5}$
Erosion	Erosion velocity	$1/n_L^{3.7}$	$1/n_L$	$n_L^{2.7}$
Sedimentation	Fall velocity	$\sqrt{n_L}$	$1/n_L$	$1/n_L^{1.5}$
Sediment transport	Saltation height	$n_L^{0.20}$	n_L	$n_L^{0.80}$
	Saltation length	$1/n_L^{1.1}$	n_L	$n_L^{2.1}$
	Bagnold	$1/n_L^3$	1	n_L^3
	Wilson	$1/n_L^3$	1	n_L^3
	Van Rijn	$1/n_L^{5.1}$	1	$n_L^{5.1}$
	Paintal	$1/n_L^6$	1	n_L^6
	Meyer-Peter-M.	$1/n_L^3$	1	n_L^3
Scouring	Erosions param.	$1/n_L^{1.5}$	1	$n_L^{1.5}$
	Scour depth	$1/\sqrt{n_L}$	n_L	$n_L^{1.5}$
	Scour radius	$1/\sqrt{n_L}$	n_L	$n_L^{1.5}$

† parameter that can be controlled
* for D_{50} > 6 mm in the scale model

B.1.3 Linear

A linear scale scenario means that both velocity and length are scaled according to the same scale factor, see also Table B.5. With $n_{D50} = n_L$, the scale effects applied to the linear scenario are as provided in Table B.6.

The linear scale scenario does not show any scale effects for the flow velocity and length diameters. On the other hand, the critical and fall velocity of a grain are overestimated, while the Shields mobility parameter is underestimated, which lead to inaccurate outcomes of the tests. All sediment transport parameters show a scale effect as well.

Table B.5 – Scale effects with linear scaling

	Parameter	Theoretical scaling	Desired scale	Scale effect
Soil	Grain diameter†	n_{D50}	n_L	n_L/n_{D50}
	Lam. Permeability	n_{D50}^2	n_L	n_L/n_{D50}^2
	Turb. Permeability	n_{D50}	n_L^2	n_L^2/n_{D50}
Ship	Trail velocity†	n_L	n_L	1
Jet	Pressure†	n_L^2	n_L^2	1
	Flow velocity	n_L	n_L	1
	Seepage velocity*	n_L^m, m>1	n_L	n_L^b, b<0
	Froude	n_L^2/n_{D50}	1	n_{D50}/n_L^2
	Reynolds	$n_L n_{D50}$	1	$n_L^{-1} n_{D50}^{-1}$
Stability	Shields	n_L^2/n_{D50}	1	n_{D50}/n_L^2
	Critical Shields*	1	1	1
	Critical velocity*	$\sqrt{n_{D50}}$	n_L	$n_L/\sqrt{n_{D50}}$
Erosion	Erosion velocity	$n_L^3/n_{D50}^{0.7}$	n_L	$n_{D50}^{0.7}/n_L^2$
Sedimentation	Fall velocity	$\sqrt{n_{D50}}$	n_L	$n_L/\sqrt{n_{D50}}$
Sediment transport	Saltation height	$n_L n_{D50}^{1.2}$	n_L	$1/n_{D50}^{1.2}$
	Saltation length	$n_L^{1.8} n_{D50}^{0.7}$	n_L	$n_{D50}^{-0.7} n_L^{-0.8}$
	Bagnold	n_L^3	n_L^2	$1/n_L$
	Wilson	n_L^3	n_L^2	$1/n_L$
	Van Rijn	$n_L^{4.2}/n_{D50}^{0.9}$	n_L^2	$n_{D50}^{0.9}/n_L^{2.2}$
	Paintal	n_L^5/n_{D50}	n_L^2	n_{D50}/n_L^3
	Meyer-Peter-M.	n_L^3	n_L^2	$1/n_L$
Scouring	Erosions param.	$n_L/\sqrt{n_{D50}}$	1	$\sqrt{n_{D50}}/n_L$
	Scour depth	$n_L^2/\sqrt{n_{D50}}$	n_L	$\sqrt{n_{D50}}/n_L$
	Scour radius	$n_L^2/\sqrt{n_{D50}}$	n_L	$\sqrt{n_{D50}}/n_L$

† parameter that can be controlled

* for D_{50} > 6 mm in the scale model

B.1.4 Conclusions

The Froude scale scenario is considered to be the best option of the three possible scale scenarios, although scale effects will still occur. The underestimation of the Reynolds number is not considered a problem as long as the flow regime remains turbulent (Re > 2000). The underestimation of the permeability and seepage velocity may affect the processes of the intrusion of the jet. An underestimation of the permeability implies an overestimation of the radial flow velocity. This should be taken into account when analysing the results of the tests, but can also be anticipated for with the set-up of the test configurations. This is discussed in Chapter 3.1.4.

When the particle diameter in the scale model is smaller than 6 mm, the critical Shields value will show some scale effects. This scale effect can however not be expressed in a value of n_L due to the nature of the critical Shields value. This scale effect will also influence other parameters, such as some sediment transport formulae en the erosion velocity. The scale effects of critical velocity depends quantitatively on the applied scale value of the test, just as the seepage velocity, see Chapter 3.1.4.

Table B.6 – Scale effects with linear scaling $n_{D50} = n_L$

	Parameter	Theoretical scaling	Desired scale	Scale effect
Soil	Grain diameter†	n_L	n_L	1
	Lam. Permeability	n_L^2	n_L	$1/n_L$
	Turb. Permeability	n_L	n_L^2	n_L
Ship	Trail velocity†	n_L	n_L	1
Jet	Pressure†	n_L^2	n_L^2	1
	Flow velocity	n_L	n_L	1
	Seepage velocity*	n_L^m, m>1	n_L	n_L^b, b<0
	Froude	n_L	1	$1/n_L$
	Reynolds	n_L^2	1	$1/n_L^2$
Stability	Shields	n_L	1	$1/n_L$
	Critical Shields*	1	1	1
	Critical velocity*	$\sqrt{n_L}$	n_L	$\sqrt{n_L}$
Erosion	Erosion velocity	$n_L^{2.3}$	n_L	$1/n_L^{1.3}$
Sedimentation	Fall velocity	$\sqrt{n_L}$	n_L	$\sqrt{n_L}$
Sediment transport	Saltation height	$n_L^{2.2}$	n_L	$1/n_L^{1.2}$
	Saltation length	$n_L^{2.5}$	n_L	$1/n_L^{1.5}$
	Bagnold	n_L^3	n_L^2	$1/n_L$
	Wilson	n_L^3	n_L^2	$1/n_L$
	Van Rijn	$n_L^{3.3}$	n_L^2	$1/n_L^{1.2}$
	Paintal	n_L^4	n_L^2	$1/n_L^2$
	Meyer-Peter-M.	n_L^3	n_L^2	$1/n_L$
Scouring	Erosions param.	$\sqrt{n_L}$	1	$1/\sqrt{n_L}$
	Scour depth	$n_L^{1.5}$	n_L	$\sqrt{n_L}$
	Scour radius	$n_L^{1.5}$	n_L	$\sqrt{n_L}$

† parameter that can be controlled
* for D_{50} > 6 mm in the scale model

The erosion velocity also shows a scale effect: it is too low in the scale model. It is assumed that the erosion velocity is not the governing process; this is considered to be sediment transport process. An underestimation of the erosion should therefore not lead to the fact that the erosion will become the governing process. As long as this is not the case, the scale effect on the erosion velocity will not be considered to be an issue, although the scale effect should be borne in mind when analysing the results.

B.2 Applied scale

From section 3.1.3.1 Froude scale scenario followed that the permeability is lower than desired for a correct scaling of the seepage processes. This means that the seepage flow in the scale model is lower than desired. Therefore, the flow available for the radial wall jet, and thus the near-bed velocity, is too high. In fact, the seepage flow does not have a big influence and is therefore relatively unimportant; but it is particularly important that the radial jet flow is correctly scaled. In order to limit the scale effects, it can be chosen to alter (one of the) other parameters that have an influence on the seepage flow. As mentioned in Section 3.1.2.3, the seepage flow depends on the jet configuration (jet pressure, stand-off distance and nozzle diameter), gravity, porosity, grain diameter and the viscosity.

Adjusting the gravity or viscosity leads to unwanted effects on the stability, sedimentation and flow processes and is therefore rejected. A relative larger grain diameter, no longer scaled with the length scale factor of 1:30, is a possibility in the case of sheet flow. It is shown that the sediment transport processes of sheet flow does not depend on the grain diameter. However, for lower flow velocities, the sheet flow does not occur and the grains are individually transported in saltating movement. This process depends on the grain diameter, though, and will therefore have a scale effect. It is consequently chosen to reject the option with an adjusted grain diameter. An adjustment of the jet configuration is a possibility, as this decreases the entire flow. The seepage flow is still not correctly scaled in that case, but the radial jet flow is.
The porosity influences the permeability of granular material, and therefore the seepage flow. It can be assumed that the packing in the prototype is close to the maximum, meaning a minimum porosity (Van der Schrieck, 2012). A higher porosity has a positive effect on the seepage flow. The seepage flow is underestimated in the scale model, so there should be a higher porosity in the scale model to overcome this scale effect. The only other parameter influenced by the porosity is the erosion velocity. However, the erosion velocity does already have a scale effect as it is too low in the scale model. An increase of the porosity increases the erosion velocity, and therefore decreases the scale effect. It is therefore chosen to apply a scale model with a loose packing and a high porosity.

Because the porosity is not easy to determine, it is assumed that the minimum and maximum values are respectively given by n = 0.30 and n = 0.45, as was already mentioned in section 2.1.1. However, a loose porosity is difficult to reach in the scale model, as always some compaction occurs when the initial bed profile is created. Therefore, an initial porosity for the scale model is chosen somewhat smaller than the loose porosity, namely n = 0.4. This leads to the scale effects as provided in Table B.7,

where the seepage flow is approximated with the values of Table 3. and with u_0 = 8 m/s and a SOD = 4.5 m in the prototype situation.

Table B.7 – Scale effects for the seepage flow with varying porosity

Parameter		**Prototype**	**Scale model n = 0.3**		**Scale model n = 0.4**	
		Value	*Value*	*Scale effect*	*Value*	*Scale effect*
dp/dy	[-]	1.21	1.21	1	1.21	1
a_f	[m/s]	2.7	0.0030	164	0.0098	51
b_f	[m^2/s^2]	0.057	0.0019	1	0.0052	0.36
u_f	[m/s]	0.25	0.0036	12.6	0.012	4.0
Q_f	[m^3/s]	0.42	6.72×10^{-6}	12.6	2.14×10^{-5}	4.0
Q_{tot}	[m^3/s]	5.70	0.001155	1	0.001155	1
Q_r	[m^3/s]	5.28	0.001071	0.93	0.001134	0.94

It can be concluded from Table B.7 that the adjustment of the porosity strongly decreases the scale effect on the laminar permeability, although it introduces a scale effect on the turbulent part of the permeability. Altogether, the increase of the porosity decreases the scale effect on the seepage flow. The influence on the scale effect of the radial jet flow is much smaller, though. The scale effect of the radial jet flow is however close to unity, and is therefore considered to be acceptable.

Another way to eliminate the scale effects for seepage flow is the application of the Reynolds scale scenario. With this scenario, all flow velocity are increased with a factor 30, and the stagnation pressure gradient is increased with 30^3 to obtain a correctly scale seepage flow velocity. This indeed means a jet flow velocity of 240 m/s with a u_0 = 8 m/s. Flow velocities with this order of magnitude are not possible with the given equipment, let alone that a high-pressure jet behaves differently compared to low pressure. This is not considered to be a viable alternative.

It is therefore chosen to accept the small scale effects occurring with the Froude scale of 1:30 on the radial jet flow.

B.3 Experimental set-up

This chapter of the appendix provides extra information about the set-up of the scale model tests. First, the possible wall effects and the implications of a symmetry wall set-up are discussed. Then some extra information about the used cameras during the tests is given. Third, the determination of the jet pressure and the contraction coefficient for each jet configuration that is used in the scale model tests is provided. Finally, the process of data acquisition with a laser beam is explained.

B.3.1 Wall effects

A water tank is not an accurate reflection of the environment of the prototype, namely the bottom of the sea. After all, the sea does not have an impermeable wall or bottom. The walls or bottom of the water tank will therefore have an effect on the scale model and influence the test results. It is obvious that these effects should be limited as much as possible.

Vertical walls reflect an incoming flow, which will lead to the fact that flow directed away from the scaled rock cover will be reflected, back to the scale model. This reflected flow would clearly not occur in the prototype. The flow velocity at the side walls should therefore be so low that the wall effects on the stability or erosion of the scale model are negligible.
The impermeable tank bottom will also have an effect, as impinging flow will be dispersed in radial direction. The prototype is located on top of sand, in which a penetrating jet flow will erode the soil. However, the erosion of sand is unwanted as it compromises the stability of the pipe or cable. It should therefore be prevented that the jet flow penetrates to the sand bottom under the rock cover. In the scale model, this means that it should be prevented that the jet flow reaches the tank bottom. “Wall” effects from the bottom on the model are therefore implicitly non-existing.

The wall effects are more pronounced when a set-up with a symmetry wall is chosen. Firstly, the side wall exerts a friction force on the jet flow that can influence the flow velocity and pattern. The wall is also an extra support for the grains: it is possible that eroded grains will pile up against the wall, which is not possible in the prototype. It therefore influences the local scour depth close to the wall. Also, the jet flow is highly turbulent in all three directions, so turbulent fluctuating flows or eddies are reflected by the wall. On the other hand, when no symmetry wall is present, these fluctuations will enter the domain from the other side of the virtual symmetry plane, where the other half of the jet is applied. So it can also be said that these reflections of the flow are a good representation of the reality.

The biggest effects occur because of the scaling of half the jet by a whole, circular jet. To determine the required diameter of the whole jet, one can choose to let the jet flow velocity be correctly scaled. With a correct scaling of the jet pressure as well, the jet flow area should be equal for the whole jet as for the half, regularly scaled, jet. This means:

$$D_{0_{whole}} = \sqrt{\frac{1}{2}{D_{0_{half}}}^2} = \sqrt{\frac{1}{2}}D_{0_{half}} = \sqrt{\frac{1}{2}}\frac{D_{0_{proto}}}{n_L} \tag{B.1}$$

It is obvious that a fully circular jet has a different entrainment process, and therefore flow profile, than half a jet (actually, the modelled configuration is jetting with two adjacent jets). It is therefore important that the nozzle is correctly placed and directed against the wall. If this is the case, it is assumed that no entrainment takes place at the wall, and the flow development in the case of the whole nozzle is similar to the case with the 'half nozzle'. Otherwise wall effects will occur as is described next.

The modelled uniform flow velocity development is described by Eq. (2.12), here repeated:

$$u_u = \frac{1}{2}\sqrt{\frac{k_j}{2}}u_0\frac{D_0}{s} \quad for\ s > 6D_0$$

If the scale factor for the jet distance is kept according to the regular scale rules, the use of a whole jet introduces scale effects in the flow velocity. It is however desired that the flow velocity is correctly scaled, which is the case if the ratio D_0/SOD is kept constant. The jet distance experiences therefore a similar scale effect as the diameter:

$$SOD_{whole} = \sqrt{\frac{1}{2}}SOD_{half} = \sqrt{\frac{1}{2}}\frac{SOD_{proto}}{n_L} \tag{B.2}$$

With accepting this scale effect for the stand-off distance, an equal value of u_0 and D_0/SOD is acquired, so there will be no scale effects of the erosion parameter E_c. However, the flow velocity of the modelled radial wall jet will experience some scale effects. The expression to determine the radial wall jet velocity is repeated here:

$$u_{u,r} = u_0\sqrt{\frac{f_2{D_0}^2}{8f_1\alpha_{mom}r^2 + 4{D_0}^2{N_3}^2\left(\frac{1}{f_2} - 4f_1\alpha_{mom}\right)}} \quad for\ s > 6D_0$$

The coefficient N_3 depends on the ratio D_0/SOD and is thus constant. When it is desired to correctly scale the radial flow velocity, a similar substitution of scale effects can be performed as with the SOD. That is, if the radial distance has the same scale factor as the jet diameter, the velocity is correctly scaled. This means a similar scale effect for the radial distance as well:

$$r_{whole} = \sqrt{\frac{1}{2}} r_{half} = \sqrt{\frac{1}{2}} \frac{r_{proto}}{n_L} \quad \text{(B.3)}$$

Since the scour depth and radius are a function of the SOD, these parameters will have the same scale effect as well. This means effectively that all length dimensions will have a scale effect of √2 if the symmetry wall nozzle is not placed and directed in the correct way.

B.3.2 Test equipment

The submerged pump has a power of 220W, which means a maximum pressure of 0.5 bar, or a maximum flow of 6000 L/hrs. These maximum values can also be found in the pump curve, provided in Figure B.1.

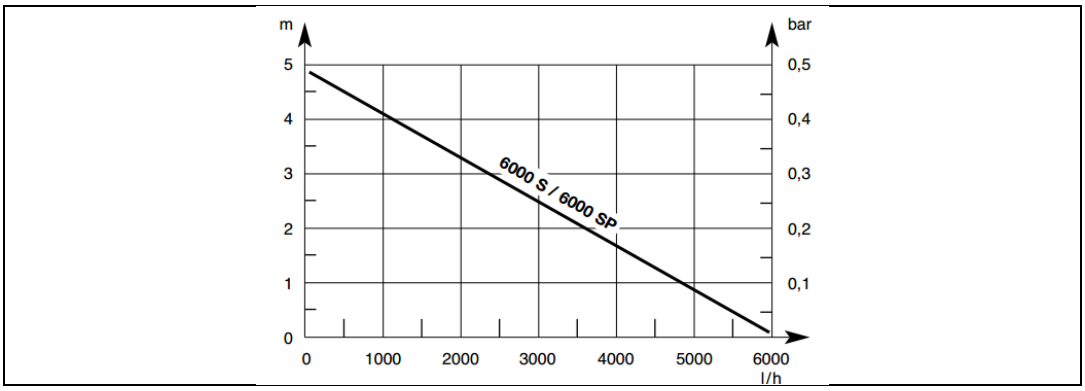

Figure B.1 – Pump curve of the used Gardena© submerged pump 6000

A detachable submerged hi-res camera, a so-called GoPro, is attached to the steel frame, so it can provide a top view of the experiments. This camera has the same velocity of the jet, so the jet remains in a fixed position with the top view. Another camera is placed outside the water tank, filming through the transparent wall. Because this camera provides a fixed view of the tank, the jet passes sideways through the image. These cameras help to observe the occurring processes and to give the test qualitative results.

The scale model is placed on a wooden board to be visible through the transparent wall from top to bottom (the transparent wall starts only a few centimetres above the bottom of the tank). This also enables the possibility to place a support piece at both ends of the wooden board. These support pieces have the same contour as the scale model requires, so it can be easily used to determine the outline of the scaled rock cover. It also creates two locations at both ends of the model to hover the jet in between two consecutive test runs, without affecting the model.

B.3.3 Jet pressure determination

A Rosemount pressure meter with a measurement range of 0 – 0.075 bar is connected to the jet system to determine the jet pressure p_j. The flow rate can be controlled by a garden hose system with a valve and T-junction, located directly after the pump. This system was already described in section 3.2.2. Four configurations are used for the tests,

with the description provided in Table B.8. The flow rate Q_0 can be determined by filling a basket with a known volume in a measured amount of time.

Table B.8 – Possible pump configurations

1	Valve open, no T-junction
2	Valve half open, no T-junction
3	Valve open, T-junction connected to system but no flow through bifurcation
4	Valve open, T-junction connected to system with flow through bifurcation

With the measured values of Q_0 and p_j, the contraction coefficient C_d can be determined for each type of jet. A jet has a contraction when the jet area A_j is smaller than the area of the nozzle; the contraction coefficient C_d is defined as the ratio between these two areas. The diameter corresponding to the circular jet area A_j is defined as the initial jet diameter D_0.

The obtained outcomes are given in Table B.9, while the values corresponding to the prototype situation are provided in Table B.10. Jet configurations that are not used in the tests are not included in the table. Next to the measured jet pressure and corresponding flow velocity, the flow rate and hydraulic power are provided as well.

Table B.9 – Outcomes of the pressure determinations, scale model values

Nozzle type	**Config.**	Q_0 [dm³/s]	p_j [bar]	u_0 [m/s]	P_j [W]	C_d [-]	A_j [cm²]	D_0 [cm]
Single circular nozzle								
Straight PVC pipe D_{noz} =1.36 cm	1	0.33	0.028	2.4	0.92	0.95	1.4	1.3
	2	0.30	0.023	2.1	0.69	0.95	1.4	1.3
	3	0.17	0.008	1.2	0.14	0.95	1.4	1.3
	4	0.12	0.004	0.9	0.04	0.95	1.4	1.3
Straight hose D_{noz} = 1.6 cm	1	0.38	0.025	2.2	0.95	0.85	1.7	1.5
	2	0.33	0.019	1.9	0.62	0.85	1.7	1.5
Inclined jet β_j = 0 deg D_{noz} = 1.6 cm	1	0.33	0.038	2.8	1.2	0.60	1.2	1.2
	2	0.29	0.029	2.4	0.85	0.60	1.2	1.2
	3	0.17	0.010	1.4	0.17	0.60	1.2	1.2
Inclined jet β_j = 30 deg D_{noz} = 1.6 cm	1	0.34	0.034	2.6	1.2	0.65	1.3	1.3
	2	0.29	0.025	2.2	0.72	0.65	1.3	1.3
	3	0.17	0.009	1.3	0.15	0.65	1.3	1.3
	4	0.12	0.004	0.9	0.05	0.65	1.3	1.3
Inclined jet β_j = 60 deg D_{noz} = 1.6 cm	1	0.34	0.029	2.4	1.0	0.70	1.4	1.3
	2	0.28	0.020	2.0	0.56	0.70	1.4	1.3
Adjusted nozzle designs								
3 nozzles D_{noz} = 4.5 mm	1	0.23	0.24[1]	7.0[1]	5.6[1]	0.70[1]	0.33[1]	0.37[1]
	3	0.16	0.12	4.8	1.9	0.70	0.33	0.37
7 nozzles D_{noz} = 4.5 mm	1	0.30	0.09	4.2	2.6	0.65	0.72	0.36
	3	0.17	0.03	2.4	0.47	0.65	0.72	0.36
10 nozzles D_{noz} = 4.5 mm	1	0.32	0.06	3.4	1.8	0.60	0.95	0.35
	3	0.17	0.02	1.8	0.27	0.60	0.95	0.35

[1] pressure was outside the reach of the meter, C_d assumed to be similar to config. 3

Especially the inclined jets show a relative large contraction. This is probably because the piece of garden hose that forms the nozzle is too short; the jet flow is not yet attached to the wall of the hose after the widening of the diameter. This process is illustrated in Figure B.2. It was already stated in chapter 2.2 Jetting that the length of the flow development region is about six times the jet diameter. This means that, with a diameter of the curved pvc pipe of 1.36 cm, the length of the piece of hose should be at least 8 cm long. This is however not possible due to limitations of the width of the water tank: the desired stand-off distance cannot be reached with such length of the nozzle.

The value of the pressure with the jet configuration with three nozzles and a high jet pressure could not be determined, as the value was out of the reach of the pressure meter. However, the contraction coefficient is assumed to be equal to the value corresponding to configuration 3 with the same nozzle design.

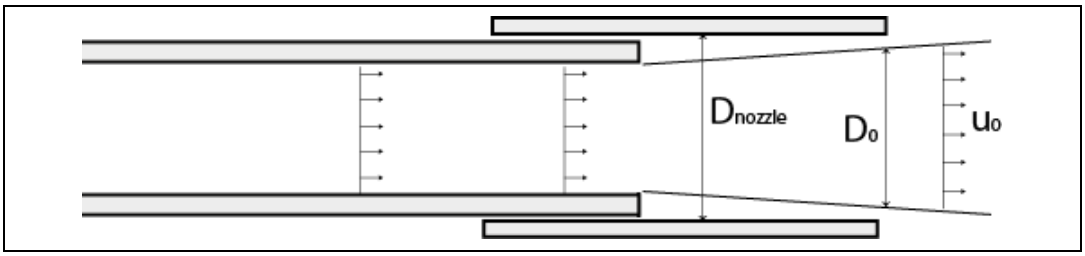

Figure B.2 – When the flow is not yet attached, the 'contraction' is higher

The values provided in Table B.9 are also graphically displayed in Figure B.3 and Figure B.4 for the situation with a single circular nozzle and an adjusted nozzle respectively.

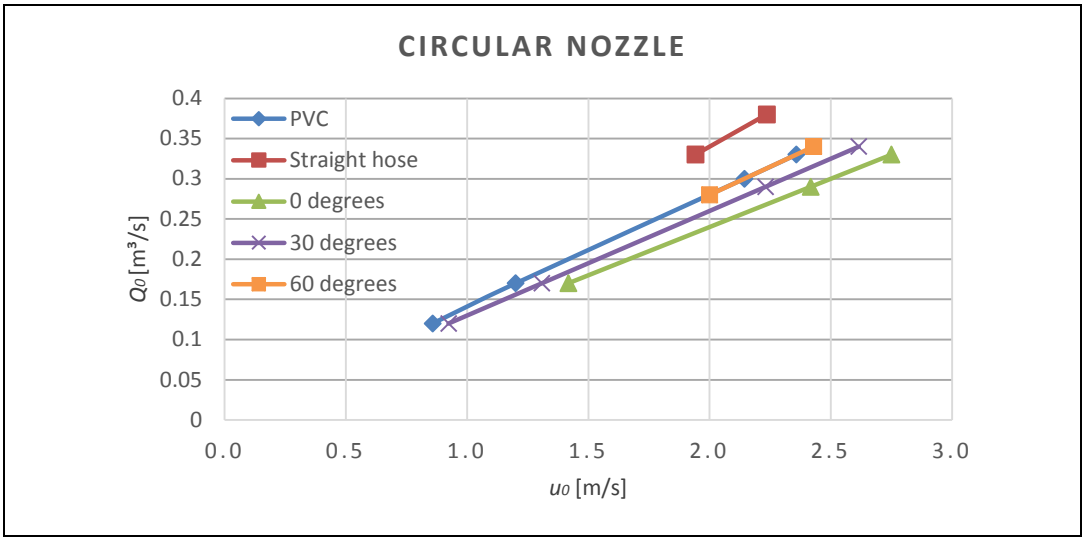

Figure B.3 – Initial flow velocity plotted against initial flow rate for a circular nozzle

However, these measured values of the pressure are obtained with the jet flowing out in open air. The difference between the nozzle and the surrounding medium is different with a submerged jet, when also some water pressure is present, depending on the water level in the tank. It is however assumed that the water flow of the 'free jet' equals the flow in the case of a submerged jet. If a higher accuracy is required, a flow or pressure meter will have to be attached to the jet system during the tests.

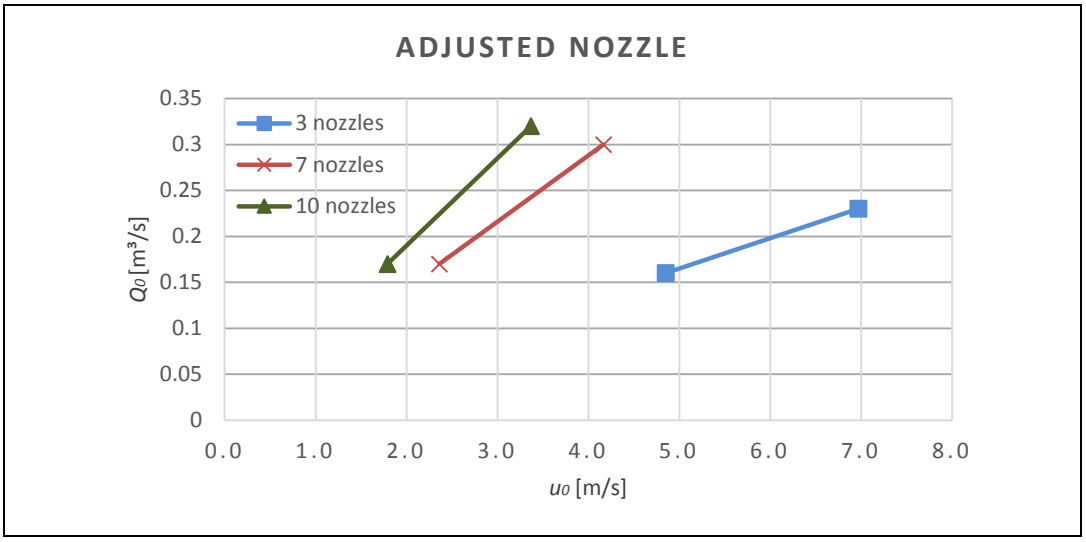

Figure B.4 – Initial flow velocity plotted against initial flow rate for an adjusted nozzle

Table B.10 – Outcomes of the pressure determinations, prototype values

Nozzle type	**Config.**	Q_0 [m³/s]	p_j [bar]	u_0 [m/s]	P_j [kW]	C_d [-]	A_j [m²]	D_0 [m]
Single circular nozzle								
Straight PVC pipe D_{noz} = 0.4 m	1	1.6	0.83	13	135	0.95	0.13	0.4
	2	1.5	0.69	12	100	0.95	0.13	0.4
	3	0.85	0.22	6.7	20	0.95	0.13	0.4
	4	0.57	0.11	4.7	6.5	0.95	0.13	0.4
Straight hose D_{noz} = 0.5 m	1	1.9	0.75	12	140	0.85	0.15	0.4
	2	1.6	0.57	11	90	0.85	0.15	0.4
Inclined jet θ_j = 0 deg D_{noz} = 0.5 m	1	1.6	1.1	15	185	0.60	0.11	0.4
	2	1.4	0.88	13	125	0.60	0.11	0.4
	3	0.85	0.30	7.8	25	0.60	0.11	0.4
Inclined jet θ_j = 30 deg D_{noz} = 0.5 m	1	1.7	1.0	14	175	0.65	0.12	0.4
	2	1.4	0.75	12	110	0.65	0.12	0.4
	3	0.84	0.26	7.2	20	0.65	0.12	0.4
	4	0.60	0.13	5.1	7.5	0.65	0.12	0.4
Inclined jet θ_j = 60 deg D_{noz} = 0.5 m	1	1.7	0.88	13	150	0.70	0.13	0.4
	2	1.4	0.60	11	85	0.70	0.13	0.4
Adjusted nozzle designs								
3 nozzles D_{noz} = 14 cm	1	1.1	7.3[1]	38[1]	830[1]	0.70[1]	0.030[1]	0.1[1]
	3	0.77	3.5	27	280	0.70	0.030	0.1
7 nozzles D_{noz} = 14 cm	1	1.5	2.6	23	380	0.65	0.065	0.1
	3	0.84	0.8	13	70	0.65	0.065	0.1
10 nozzles D_{noz} = 14 cm	1	1.6	1.7	18	270	0.60	0.086	0.1
	3	0.85	0.5	10	40	0.60	0.086	0.1

[1] pressure was outside the reach of the meter

B.3.4 Data acquisition

The measuring method with the use of a ruler as used in the preliminary tests is laborious and has a relatively low accuracy. It is therefore chosen to apply a different data acquisition method for the working method tests. A simple laser beam will be used to determine the bed profile for these tests. The laser is directed on a mirror which reflects the beam towards the bed, see also Figure B.5. The point where the laser reflects on the bed is visible as a green line. Because the laser beam is directed on the bed at an angle, differences in the bed level are visible as a horizontal displacement of the green reflection. This is illustrated in Figure B.6, which shows clearly that a change in the bed level will cause the laser beam to be reflected at a different point. A flat bed will cause a straight green line to occur, an irregular bed will create an irregularly curved green line. The most obvious angle of the laser beam is 45 degrees, at which the vertical and horizontal displacements are equal to each other.

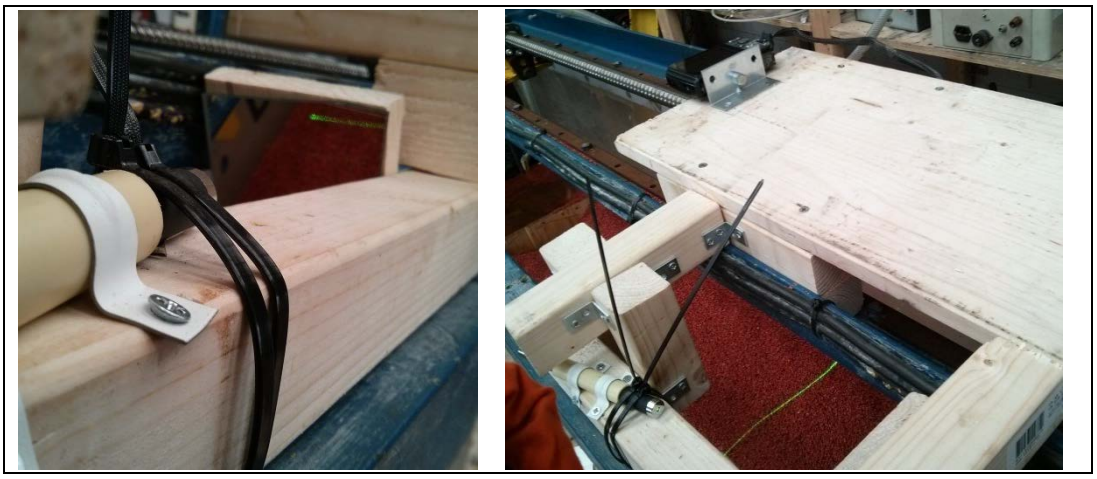

Figure B.5 – The laser beam is reflected towards the bed

A disadvantage of this method is that it is required to empty the water tank each time the bed level is measured. A transition from air to water will cause a refraction of the laser beam, which changes the angle of the beam. It was however observed that the filling or emptying of the tank had no influence on the bed profile.

A picture is taken of this green line at the three fixed measuring points, which will be processed to translate the irregularities into a cross section of the bed at the corresponding point. The three outcomes are combined to obtain the average profile.

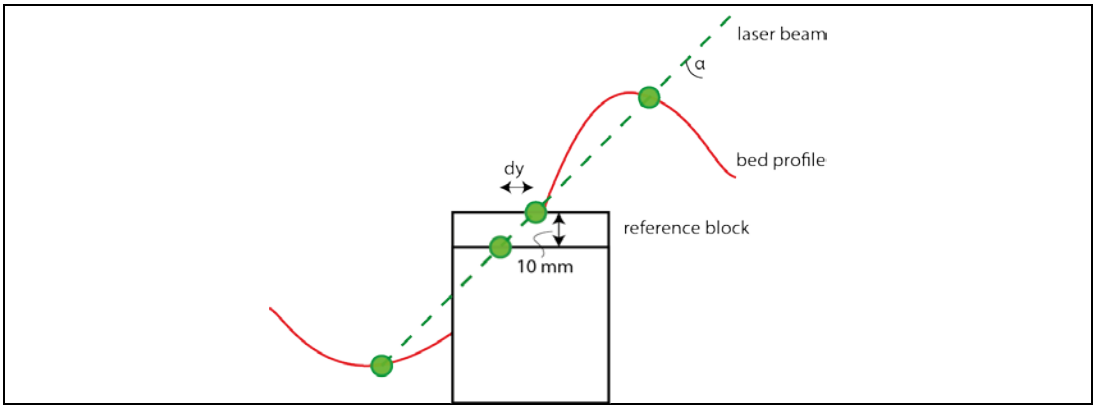

Figure B.6 – A vertical difference is translated to a horizontal displacement

Unfortunately, the width of the laser beam is not sufficient to cover the entire width of the tank. However, the focus of the study is only on the middle part, where the pipe is located. Moreover, if the bed level would change at the outer parts of the tank, the flow velocity at these points are of such a high value, that wall effects would probably occur. The bed profile of the scale model at these points is therefore not fully reliable and should have been neglected in the results anyway.

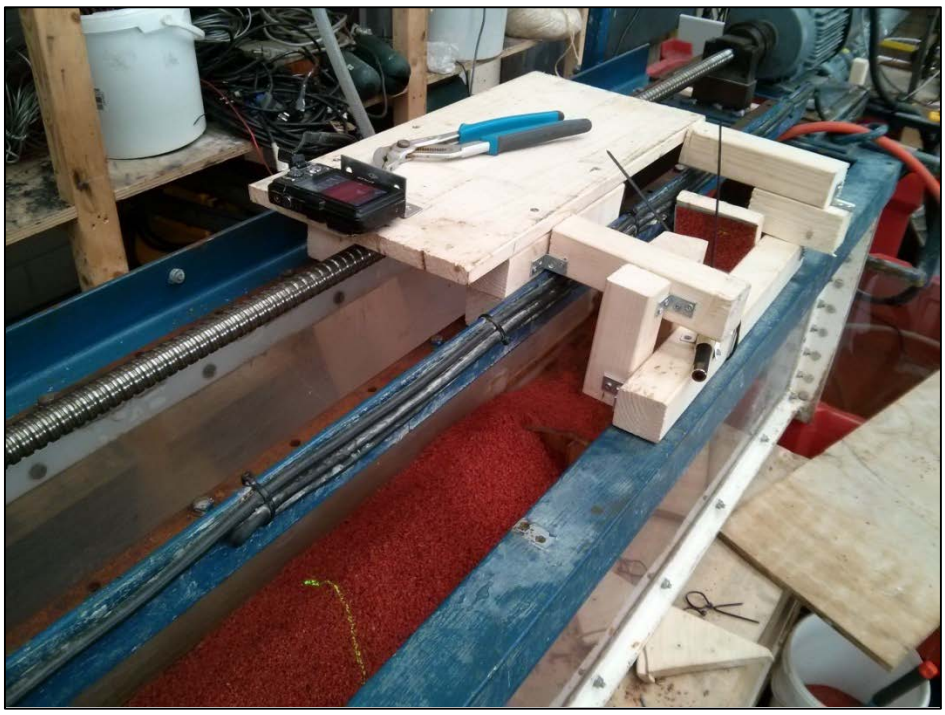

Figure B.7 – The laser beam data acquisition tool

A picture will be taken of the bed level before the test, the so-called initial bed level, and after each run. To compare each profile with each other, it is important that the laser is reflected on some kind of reference point, which remains in fixed position during the test. In this way, minor displacements of the profile, for instance due to a movement of the camera, can be adjusted. After all, the reference point should have the same value in each cross section. If the bed profile along the entire length of the laser line is

expected to be changed, a custom reference point can be placed in the scale model. If a known height difference is included in the reference block, the angle of the laser beam can be verified or determined by measuring the distance *dy*. This is also sketched in Figure B.6. The reference point should be placed on a location where its presence does not influence the sedimentation or erosion processes.

Appendix E Erosion model

E.1 Outcomes erosion model

The general overview of the erosion model set-up is described in section 6.1. However, running the erosion model according to the theory gives results than cannot be accepted without discussion. A possible reason is that the theory is based on empirical functions which applicability should be assessed before it is used. An analysis of the results and the possible adjustments of the model is performed in this appendix.

E.1.1 Maximum bed angle

The modelled profiles show a vertical slope shortly after the point of impingement, implying that the erosion velocity is higher than the trail velocity at the beginning of penetration. However, such a steep slope was not observed during the tests. Pictures taken during tests 1 and 2 are given in Figure E.1 and Figure E.2 respectively.

Figure E.1 – Observed penetration profile for p_j = 0.023 bar and v_{trail} = 0.07 m/s

Figure E.2 – Observed penetration profile for p_j = 0.008 bar and v_{trail} = 0.05 m/s

Because the jet pressure is about three times as large in the first test, the flow velocity in this test is about √3 as large, and therefore the Shields parameter a factor 3 larger as well. Even with a similar porosity, this would mean that the erosion velocity in the first test is about $3^{1.5} \approx 5$ times larger, whereas the trail velocity is only 1.4 times as large. Theoretically, the bed angle should therefore have been a lot larger in the first test. However, the observed bed angle is about equal and has a value that is remarkably close to the angle of repose φ. Multiple explanations could be given for this difference between the theory and the observed behaviour.

Firstly, the jet pressure may not be correctly determined. This is not likely, as this behaviour was observed in multiple tests. Moreover, the jet penetration in the first test is obviously higher (it reaches the bottom of the tank) than in the second test. The trail velocity has been determined multiple times, during both the execution of the test as in the recorded video. An incorrect determination of the test configurations is therefore rejected as explanation.
Another explanation could be that the jet actually penetrates the soil vertically, but the steep slope in front of the jet collapses, resulting in a bed angle equal to φ. This would mean that the soil is breached in front of the jet. This process does not seem to happen for two reasons. Firstly, the breach velocity is a soil characteristic and does not depend on the trail velocity. The occurring breach angle should therefore be different for a different trail velocity, however, the bed angle is similar for both trail velocities. Furthermore, a breaching process was only observed with a different test with v_{trail} = 0.02 m/s; the measured head-wall velocity was about similar with $v_{wall} \approx 0.02$ m/s. This would mean that the breach angle would be 90 degrees with $v_{trail} > 0.02$ m/s, which obviously did not occur in both tests. Finally, it was also observed in both tests that the jet impinged on the slope, and not 'before' the slope. A breaching or collapsing process of the soil can therefore not cause the observed bed slope.
Finally, it is remarkable that the bed angle remains about 45 degrees in the first test over almost the entire front side of the penetration profile. A gradual decrease of the bed angle, due to the decrease of the flow velocity of the jet, should have been expected.

Apparently, when considering all above, there is a governing factor in the erosion process that limits the maximum achievable bed angle. The reason for this limiting factor is not yet fully understood, but could be one of the following:

- The entrainment capacity of the jet is not sufficient to reach an erosion velocity as high as predicted by the theory. The soil is eroded layer by layer, at which stones are individually 'shot away' to make a saltation. It takes therefore time to erode multiple layers. It is possible that this development is not fast enough to 'reach' as much as the theoretically predicted number of stones. The erosion velocity is therefore limited by the entraining capacity of the jet. This would however not explain the penetrating behaviour of the jet with v_{trail} = 0.2 m/s, where the value of v_e was higher than $v_e > 0.07$ m/s. This means that a jet is indeed capable of reaching an erosion velocity that would cause a vertical slope in the tests of Figure E.1 and Figure E.2.
- The erosion theory is valid for a longitudinal flow, i.e. where the flow has the same direction as the bed slope. This is however not the case where the jet impinges on the soil: the flow direction is now perpendicular to the horizontal

bed. It was assumed that the eroding capability of the flow causes an immediate penetration, resulting in a flow in the same direction as the bed slope. However, it is possible that the eroding capability of the jet in the studied tests is not sufficient for an instant penetration: the jet is (partly) deflected in radial direction. Moreover, the jet flow is highly turbulent in the impingement zone, which also causes fluctuations in the flow direction. This would mean that the erosion processes in the zone of jet impingement are quite different than assumed in the theory, which can cause an inaccurate calculation of the erosion velocity.

Since the flow parameters such as the velocity, direction and turbulence in the impingement zone could not be determined during the tests, it is chosen to still apply the erosion theory of longitudinal flow. In order to correctly model the erosion according to the observed behaviour, a maximum bed angle is introduced. This is in fact a limitation of the erosion velocity, proportional to the trail velocity. The most logical value for this maximum bed angle would be the observed $\alpha_{bed,max} = \varphi = 45$ degrees. The modelled penetration profile with and without this limiting $\alpha_{bed,max}$ are provided in Figure E.3 for the situation with $p_j = 0.023$ bar and $v_{trail} = 0.07$ m/s.

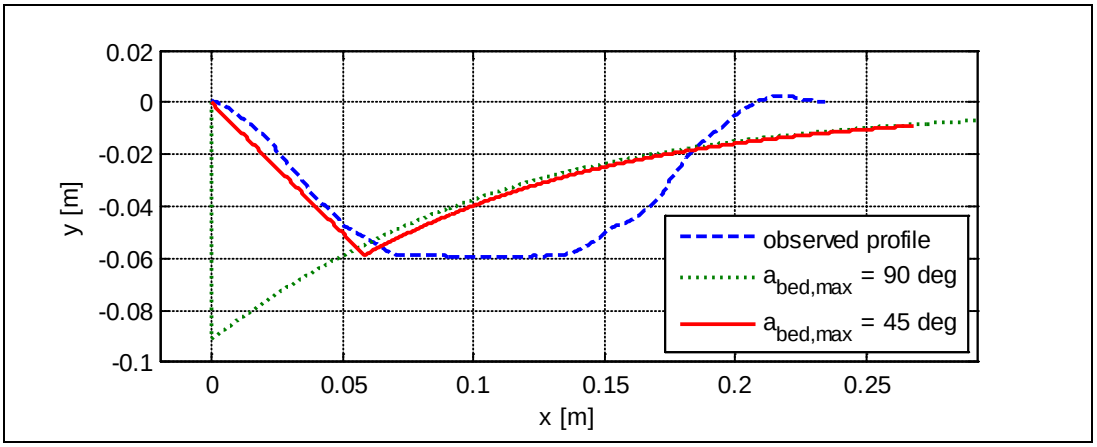

Figure E.3 – Profiles with $\alpha_{bed,max} = 90$ deg and $\alpha_{bed,max} = 45$ deg for Test 1

Note that the penetration depth in the observed model is limited due to the bottom of the tank. It shows that the assumption of the maximum bed angle gives a more accurate model, although the observed penetration depth is not yet reached. This can however be explained by the fact that the jet now impinges on a slope, which causes that a part of the jet flow is deflected forwards as well. As a result, stones are also eroded and transported in the same direction as the nozzle's movement, creating a small berm in front of the jet. This local increase of the bed level is also clearly visible in Figure E.1 and Figure E.2. The magnitude of this increase can be easily calculated by the distribution of an impinging flow (Battjes, 2002):

$$Q_{1,2} = \frac{1}{2} Q_0 (1 \pm \sin \alpha_{bed}) \qquad \text{(E.1)}$$

With $\alpha_{bed} = 45$ degrees, this distribution is about 0.15/0.85. It is therefore assumed that the height of the berm in front of the jet, the so-called erosion front, is about 15% of the

total penetration depth. This effect should be added to the eventual results of the model. The application of Eq. (E.1) does however also mean that the amount of flow and momentum available for the erosion also decreases.

However, the modelled penetration profiles are now formed with a slope angle of α_{bed} = 45 degrees over almost the entire part where erosion is dominant. The transition into the sedimentation-dominated part is only a few gird points long, resulting in a very sharp edge in the calculated profile, as is illustrated in Figure E.4. This transition is far more gradual in the observed profile. This sudden transition is caused by the effect of the slope correction factor $k_{slope,//}$ on the critical Shields parameter.

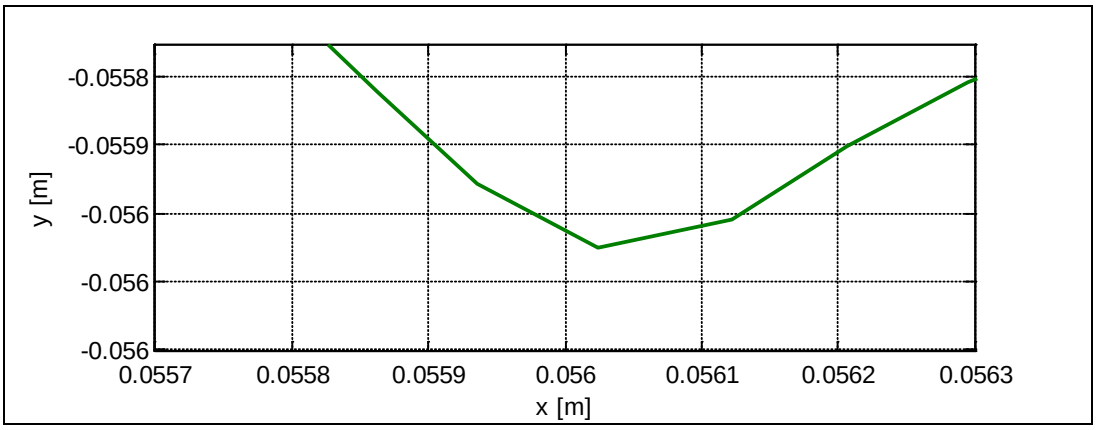

Figure E.4 – Transition between erosion and sedimentation for Test 1

E.1.2 Effect of slope correction factor

The slope coefficient $k_{slope,//}$, given by Eq. (E.2), takes the influence of the bed slope on the critical Shields parameter into account. After all, a stone is less stable on a downhill slope and vice versa. However, this equation is only valid for $|\alpha_{bed}| < \varphi$; when the (negative) bed angle is greater than the angle of repose, $k_{slope,//}$ and thus θ_{cr} becomes zero. This seems logical, since a stone on a slope steeper than the angle of repose has no stability and any load will then cause movement.

$$\begin{aligned} k_{slope,//} &= \frac{\sin(\varphi + \alpha_{bed})}{\sin\varphi} && for\ |\alpha_{bed}| < \varphi \\ k_{slope,//} &= 0 && for\ \alpha_{bed} \le -\varphi \\ k_{slope,//} &= 2 && for\ \ \alpha_{bed} \ge \varphi \end{aligned} \qquad \text{(E.2)}$$

The slope correction factor is also incorporated in the modified critical Shields parameter:

$$\theta_{cr}{}' = \theta_{cr}\left(k_{slope,//} + \frac{v_e}{k}\frac{n_l - n_0}{1 - n_l}\frac{1}{\Delta(1 - n_0)}\right) \qquad \text{(E.3)}$$

This means that with $-\alpha_{bed} \ge \varphi$, only the last part of Eq. (E.3), which takes the dilatancy effect into account, prevents that θ_{cr}' becomes zero. A value of θ_{cr}' approaching zero would mean that the calculated pick-up flux, repeated in Eq. (E.4) becomes infinite. Obviously, an infinite erosion velocity is physically not possible. In the model, this is prevented by applying an upper limit of the calculated bed angle of $\alpha_{bed} = \alpha_{bed,max}$.

$$\psi_e = 0.00033\rho_s\sqrt{\Delta g D_{50}}{D_*}^{0.3}\left(\frac{\theta - \theta_{cr}{}'}{\theta_{cr}{}'}\right)^{1.5} \quad \text{(E.4)}$$

However, the flow velocity in the jet decreases with an increasing distance while the settling flux also becomes more relevant due to the increase of the near-bed concentration. These two factors causes a decrease of the erosion velocity, eventually leading to a decrease of the calculated bed angle so that $\alpha_{bed} < \varphi$. In this situation, the slope correction factor is no longer zero. Since the dilatancy effect is already small due to the relative large permeability, $k_{slope,//}$ becomes very quickly dominant in Eq. (E.3). The effect of an increase of θ_{cr}' has also a large effect on the pick-up flux, provided by Eq. (E.4). A snowball effect is then initiated, because a decrease of the pick-up flux leads to a decrease of the bed angle, further increasing the slope correction factor and again decreasing the pick-up flux. In only a few steps, the pick-up flux is sharply reduced, as is illustrated in Figure E.5. Since the bed angle becomes more flat, the value of the settling flux also increases slightly. This combined effect causes the sudden transition between the erosion- and sedimentation dominated part, which is visible as the sharp edge in the profile.

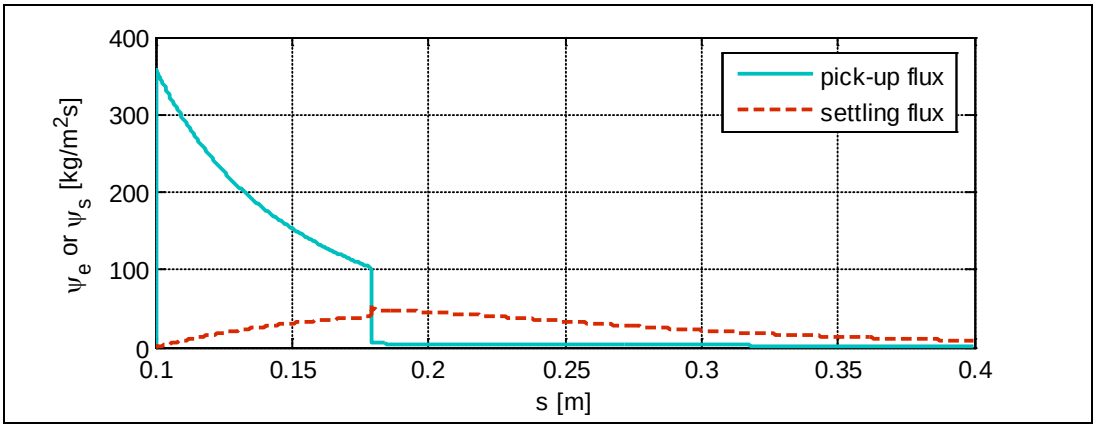

Figure E.5 – ψ_e and ψ_s plotted against s for p_j = 0.023 bar and v_{trail} = 0.07 m/s

A similar snowball effect occurs when the erosion velocity at one of the first grid points is large enough to create a bed angle that leads to a decrease of the slope correction factor, subsequently leading to an increase of the pick-up rate. This eventually leads to a vertical slope, which is retained long due to the zero value of $k_{slope,//}$. When the erosion velocity does not exceed this threshold value, the pick-up rate and the bed slope remains low, i.e. they do not stimulate each other.
This is illustrated by taking two hypothetical cases with p_j = 0.008 bar and v_{trail} = 0.05 m/s but with slightly different flow rates: one with Q_0 = 0.32 dm³/s and one with Q_0 = 0.33 dm³/s. Both obtained profiles are illustrated in Figure E.6, obviously without the use of $\alpha_{bed,max}$ = 45 degrees. Such a difference in the pick-up rates as illustrated in Figure E.7 while the flow velocity only very slightly differs, is not logical.

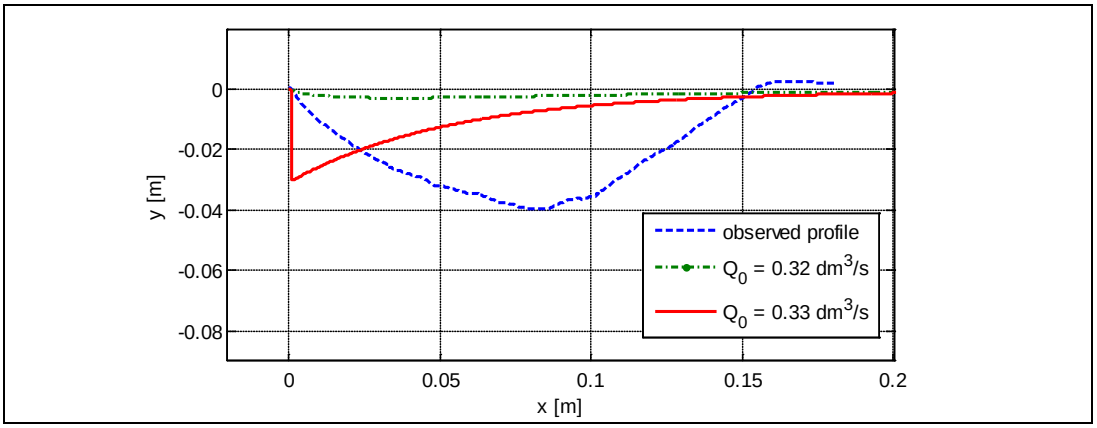

Figure E.6 – Profiles for p_j = 0.008 bar and v_{trail} = 0.05 m/s with varying Q_0

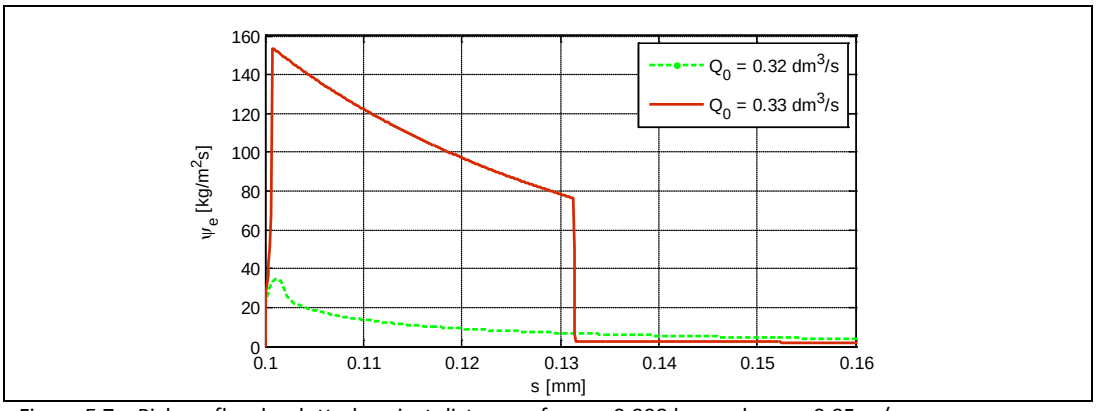

Figure E.7 – Pick-up flux ψ_e plotted against distance s for p_j = 0.008 bar and v_{trail} = 0.05 m/s

E.1.3 Application of pick-up function of Fernandez Luque

Since the division by θ_{cr}' has a large effect on the modelled pick-up rate, another pick-up function without this division may be more suitable, such as the equation of Fernandez Luque, which is, moreover, based on bed-load erosion:

$$\psi_{e,FL} = \epsilon \rho_s \sqrt{\Delta g D_{50}} (\theta - \theta_{cr}')^{1.5} \qquad \text{(E.5)}$$

Fernandez Luque found its function empirically after performing tests with various types of sediment, up to D_{50} = 3 mm; also used in the scale tests of this study. However, he used a longitudinal flow with $\theta < 0.5$ and $\alpha_{bed} < 22$ deg, both smaller than in this study.
He found that a value of ϵ = 0.04 gave a good agreement to all obtained results, although later Van Rijn found that the value partly depended on the grain diameter. A larger value of ϵ = 0.14 gave a better agreement with his results with particles of D_{50} = 1.5 mm. However, the best agreement with the current observed results were obtained with an even larger value of ϵ = 0.6, see also Figure E.8.

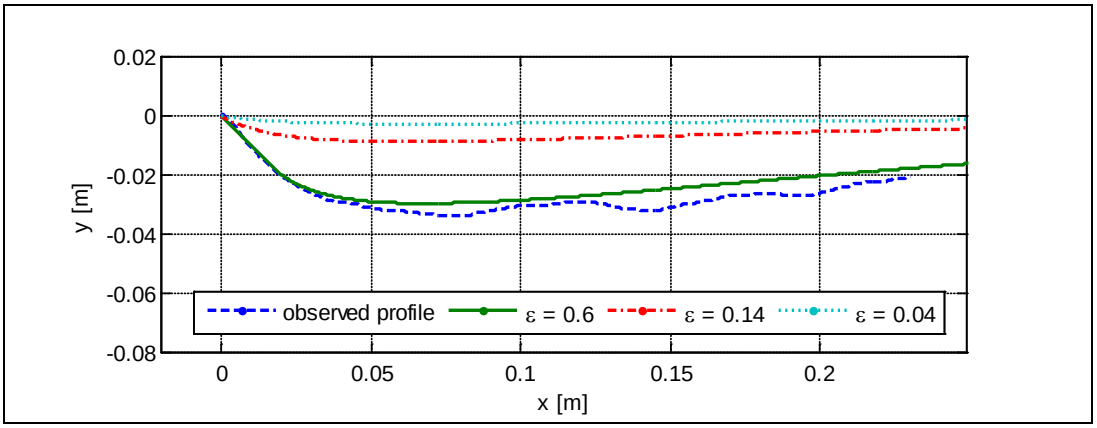

Figure E.8 – Profiles for p_j = 0.028 bar and v_{trail} = 0.2 m/s with varying ϵ

Note that again a value of $\alpha_{bed,max}$ = 45 deg is used to prevent a vertical penetration of the jet.

E.1.4 Incorrect settling flux

The use of the pick-up function of Fernandez Luque with ϵ = 0.6 results in a very good agreement with Test 3, but the calculated penetration depth is too small for Test 1 and 2. An increase of ϵ does not lead to a significant better agreement than with the function of Van Rijn; the correct penetration depth is only achieved with improbable high values of ϵ, see also Figure E.9 where a value of ϵ = 2.6 is used.

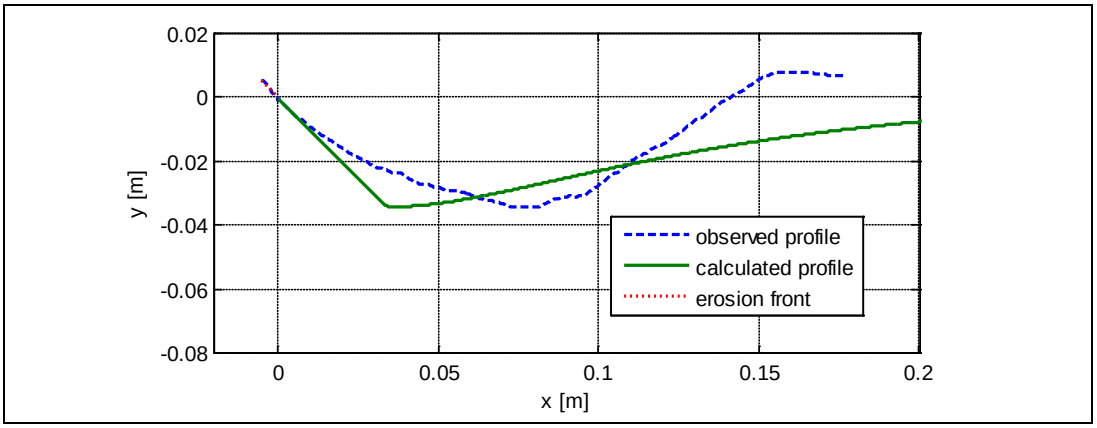

Figure E.9 – Profiles for p_j = 0.008 bar and v_{trail} = 0.05 m/s with ϵ = 2.6

Instead of an incorrect modelling of the pick-up flux, the low penetration depth can also be caused by an incorrect modelling of the settling flux. After all, the sedimentation-dominated part of the observed profile starts further on and is more pronounced than in the calculated profile, which has a long and shallow sedimentation profile. When the penetration profile is calculated without settling, it shows that the erosion-dominated part of the profile has a relative accurate agreement, see Figure E.11 and Figure E.10 where the profiles without settling have a similar gradual decrease of the bed angle as the observed profile. However, the profile obtained without settling for p_j = 0.028 bar, illustrated in Figure E.12, shows too much erosion. Apparently, the combination of pick-up and settling is modelled correctly for this situation.

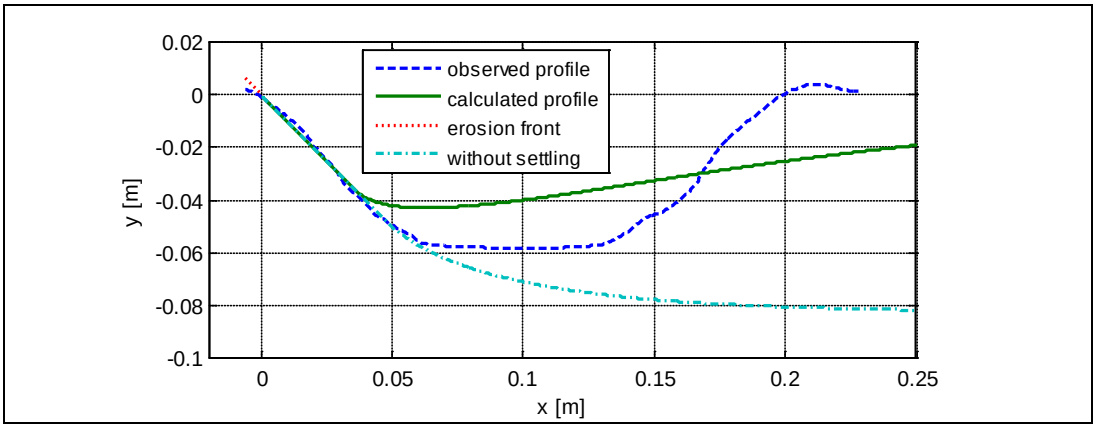

Figure E.10 – Profile with and without settling with p_j = 0.023 bar and ϵ = 0.6

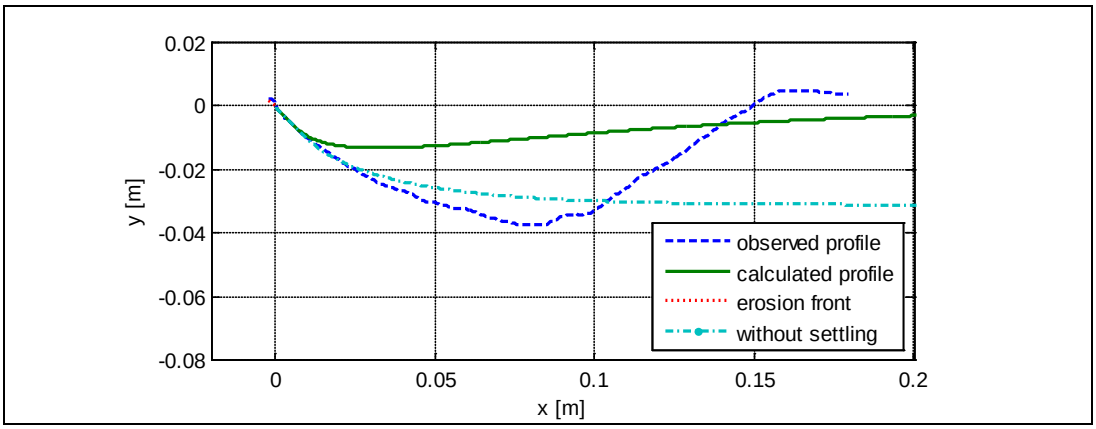

Figure E.11 – Profile with and without settling with p_j = 0.008 bar and ϵ = 0.6

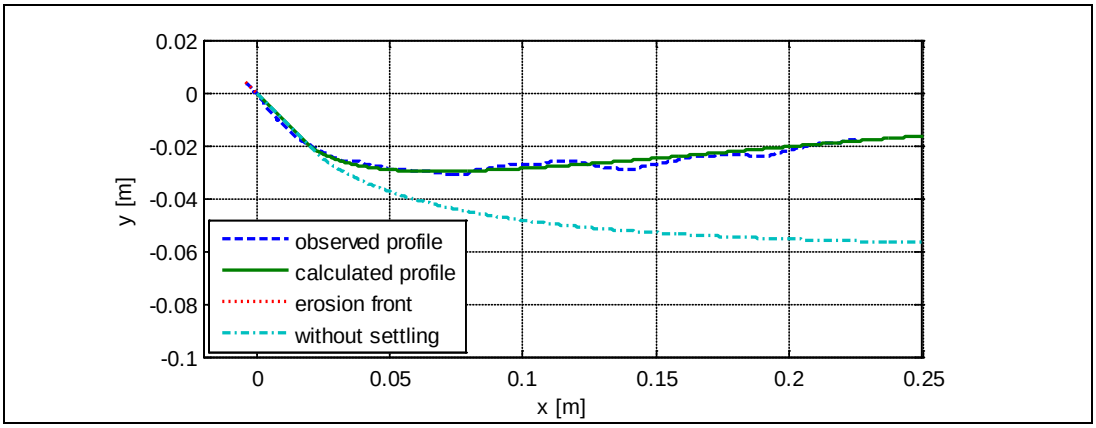

Figure E.12 – Profile with and without settling with p_j = 0.028 bar and ϵ = 0.6

The pick-up and settling processes should be studied in more detail in order to explain the discrepancies between the modelled and observed profile. A possible reason could be one of the following processes:

- It can be argued that the transition between the erosion- and settling-dominated parts is modelled 'too early' in test 1 and test 2. An overall lower settling flux would postpone the point of transition, but would also cause that the slope in the settling part becomes too small, i.e. the sedimentation velocity would then be too low.

- It is possible that the effect of hindered settlement is larger in the erosion-dominated part than is modelled, leading to a lower settling flux in this part of the profile. This can for instance be caused by an incorrect calculation of the near-bed concentration, which is now assumed to be twice the average concentration. A limited settling flux in this part causes also an increase of the concentration, which can result in a higher sedimentation velocity once the extra effect of hindered settlement is stopped. This results in a steeper slope, with a closer resemblance to the slope that is observed during the tests.
- It is also possible that turbulent fluctuations of the flow affects the concentration profile, which is assumed to be linear. An upward fluctuation can also decrease the fall velocity of a grain. Turbulence is not incorporated in the model, since a uniform flow is assumed and the magnitude of turbulence in the scale model is difficult to determine. Moreover, turbulent fluctuations are important in the case of incidental erosion with values of θ close to the threshold of motion. The effect of turbulence on continuous erosion with relative high values of θ is probably lower. However, if turbulence would be taken into account in the model, the pick-up flux would also increase. After all, turbulence increases the Shields parameter as expressed in Eq. (2.46). This would lead to a decrease of ϵ in order to obtain a good agreement with the observed profile. With r_t = 0.1, such a good agreement can be found with ϵ = 0.25, leading to a similar pick-up rate as in the case of ϵ = 0.6 and without turbulence.
- Bed-load transport is a combination of rolling, saltations and sheet flow. It is possible that the settling processes with bed-load are different than in a 'normal' situation with settling suspended sediment. The settling of the stones can possibly be a more kinematic process. In this way sedimentation (i.e. bed level increase) starts when the velocity of the stone is not sufficient anymore to transport the stones over the highest point of the 'berm', where the flow velocity is close to the critical velocity u_{cr}. If a linear profile is assumed, i.e. a constant 'erosion' velocity, the value of the flow velocity at the start of sedimentation, u_s, can be calculated. This situation is sketched in Figure E.13. However, the correct value of h_{pen} and $\tilde{v}_e$ has to be iteratively calculated in the model, which is a rather complex process and is not applied to the current model. Also, the effects of the slope on the stability of the stones, $k_{slope,//}$, and the drag coefficients has to be taken into account.
- The flow can be modelled as a two-layer model, with the upper layer as a low-density fluid with some suspended sediment, and the lower layer as the movable bed, modelled as a high-density fluid. This model is based on the idea of sheet flow that does not comprise the entire jet flow. Since both layers have a different flow development, this may result in a better agreement with the observed processes.

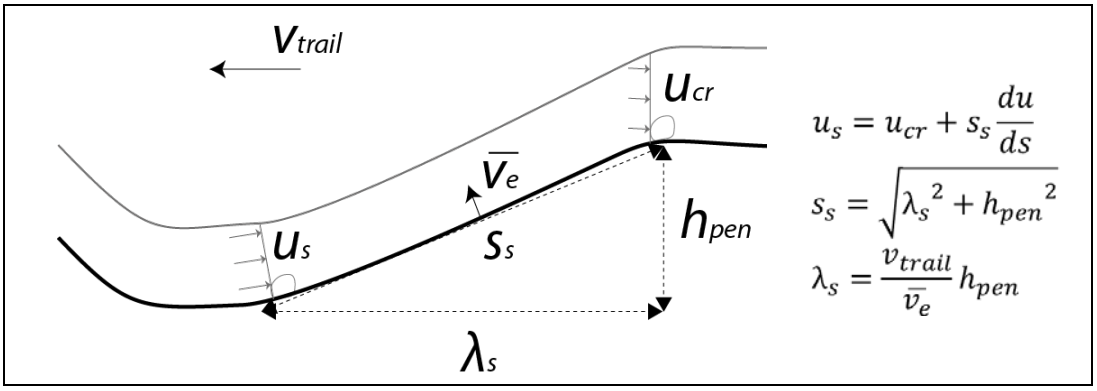

Figure E.13 – A kinematic approach to model the settling processes

A 'delay of sedimentation' can be modelled in the current model by introducing a forced transition between the parts with and without settling, i.e. the settling flux is forced to be zero until the transition value of the flow velocity u_s. The values of u_s are obtained by trial-and-error and are different for each test. The agreement with the observed profile is reasonably good.

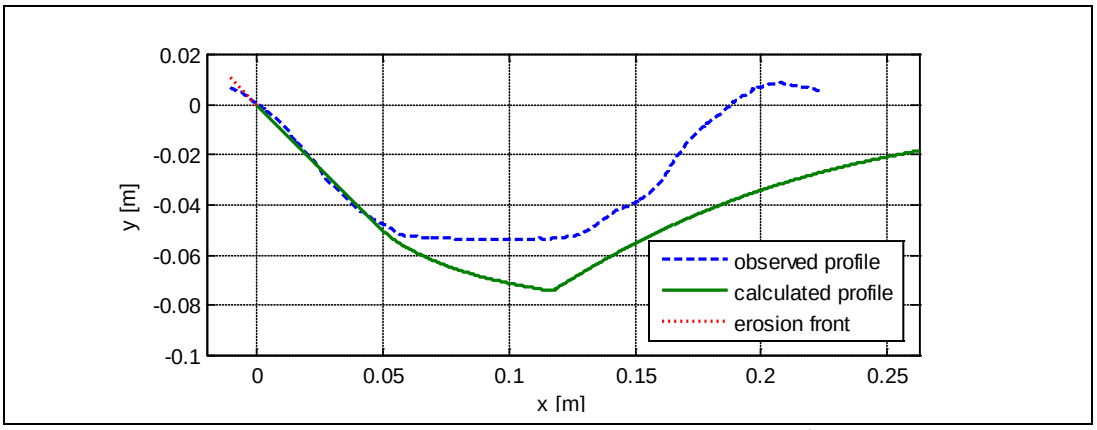

Figure E.14 – Calculated and observed profile with p_j = 0.023 bar and u_s = 0.45 m/s

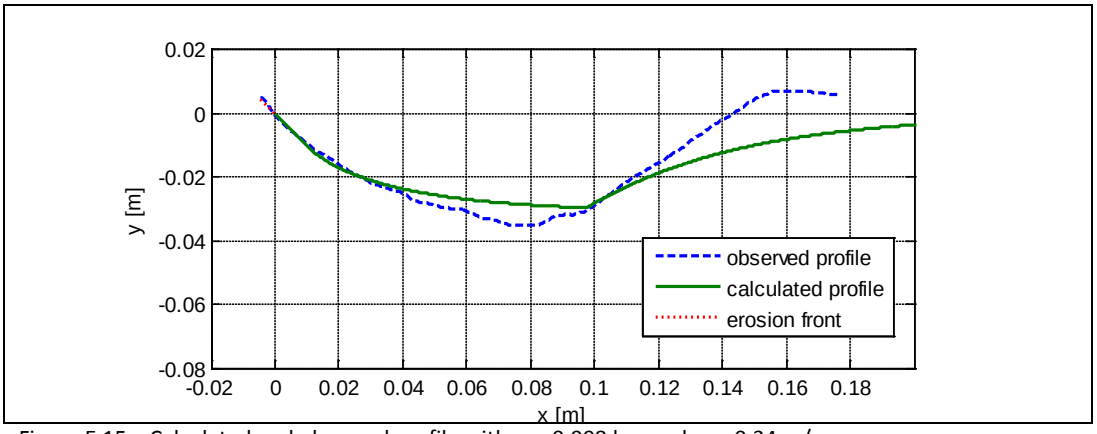

Figure E.15 – Calculated and observed profile with p_j = 0.008 bar and u_s = 0.34 m/s

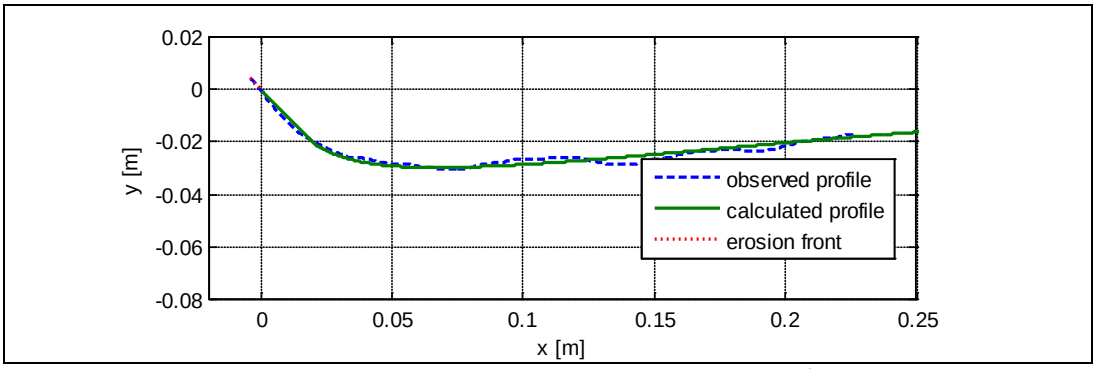

Figure E.16 – Calculated and observed profile with p_j = 0.028 bar and u_s = 0.85 m/s

E.1.5 Bed-load transport gradient

It is also possible to neglect the processes of pick-up and settling; instead, the gradient of the sediment transport capacity can be used to calculate the erosion velocity, see Figure E.17.

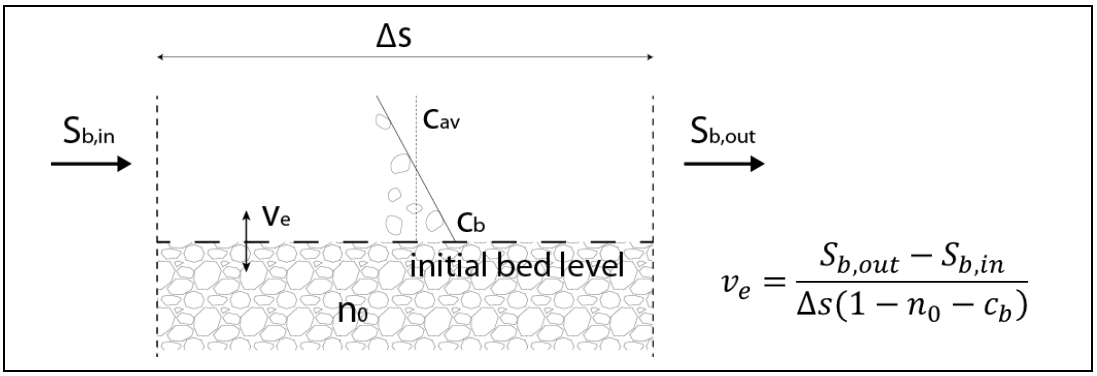

Figure E.17 – The erosion velocity can be seen as the gradient of the transport capacity

The transport capacity is given by Wilson for bed-load transport:

$$S_b = \frac{11.8{u_*}^3}{g\Delta} = 11.8\sqrt{(g\Delta {D_{50}}^3)}\theta^{1.5} \qquad \text{(E.6)}$$

However, the Shields parameter decreases along the flow trajectory; i.e. erosion will only occur at the first grid point, afterwards the decrease of transport capacity leads to settling of the sediments. Such an approach is therefore actually not applicable to erosion by a jet flow. However, the transport capacity is not reached instantaneously and due to the trail velocity, only a limited number of stones can be eroded at every point. Therefore, the gradient between the capacity and the total entrained soil per unit width in the flow is used:

$$v_e = \frac{S_b - {Q_s}/{b_j}}{\Delta s(1 - n_0 - c_b)} \qquad \text{(E.7)}$$

When this expression of the erosion velocity is used in the model, the profile as illustrated in Figure E.26 is obtained for Test 2. It shows that the available transport

capacity is capable to erode all possible sediment, resulting in a vertical penetration. Along the flow trajectory, the capacity decreases while the entrained soil in the flow increases. This eventually leads to the situation where the capacity is not large enough to erode all available sediment, leading to a decrease of the bed angle. However, in only a few steps, the capacity is not sufficient anymore to entrain sediment at all. Since the capacity also decreases with increasing flow distance, stones in the flow eventually has to settle, leading to an increase of the bed level.

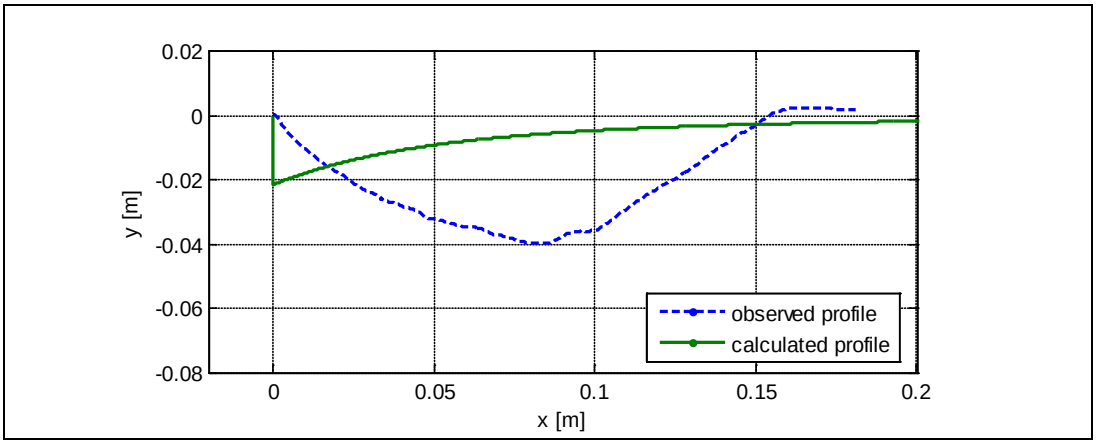

Figure E.18 – Profiles for p_j = 0.008 bar and v_{trail} = 0.05 m/s, transport gradient

When the maximum bed angle is set to $\alpha_{bed,max}$ = 45 deg, the results as illustrated in Figure E.19. Remarkably, this result is very similar to the profile obtained with the Van Rijn pick-up function. This also means that the steep slope, imposed by $\alpha_{bed,max}$, and the sharp transition to the settling-dominated part is present, while these two processes are not observed during the tests. The transport capacity S_b is plotted against the distance s, together with the total entrained soil per width Q_s/b_j in Figure E.20.

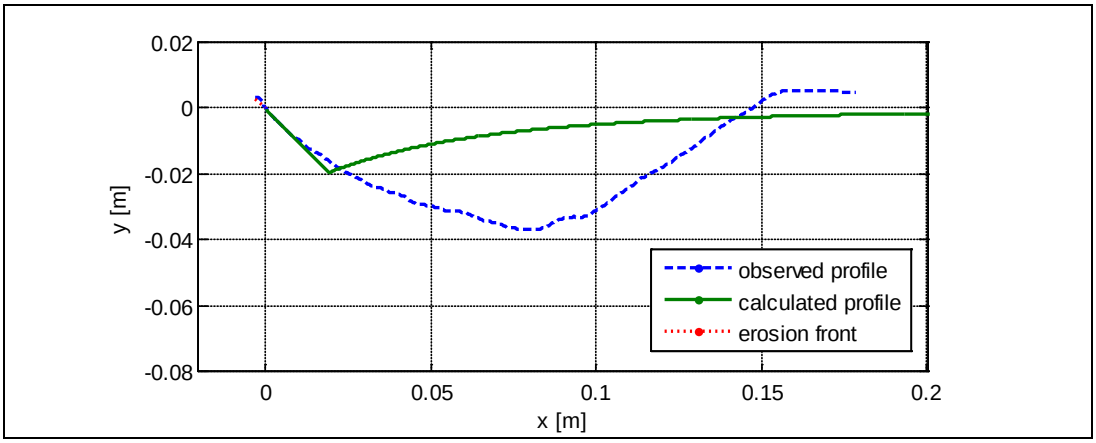

Figure E.19 – Calculated and observed profile for $\alpha_{bed,max}$ = 45 deg, transport gradient

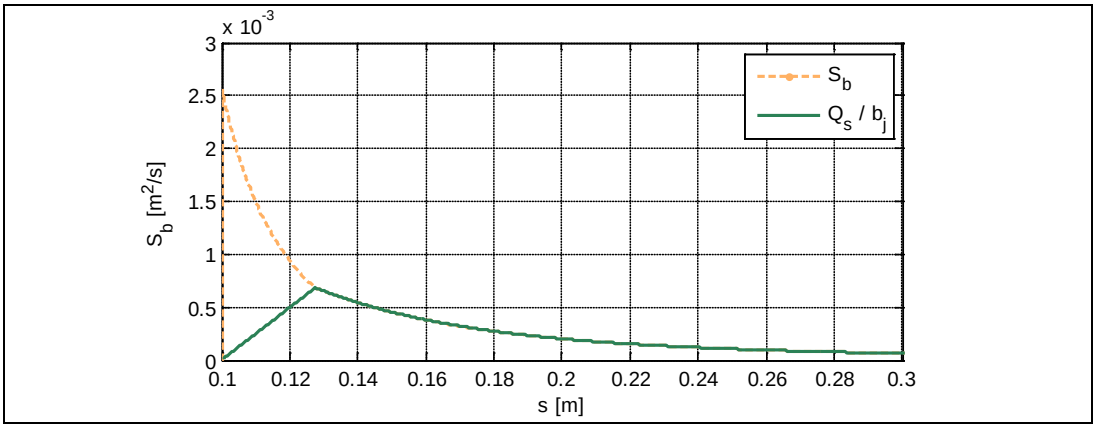

Figure E.20 – Transport capacity and entrained soil per width plotted against distance s

Note that the bed slope also influences the transport capacity: the flow is able to transport more sediment on a downward slope and vice versa. However, the terms to incorporate this effect into the equation for the transport capacity is similar to the slope correction factor for the stability, $k_{slope,//}$. This also means that this factor is not applicable anymore with $\alpha_{bed} \geq \varphi$. A slope correction factor is therefore not used in the calculation for the transport capacity. However, an inclusion of the correction would only mean an increase of the capacity during erosion (downward slope) and a decrease during sedimentation (upward slope). The effects of a vertical penetration and the sudden transition towards a settling-dominated part with increasing bed level would only be higher with a slope correction factor.

E.2 Prediction of penetration

Extra information belonging to section 6.3 is provided in this appendix.

E.2.1 Penetration parameter

The penetration depth h_{pen} can be seen as the deepest point in the penetration profile, i.e. the lowest value of y in the model. The value for h_{pen} is calculated for various combinations of the jet pressure p_j and trail velocity v_{trail}, and is illustrated in Figure E.29. Note that the settling is not taken into account, since it is assumed that there is no sedimentation in the zone of impingement. This leads to a hypothetical situation, but the focus is not on the results but on the relationship between the parameters. The stand-off distance and nozzle diameter are kept equal to the situation of the scale tests that were used to validate the model.

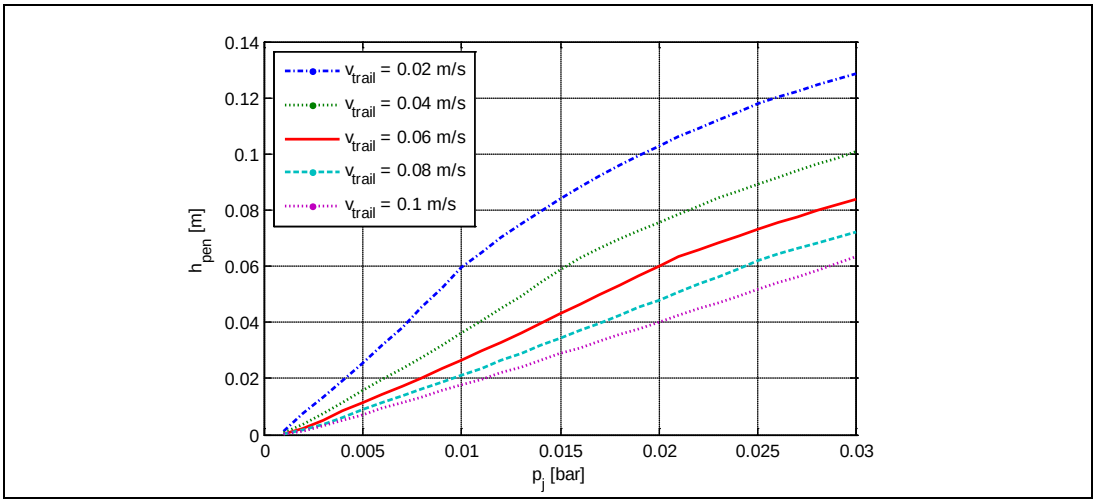

Figure E.21 – Penetration depth h_{pen} plotted against jet pressure p_j

Figure E.29 shows that the penetration depth depends on both the jet pressure and the trail velocity. With a constant pressure, the value of h_{pen} decreases if the trail velocity is increased. This was to be expected, as the bed angle is smaller with a higher value of the trail velocity.

In Figure E.30, the same calculated values of h_{pen} as were illustrated in Figure E.29 are now plotted against E_{pen}; so with a constant value for SOD and D_0. The fact that there is only very little scatter between the points means that the E_{pen} is indeed a suitable parameter to describe the penetration behaviour.

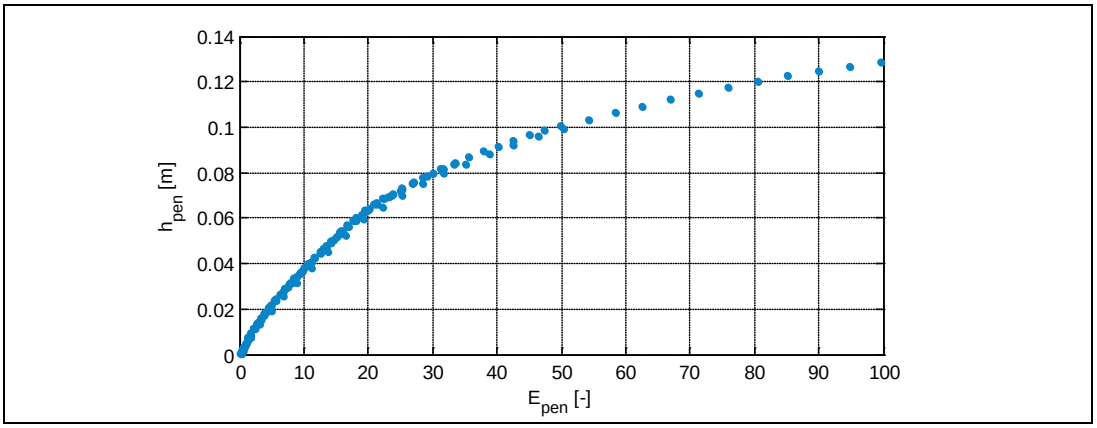

Figure E.22 – Penetration depth h_{pen} plotted against erosion parameter E_{pen}

In order to determine whether the influence of the other parameters are correctly incorporated into the penetration parameter and the penetration is still a function of E_{pen}, a sensitivity analysis is performed. The erosion model is executed with the same values of p_j = 0.001 – 0.03 bar and v_{trail} = 0.02 – 0.1 m/s, but now in combination of a varying D_0. The used values are: D_0 = 1.9 cm, D_0 = 1.4 cm and D_0 = 0.9 cm. The calculated penetration depth h_{pen} is plotted against E_{pen} in Figure E.31. It still shows only little scatter, implying that the use of E_{pen} is also valid for a variable jet diameter.

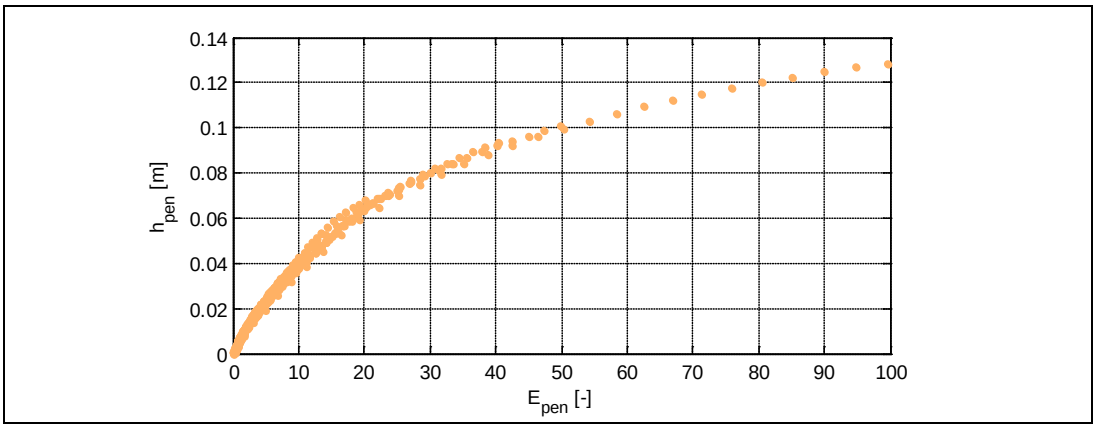

Figure E.23 – Penetration depth h_{pen} plotted against erosion parameter E_{pen} with varying D_0

Adding a variable stand-off distance, with *SOD* = 0.10 m *SOD* = 0.12 m, *SOD* = 0.14 m and *SOD* = 0.16 m, the predicted penetration depth plotted against E_{pen} is as illustrated in Figure E.32. This shows more scatter, which means that the effect of an increasing stand-off distance on the penetration cannot be as easily incorporated in E_{pen} as assumed. This can be explained by the fact that with D_0 = 0.019 m, the jet flow is still in the development zone with *SOD* = 0.10 m, resulting in a different flow rate than jets in the developed zone. When the results with a developed jet are filtered, Figure E.33 is obtained. However, the agreement with the lower values of E_{pen} is still reasonably good in both graphs, implying that the conditions expressed in Eq. (6.33) are still valid, which is the most important.

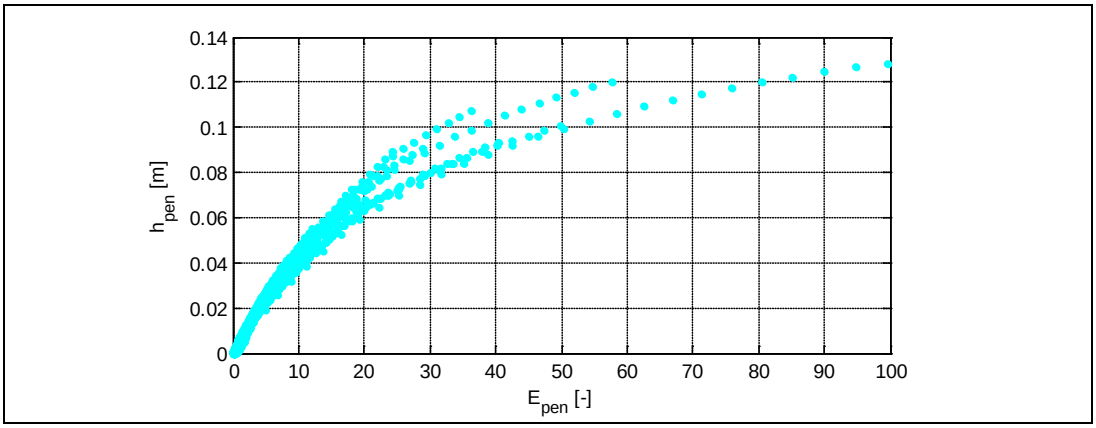

Figure E.24 – h_{pen} plotted against E_{pen} with varying D_0 and *SOD*, in both jet flow regimes

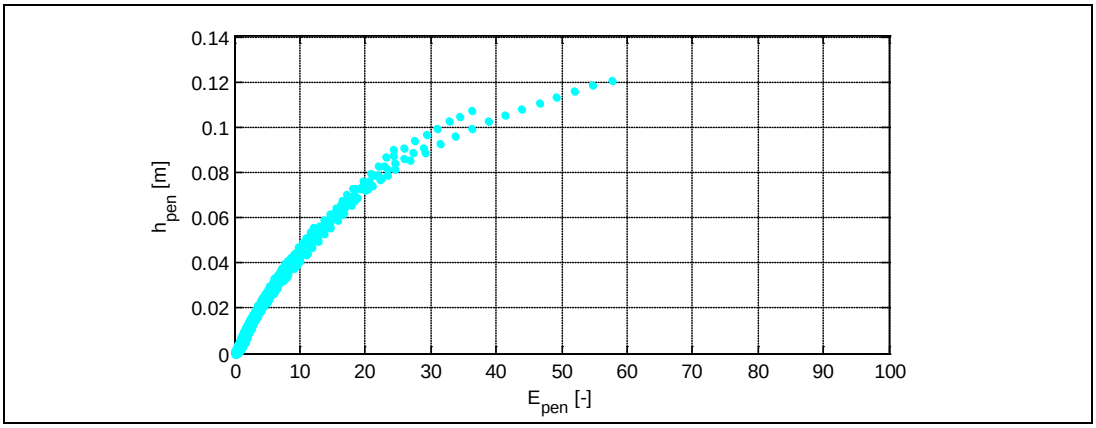

Figure E.25 – h_{pen} plotted against E_{pen} with varying D_0 and *SOD*, developed jet flow

A variation of the stone diameter seems to be more precarious, since its effect on the stability and erosion parameters is more complex. However, this effect is less dominant with relative large stone diameters, as the critical Shields parameter θ_{cr} is constant and thus independent of D_{50}. The assumption of a multifaceted effect is more or less confirmed by Figure E.34, which shows the results with D_{50} = 3 mm, D_{50} = 6 mm and D_{50} = 9 mm with more scatter, including the points with a low value of E_{pen}. It is therefore questionable whether the conditions of Eq. (6.33) still apply for situation with another stone diameter, although it may remain suitable for a simple first approximation.

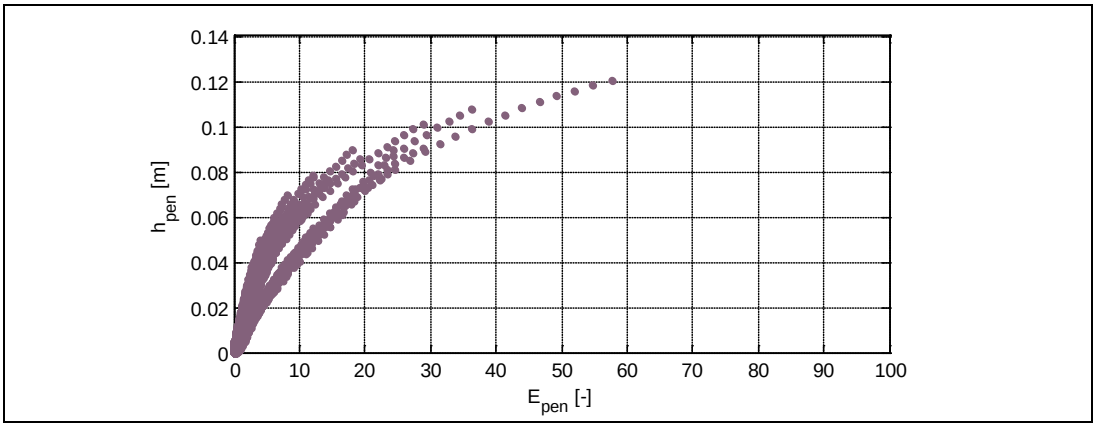

Figure E.26 –h_{pen} plotted against E_{pen} with varying D_0, *SOD* and D_{50}